Probing CD95 Receptor and Ligand Interactions with Multiparametric Image Spectroscopy and Superresolution Microscopy

Inaugural-Dissertation
zur Erlangung des Doktorgrades der
Mathematisch-Naturwissenschaftlichen Fakultät der
Heinrich-Heine-Universität Düsseldorf

vorgelegt von

Xiaoyue Shang
aus Xi'an

Düsseldorf, June, 2025

From the Department/Institute of Experimental Medical Physics
of Heinrich-Heine-Universität Düsseldorf

Printed by the permission of the Faculty of Mathematics and Natural Sciences of
Heinrich Heine University Düsseldorf

This is a modified and corrected version in comparison to the original submitted thesis. Date: November, 2025.

Examiners:
1. Prof. Dr. Cornelia Monzel
2. Prof. Dr. Claus Seidel

Date of the oral defense:

Acknowledgement

I would like to express my deepest gratitude to my esteemed supervisor Prof. Dr. Cornelia Monzel, who enrolled me as a member of her team and supported my PhD journey with visionary guidance and strategic direction. From you, an excellent scholar, I have learned not only scientific research ability but also comprehensive soft skills. Your tireless teaching, patience, and trust shaped me with a better personality and paved the road for a good beginning as a researcher. I am also deeply indebted to Prof. Dr. Claus Seidel as my second supervisor, who shared laboratory space and lab equipment especially thank for the usage of Abberior STED microscope. I learned from you, as a prestigious professor, a systematic knowledge in the field of FRET/STED and the spirit of rigorous research. Next, I want to thank CRC1208 for supporting my PhD study and international conference in the United States. Prof. Dr. Lutz Schmitt, the Spokesperson of CRC1208, and Dr. Cordula Kruse, CRC1208 Coordination, thank you! I'd like to acknowledge my collaborators, Johann Moritz Weck and Prof. Amelie Heuer-Jungemann, for your nice DNA origami sample preparation and discussion with DNA/protein labeling. I cannot finish this work without your collaborative support!

I want to give my special thanks to Dr. Nina Bartels, you introduced me with all cell culture skills and microscopy skills from basics to Abberior STED with great patience. You led me to part of your research topic 'CD95', where I started my research journey. Your spirit of hardworking and positivity influenced me and encouraged me to keep going through a lot of difficulties. Speaking of my colleagues in Prof. Monzel's group, I want to first thank Dr. Andreas Neusch for not only the introduction of Matlab and Äkta, but also your kindness of helping me with integration into the group. As a foreign student, I thank all my colleagues for your patience, help and tolerance with respect to language, culture, teamwork and so on. Many thanks to Dr. Philipp Hagemann for your help with STED microscope alignment and teaching, your punctuality at work is impressive. Thank Siegrun Land and Christiane Quindt for ordering chemicals for me and assistance with documents. Soner Durmus, thank you for your help with cell culture lab preparations. Thank all my colleagues, Luisa Coen, Jan Lange, Hadeel Khalouf, Dr. Iuliia Novoselova, Dr. Daniel Kuckla, thank you for all your silent help in the lab!

Speaking of members in Prof. Seidel's group, I'm also grateful to Dr. Nicolaas van der Voort for your systematical introduction of Abberior STED microscope, cells/origami measurements and other physics knowledge. I want to thank Dr. Julian Koch and Dr. Annemarie Greife for your introduction to western blot and cell culture. I am also thankful to Dr. Jakub Kubiak and Alexander Larbig for your discussion of biochemistry regarding site specific labeling, click chemistry, Äkta usage and so on. I owe great thanks to Dr. Suren Felekyan for your knowledge of data analysis and softwares. And thank Dr. Ralf Kühnemuth for your help with STED microscope alignment and laser knowledge. Noah Salama and Dr. Oleg Opanasyuk, thank you for your help with interpreting the FRET nanoscopy code. I especially thank Noah Salama for your great patience of explanation of FRET and STED related knowledge. Matthias Fröscher,

thank you for your help with IT questions with computer errors or connection problems. Bekir Bulat, thank you for your help with all chemical knowledge.

Thanks should also go to Prof. Dr. Alexej Kedrov for providing the Amersham imager. I'd like to recognize Dr. Marius Otten for help with preparation of TEM imaging. Thank Dr. Stefanie Brands for sharing the multi-tip pipette and Tecan plate reader. Finally, I want to thank my family and friends, for your emotional support all along my journey.

Abstract

TNFRSF/TNFSF superfamily members showed great potential in recent cancer immunotherapies development. CD95/CD95L as a classic member of TNFRSF/TNFSF, however their signaling pathway and stoichiometry upon apoptosis initiation has not been solved yet. In this study, I focused on two goals: i) interpreting the stoichiometry of membrane CD95 upon CD95L variants (IZ-CD95L or Flag-CD95L) binding using Hela WT cell line; ii) understanding of CD95 extracellular domain (ECD) interactions in vitro.

To this end, I first successfully designed and produced both CD95 receptor and IZ-CD95L protein to be used in biomedical and afterwards biotechnological assays. IZ-CD95L was expressed using HEK293T cell line and modified afterward. I verified biological activity of IZ-CD95L using apoptosis dynamics analysis and systematically compared its cytotoxicity with Flag-CD95L with or without anti-Flag mAb crosslinking at varying concentrations. The result shows that at 1000 ng/ml, IZ-CD95L showed better performance than Flag-CD95L. This is further tested by surface plasmon resonance measurement. To interpret the stoichiometry of membrane CD95 from a molecular perspective, STED imaging was performed. I have been able to perform and improve STED staining and imaging data analysis. From these experiments, CD95 was identified as pre-existing monomer/dimers. Upon ligand triggering, CD95/CD95L form monomers/trimers and dimers/trimers rather than higher oligomers, excluding the previously proposed hexagonal CD95 configurations in Hela WT cell line.

Secondly, I aimed at CD95 ECD interactions and spacing on DNA origami nanoplatform. CD95 ECD was in vivo biotinylated using co-transformation of BirA plasmid with CD95 ECD construct using *E.coli* cell line. The protein was successfully labelled with ATTO 643 and ATTO 594 using NHS ester N-terminus labelling and degrees of labelling were achieved with 1.12 and 1.22 respectively. I coupled CD95/streptavidin/DNA origami construct for FRET nanoscopy. The DNA origami was labelled with a high FRET pair and was used as positive control and showed detected FRET events. However, no significant FRET was detected using CD95/streptavidin/DNA origami constructs. By using true FRET pair as a positive probe, I performed and improved a protocol of sample preparation, FRET nanoscopy data acquisition and imaging data analysis. I figured out that in the case of CD95/streptavidin/DNA origami, FRET can be detected but not as expected sufficiently high. Further controls need to be for verification of this finding including, data analysis code improvement, Abberior STED microscope alignment and labeling efficiency improvement. Since FRET is detected only in rare cases, we can exclude the formation of stable CD95 dimers, but rather have a low fraction or transient interaction between CD95 receptor pairs.

Contents

Preface

Part of this thesis has been published in preprints:

Content in Materials and Methods part (Chapter 4.4.3) and Results part (Chapter 6.2.1) was published in:
Shang X, et al. High yield purification of an Isoleucine zipper modified CD95 Ligand with either biotin or DNA-oligomer binding domain for efficient Cell Apoptosis Induction. bioRxiv. 2024:2024-10.

Content in Materials and methods part (Chapter 5.3.4) along with the original code was published in:
Budde JH and Van Der Voort N, et al. FRET nanoscopy enables seamless imaging of molecular assemblies with sub-nanometer resolution. arXiv:210800024. 2021 Jul 30.

These parts are rewritten and included in the thesis for coherency. Besides, I performed data analysis on dummy dataset and wrote interpretation of the code in results part (Chapter 9.2).

I Introduction

1. Cell Apoptosis and the CD95 Receptor and Ligand interaction

1.1 Cell death

Cell death is the process by which a cell stops functioning. Cell death can be divided into two general types based on morphological differences, programmed cell death (PCD) and necrotic cell death. PCD is a natural process mediated by cellular programs, whereas necrosis is caused by external stimuli such as infection, disease, or injury (1). PCD is also referred to as cellular suicide and can be subdivided into two types, apoptosis as the type I cell death and autophagy as the type II cell death. Cell apoptosis, the type I cell death, is a highly regulated and controlled process. It is characterized by morphology changes including blebbing, cell shrinkage, and DNA fragmentation (2). Autophagy, type II cell death, is characterized by large cytoplasmic vacuoles that eradicates damaged cell organelles (3). Necrotic cell death is a form of cell death characterized by breakage of cell membrane, during which a cell undergoes swelling, proteases leakage, and release of cellular contents (4).

Cell death plays a fundamental role multicellular organism including tissue development, homeostasis maintenance, and immune regulation. (5). PCD function as deleting cells in a controlled manner. This result in four functions in developmental biology. First, it helps with sculpting the organ such as tissues between fingers. Second, the unwanted structures, such as the tail from an anura, can be removed. Third, excess cells need to be removed during organ development such as development of nervous system. Last, abnormal or injured cells need to be removed for homeostasis during cell proliferation. Therefore, the biological functions of cell death overall improve immune system, cancer prevention, aging and so on (6).

1.1.1 Cell apoptosis

Apoptosis includes several biochemical events that lead to characteristic cell changes and death. Apoptosis can be triggered by two pathways: the extrinsic and the intrinsic/mitochondrial pathways. Both pathways involve activation of caspases. The intrinsic pathway is activated by intracellular signals when cells are stressed by DNA damage or irradiation. which activates apoptosis regulators BAX (Bcl-2-associated protein x) and BAK (Bcl-2 homologs killer). The activated BAX and BAK cause the formation of pores on the mitochondria membrane, leading to cytochrome c release. The released cytochrome c facilitates APAF1 (apoptotis peptidase activating factor 1) oligomerization and apoptosome formation. The apoptosome complex binds with pro-caspase-9 and cleaves the pro-caspase-9 to its active form of caspase-9. Next, caspase 9 cleaves and activates the effector caspase-3 from pro-caspase-3, leading to the eventual cell death. The extrinsic pathway is activated by ligand and membrane receptor interaction, which leads to the formation of a death-inducing signaling complex (DISC). Three mechanisms are well known in the extrinsic pathway, the CD95 ligand (CD95L), the tumor necrosis factor-α (TNF-α) or

TRAIL (TNF-related apoptosis-inducing ligand) pathway. All of them involve the activation of receptors belonging to the TNF receptor superfamily (TNFRSF) and caspases activation (7).

1.1.2 The TNF and TNFR Superfamily

The tumor necrosis factor (TNF) and receptor (TNFR) superfamily members are well known for their role in cell apoptosis or proliferation pathways. Understanding the structural principles of TNFR and TNF superfamily plays a fundamental role in development of cancer immunotherapy (8). The tumor necrosis factor superfamily (TNFSF) is a protein superfamily of type II transmembrane proteins. TNFSF members exhibit a conserved TNF homology domain (THD) and most of them form noncovalent homotrimers. These proteins are expressed primarily on the surface of immune cells (9). This superfamily contains 19 members and can be cleaved into soluble forms by extracellular proteolytic cleavage. The membrane-bound forms of TNFSF members initiate apoptosis signalling with much higher efficiency than their soluble forms. They play important roles in cell apoptosis, proliferation, and differentiation. TNFSF members share high structure homology. Except for dimeric murine GITRL (glucocorticoid-induced TNFR-related protein) (10), all other TNFSF members form heterotrimers/homotrimers. With beta sheets included in THD domains, each monomer forms a 'jelly roll' structure. The homotrimer therefore resembles a cone shape (11). Each cognate receptor binds to the groove of two adjacent dimers of TNFSF ligand and trimeric ligand bound with up to three receptors (12).

The tumor necrosis factor receptor superfamily (TNFRSF) is a protein superfamily of type I transmembrane proteins which are conserved with cysteine-rich domains (CRDs). This family contains 29 members. They are characterized by binding with their cognate ligand within TNFSF. Each TNF receptor contains an ectodomain, a transmembrane domain (TMD), and an intracellular domain for adapter protein recruitment. The ectodomain contains several cysteine-rich domains (CRDs) and forms a rod-shaped structure (13). Most TNFRSF receptors form inactive dimers and transform into active trimers after binding with corresponding ligands (14). The signaling initiation involves in most cases adaptor proteins such as FADD, TRAF (tumor necrosis factor TNF receptor-associated factors), and RIP (ribosome-inactivating protein). TNFRSF can be functionally divided into three groups: i) death receptors (DRs), ii) TRAF-interacting receptors, and iii) decoy receptors (DcRs). DRs contain intracellular death domains (DDs) and trigger apoptosis initiation. DcRs contain no intracellular domains and therefore inhibit apoptosis signaling initiation. TRAF-interacting receptors are characterized by TRAF interacting motifs (15).

1.1.3 CD95 Signaling Pathways

The apoptosis signaling pathway: The CD95 (cluster of differentiation 95) receptor, also known as Apo-1 or Fas, is a member of TNFRSF. CD95 binds exclusively to the CD95 ligand (CD95L). The THD domain of CD95L binds to CD95 on the cysteine-rich domains CRD2 and CRD3 (13). Binding of CD95L triggers recruitment of CD95 on the cell membrane and its activation upon binding to CD95L. The active CD95 exhibit a conformational change in the intracellular death domain (DD), leading to the recruitment of adaptor protein fas-associated death domain protein (FADD) (16). FADD binds with DD *via* homotypic interactions and further recruits pro-casepase-

8. This results in the formation of a death-inducing complex (DISC) formation, composed of DD, FADD, and pro-caspase-8. The effect of complex formation leads to cleavage of pro-caspase-8 into activated caspase-8. Specifically, FADD contains one death effector domain (DED) that binds with pro-caspase 8 via DED filament nucleation (17). Pro-caspase-8 contains two death effector domains: DED1 and DED2 and two sub-units at the C-terminus: the large p18 subunit and the small p10 subunit. The formation of the DED filament allows for pro-caspase-8 dimerization and self-cleavage into an activated form of caspase-8 composed of p10 and p18 subunits. Next, the mature caspase-8 cleaves effector caspases (caspase-3, caspase-6, or caspase-7) into their mature forms leading to the eventual cell death (18).

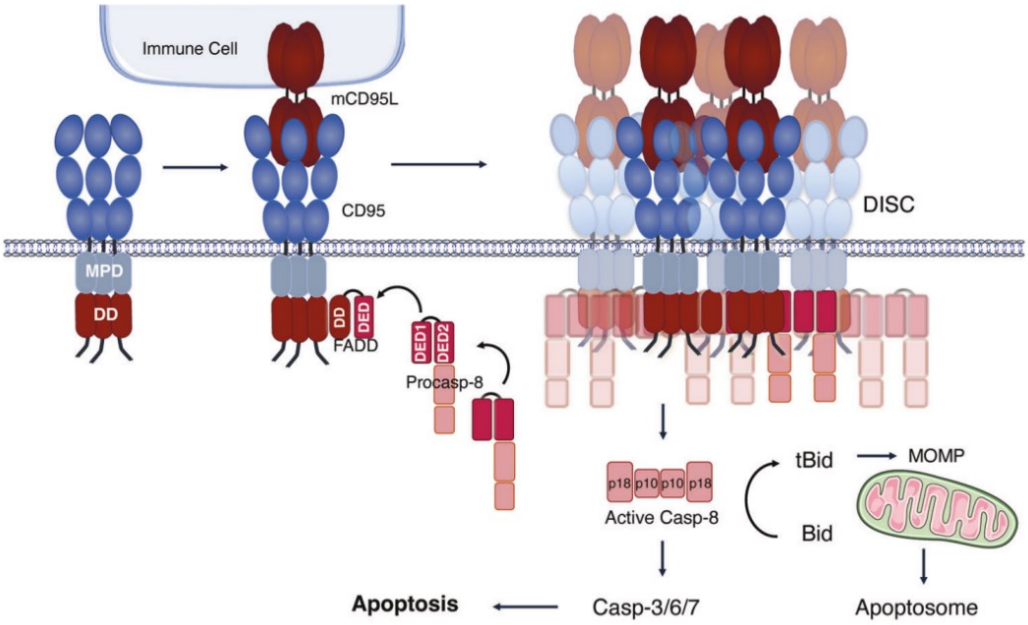

Figure 1. 1 CD95-dependent apoptotic signaling pathway. The figure is taken from (18).

Non-apoptosis signaling pathways: CD95 has been recently reported to be involved in non-apoptotic signaling pathways that result in cell survival/proliferation/migration (19,20). The interaction between CD95 and its ligand CD95L recruits several adaptor proteins resulting in activation of the i) MAPK (mitogen-activated protein kinases), ii) NF-κB (nuclear factor kappa B), and iii) PI3K (phosphoinositide 3-kinase) pathways. All non-apoptotic pathways require CD95L and CD95 binding and DISC formation for downflow protein recruitment. Specifically, the MAPK pathway involves a phosphorylation cascade including activation of RAF-1 (RAF proto-oncogene serine/threonine-protein kinase), MEF (myocyte enhancer factor), and ERK (extracellular signal-regulated kinase) (21). Next, the translocation of ERK facilitates the induction of transcription of proliferation/pro-inflammatory genes in the nucleus (22). In the NF-κB pathway, caspase 8 activates the IKK (the IκB kinase) mediated phosphorylation and of IκB (IkappaB), leading to release of NF-κB from inactivation (23). The activated NF-κB is a heterodimer composed of p65 and p50 subunits. NF-κB translocation into the nucleus promotes the transcription of genes responsible for the pro-inflammatory, proliferation or migration processes (24). The PI3K (phosphoinositide 3-kinases) pathway involves phosphorylation and activation of Akt (protein kinase B) mediated pathways (25).

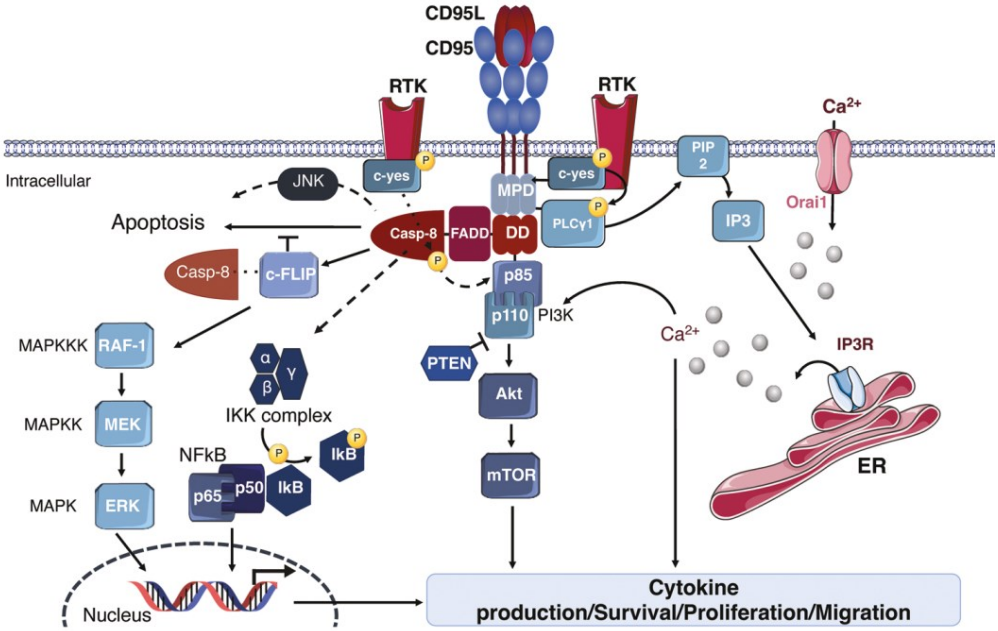

Figure 1. 2 CD95-dependent non-apoptotic signaling pathway. The figure is taken from (18).

1.1.4 Models of CD95 Apoptosis Signal Initiation

A hexagonal model of extracellular and intracellular signalling networks. Based on high structural homology in TNFRSF members and shared downstream signalling partners (15,18), a unified model of the TNFRSF signalling initiation pathway was previously proposed. As described in this model, TNFRSF receptors represent two states: the resting/inactive and the active state. In the resting state, each monomeric receptor binds with another monomer between the cysteine rich domains CRD1 and CRD2, thus burying the ligand-binding sites. Two monomers form an anti-parallel dimer on the surface with a spacing of ~ 12 nm. The surrounding dimers are prearranged in a hexagonal network with each dimer on one edge of the hexagon (see Figure 1. 3 Model 2). At each corner of the hexagon, the monomeric transmembrane domains of from three surrounding dimers cluster and form a trimer. The symmetrical arrangement of trimers and dimers in each hexagon is extended in a large network, with a diameter of ~ 24 nm for each hexagonal unit (26,27). This hexagon arrangement allows for cooperative signalling leading to a twofold amplification of output (28). TNFSF ligand binds on the stalk region of anti-parallel dimers, located at the corner of each hexagon. This binding results in the trimerization of the receptor transmembrane domains and triggers the conformational change of anti-parallel dimers into parallel trimers. This conformational change brings the intracellular parts of receptors (such as death domains DDs) into the vicinity, which is crucial for downstream signalling protein (such as FADD and pro-caspase-8) recruitment to initiate apoptosis. The resting state of the receptors can be stabilized by antagonist antibodies which cover the ligand binding sites and lock the nonsignaling state (29). In contrast, agonist antibodies stabilize the active state by cross-linking two neighbouring trimeric receptors thus enhancing apoptosis initiation (30).

A minimal model of TNFR apoptosis signalling pathway. Our group in a recent study proposed a minimal model of TNFR/TNF apoptosis signalling initiation by employing super-resolution microscopy and multi-parametric fluorescence spectroscopy techniques (31). As described in this model, inactive CD95 mostly forms monomers on cell membranes. After the trimeric CD95L binding, CD95 and CD95L form monomer-trimer, dimer-trimer, or trimer-trimer complexes. This minimal model suggests a direct apoptosis initiation from the extracellular into the intracellular region without the need to form large signalling complexes, such as the hexagonal shaped assembly (15). Specifically, the oligomeric states of CD95 were studied by the cell lifetime FRET (Förster resonance energy transfer) image spectroscopy (CELFIS), with CD86 as a monomer/no FRET control and CTLA4 (cytotoxic T-lymphocyte associated protein 4) as a dimer/high FRET control. CD95 or control proteins were fused with GFP (the donor) or mCherry (the acceptor) as a FRET pair. Cells were transfected with designed protein constructs and measured by lifetime FRET imaging. The distribution of donor fluorescence lifetimes in the absence and presence of acceptor was measured, where the FRET ratio x_{FRET} was calculated and converted into oligomer fractions with a factor of 2.8 oligomer per 1 % x_{FRET}. As controls, CD86-expressing cells showed a low average x_{FRET} of ~ 3 % and CTLA4-expressing cells showed x_{FRET} of ~ 37 %, manifesting monomers and dimers respectively. As revealed by the CELFIS experiment, there are more than ~ 96 % CD95 monomers and up to 4 % dimers at the resting state. After ligand binding, ~ 15 % of receptors form small, discrete complexes (CD95 X-mer/CD95L trimer complexes). This result was supported by confocal photobleaching step analysis (cPBSA) and stimulated emission depletion (STED) data analysis. As a molecular-sensitive tool, cPBSA was used to detect CD95

stoichiometries. In the case of CD95 before and after ligand addition, the number of bleaching steps (N_{steps}) was detected as less than 5, indicating no large hexagon (N_{steps} of hexagon is more than 6) formation. The quantitative spot analysis of STED data confirms that high-order CD95 oligomers do not form, since only diffraction-limited spots were detected.

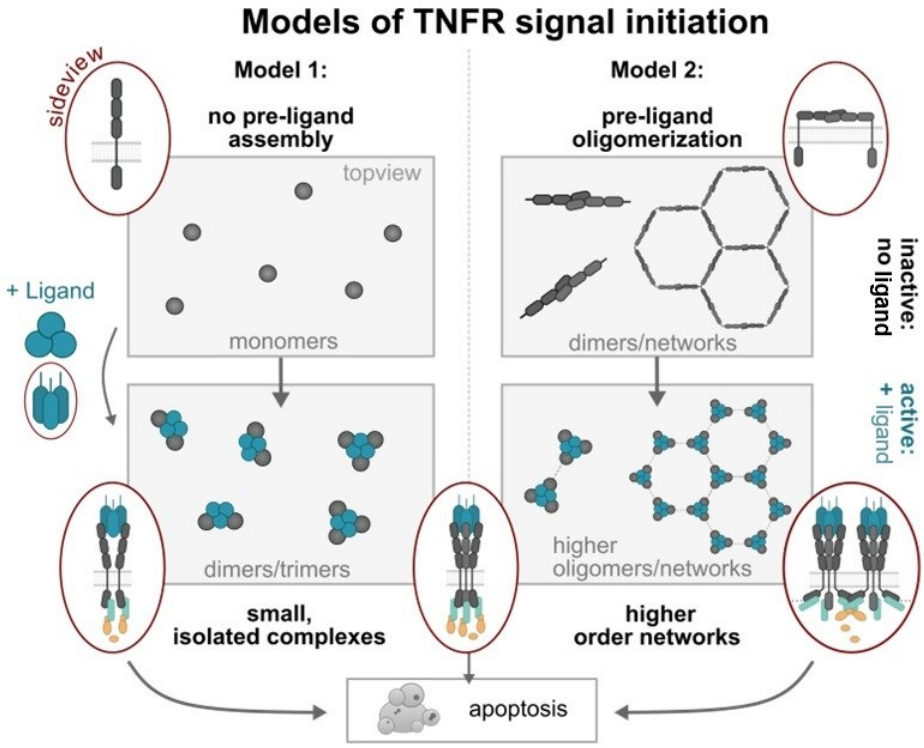

Figure 1. 3 Illustration of the hexagon and minimal CD95 signal initiation models. The image was taken from (31). Right panel: a previously proposed hexagonal model of CD95 apoptosis signalling initiation. Left panel: a minimal model of CD95 apoptosis signalling pathway.

1.2 The CD95 - CD95L interaction

1.2.1 Structure of CD95

CD95 (cluster of differentiation 95), also known as fas, Apo-1 or TNFRSF6, is a member of TNFRSF family. CD95 is type I transmembrane protein. The mature CD95, without the 17 aa signal peptide, is composed of 319 amino acids (32), including the extracellular domain (ECD), a transmembrane domain (TM), and the intracellular domain (ICD) (see Figure 1. 4A). The ECD features three cysteine-rich domains (CRDs), each of which contains six cysteines to form three disulfide bridges. The crystal structure of CD95 ECD resembles a rod shape due to the repeated CRDs (33). The ICD contains a death domain (DD) with 93 amino acids (26). CD95 exists on the plasma membrane mostly as monomers (31) or homodimers (15) without its sole cognate ligand, CD95L. The dynamic equilibrium among different oligomeric states is influenced by the expression level of CD95 on the membrane (31). The death domain (DD) serves as a scaffold, recruiting fas-associated death domain protein (FADD) and pro-caspase-8 to form the death-inducing signalling complex (DISC) (34), which subsequently triggers caspase-8 activation and downstream apoptosis signalling (35). Noteworthy, the CD95L/CD95 has also been reported to be involved in a non-apoptotic pathway leading to proliferation or migration (20) (See Figure 1. 2).

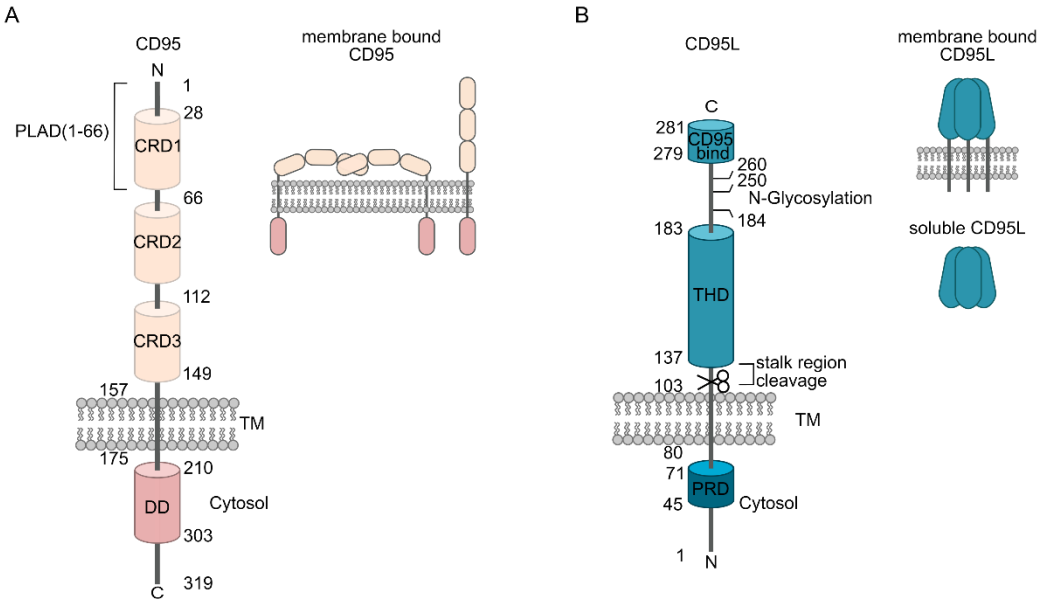

Figure 1. 4 Sketches of CD95 (A) and CD95L (B) with main domains. A: Sketches of monomeric CD95 structure with three cysteine-rich domains (CRDs), a transmembrane domain (TM), and an intracellular death domain (DD). CD95 exists as a monomer or homodimer on the cellular membrane. B: Sketches of monomeric CD95L structure with a C-terminal CD95 binding domain (CD95 bind), a TNFSF homology domain (THD), a transmembrane domain (TM), and a proline-rich domain (PRD). CD95L contains three N-glycosylation sites at Asn184, Asn250, and Asn260. CD95L exists as homotrimer on membrane or cleaved soluble form.

1.2.2 Structure of CD95L and its Synthetic Variants

CD95 ligand (CD95L), also known as fas ligand or CD178, is a 40 kDa type II transmembrane protein (13). It is predominantly expressed on multiple immune cells such as cytotoxic T-lymphocytes and monocytes (36). The extracellular domain of CD95L at the C-terminal (amino acids 103-281) is composed of a TNF homology domain (THD) and a CD95 binding domain (CD95 Bind) (see Figure 1. 4B). THD is composed of aromatic and hydrophobic residues thus causing CD95L to self-associate into homotrimers (37). The proline-rich domain (PRD) plays a role in the expression level and stability of CD95L (38). The transmembrane domain enhances the stability of the CD95L trimer which is crucial in the apoptosis initiation (39). CD95L exists as membrane-anchored (mCD95L) or soluble forms (sCD95L) through cleavage at its stalk region *via* multiple matrix metalloproteases (MMPs) (40), which turned out to be significantly less efficient in apoptosis initiation than its membrane counterparts (41,42). The binding of mCD95L with its cogent receptor CD95 activates previously discussed programmed cell death (35), which can be impeded by a CD95 antagonist, blocking the binding sites on CRDs, or enhanced by agonists, either mimicking the geometry of CD95L binding or stabilizing the CD95/CD95L complex (15) (Figure 1. 5 lane 3).

Structural modifications with fusion tags. sCD95L purification has been widely investigated in both eukaryotic and prokaryotic expression systems before (43–46). THDs induce trimerization of CD95L but this alone is not sufficient to ensure proper receptor binding and signalling activation. Therefore, the purified sCD95L forms a homotrimer (47) but fails to trigger apoptosis (42). The stalk region of membrane bound CD95L stabilizes and contributes to its secondary aggregation, rendering mCD95L with high local concentration and binding affinity with CD95 (48). Efforts have been made for sCD95L stabilization to achieve its high biological activity. One of which is the addition of extra trimerization motifs at the N-terminus to increase structural stability and spatial fixation of THD. For example, Tenascin-C (TNC) motifs form disulfide bridge-connected trimers, which stabilize THD homotrimerization and decrease structure disturbance upon binding with CD95 (48). Another example is the isoleucine zipper (IZ) with a coiled-coil motif, characterized by seven residues repeat (a, b, c, d, e, f, g) n, with hydrophobic residues at position a and d and polar residues elsewhere. Protein fused with isoleucine zipper motif harbours stabilized trimeric conformations (49). Examples such as isoleucine zipper (IZ-sCD95L) (50,51), TNC (tenascin-C) domain (TNC-sFasL), and T4 foldon (T4-sFasL) (52) trigger intermediate apoptosis signalling (Figure 1. 5 lane 1).

High-order cross-linking. A secondary oligomerization of sCD95L is necessary to achieve superior performance of apoptosis signal initiation. While trimerization motifs alone do not lead to high-order aggregation of sCD95L, cross-linking can be achieved by employing monoclonal antibodies against fusion tags such as a Flag-tag (Flag-sCD95L) (48). Besides, fusing sCD95L with the Fc portion of immunoglobulin G1 (Fc-sCD95L) or with the collagen domain of adiponectin ACRP30 (ACRP-sCD95L) has been reported to assemble a hexamer (two sCD95L trimers) (53). sCD95L interaction with CD95 can be further enhanced by the combination of antibody cross-linking plus fusion with a trimerization motif (Flag-TNC-sCD95L) (48). Theoretically speaking, the difference between sCD95L and mCD95L lies in the freedom of THD at the N-terminus. THD in the soluble form is relatively free, whereas membrane-bound ligands

are constrained by the stalk region and transmembrane domain, rendering mCD95L with structural stability and orientational accuracy. Inspired by this, sCD95L has been also fused with the stalk region, which shows a better cytotoxicity after cross-linking with anti-Flag mAb (Flag-stalk-sCD95L) (54). The killing efficiency of Flag-stalk-sCD95L on Jurkat cells was reported equivalent to that of membrane-bound CD95L (mCD95L) and approximately 10-fold stronger than that of an agonistic anti-CD95 antibody (clone CH-11) (55). Other strategies have been investigated, such as DNA origami as a scaffold to immobilize sCD95L with nanoscale precision showed high apoptosis signal initiation. Other than the previously discussed structure hierarchy, flexibility plays a role in signalling efficiency. For example, plasma membrane or DNA origami platforms renders ligands with fixed pre-orientation that enhance the binding affinity towards CD95 on the cellular membrane. Considering a high-order hexagonal architecture may lead to enhanced apoptosis initiation (56), the DNA origami/sCD95L hybrid construct was fabricated. In this configuration, T4-sCD95L proteins were anchored in a hexameric structure with 10 nm intermolecular spacing. This T4-sCD95L-DNA construct showed a fast time-to-death kinetics (57) (Figure 1. 5 lane 2).

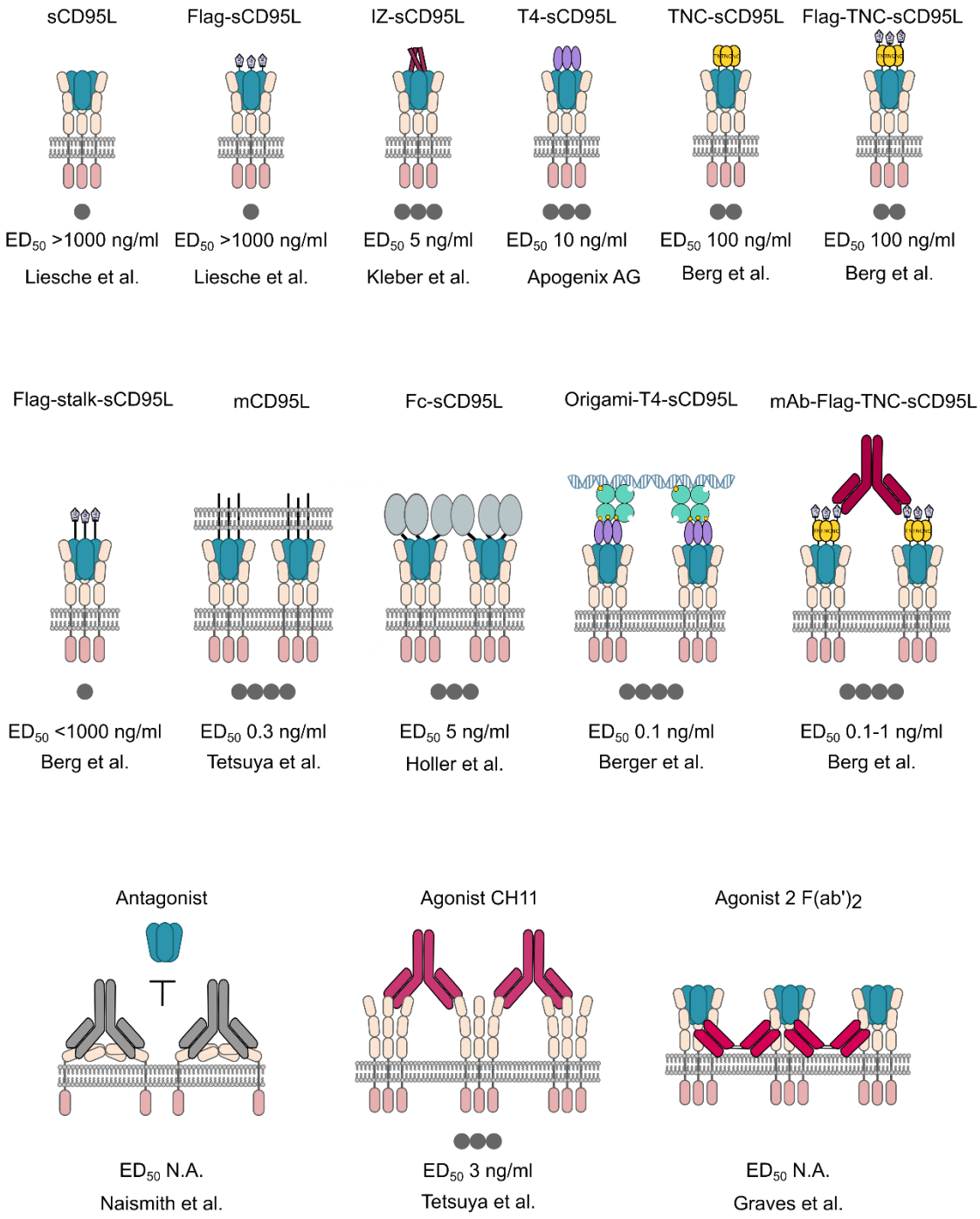

Figure 1. 5 Structures of CD95L variants. Lane 1 shows different structural modifications of CD95L variants. Lane 2 shows high-order cross-linking of CD95L variants. Lane 3 shows the mechanism of CD95 antagonist or agonist antibodies. Gray dots indicate the relative apoptosis initiation efficiency based on their reported effective doses 50 % (ED_{50}) numbers, with one dot as the lowest and four dots as the highest efficiency.

1.2.3 The CD95 homolog interaction

The homotypic interaction of CD95 is primarily mediated by the N-terminal pre-ligand assembly domain (PLAD) with amino acids 17-82 independent of its ligand (58). Besides, other domains may contribute to receptor homodimerization, in view of the reported low affinity of PLAD domain (59). Recent studies showed that the TM domains of CD95 form stable trimers through van der Waals forces and contribute to high-order aggregation, which induces apoptosis independent of the extracellular region (39,60). The complete 3D structure of CD95 has not been solved yet, but individual domains including ECD, TM or ICD have been determined by X-ray crystallography, or NMR (39,61,62). The structure of the CD95 extracellular domains has been solved together with agonistic CD95 antibodies bound to the CRD1 and CRD2 (61). Even without its ligand, the oligomerization of CD95 *via* homotypic interactions is crucial for the receptor's signaling potential. Since it makes clusters of intracellular DDs, which facilitates the recruitment of adaptor proteins FADD (fas-associated death domain), promotion of FADD/pro-caspase-8 homotypic interactions and the initiation of the downstream apoptotic signaling. This inspired the development of TNFRSF agonistic antibodies (e.g. combination of TRAIL/DR5) to use in cancer immunotherapy.

1.2.4 The CD95-CD95L interaction

The crystal structure of the CD95L extracellular domain has been resolved in previous studies (63) (see Figure 1. 6). The trimeric CD95L encompasses a cone-shaped structure, within which each monomer adopts a jelly-roll fold with two beta-sheets. This configuration provides CD95L with an optimal spatial arrangement of the binding sites for CD95 with high affinity. Up to three CD95 monomers can bind to the trimeric CD95L, each binding to the groove between two CD95L monomers. Every CD95L monomer has three N-linked glycosylation sites at positions Asn184, Asn250, and Asn260 (64,65), and two cysteine residues, Cys202 and Cys233, forming an intracellular disulfide bridge enhancing stability. Interactions between monomer subunits involve van der Waals forces and hydrogen bonds amid the beta-sheets. In contrast, it has been shown in a mutagenesis study that charged and polar amino acids, e.g. cysteine (Cys) and asparagine (Asn) mainly mediate CD95-CD95L interactions (66).

The crystal structure of the CD95/CD95L complex has not been solved yet, but it's assumed that CD95L and CD95 bind in a trimer-to-trimer geometry based on the structure homology of the TNFSF/TNFRSF complex. Therefore, the crystal structure of CD95L with its decoy receptor DcR3 complex has been solved which can be used as a template. To this end, I performed superimposition of the CD95 ECD to the DcR3 receptor on the DcR3/CD95L complex using PyMol, resulting in a trimer-trimer CD95L/CD95 complex structure (see Figure 1. 6). The complex conformation shows a 70 Å distance between two CD95 monomers at the top (N-terminus) and a 40 Å distance at the bottom (C-terminus). The complex shows the height of ECD with 80 Å. The homotrimerized CD95L is surrounded by three receptor monomers at each groove. One single receptor monomer is bound with two neighboring ligand subunits.

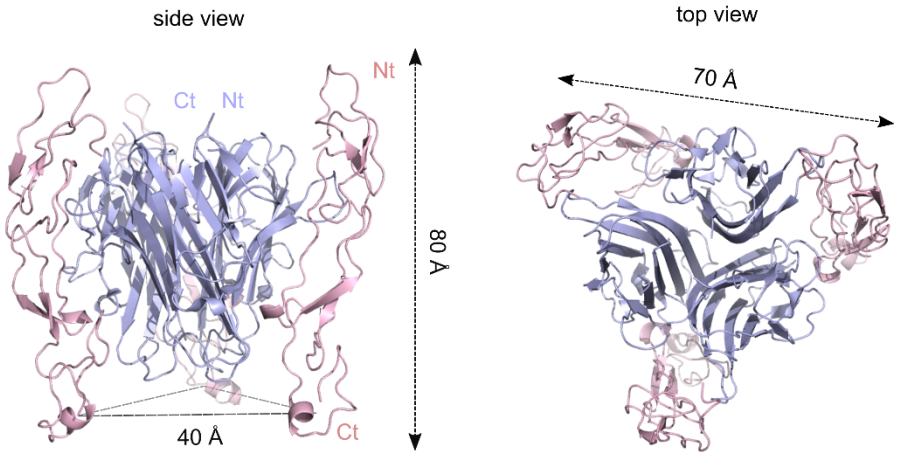

Figure 1. 6 Crystal structures of the CD95L/CD95 complex. Three CD95 monomers with amino acids 55-161 (pink) (PDB: 3TJE_F) interacting with the cone-shape CD95L trimer (blue) are shown in the side view (left) and top view (right). Each CD95 monomer is bound with two adjacent CD95L monomers at the groove. The CD95L trimer interacts with CD95 mostly on its CRD1 and CRD2. CD95 shows a height with 80 Å (side view), 70 Å between two monomers at the top (top view), and 40Å between two monomers at the bottom of the complex (side view). Nt: N-terminal, Ct: C-terminal. This complex structure was made by superimposing CD95 (PDB: 3TJE_F) to the CD95L/DcR3 complex (PDB: 4MSV) using PyMol with a root mean square deviation (RMSD) of 2.852 between DcR3 and CD95.

2. Towards Single Molecule Analyses using Advanced Fluorescence Microscopy and Nanotechnological Platforms

2.1 From Basics to Advanced Microscopy Techniques

2.1.1 Optical microscopy

Widefield Microscopy. Widefield microscopy is the most widely imaging method, where white light source is used to illuminate the entire sample. Brightfield microscopy is the most basic microscopy technique including key components such as illuminator, condenser lens, objective lens and ocular lens. The overall magnification power is the product of magnification of the objective lens times that of the ocular lens. Two types of light sources are often included: a halogen bulb as transmitted illumination and a mercury lamp as reflected illumination. Other specialized techniques such as phase contrast and epifluorescence can be applied to resolve transparent small cellular structures that are not visible under widefield mode (67) (page 1-5).

Phase contrast microscopy. Phase contrast microscopy improves the resolution of images without additional staining of cell samples. First, the light source was modified by a condenser annulus into a hollow cone shape and illuminated on a sample. When the light passes through a transparent sample, phase shifts can be introduced by refractive indices of different cellular regions. A phase plate is inserted in the objective with a ring-shaped region that shifts the phases of lights. When lights cross the phase plate, the phase of non-diffracted light is shifted by - 90° whereas the diffracted/scattered (by sample) light is not changed. The diffracted and non-diffracted light then interfere with each other. The phase difference between them causes the change in intensity, thus enhancing the image contrast (67) (page 121-125).

Fluorescence microscopy. Fluorescence microscopy allows a high image contrast for by staining or labelling samples with fluorescent markers, such that only the labeled object appears bright, whereas the background remains dark. Fluorescent proteins (such as green fluorescent protein (GFP) and mCherry) or dyes (such as ATTO594 and ATTO647N) absorb light at specific excitation wavelengths and emit light with longer wavelengths. Based on the principle of fluorescence, the microscope employs an excitation light source, filters, a dichroic mirror, and a detector. The excitation light is first filtered by excitation filter and reflected by a dichroic mirror on the whole sample, fluorescence signal is collected by the objective, passed through the dichroic mirror, filtered by emission filter and detected by a CMOS camera (67) (chapter 11).

Confocal microscopy. Confocal laser scanning microscopy is an optical imaging technique for increasing the contrast of images by applying a pinhole (PH), which allows to record particular slices of the sample and to exclude any light from unwanted regions below or above the slide. The fact that the contrast is a desirable consequence of the slice selection. In a conventional widefield fluorescence microscope, the whole sample is illuminated, and the fluorescence signal is detected with unfocused background light. Confocal microscopy increases the resolution by using point illumination on the sample and blocks the background signal by placing a pinhole in front of the detector. Fluorescence above and below the focal plane cannot be detected in this configuration. By changing the positions of the sample and focal planes, the whole 3D structure of the sample can be recorded. Due to the usage of a pinhole, the improved resolution is at the expense of the drop in signal intensity. Therefore, sensitive detectors such as photomultiplier tube

(PMT) should be used. A typical confocal microscope can achieve a lateral resolution of ~200 nm (67) (chapter 13). However, due to the nature of light, the point illumination is diffraction-limited with a point spread function (PSF).

2.1.2 Transmission electron microscopy (TEM).

Transmission electron microscopy (TEM) is an imaging technique based on electrons transmission of thin-layer samples (< 200 nm) with atomic resolution. Instead of using light source, a transmission electron microscope uses electron beam illumination due to its wave-particle duality. The major components include an electron emission source, electromagnetic lenses, and an electron detector such as fluorescence screen. Electron lenses employ electromagnetic coils to resemble optical lenses. It is important to generate a radially symmetrical field to prevent astigmatism and spherical/ chromatic aberration. Therefore, the TEM microscope needs to be aligned before usage (see methods part). The TEM specimen stage uses an airlock for minimal loss of vacuum during sample holder insertion. A thin layer sample is placed under the electron beam, which is generated and accelerated then focused by condenser lenses on the sample. When the electron beam passes through the sample it will be scattered or absorbed by the sample based on its shape, thus forming the image. The mass of an electron is much heavier than a photon, resulting in a much longer wavelength. This leads to less diffraction and sharpening of the image, which is magnified and detected on a fluorescent screen (68).

2.2 Superresolution Microscopy and Multiparametric Image Spectroscopy

2.2.1 Stimulated Emission Depletion (STED) nanoscopy

Stimulated emission depletion (STED) as one of the super-resolution microscopy techniques has been widely used in cell biology to achieve higher spatial-resolution imaging. STED employs a high-power depletion laser to selectively deactivate fluorophores in the periphery of excitation laser beam center, thereby minimizing the effective fluorescence area and improving image resolution. Because STED applies the idea of switching fluorescence between on and off states at a defined spatial coordinate, it is also referred to as coordinate-targeted nanoscopy (69). In traditional fluorescence microscopy, the resolution is limited by the diffraction of light, as described by Ernst Abbe's formula (70):

$$D = \frac{\lambda}{2n\,sin\alpha} = \frac{\lambda}{2NA} \tag{1}$$

It describes D as the smallest distance between two points which are distinguishable, which is the quotient of the wavelength λ divided by the numerical aperture NA, with NA being the product of refractive index n and the sine of incidence angle α. Normal fluorescence occurs when an electron is excited by an excitation laser, it transits from the ground state (S0) to the excited state (S1). After relaxing back to S0, a photon is emitted as fluorescence. Due to the lack of interruption, this process is also referred to as spontaneous emission. STED interrupts this process by stimulating the excited electron to the ground state with a photon at a specific wavelength, forcing the electron to drop into a higher vibrational energy level of the S0 state by stimulated deactivation, with an emission of two photons at the same wavelength. The reduced energy difference between the two states causes emission with lower energy, namely red shifting the fluorescence to the spectrum end. To achieve depletion by stimulated deexcitation, sufficient incident photons are needed. This requires a high laser intensity for generating an adequate number of incident photons. However, high laser power can cause photobleaching of the fluorophore which compromises the fluorescence signal. The precondition of the efficient STED effect is that the STED laser matches energy of the transition state in the emission spectrum of the chosen fluorophore (71).

The STED microscope is based on laser modulation of conventional confocal microscopy. Both the excitation laser and STED laser are synchronized pulsed lasers. The point spread function of both lasers is modified including the pulse width, intensity, and phase. The duration of the excitation laser pulse is usually 10 to 300 picoseconds which is shorter than the STED laser pulse. The STED beam is generated using fixed phase plates or a spatial light modulator with a doughnut shape and circular polarization. The STED laser is superimposed with the excitation laser with zero intensity in the center but increased intensity in the periphery of the excitation laser. Mathematically, a modified Abbe equation of STED resolution can be described as (72):

$$D = \frac{\lambda}{2n\,sin\alpha\sqrt{1+\frac{Imax}{I_S}}} = \frac{\lambda}{2NA\sqrt{1+\sigma}} \tag{2}$$

where *Imax* is the maximum of the applied STED laser intensity, *Is* is the saturation intensity, corresponding to half of the emission signal, which is dependent on fluorophore rotational

orientation, STED laser polarization, and wavelength (72). Practically, STED microscopy can typically achieve a lateral resolution of ~ 40 nm and an axial resolution of ~ 143 nm for biological samples (67) (page 349-355).

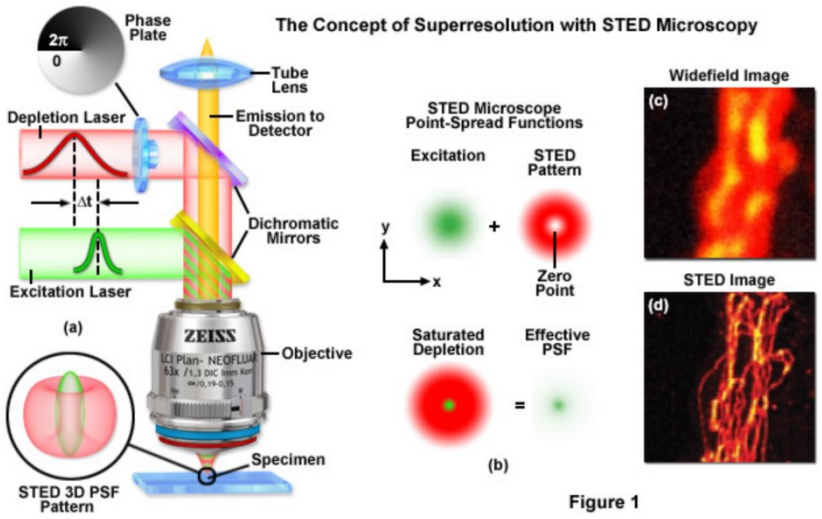

Figure 2. 1 The concept of STED microscopy. The image was modified from (73).

2.2.2 The optical elements of the Abberior STED microscope

Lasers. A laser is a beam of monochromatic and coherent photons that have the same frequencies. The name of laser is shortened for 'light amplification by stimulated emission of radiation'. When a photon hits an excited atom, the atom falls back to the ground state and emits a new photon with the same energy (wavelength) as the first photon. A laser is filled with multiple excited atoms between two mirrors. When a first photon stimulates an atom with the emission of a second photon, the two photons then bounce between mirrors and stimulate neighboring atoms in a chain reaction manner. Due to the coherency of all emitted photons, they are collected as a laser beam. A laser contains a gain medium and an energy source, which keeps the material at excited metastable states for a long period to fulfill the chain reaction. Lasers can be used as continuous wave (CW) lasers or pulsed lasers. Compared with an averaged low power CW laser, the pulsed laser can achieve high power at short duration ranging from femtosecond to milliseconds (74) (chapter 1-2, page 88). In the customized Abberior STED microscope, two pulsed lasers at 561 nm and 640 nm with durations < 100 ps were used as excitation lasers. One STED depletion laser at 775 nm with a pulse width of 1.2 ns was synchronized at 40 MHz (25 ns repetition) and is used for depletion at both excitation lasers. The STED 775 nm laser is modulated by a spatial light modulator (SLM) to generate a 2D doughnut shape.

Light polarization. Polarization describes a defined orientation of the electromagnetic wave/light. In addition to the information provided by wavelength and intensity of light, polarization also provides important aspects such as the degree of freedom of biological samples. Common light such as halogen light generates unpolarized light because of the random directions of the electric field. On the other hand, lasers are often polarized. A single photon generates an electromagnetic wave which can be described as linearly polarized or circularly polarized based

on the orientation of its electric fields. A linearly polarized photon can be termed as horizontally or vertically linear polarized (p-polarized as parallel and s-polarized as perpendicular) based on its orientation relative to the incidence surface. If two linearly polarized lights with the same amplitude are perpendicular but different in phase of π/2, they can add up to form a circularly polarized light. Depending on the rotation orientation, it can be described as right or left circularly polarized. Fluorescence polarization (FP) or anisotropy (*r*) measurements are used for the analysis of size, conformational changes, or binding interactions of biological molecules. Whether the emission of fluorescently-labeled biological molecules is polarized light or not depends on their flexibility. More precisely, the anisotropy measures the degree of polarization of emitted light after polarized excitation. Large biomolecules rotate slowly in solution and do not change their orientation. Therefore, after being excited by a polarized light, their emission remains polarized. Yet small molecules rotate fast thus resulting in depolarization of the emission light. In an optical system polarization measurement can be achieved. First, the polarizing filter is placed in front of the excitation laser thus generating polarized incident light. Detection is achieved by using a beam polarization splitter (BPS) placed in front of the detector. Photons with different polarizations can be separated and filtered through a polarized filter followed by detection. Mathematically, fluorescence anisotropy *r* is calculated as:

$$r = \frac{I_{II} - I_{\perp}}{I_{II} + 2I_{\perp}} \tag{3}$$

With $I_{||}$ being the intensity of the emitted light in the p-channel, and $I_{\perp}$ being the emitted light in the s-channel. Factors influencing *r* include the fluorescence lifetime and viscosity. Longer lifetime and less viscosity lead to longer times to integrate over the rotational diffusion, resulting in less polarization (75,76). In the customized Abberior STED microscope, linearized excitation lasers are used for detection of polarized emissions. The STED laser is operated in circularly polarized to avoid polarization effects and achieve depletions at all orientations.

Pulsed interleaved excitation (PIE). The PIE technique is widely used in single-molecule Förster resonance energy transfer (smFRET) experiments. It synchronizes interleaved laser pulses with different wavelengths, allowing for time-resolved signal detection and separation from different fluorophores with reduced crosstalk (77). Specifically, two excitation laser pulses with different colors are alternated and synchronized detectors, and emission from fluorophores by different excitation pulses can be distinguished. This is especially helpful in a FRET measurement where the FRET efficiency can be calculated from fluorescence signals belonging to different excitation pulses. A measurement window is composed of a prompt window and a delayed window, measuring measures fluorescence after green and red laser excitation respectively. Two laser pulses are repeated with a certain frequency rate over time. As shown in the Figure 2. 2A, the laser frequency is ~ 26 MHz, and the repetition time (rep.) is the reciprocal of it, namely $t_{rep.}$ = 38.5 ns. The advantage of using PIE is that the information of acceptors independent from donors can be obtained. The colors of detected photons in this mode are named accordingly: i) the donor fluorescence after green laser (donor laser) excitation detected by APD 1 and APD 3 is referred as green photons; ii) the acceptor fluorescence after green laser (donor laser) excitation detected by APD 2 and APD 4 is referred as red photons; iii) the acceptor fluorescence after red

laser (acceptor laser) excitation detected by APD 2 and APD 4 is referred as yellow photons (Figure 2. 2B and C) (78).

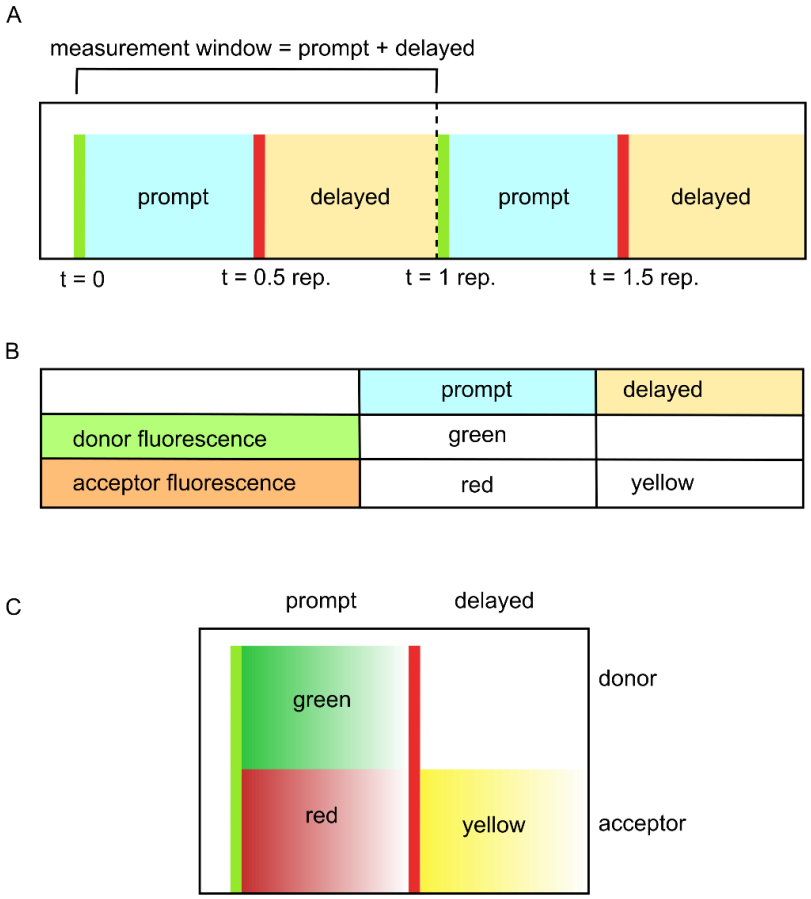

Figure 2. 2 Principles of pulsed interleaved excitation PIE. A. Measurement window is composed of two components: the first (prompt) window after donor laser pulse and the second (delayed) window after acceptor laser pulse. The naming of colors of the photons depends on the measurement window and detectors shown in table B or sketch C. The image is adapted and redrawn from the figure of Claus Seidel laboratory (internal resource).

Waveplates. A waveplate, also referred to as a retarder, is made of a birefringent material such as mica. It is an optical device that can alter the direction of light. When a linearly polarized light passes through the half-wave plate, it will be split into two perpendicular optical axes, a fast and a slow axis. Due to the arrangement of atoms in the crystal, a waveplate shows different resonant frequencies for lights with different orientations, rendering it with different refraction indices in the two axes. This causes changes in phase between the p-polarized and s-polarized components, leading to an overall shift in the direction of the light. Whether it is a half-wave or quarter-wave shift depends on the thickness of the plate material, the index of refraction, and the wavelength of the light. There are two most frequently used wave plates, the half-wave and the quarter-wave plate. If the linearly polarized light passes through a half-wave plate, the component on the slow axis is retarded by a half wavelength (one π) whereas the perpendicular component is not changed. This results in a rotation of the overall vector of the light with one π. In a quarter-wave plate, the parallel component on the slow axis is retarded by a quarter wavelength ($\pi/2$) with no change in the fast axis, resulting in an overall circularly polarized vector. Wave plates are helpful with the

modification of lights with a uniform phase shift or polarization change (79). However, spatial variation of light beams such as doughnut-shaped STED with a central zero intensity is not achievable. Besides, wave plates are static components that are not programmable in real time. These can be solved by using a spatial light modulator.

The spatial light modulator (SLM). An SLM is an optical device that modulates the amplitude, phase, and polarization of light in a pixel-by-pixel manner. It is made of multiple layers including reflective surfaces, a liquid crystal layer, silicon backplanes, and electrode layers. The silicon electronics contain a grid of pixels, each of which can be addressed with different electric fields. This changes the orientation or refractive index of liquid crystal on each pixel with tunability in real time. Thus, laser beams can be customized with different shapes, polarities, and intensities in a dynamic mode with high resolution (80) (chapter 12, page 956-959). The doughnut-shaped STED beam is made by a SLM speculatively with a spiral phase pattern, where the electric field varies azimuthally around the axis of a beam and destructively interferes at the center to form a zero intensity at the center (81).

Optical filters and mirrors. Optical filters and mirrors are used in a microscopic optical train to improve image contrast, including band-pass filters, notch filters, and dichroic mirrors. Band-pass filters are made of glass or quartz coated with dielectric stacks that transmit light within a broadband of wavelengths and absorb other components. It is usually placed before the detector to collect fluorescence emissions and block the others to reduce background. Notch filters are band-stop filters that attenuate a narrow band of wavelength, which are the reverse of band-pass filters. A notch filter uses destructive interference coatings to block a specific laser line. Dichroic mirrors are coated with materials that reflect specific wavelengths and transmit some others. It is used for the separation of excitation and emission lights in the light path to prevent bleed-through effects. A polarized beam splitter (PBS) is a cube made by a joint of two prisms with multi-layer dielectric coatings in between and anti-reflection coating on the surface. It separates two parts of lights by reflecting the s-polarized light 90° and transmitting the p-polarized light (82) (chapter 2.4, page 38-41).

Detectors. Different detectors can be used in microscopes such as charge-coupled devices (CCD) and complementary metal oxide semiconductors (CMOS) cameras, photomultiplier tubes (PMTs), and avalanche photodiodes (APDs). The APD detector is used in the Abberior STED microscope and coupled with the time-correlated single photon counting (TCSPC) counting unit. APD, a highly sensitive photodiode, is made of semiconductor materials that convert light into electricity. In a p-n photodiode, an incoming photon produces only one electron-hole pair. In contrast, APDs use optimized structures and high voltage, multiplying the photoelectric effect by avalanche breakdown effects. Thus, APDs amplify weak light signals into larger currents and make them useful in detecting fluorescence with low intensity (80) (chapter 9, page 532-537).

Time-correlated single photon counting (TCSPC). TCSPC is a technique used to measure fluorescence lifetime with picosecond resolution. It detects the relative time between an excitation pulse and a single emitted photon, which can be converted into an electronic pulse by a photomultiplier detector (PTM). After thousands of repeated recordings, a histogram of all

relative arrival times can be drawn (Figure 2. 3). To achieve only one photon counted after the excitation, TCSPC uses an excitation laser with a very high repetition rate (within the megahertz (MHz) range) than the photon detection rate. In the confocal laser scanning microscope, the relative arrival time of each photon is synchronized with the coordinate of the laser beam in the scan area. Thus, both the fluorescence intensity and lifetime are stored in a three-dimensional matrix (x, y, t) for each pixel of the image. The minimum lifetime that can be measured in TCSPC is limited by the instrument response function (IRF), which is the total response time of the excitation and detection system. Four elements are included: i) the pulse width of the excitation laser; ii) the response width of the detector; iii) the timing jitter of TCSPC electronics; iv) the optical dispersion of the emission, with the first two being the limiting factors. The instrumental IRF can be obtained by measuring the full-width half maximum (FWHM) of a diluted fluorescent dye after excitation (82) (page 103-107). The fluorescence lifetime is derived from fitting the decay curve builds up by detection of each single arrival times. For single-exponential decays:

$$I(t) = I_0 e^{-t/\tau} \tag{4}$$

Where *I(t)* is the fluorescence intensity at time *t*, I_0 is the initial fluorescence intensity at $t = 0$ (the time at which the excitation pulse hits the sample), τ is the fluorescence lifetime (the time at which the fluorescence intensity has decayed to 1/e of its initial value). For multi-exponential decays:

$$I(t) = \sum A_{\mathrm{i}}\, e^{-t/\tau_{\mathrm{i}}} \tag{5}$$

Where A_i is the per-exponential factor (the amplitude) corresponding to the *i*-th decay component, τ_i is the fluorescence lifetime of the *i*-th component. Each A_i and τ_i represents a different decay pathway or species, and their contribution to the overall decay is determined by the relative amplitudes A_i. The reduced chi-square (χ^2) values evaluate the goodness of the fit (82) (page 99-102).

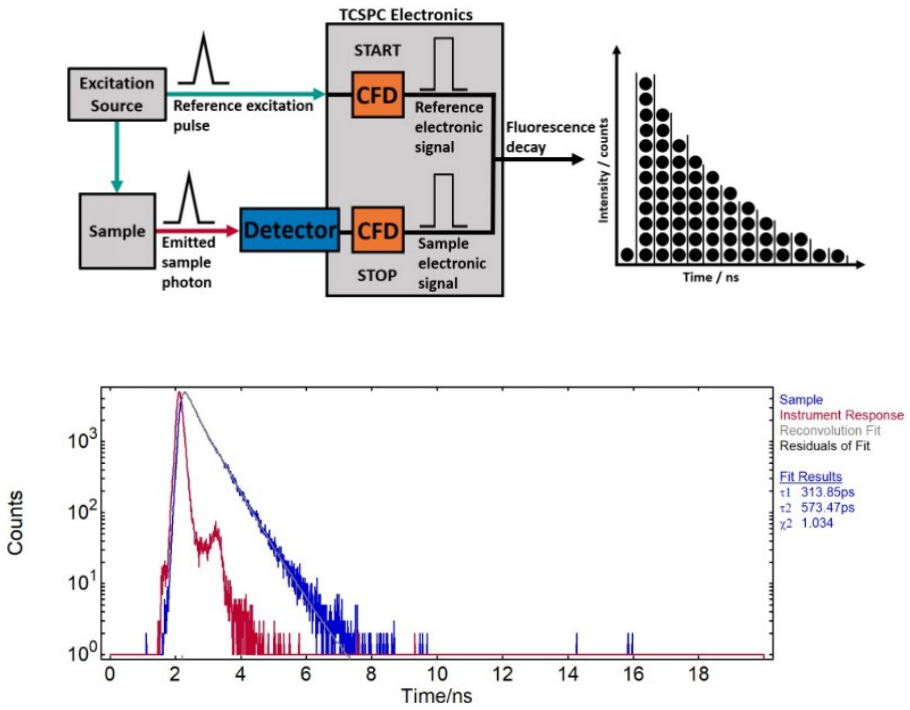

Figure 2. 3 The principle of TCSPC. The figure was taken from (83)**.** Upper panel: overview of TCSPC principle. TCSPC is synchronized with two inputs, the excitation as a START reference and the photon from sample fluorescence as a STOP reference. TCSPC measures the relative arrival time in between, mimicking a 'stopwatch'. All detected arrival times contribute to making a histogram where the fluorescence lifetime can be fitted from the decay. CFD is the constant fraction discriminator, designed to find a maximum of a pulse. Lower panel: an example data analysis of TCSPC lifetime measurement (blue) with IRF (red) and fitting result (grey).

Time-gated detection. Time-gated detection can be used to improve the spatial resolution of STED by removing photons that arrive early during the depletion pulse (84,85). The traditional STED requires high laser power, increasing the background noise and possibly leading to a photobleaching effect. Therefore, it is limited to fixed-cell imaging. As introduced previously (85), continuous-wave STED (CW-STED) laser was employed with an average low power to minimize photobleaching. This is important in live-cell imaging but compromised with depletion resolution. Considering that early arrived photons after excitement are still in their excited states which are not depleted yet. STED resolution was increased by applying a time gating filter (g-STED) that collects photons only after first 15-25 TAC bins (1.92-3.2 ns) of TCSPC arrival times. In this way, the effective point spread function (PSF) of the excitation pulse upon g-STED is improved as well as the image sharpness. In this study, the STED laser is modulated with a time delay relative to excitation laser. We applied the time gating using a pulsed STED laser.

The optical train of Abberior STED microscope. Two pulsed excitation lasers at 561 nm and 640 nm (width < 100 ps) are used for ATTO 594/Alexa flour 594 and ATTO 647N/ATTO 643. In front of each excitation laser is a half-wave plate and a quarter-wave plate that can be electronically controlled. One depletion laser STED at 775 nm with a repetition rate of 40 MHz

(pulsed width of 1.2 ns) is used for depletion at both excitation channels. Excitation lasers are linearly polarized, and the STED laser is circularly polarized. Line interleaved donor and acceptor excitation was applied to prevent crosstalk. The STED laser was shaped by the spatial light modulator SLM775. The STED laser is synchronized with excitation laser temporally and spatially. The excitation and depletion lasers are superimposed by three notch filters NF594 with tuned angles for the excitation laser at 561 nm, NF658 with tuned angles for the excitation laser at 640 nm, and NF775 for the STED laser at 775 nm. and NF775 for the STED laser at 775 nm. The angles of notch filters need to be adjusted for attenuation at the correct wavelength (86).

$$\lambda' = \lambda \cdot \sqrt{1 - \left(\frac{\sin(\theta)}{n}\right)^2} \tag{6}$$

The notch angle in our case is possibly around 29.5° to attenuate the excitation laser at 561 nm:

$$\lambda' = 594\ \text{nm} \cdot \sqrt{1 - \left(\frac{\sin(29.5°)}{1.5}\right)^2} \approx 561\ \text{nm} \tag{7}$$

The fluorescence signal was collected by 100x oil objective and passed through a pinhole with 1.3. The PMT detector was used for gold bead alignment based on light reflection. The fluorescence signal was first passed through a pinhole (PH) (see Figure 2. 4), then split into parallel and perpendicular orientations by a polarizing beam splitter (PBS). Afterward, the polarized signal was separated by color using band-pass filters at 640 nm indicated by D1 and D2. Fluorescence photons at two colors and two polarizations were registered by four APD detectors, which are synchronized with a time-correlated single photon (TCPSC) counting unit.

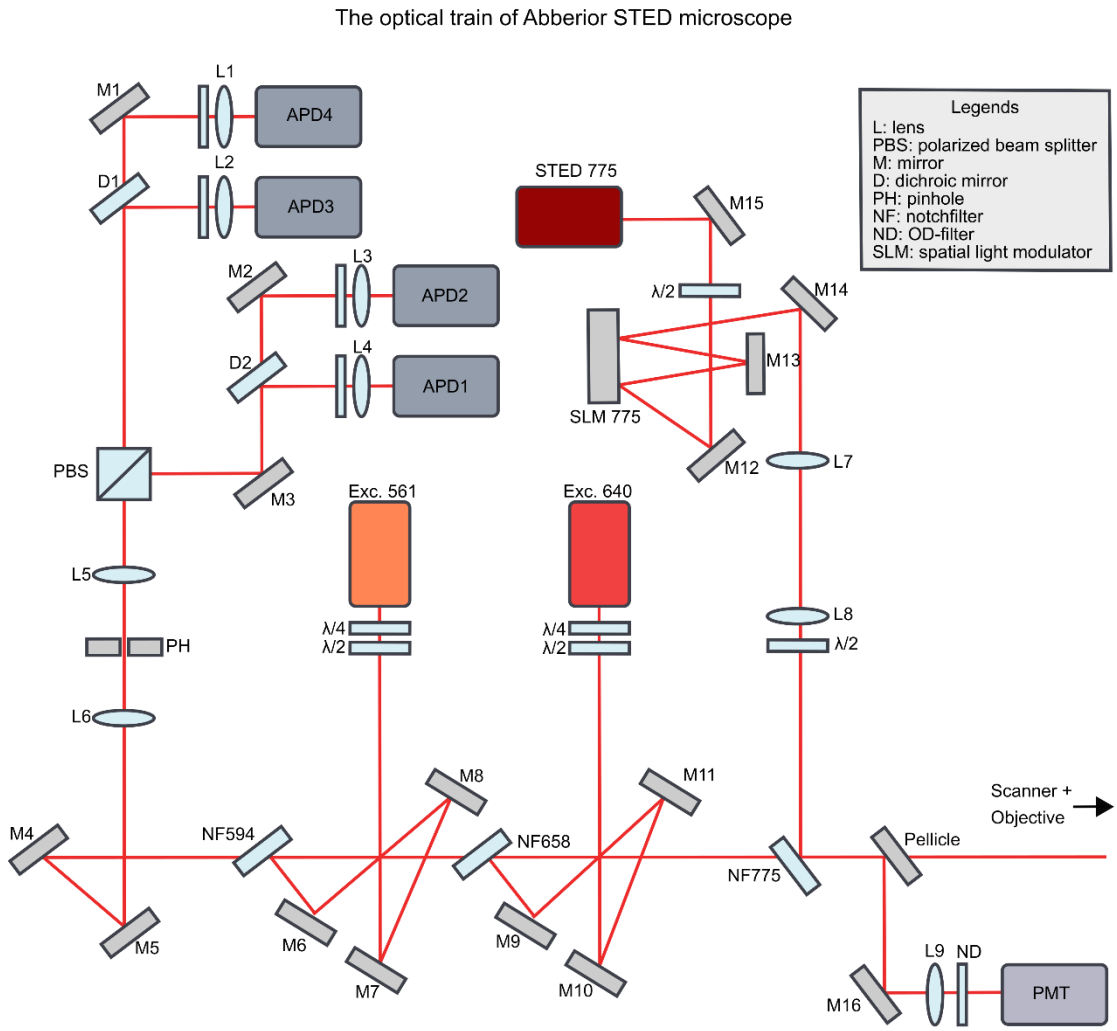

Figure 2. 4 The optical alignment of the Abberior STED microscope. All optical elements were inserted in legends. The image is adapted and redrawn from the figure of Claus Seidel laboratory (unpublished internal resource).

2.2.3 Applications using STED Microscopy

High-precision structural microscopy. STED super-resolution microscopy opens the avenue of elucidating subcellular architectures that cannot be resolved by conventional optical imaging. STED microscopy has been widely used for protein structure analysis such as microtubular cytoskeleton (87). STED microscopy has been used to resolve high-order protein complexes and clusters such as the nanoscale distribution of Tom20 (translocase of outer mitochondrial membrane 20) clusters and SNAP25 (synaptosome associated protein 25)/syntaxin complexes (88). Besides, two or three-color STED imaging enables precise colocalization analysis of multiple labeled proteins. To achieve high-quality data using STED microscopy, minimization of sample disturbances and maximizing of available photons are required. This relies on the precise alignment of excitation/depletion lasers and stabilized samples to prevent drift. Therefore,

samples need to be fixed by chemical crosslinker such as formaldehyde. This makes it difficult for live cell imaging.

STED in live cell and *in vivo* imaging. Live cell imaging using STED is challenging due to the low photon budget, high photobleaching, and high demand in temporal/spatial resolutions. Other challenges exist in thicker tissue imaging, such as autofluorescence and changeable local compositions. A recent study tackled the problems by using fluorescent protein as labels and optimized power settings and shaping of laser. In this way, the sub-diffraction resolved real-time imaging of the endoplasmic reticulum (ER) inside a live mammalian cell was achieved (89). Specifically, the ptK2 cell line was transiently transfected with yellow fluorescence protein (YFP) citrine. The excitation laser at 490 nm was synchronized with a converted 595 nm STED depletion laser. A lateral (x,y) resolution of < 50 nm inside the living cell was achieved (89). STED nanoscopy has been successfully used in a living anesthetized mouse. This was accomplished by applying a cover glass sealed cranial window for optical access. The neurons were labeled with enhanced yellow fluorescent protein inside the somatosensory cortex and this method allows observation of the dynamics of dendritic spines for weeks (90).

2.2.4 single molecule Förster Resonance Energy Transfer (smFRET)

Förster resonance energy transfer (FRET) or fluorescence resonance energy transfer (FRET) is a non-radiative energy transfer process between a donor and an acceptor fluorophore. Upon excitation, the electron from the donor fluorophore is excited from the ground S_0 state to the excited S_1 state. Instead of dropping back to the S_0 state with fluorescence emission, the donor transfers the energy to the acceptor by dipole-dipole coupling reaction, triggering the acceptor fluorescence. The precondition of this process is that the emission spectrum of the donor fluorophore overlaps with the acceptor excitation spectrum. Second, the two fluorophores should be placed in the vicinity within typically 1 - 10 nm. Additionally, the moment orientation of the donor dipole should match with the acceptor dipole. The FRET transfer efficiency also depends on the quantum yield of the donor fluorophore. Transfer efficiency *E* can be described in various ways as:

$$E = \frac{k_{\mathrm{ET}}}{k_{\mathrm{f}} + k_{\mathrm{ET}} + \sum k_{\mathrm{i}}} = \frac{1}{1 + \left(\frac{r}{R_0}\right)^6} \tag{8}$$

with k_{ET} being the FRET rate, k_{f} is the fluorescence rate, and k_i being the other non-radiative rates such as internal conversion, intersystem crossing and so on. Transfer efficiency *E* can be described based on the donor-acceptor distance *r*, and R_0 is the Förster distance of this pair of donor and acceptor (the distance at which *E* is 50 % between the two dyes). Since *E* is reversely proportional to the 6 power of inter-dye distance, this calculation is sensitive to small changes. Therefore, it can be used in the measurement of biological molecules with small sizes. R_0 is the Förster radius, which is specific to the dye pair, described by:

$$(R_0)^6 \propto \frac{J \cdot \kappa^2 \cdot \Phi_{\mathrm{D}}}{n^4} \tag{9}$$

With n being the refractive index of the medium, Φ_D being the fluorescence quantum yield of donor in the absence of acceptor and κ^2 being the dye orientation factor. J is the integral of spectral of overlapped between donor emission and acceptor absorption. κ^2 is the orientation parameter, which depends on the angle θ_{DA} θ_{D} θ_{A} described by:

$$\kappa^2 = (\cos\theta_{\mathrm{DA}} - 3\cos\theta_{\mathrm{D}}\cos\theta_{\mathrm{A}})^2 \tag{10}$$

With θ_{DA} being the angle between donor dipole and acceptor dipole moment, θ_D and θ_A being the angles between these dipoles and the vector joining the donor and the acceptor. The value of κ^2 ranges from 0 to 4: κ^2 = 0 when dipoles are perpendicular; κ^2 = 1 when dipoles are parallel; and κ^2 = 4 when dipoles are collinear. Considering the free orientation of dyes in solution, an averaged $\langle\kappa^2\rangle = 2/3$ is often used for all possible angles and assuming they are adapted isotroptically during FRET measurement. GFP and mCherry as a classic FRET pair have been used in various biophysics studies (91). Specifically in this study we used ATTO594/Alexa fluor 594 and ATTO647N/ATTO643 as FRET pairs.

2.2.5 Combining STED and smFRET

An ideal microscope should provide a seamless resolution enhancement, from a macro perspective imaging of cell dimensions, through cellular and sub-cellular structures, to a micro perspective of the molecular structure of biomolecules (Figure 2. 5). This is achieved by the recently developed FRET nanoscopy on the Abberior STED microscope (92). A STED microscope is based on a confocal laser scanning microscope, where the resolution is increased by applying an optical pinhole (PH) with a lateral resolution of ~ 200 nm and an axial resolution of ~ 600 nm (93). Confocal resolution is achieved by two pinholes used in this microscope, with the first one placed in front of the light source and the second one placed in front of the detector. The complete sample image is formed by scanning the image pixel by pixel via an x-y scanner. STED resolution is accomplished by synchronizing one depletion laser with the excitation lasers. Specifically, a single depletion laser at 775 nm is superimposed with two excitation lasers at 561 nm and 635 nm. The 775 nm STED laser is operated in the higher TM01* mode, the mode which results in the doughnut shape of the laser excitation. This STED laser depletes both acceptor and donor fluorophores and achieves a practical resolution of ~ 40 nm. Both excitation and depletion lasers are polarized, providing the parallel and perpendicular component of the emitted light to reconstruct the polarization-free fluorescence lifetime decay. STED resolution is further improved by statistical colocalization (cSTED) by measuring identical samples and colocalizing the detected positions, where a histogram of localizations is obtained. The histogram typically exhibits a Gaussian shape, whose central point then enables to improve the localization precision to several nanometers. While STED measures the projected distances of two dyes on the image plane, FRET measures the direct vector distance of two dyes. With the combination of cSTED and FRET, the 3D orientation of two dyes can be calculated using Pythagoras' theorem. FRET-measured distances are obtained from fitting the cumulative donor fluorescence decay in the

absence or presence of an acceptor, with the derived donor-acceptor distance R_{DA} of 4-12 nm. Thus, the continuous enhancement of resolution from micrometers to a few nanometers is achieved.

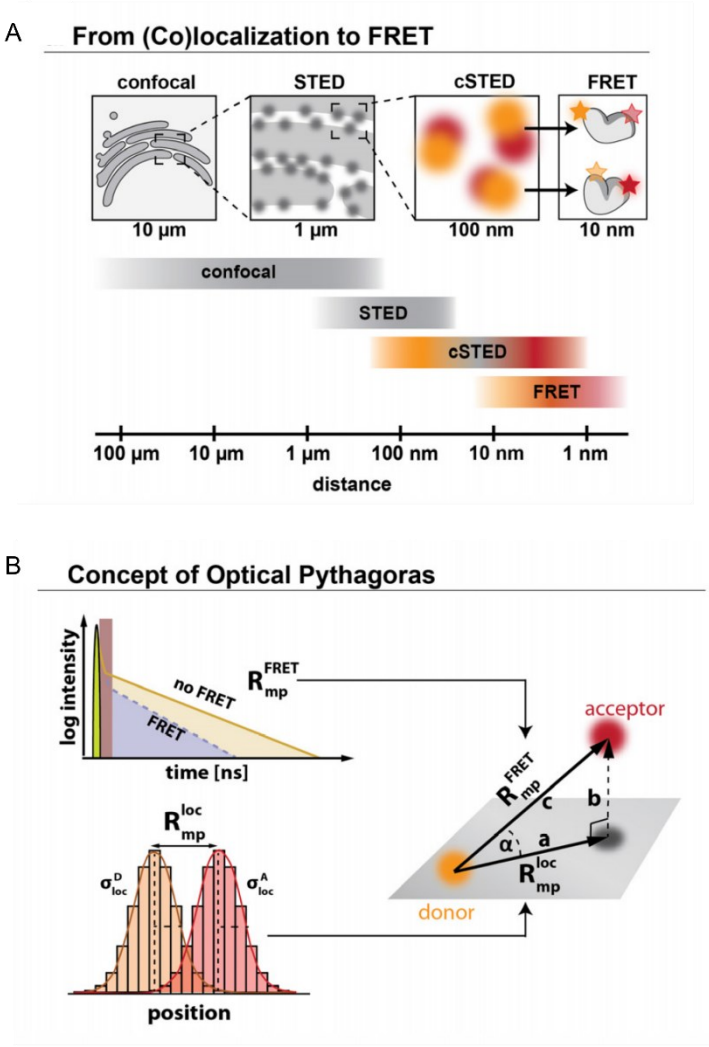

Figure 2. 5 Principles of the FRET nanoscopy, unchanged figure from (92). A. Seamless increasement in resolutions from confocal through STED, colocalization STED (cSTED) and FRET. B. The concept of optical Pythagoras. The FRET derived distances are obtained from cumulative donor fluorescence decay, where the averaged donor acceptor distance $\langle \boldsymbol{R_{DA}} \rangle$ can be converted to the FRET-based distance between the mean dye positions $\boldsymbol{R_{mp}^{FRET}}$. Next, the positions of the donor and acceptor fluorophores can be obtained from the mean localization result $\boldsymbol{R_{mp}^{loc}}$. Therefore, the three-dimensional orientation of the molecule can be obtained by applying Pythagoras' theorem (94).

To achieve high-quality imaging using FRET nanoscopy, it is important to perform precise alignment of the microscope (details described in the materials and methods part). Images were obtained by first recording an overview region of interest (ROI) of 20 x 20 µm^2 under confocal mode. Then, a zoomed 1 x 1 µm^2 of each ROI was measured under STED conditions. FRET information is determined by lifetime-based calculation assuming the absence of or averaging over the molecular dynamics:

$$E = 1 - \frac{\tau_{D(A)}}{\tau_{D(0)}} \tag{11}$$

With $\tau_{D(A)}$ being the fluorescence lifetime of the donor in the presence of the acceptor and $\tau_{D(0)}$ being the fluorescence lifetime of the donor in the absence of the acceptor. Two FRET pairs are measured in the lifetime measurement: a no-FRET pair (with a distance between donor and acceptor of 35 nm) and a high FRET pair (with donor and acceptor of 5 nm or 10 nm for CD95 anchoring). The two FRET pairs are placed at two edges of one rectangular DNA origami with a 75 nm distance. Under confocal mode, the different positions of the fluorophores cannot be resolved therefore each detected spot is identified as one DNA origami molecule. The number of fluorophores on each origami was measured by localization fitting on each channel. The FRET calculation of donor fluorescence decay under STED conditions was fitted with a single-exponential model function with a time gating filter where the initial part of the decay was removed. Afterward, the orientation of a randomly placed DNA origami is aligned. The no-FRET pair on each platform is meant to be used for the colocalization (84).

2.2.6 Correction factors in single molecule studies

There are some correction factors to be considered in FRET efficiency calculations (95). First, the crosstalk α is the detection of donor fluorescence in the acceptor channel, when the tail of the donor emission spectrum overlapped with the acceptor filter band:

$$\alpha = \frac{F_{D|R}}{F_{D|G}} = \frac{N_{GR}}{N_{GG}} \tag{12}$$

With $F_{D|R}$ being the fluorescence intensities from the red channel after the donor excitation, and $F_{D|G}$ being the fluorescence intensities from the green channel after the donor excitation. Secondly, the acceptor fluorescence can be caused not only by FRET from the donor but also direct excitation by the donor laser line overlapped with acceptor excitation spectrum. Therefore, the correction factor δ is introduced by integration of the donor laser line divided by integral of the acceptor laser covering the acceptor absorption spectrum:

$$\delta = \frac{\int \varepsilon_A(\lambda_{D,ex}) \cdot P_{D,ex}(\lambda) d\lambda}{\int \varepsilon_A(\lambda_{A,ex}) \cdot P_{A,ex}(\lambda) d\lambda} \tag{13}$$

With ε_A being the extinction coefficient of the acceptor or the donor fluorophore and P being of their laser powers. The correction factor δ is therefore based on the strength of the donor laser. The higher the donor laser power is in comparison with the acceptor laser, the greater the value of direct excitation.

Next, the detector efficiencies at different channels need to be considered (gR and gG) due to their varying sensitivities towards different wavelengths. Together with quantum yields of the

donor (Φ_{FD}) and the acceptor (Φ_{FA}) fluorophores, the correction factor γ is calculated. Quantum yields are the intrinsic characters of fluorophores due to their different molecular structures and excited state dynamics.

$$\gamma = \frac{gR}{gG} \cdot \frac{\Phi_{FA}}{\Phi_{FD}} \tag{14}$$

FRET efficiency E is used to measure the distance from the donor to the acceptor, which can be presented by the donor lifetime in the absence of acceptor $\tau_{D(A)}$. In the absence of acceptors, the lifetime of the donor corresponds to the expected value without energy transfer to the acceptor. The presence of the acceptor leads to the quenching of the donor fluorescence and shortening of the donor lifetime. Therefore, the relationship between E and $\tau_{D(A)}$ can be expressed as:

$$E = 1 - \frac{\langle \tau_{D(A)} \rangle_F}{\langle \tau_{D(0)} \rangle_F} \tag{15}$$

Which describes a linear relationship between the FRET efficiency E and the donor lifetime with or without the acceptor $\langle \tau_{D(A)} \rangle_F$. The line shown in Figure 2. 6 describes the static FRET line, follow which describes the relationship between E and $\tau_{D(A)}$ of static molecules. In real experiments, due to the flexible linker on dye molecules, FRET efficiency can deviate from the static line to higher values as depicted in the Figure as linker effects. Deviations from the static line indicate the dynamic FRET events such as conformational changes. For example, exchanging between the open and closed states of a dual labeled biomolecule. Noteworthy, the deviations from the static line can be also introduced by the above mentioned factors α, γ, and δ (78).

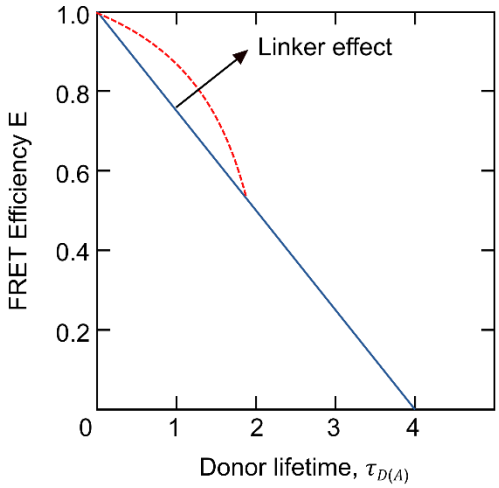

Figure 2. 6 Illustration of linear relationship between FRET efficiency *E* and donor lifetime $\tau_{D(A)}$ (96). The linker effect is shown in dashed lines.

2.3 DNA Origami as Versatile Nanotechnological Platforms

The DNA origami principle. DNA origami, a recently developed bottom-up nanomaterial, has been widely used in biophysics studies. As a cover story of *Nature* in 2006, it was developed by Paul Rothemund (97). The formation of DNA origamis is driven by bottom-up self-assembly, achieving desired two-dimensional (2D) or three-dimensional (3D) structures with nanometer sizes (98). The folding process employs a long single-stranded DNA as a scaffold and hundreds of short oligo DNA strands as staples. The desired structure is formed by the specific binding of each oligo strand on its complementary sequence on the scaffold driven by Waston-Crick base pairing. The long single-strand scaffold is from the genomic DNA of the M13 bacterial phage with 7249 nucleotides length. All ~200 staple strands are around 20-30 nucleotides long, designed by open-source software such as caDNAno (99). DNA origami can be functionalized by modifying staple strands with biotin, fluorophore, protein adapter, or single-stranded DNA linker. This renders DNA origami a versatile platform to anchor the biomolecules of interest. For example, the target biomolecule can be anchored *via* the biotin /streptavidin coupling, protein-protein interaction, or DNA hybridization (100).

In the lab, the assembly of scaffold and staple strands can be achieved by an annealing protocol using a thermal cycler, where all DNA components are mixed in a reaction buffer going through the heating and cooling steps that allow the formation of double-stranded helixes. Since each oligo strand contributes to the hydrogen bonding resembling a stapler, all provide enough force to shape the entire structure. The folded structure of DNA origami can be imaged by electron microscopy (EM), atomic force microscopy (AFM), or fluorescence microscopy if functionalized with fluorophores (97). The powerful characteristics of this DNA origami include tunable addressability and nanoscale spacing. This is of great importance to study protein-protein interactions or protein dynamics with high demands in spatial resolutions.

Applications. Since DNA origami uses DNA as the building blocks, compatible with biological environments, it is widely used in biomedical engineering fields such as drug delivery (101). For example, the virus particles coated by DNA origami cage have been proven to show less immunogenicity than the bare virus after administration into mice (102). In a recent study, a 3D DNA origami cube with a size of 18 x 18 x 24 nm^3 was fabricated with a hollow center and switchable lid, which can be repeatedly opened and closed by specific DNA strands (103). This study shows the potential of drug delivery using DNA origami in a controlled manner. DNA origami has also been used in single-molecule studies (104). As an example, the combination of DNA origami and single molecule force spectroscopy enables precise measurement of stability and dynamics of complex biological machinery PIC (Pol III pre-initiation complex). Due to tunable spacing with high resolution at the nanometer scale, DNA origami provides a versatile platform for single-molecule FRET studies (105). It enables the placing of DNA hairpins with precise localization for single-molecule FRET measurements where the fast dynamics of DNA hairpins can be resolved. As mentioned in the previous chapter, a predicted hexagonal model of TNFRSF receptors was probed using a DNA origami platform. Specifically, soluble CD95L proteins were placed on a rectangular DNA origami platform with different spacings (5 nm, 10

nm, or 20 nm) and architectures (dimers or hexagons). Compared with treatment with only soluble CD95L, the hexagonal arrangement of CD95L on DNA origami with 10 nm spacing showed 100x higher killing efficiency on Hela WT cells (57). This study shows a new potential therapeutic origami agent and inspired the concept of studying CD95 interaction on DNA origami probed by FRET nanoscopy.

2.4 CD95 Interaction probed by FRET nanoscopy on DNA Origami Platform.

As discussed in the previous chapter, CD95 can form anti-parallel dimers (around 12 nm) or singular monomers without ligand addition as their resting state. The nanoscale arrangement of CD95 dimers or monomers can be tested by FRET measurement with specific spacing at 5 nm or 10 nm using DNA origami as a scaffold. The previously described FRET nanoscopy provides molecular-sensitive measurement with nanometer resolution. As a recall, it is combined with colocalization STED (cSTED) and FRET, with information of both projected and vector distances between two molecules. The formation of CD95 anti-parallel dimers or singular monomers can be therefore distinguished by FRET nanoscopy measurements. To this end, the CD95 extracellular domain was purified from the *E.coli* expression system and labeled with biotin *in vivo* by co-expression with the BirA plasmid (kindly provided by Prof. M. Schlierf, BCube, Dresden). Afterward, CD95 protein was labeled separately with ATTO 594 and ATTO 643 using versatile bioconjugation methods. The DNA origami is designed and fabricated by (Johann Moritz Weck, group of Prof. A. Heuer-Jungemann, Chemie und Chemische Biologie, TU Dortmund) with two biotinylated staple strands and two pseudo markers (ATTO 594 and ATTO 647N). Two biotinylation sites are placed with 5 or 10 nm to test FRET efficiencies. Two pseudo markers are placed around 37 nm for orientation and particle averaging of origami platforms in later data analysis. The pseudo-FRET pair and two biotin conjugation sites are placed around 75 nm to ensure no crosstalk between the two pairs. The FRET and cSTED information of two FRET pairs can be obtained, thus providing the 3D information of two CD95 monomer proteins.

II Study Outline

3 Aim of This Work

3.1 Thesis Outline

The goal of this work was to understand the behavior of CD95 receptor on the cellular membrane and how its interactions give rise to signaling initiation. To this end, super-resolution microscopy was investigated to probe CD95 directly on the Hela WT membrane. To activate CD95 differently, we designed different CD95 ligand. On the other hand, in vitro system on the molecular scale was established. In this phD thesis, I focused on two projects. In the first project, a variant of IZ-CD95L was designed and purified using a mammalian expression system, that increased the apoptosis initiation efficiency compared to a commercially available soluble CD95L. To this end, the extracellular domain of CD95L was fused with an isoleucine zipper domain that enhances the structural stability of soluble CD95L. I chose a mammalian expression system using the HEK293T cell line for protein expression. Mass production of protein was achieved by a cost-friendly transfection reagent polyethyleneimine (PEI) and IZ-CD95L was secretionally expressed. I established a lab-based protocol for cost-efficient mammalian protein expression using a 10-layer cell factory, which greatly reduced the cost and time of cell culture. This protocol does not need additional lab equipment and establishment of a stable cell line. The purification was achieved using affinity beads coupled with anti-His-tag antibodies.

To verify the biological activity of IZ-CD95L, I performed live cell imaging with phase contrast mode using an inverted microscopy (IX83 from Olympus). I compared the apoptosis initiation efficiency of lab-purified IZ-CD95L with commercially available sCD95L using apoptosis dynamics analysis, where cells were treated with CD95L variants under different concentrations and conditions and recorded overnight. From those experiments, multiple parameters including maximum apoptosis ratio, half-lifetime, and apoptosis rate can be derived. These give me a first glimpse of the effects of CD95L on cells from a macro-perspective. Next, to understand apoptosis induction difference from a nano-perspective, I performed STED imaging of cells treated with CD95L variants using a customer-aligned Abberior STED microscope. I increased the staining efficiency of fixed cell samples and performed quantitative STED data analysis using advanced deconvolution software and software of Seidel group Ani for STED image spot analysis, where most stained CD95 presented diffraction-limited spots, excluding the previously proposed hexagonal network and further supported the minimal model, as found by other group members in a previous work. STED results were further supported by biochemical analyses including surface plasmon resonance (SPR), enzyme-linked immunosorbent assay (ELISA), and blue native page (BN-PAGE). I then concluded that the difference in apoptosis initiation among CD95L variants relies on their different binding affinities towards CD95 on cellular membranes.

In the second project, I aimed to resolve the distance of CD95 dimers under strictly controlled nano-spacing using DNA origami as a platform. To this end, I designed, purified, and labeled the extracellular domain of CD95. Specifically, the CD95 construct was fused with an avi-tag and co-transformed with biotin ligase BirA to achieve *in vivo* biotinylation in *E.coli*. The purification was achieved using a modern next-generation chromatography (NGC) purification system. I

labeled the purified CD95 with a FRET pair ATTO594 and ATTO643 via specific labelling of the N-terminus Amino group using fluorescent dyes with a NHS-ester for coupling at low pH. then coupled them on DNA origami (fabricated by Moritz Weck). Next, I used a newly developed FRET nanoscopy method to perform FRET imaging of the CD95/DNA origami complex under STED conditions, where the STED resolution was improved by advanced colocalization analysis and lifetime-based FRET resolution was improved by time-gated imaging.

3.2 Contributions

In this work, my supervisor, Prof. Cornelia Monzel conceived the idea of using STED imaging to decipher the apoptosis mechanism of CD95L variants and using DNA origami nanotechnology to understand CD95 organizations. Afterward, I did almost everything by myself including the design, implementation, and execution of all experiments under the strategic direction of Prof. Cornelia Monzel. Specifically, in the cell STED imaging project, I first finished the expression, purification, and modification of IZ-CD95L proteins. Next, I performed cell culture with CD95L variants under different conditions and performed cell immunofluorescence staining. Afterward, I performed STED imaging of fixed cell samples and data analysis. In the FRET nanoscopy part, I first finished the expression, purification, and modification of CD95 proteins. Next, I performed FRET-STED imaging of the CD95/DNA origami complex followed by data analysis. My colleague, Dr. Nina Bartels helped me with establishment of apoptosis dynamics measurement and data analysis, as well as staining and workflow of STED imaging and data analysis. Dr. Nicolaas van der Voort helped with STED microscope alignment, Imspector software settings, Huygens Professional software deconvolution and introduction to FRET nanoscopy project. Dr. Andreas Neusch, helped me with the surface plasmon resonance experiment in the IZ-CD95L project. Dr. Oleg Opanasyuk and Noah Salama, contributed to the improvement of FRET nanoscopy code, which was originally developed by Dr. Jan-Hendrik Budde and Dr. Nicolaas van der Voort et al under supervision of Prof. Claus Seidel. In the DNA origami project. Dr. Suren Felekyan contributed data analysis and software support for STED measurements. DNA origamis were kindly provided by Moritz Weck, from the Prof. Heuer-Jungemann group (Chemie und Chemische Biologie, TU Dortmund). Their contributions account for ~ 1 % of this work. Master students Gajen Thaventhiran/Magdalena Kuom participated in parts of STED experiments for their theses which I co-supervised. ChatGPT was used for literature search in introduction part and python study in chapter 9.2 with an open-source code. A line by line reading and commenting has been performed manually with summary in chapter 9.2.

3.3 Publications

I contributed to the following publications [P] and manuscripts [M] in preparation with my name shown in bold.

[P1] Nina, Bartels, Nicolaas TM van der Voort, Oleg Opanasyuk, Suren Felekyan, Annemarie Greife, **Xiaoyue Shang**, Arthur Bister, Constanze Wiek, Claus AM Seidel, and Cornelia Monzel. "Advanced multiparametric image spectroscopy and super-resolution microscopy reveal a minimal model of CD95 signal initiation." published in Science Advances 10, no. 35 (2024): eadn3238.

[P2] Xiaoyue Shang, Nina Bartels, Johann Moritz Weck, Sabine Suppmann, Jérôme Basquin, Gajen Thaventhiran, Amelie Heuer-Jungemann and Cornelia Monzel. "High yield purification of an isoleucine zipper-modified CD95 ligand for efficient cell apoptosis initiation and with biotin or DNA-oligomer binding domain to probe ligand functionalization effects." published in BMC Biotechnology 25, no. 1 (2025): 64.

[P3] Johann M. Weck, Riya Nair, Merve Z. Kesici, **Xiaoyue Shang**, Cornelia Monzel, Amelie Heuer-Jungemann. "Nanoscale clustered FasL-DNA origami nanoagent yields effective apoptosis induction in large 3D tumoroid model." published in Small (2025): 2502490.

[M1] Xiaoyue Shang, Nina Bartels, Nicolaas van der Voort, Andreas Neusch, Noah Salama, Gajen Thaventhiran, Claus Seidel, Suren Felekyan, Cornelia Monzel. "CD95 signaling depends on ligand binding affinity. " In preparation.

[M2] Xiaoyue Shang and Cornelia Monzel. "Engineered Ligands and Antibodies of the TNF receptor CD95/Fas for Gradual Signaling Activation." In preparation.

Furthermore, this work has been presented in the form of posters [Po] or talks [T] at the following conferences/seminars:

[Po1] DGfB 'International Cellular Biophysics Workshop' | Sep. 29th, 2021 | online
Xiaoyue Shang, Nina Bartels, Moritz Weck, Amelie Heuer-Jungemann, Cornelia Monzel.
CD95 Activity States Studied with DNA Origami Platforms and Single Molecule FRET.

[Po2] CRC1208 conference | Mar. 7th-9th, 2023 | Düsseldorf, Germany
Xiaoyue Shang, Nina Bartels, Nicolaas v. d. Voort, Claus Seidel, and Cornelia Monzel.
Uncovering CD95 Membrane Protein Complex Formation with Multiparametric Image Spectroscopy**.**

[Po3] CRC1208 on-site review | May 4th-5th, 2023 | Düsseldorf, Germany
Xiaoyue Shang, Nina Bartels, Nicolaas v. d. Voort, Claus Seidel, and Cornelia Monzel.
The CD95 Membrane Protein Complex in the Signaling for Apoptosis**.**

[T1] CRC1208 retreat | Nov. 13th-15th, 2023 | Radevormwald, Germany
Xiaoyue Shang and Cornelia Monzel.
Interrogating CD95 Membrane Protein Complex Formation and its Signalling for Life or Death**.**

[Po4] Biophysical society annual meetings | Feb. 10th-14th, 2024 | Philadelphia, USA
Xiaoyue Shang, Gajen Thaventhiran and Cornelia Monzel
STED Microscopy and Single Molecule FRET to Uncover Membrane Receptor–Ligand Interactions in Apoptosis Signal Initiation.

[T2] CRC1208 seminar | May 23rd, 2024 | Düsseldorf, Germany
Xiaoyue Shang and Cornelia Monzel.
Interrogating CD95 Membrane Protein Complex Formation and its Signalling for Life or Death**.**

[Po5] WE Physik symposium | Jul. 16th, 2024 | Düsseldorf, Germany
Xiaoyue Shang, Nina Bartels, Nicolaas v. d. Voort, Claus Seidel, and Cornelia Monzel.
Uncovering CD95 Membrane Protein Complex Formation with Multiparametric Image Spectroscopy**.**

[Po6] Symposium 2025 – From Single Molecules to Cell Functions in Biomembranes | Apr. 2nd – 4th, 2025 | Düsseldorf, Germany
Xiaoyue Shang, Gajen Thaventhiran and Cornelia Monzel.
Probing Receptor – Ligand Interactions in CD95 Apoptosis Signal Initiation**.**

III Materials and Methods

4 Molecular Biochemistry and Cell Biology

4.1 Design of CD95 and CD95L plasmids

The design of CD95 plasmids: CD95 with a streptavidin-binding peptide (SBP) tag. The plasmid pET-21a(+)_Cys-CD95(17-173)-SBP-TEV-His6 was used for expression, purification, and modification of the CD95 receptor protein (version 1). The CD95 extracellular domain with amino acids 17-173 was fused with a streptavidin binding peptide (SBP) tag, a tobacco etch virus (TEV) protease recognition sequence ENLYFQ↑G, and a 6x histidine tag at the C-terminus. One extra cysteine was designed at the N-terminus for fluorescent dye labelling using cysteine-maleimide chemistry. The construct was inserted with pET-21a(+) backbone and ordered from Biocat (BioCat GmbH, Heidelberg, Germany). The theoretical molecular weight (MW) with his tag and isoelectric point (pI) can be calculated from Expasy (https://web.expasy.org/compute_pi/) as pI/MW: 6.75/24.9 kDa. After his tag cleavage, CD95-SBP has theoretical pI/MW: 6.55/23.9 kDa. The full sequence of the CD95-SBP construct reads as:
*MCRLSSKSVNAQVTDINSKGLELRKTVTTVETQNLEGLHHDGQFCHKPCPPGERKARDCTV NGDEPDCVPCQEGKEYTDKAHFSSKCRRCRLCDEGHGLEVEINCTRTQNTKCRCKPNFFC NSTVCEHCDPCTKCEHGIIKECTLTSNTKCKEEGSRSNSTSPVWWMDEKTTGWRGGHVVEG LAGELEQLRARLEHHPQGQREPSSGENLYFQ|GGSSHHHHHH**

The design of CD95 plasmids: CD95 with an Avi (*in vivo* biotinylation) tag. Similarly, the plasmid pET-21a(+)_Cys-CD95(17-173)-AVI-TEV-His6 was used for expression, purification, and modification of the CD95 receptor protein (version 2). The CD95 ECD with aa 17-173 was fused with an Avi-tag for *in vivo* biotinylation, a tobacco etch virus (TEV) protease recognition sequence, and a 6x histidine tag at the C-terminus. Same here, one extra cysteine was designed at the N-terminus for fluorescent dye labelling using cysteine-maleimide chemistry and the construct was designed with pET-21a(+*)* backbone. The theoretical molecular weight (MW) and isoelectric point (pI) can be calculated as MW of 22.0 kDa and pI of 6.52. After his tag cleavage, CD95-Avi has theoretical pI/MW: (6.24/ 20.9 kDa). The full sequence of the CD95-Avi construct reads as:
*MCRLSSKSVNAQVTDINSKGLELRKTVTTVETQNLEGLHHDGQFCHKPCPPGERKARDCTV NGDEPDCVPCQEGKEYTDKAHFSSKCRRCRLCDEGHGLEVEINCTRTQNTKCRCKPNFFC NSTVCEHCDPCTKCEHGIIKECTLTSNTKCKEEGSRSNSSGGLNDIFEAQKIEWHESSGENLY FQ|GGSSHHHHHH**

The design of IZ-CD95L plasmids. For the plasmid pcDNA3.1(-)_IL2pept-His8-TEV-Cys-IZ-CD95L (137-281) the extracellular domain of CD95L consisting of amino acids 137-281 was fused at its N-terminus with an isoleucine zipper (IZ) (106) domain to stabilize the trimerization of CD95L. One extra cysteine was added after the IZ for biotinylation or DNA hybridization. Next to the cysteine, a TEV protease cleavage site and 8x histidine were inserted. The interleukin 2 (IL-2) signal peptide (IL2pept) was fused for secretion expression at the N-terminus (107). It has a theoretical pI of 9.10 and M.W. of 26.3 kDa calculated by Expasy. The corresponding DNA was inserted into a plasmid with a backbone with

a 5‘restriction site EcoRI and a 3‘restriction site BamHI. The plasmid was ordered from BioCat with codon optimization. The complete amino acid sequence of the insert reads: *MRRMQLLLLIALSLALVTNSHHHHHHHHHENLYFQGCGDRMKQIEDKIEEILSKIYHIENEIAR IKKLIGERTSGGSGGTGGSGGTGGSPPEKKELRKVAHLTGKSNSRSMPLEWEDTYGIVLLSG VKYKKGGLVINETGLYFVYSKVYFRGQSCNNLPLSHKVYMRNSKYPQDLVMMEGKMMSYCT TGQMWARSSYLGAVFNLTSADHLYVNVSELSLVNFEESQTFFGLYKL*.*

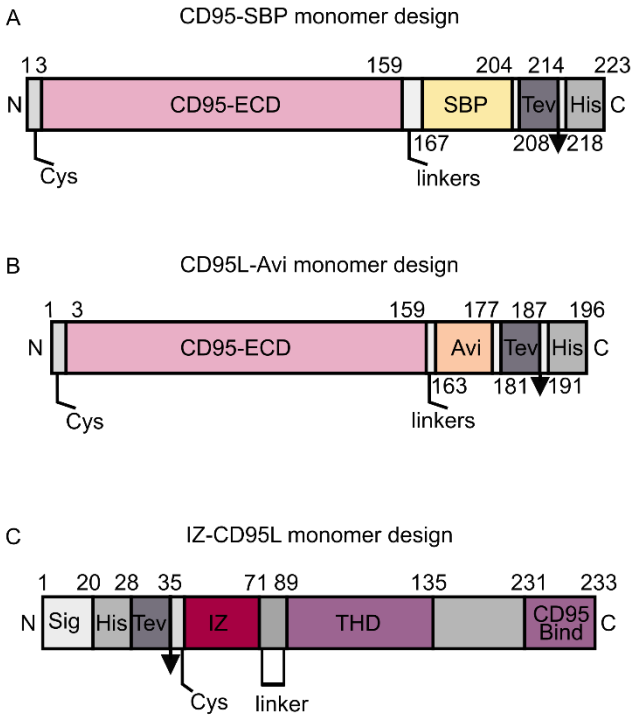

Figure 4. 1 The design of CD95 and CD95L constructs. A. The design of CD95 with a streptavidin-binding peptide (SBP) tag. B. The design of CD95 with an Avi-tag. C. The design of IZ-CD95L plasmids.

Table 1 Amino acids sequences of used fusion tags.

Fusion tags	Amino acid sequence
SBP tag	*MDEKTTGWRGGHVVEGLAGELEQLRARLEHHPQGQREP*
TEV recognition site	*ENLYFQ↑G*
Avi-tag	*GLNDIFEAQKIEWHE*
6 His-tag	*HHHHHH*
IL-2 peptide	*MRRMQLLLLIALSLALVTNS*
IZ domain	*GDRMKQIEDKIEEILSKIYHIENEIARIKKLIGER*
8 His-tag	*HHHHHHHH*

4.2 Cell Lines, Cell Culture and Transfection

4.2.1 E. coli Culture and Transformation

Heat Shock transformation of the CD95-SBP plasmid into *E. coli*_RIPL. The plasmid DNA CD95-SBP was transformed into *Escherichia coli* BL21 Condon plus (DE3) RIPL by heat shock transformation. Specifically, 50 µl of competent cells (Agilent Technologies, Santa Clara, CA, USA) were thawed on ice. 1 µl of plasmid DNA was added into cells and mixed by pipetting up and down several times. Cells with DNA were incubated on ice for 30 min followed by heating in a pre-warmed water bath at 42 °C for 45 seconds. Cells were then cooled on ice for another 2 minutes for recovery. Afterward, 950 µl of lysogeny broth (LB) medium without antibiotics was filled in the Eppendorf tube followed by incubation at 37 °C for 1 h at 300 rpm. 100 or 300 µl cells were spread on pre-warmed LB agar plates with ampicillin at 37 °C overnight. The next day, a single colony was picked up for pre-culture.

Pre-culture and main culture of *E. coli*_RIPL_CD95-SBP. On the second day after transformation, a single colony was resuspended in 50 ml LB/ampicillin and cultured at 37 °C incubator Infors HT Multitron (Infors AG, Bottmingen, Switzerland) with shaking at 280 rpm until the optical density at 600 nm (OD_{600}) value reached 0.6. Then the 50 ml pre-culture was transferred into 1 L LB/ampicillin and induced with 1 mM isopropyl-ß-D-thiogalactopyranoside (IPTG) at OD_{600} = 0.73. Cell culture after induction was continued with shaking at 37 °C/ 200 rpm for an additional 4 h. Cells were washed and harvested with phosphate-buffered saline (PBS) by centrifugation with fixed-angle rotor at 8000 x g for 30 min at 4 °C.

Sequential transformation of CD95-Avi and BirA plasmids into *E. coli* Rosetta™ pLysS. To achieve *in vivo* biotinylation of CD95 using an Avi tag, the designed CD95-Avi plasmid was co-transformed with the biotin ligase BirA plasmid (kindly provided by Prof. Micheal Schlierf at Bcube, Dresden, Germany). Due to the low co-transformation efficiency of two plasmids simultaneously, they were transformed sequentially. First, the pCDF_BirA plasmid (spectinomycin resistance) was heat shock transformed into *Escherichia coli* (DE3) Rosetta™ pLysS competent cells (Sigma-Aldrich, St. Louis, MO, USA). To increase the transformation efficiency, the competent cells were reduced with 25 mM ß-mercaptoethanol (ß-ME) for 10 min on ice. Next, 600 ng of plasmid was added to 50 µl of competent bacteria and incubated for 30 min on ice. Heat-shock was at 42 °C for 45 s and selection was achieved using spectinomycin LB agar plates. The next day, a single colony was picked up and transferred into a 50 ml LB containing 1 g/L glucose (no antibiotics). The *E. coli* Rosetta™ pLysS_ BirA cell line was chemically made competent and transformed with the CD95-Avi plasmid (ampicillin resistance). The successful transformation of the second plasmid was selected with both spectinomycin and ampicillin.

Preparation of chemically competent cells. A single colony from the spectinomycin/LB agar plate (of *E. coli* Rosetta™ pLysS_ BirA cells) was picked up and cultured in 50 ml LB with 1 g/L glucose (w/o antibiotics) until OD < 0.4. Cells were then collected by centrifugation at 4000 g at 4 °C for 10 min. The cell pellet was chilled on ice for 15 min and resuspended in 20 ml ice-cold 100 mM $CaCl_2$, followed by chilling on ice for another 15 min. Next, cells were collected by centrifugation with 4000 g at 4 °C for 10 min. The cell pellet was resuspended with 2 ml 100 mM

$CaCl_2$/ 15 % glycerol and chilled on ice for an additional 10 min. Last, cell resuspension was aliquoted for storage or immediately used for another round of heat-shock transformation.

Pre-culture and main culture of *E. coli* Rosetta™ pLysS_ BirA_CD95-Avi. A single colony was picked from the LB/spectinomycin/ampicillin agar plate and inoculated into a 10 ml LB medium with streptomycin (50 mg/ml) and ampicillin (100 mg/ml), growing overnight at 37°C with shaking at ~ 200 rpm. The next day, the 10 ml starter culture was transferred into 1 L of LB media supplemented with streptomycin and ampicillin, growing at 37 °C incubator with shaking at ~ 200 rpm until OD reached 0.5-0.7. The temperature of the shaker was set to 18 °C. Cell culture was taken out and cooled at R.T. for 1 h until the shaker was ready. Cultures were induced with 0.1 mM IPTG and 0.1 mM biotin overnight at 18 °C. The next day, cells were collected by centrifugation at 6000 rpm 4°C for 30 min (Avati JXN-26, Beckman GmbH). The cell pellet was washed with 1 x PBS buffer at pH 7.4 and collected at 6000 rpm 4°C for 30 min.

4.2.2 HEK293T, Hela Cell Cultivation and Transfection

The Hela wild type (Hela WT) cell line and human embryonic kidney 293 T (HEK293T) cell were ordered (both from ATCC® CCL-2™, ATCC, Manassas, VA, USA). The stable cell line Hela CD95 knock out (Hela $CD95^{KO}$) was generated using clustered regularly interspaced short palindromic repeats (CRISPR/Cas9) as described in (108) with a guide RNA (51). All cell lines were cultured in Dulbecco's modified eagle medium (DMEM) + GlutaMAXTM (Gibco, Life Technologies Inc., Carlsbad, CA, USA) containing 10 % fetal bovine serum (FBS) (Gibco) and 1 % penicillin/streptomycin (P/S) solution (Sigma-Aldrich, Merck KGaA, Darmstadt, Germany) humidified with 5 % (v/v) CO_2 in an incubator (Labogene Scanlaf Mars, Lillerød, Denmark). T25 flasks (Sarstedt AG & Co. KG, Nümbrecht, Germany) were used for cell culture and passivation every 2-3 days at a confluency level of ~ 70 %. Cell morphology and sterile conditions were monitored regularly. For passivation, cells were treated with trypsin-EDTA solution (Sigma) for 5 min for detachment. The reaction was stopped by dilution with 5 ml of DMEM complete medium. Next, cells were collected by centrifugation at 1300 g for 5 min at room temperature (R.T.). The cell pellet was resuspended in the fresh medium and seeded into a new T25 flask with 1:5 dilution. The adherent HEK293T cell line was used for IZ-CD95L secretory expression.

4.3 Mammalian Cell Sample Preparation

4.3.1 Live Cell Sample Preparation

Apoptosis dynamics assays were performed to test the killing efficiency of IZ-CD95L and to compare with a soluble variant Flag-CD95L (Enzo Life Sciences Inc.). To this end, Hela WT cells were seeded in an 8-well glass slide with thickness No.1.5 (Sarstedt) at least one day before the experiment. Before the addition of the CD95L variants, the old culture medium was replaced with pre-warmed 200 µl Leibovitz's L-15 medium without phenol red (Gibco, Life Technologies Inc., Carlsbad, CA, USA) supplemented with 10 % FBS (Gibco) + 1 % P/S (Sigma-Aldrich). IZ-CD95L, Flag-CD95L, or Flag-CD95L + enhancer (Enzo Life Sciences Inc.) was added to the 8-well plate with a final volume of 300 µl in each well at the desired concentration. As a general control, cells on one well were incubated with a blank L-15 complete medium, where no apoptosis of cells was observed. The 8-well chamber was mounted on an IX83 widefield microscope (Olympus Europa SE & CO. KG, Hamburg, Germany) and imaged using a 20x air objective (NA 0.85, UPLSAP 20x O). The measurement was set at 37 °C on a temperature-controlled stage (PeCon GmbH, Ulm, Germany).

4.3.2 Cell Fixation and Immunostaining

For STED sample preparation, sterile cover slides (13 mm in diameter, no. 1.5 H, Paul Marienfeld GmbH & Co. KG, Lauda- Königshofen, Germany) were placed on each well of a 12-well plate and then received ~ 100 x 10^4 cells. Before ligand incubation, cells were washed with Dulbecco's phosphate-buffered solution DPBS (Gibco) briefly. Flag-CD95L (Enzo Life Sciences Inc.) with or without enhancer and IZ-CD95L was diluted in L-15 (Gibco) /10% FBS/1 % P/S for 2 h at 37 °C. Immunofluorescence staining was performed after ligand incubation. Cells were briefly washed with DPBS (Gibco) and then fixed with 4 % formaldehyde in DPBS (16 % stock, methanol-free, Thermo-Scientific) at R.T. for 10 minutes. Afterward, cells were washed with 0.5 ml DPBS briefly followed by three times for 5 minutes on an orbital shaker. To increase antibody binding efficiency, fixed cells were treated with 300 µl antigen retrieval buffer (5 % Urea (w/v) in 100 mM Tris at pH 9.5) preheated at 95 °C for 10 min followed by three times washing with DPBS. Next, cells were permeabilized with 300 µl 0.2 % Triton X-100/ DPBS and washed three times with DPBS. To reduce unspecific staining cells were blocked with 0.5 ml blocking buffer (1 % bovine serum albumin (BSA), 22 mg/ml glycine, 0.1 % Tween-20 in DPBS) at R.T. for 30 min. The primary antibody was diluted in 200 µl blocking buffer and incubated on cells at 4 °C overnight. The next day, antibodies were removed, and cells were washed first with 0.5 ml DPBST (0.05 % Tween-20 in DPBS) briefly followed three times for 10 min. The secondary antibody was diluted in 200 µl DPBST and incubated on cells at R.T. for 1h at dark and washed afterward. Last, cells on the cover slide were cured on a microscope slide using ProLong Diamond anti-Fade Mountant (Invitrogen, Life Technologies Inc., Carlsbad, CA, USA) overnight at 4°C. STED imaging was performed within the first week after sample preparation to achieve the best imaging quality.

4.4 Methods for Protein Expression and Purification

4.4.1 SDS-PAGE, Native-PAGE and Western Blot

Here I summarize the general protocols of SDS-PAGE, native PAGE, and western blot. The different experiments using different gel components or electrophoresis conditions were mentioned differently in the specific experimental part.

Sodium dodecyl-sulfate polyacrylamide gel electrophoresis (SDS-PAGE). SDS-PAGE was used for protein size analysis. As a rule of thumb, ≤ 20 µg of protein in a mixture or ≤ 2 µg of purified protein were loaded along with 5 µl of pre-stained protein marker (Thermo Fisher Scientific). Hand-cast or pre-cast gels (Mini-PROTEAN® TGX™, Bio-Rad, Hercules, CA, USA) were used. Protein was loaded into a final volume of 10-25 µl 1x Laemmli sample buffer with 50 mM tris(2-carboxyethyl)phosphine (TCEP·HCl) and heated at 95 °C for 5 min. Unreduced SDS-PAGE was performed without reducing or heating the sample. Electrophoresis was performed at 130-200 V (Mini-PROTEAN Tetra Vertical Electrophoresis Cell, Bio-Rad) with tris-glycine-SDS running buffer (Fischer Bioreagents). The gel was stained with SimplyBlue™ Safe Stain (Thermo Fisher Scientific) according to the manufacturer's protocol.

Western blot (WB). For WB analysis, a ROTI®PVDF membrane (Carl-Roth GmbH & Co. KG, Karlsruhe, Germany) was activated with 100 % methanol for 1 min, distilled water for 2 min, and blotting buffer (25 mM tris, 192 mM glycine, pH 8.3, 20 % methanol) for 5 min (under the hood). The membrane was placed on a prewet (5 min in blotting buffer) thick filter paper (diameter 110 mm), followed by placing the gel on the membrane and covered by another filter paper. The transfer was performed using a semi-dry system (Trans-Blot Turbo Transfer System, Bio-Rad) at 25 V 2.5 A for 20 min. Afterward, the membrane was blocked with 5 % albumin fraction V (BSA) (ITW Reagents Pancreac, Barcelona, Spain) in TBST buffer (tris-buffered saline, 0.1 % tween-20) at r.t. for 1 h and probed with primary antibody at 4 °C overnight. The next day, after washing 4 times with TBST each 10 min, the membrane was treated with goat anti-mouse (1:1000) or goat anti-rabbit (1:1000) secondary antibody coupled with horseradish peroxidase (HRP) (Cell Signaling Technology, Danvers, MA, USA) at r.t. for 1 h. The blot was then treated with Westar eta c ultra 2.0 substrate (Cyanagen Srl, BO, Italy) for 10-30 s and imaged using Amersham™ Imager AI680 (Cytiva).

Clear native PAGE (CN-PAGE). To see the band shift or large protein complex, clear native PAGE (CN-PAGE) was used. The gel components and electrophoresis conditions need to be adjusted by specific proteins in CN-PAGE. As an example, IZ-CD95L has a theoretical pI of 8.8 (basic protein), and CD95 has a pI of 6.8 (acid protein). To test the band shift of IZ-CD95L after binding with CD95, a hand-cast native gel without SDS (7.5 % acrylamide, 0.1 % ammonium persulfate (APS), 0.1 % tetramethylethylenediamine (TEMED), 375 mM Tris, pH 9.4) was freshly prepared. Protein samples of 100 ng CD95 alone (Sino Biological, Beijing, China) or incubated with 100 ng biotin-IZ-CD95L (at 37 °C for 1 h) were loaded with 10 % glycerol into the final 10 µl loading volume. Electrophoresis was performed at 4 °C with 200 V for 0.5 h with native running buffer (50 mM Tris, 192 mM Glycine, pH 9.14) followed by western blot. The blot was probed with an anti-His-tag antibody (BioLegend).

Blue native PAGE (BN-PAGE). Since band positions in CN-PAGE depend on both protein size and charge, it is difficult to explain the scenarios. BN-PAGE was used for a more straightforward qualitative comparison. Protein samples of one species or in the complex were loaded with 50 % glycerol and 5 % Coomassie blue G-250 with a final volume of 10 µl. The electrophoresis was performed with gradient voltage at 50 V, 75 V, and 100 V each for 30 min at 4 °C with anode running buffer (25 mM Tris/ 192 mM glycine/ pH 8.3) and cathode running buffer (25 mM Tris/ 192 mM glycine/ 0.02 % G-250/ pH 8.3). Cathode running buffer was replaced with anode running buffer when G250 migrated one third or half of the gel and let run until finish. Afterward, proteins from the native gel were transferred to the PVDF membrane and probed with corresponding antibodies.

4.4.2 Cell culture and IZ-CD95L Expression using Cell Factory

A small-scale test expression was performed in a T75 flask, and protein expression and secretion were verified using western blot and apoptosis dynamics. Afterward, a 10-layer cell culture vessel (Nunc™ EasyFill™ Cell Factory™ Systems, Thermo Fisher Scientific) was used for large-scale cell culture and IZ-CD95L expression. The number of cells was scaled up to $\sim 10^8$ before using the large cell factory to achieve sufficient surface density of cells. For this, cells were first growing in a T25 flask, then transferred into a T175 flask and growing to $\sim$ 80-90 % confluency. After 3 days, all cells ($\sim$ 2.3 x 10^7) in the T175 flask were collected and transferred into seven T175 flasks with equal distribution. The cells were again growing for 3 days to $\sim$ 80-90 % confluency. This yielded enough number of seeding cells for cell culture using the 10-layer factory. Before transferring cells, the 10-layer cell factory was filled with 1.23 L of DMEM complete (supplemented with 10 % FBS +1 % P/S) from the inlet under sterile conditions (avoid wetting the inlet to prevent contamination). All cells from the seven T175 flasks were collected and evenly distributed among each layer by placing the vessel on the long edge (with layers vertically to the surface). Due to the large size of the vessel, it is difficult to monitor cell growth using a microscope. Therefore, one additional T175 flask was prepared simultaneously with the same cell density. After 3 days of cell culture (when cells reached a confluency of 70 - 80 %), the DMEM complete medium in the cell factory was carefully removed from the outlet. The vessel was filled with the Opti-MEM complete (10 % FBS +1 % P/S) medium. Polyethylenimine (PEI) was used for a large amount of transfection due to its cost-effectivity. In detail, 1.28 mg of plasmid DNA of IZ-CD95L construct was diluted into 60 ml Opti-MEM plain, and 3.84 mg of (PEI) was diluted into 60 ml Opti-MEM plain with a mass ratio of DNA to PEI as 1:3. In total 120 ml solutions were mixed incubated at r.t. for 30 min. Afterward, the mixture was added to the 1.23 L fresh Opti-MEM complete medium (in total 1.35 L medium). Cell morphology and sterile conditions were checked everyday post-transfection. 3 days/72 h after transfection all medium was harvested, which yielded a total of 472 µg purified protein. More details can be found in (109).

4.4.3 Purification, Modification, and Characterization of engineered CD95/CD95L variants

This part describes the production methods for three constructs CD95-SBP, CD95-Avi and IZ-CD95L. Noteworthy that method related to IZ-CD95L has been published in a preprint (109). Here I rewrite and include it for a better understanding in the results part and to improve the context. First, CD95-SBP was expressed in *E. coli* as inclusion bodies. Therefore, I purified it in

denatured conditions with 8 M urea and renatured it using combination of rapid dilution and gradient dialysis.

Isolation of inclusion bodies and protein purification of CD95-SBP-His. The cell pellet was suspended in 10 ml of cold 50 mM Tris•HCl buffer (pH 8.0) containing 10 mM ß-ME, 1 mM ethylenediaminetetracetic acid (EDTA), and 100000 U/ml lysozyme, kept on ice for 30 min. Genomic DNA was fragmented by sonication (Hielscher, UP200ST-G-Ultrasonic generator) for 20 s and rest for 20 s with 5 repetitions. The crude extract was centrifuged (Centrifuge 5810 R, Eppendorf, Hamburg, Germany) at 14,500 x g for 20 min at 4 °C and discarded. The cell pellet was dissolved at room temperature for 1 h in 20 ml denaturing buffer (100 mM phosphate buffer, pH 7.5, 8 M urea, 10 mM imidazole). The dissolved solution was filtered through a 0.2 µm cut-off filter (Filtropour S 0.2, Sarstedt, Nübrecht, Germany). Protein purification was performed with His-trap HP column 5 ml (Cytiva) using ÄKTA prime plus (Cytiva). The purification system and column were equilibrated with 5 column volumes (CV) of 20 % ethanol, 5 CV water, and 5 CV buffer A. The denatured sample was loaded with 5 ml/min followed by 5 CV column wash. Elution was performed with linear gradient elution with a 3 ml fraction size. Protein fractions were checked with 10 % hand-cast gel by SDS-PAGE at 130 V for 2 h. Here, 5 µg of purified protein or 50 µg of protein mixture was reduced with TCEP/heating, loaded together with 3 µl prestained protein standard (Thermo Fischer).

Denatured size exclusion chromatography (SEC). To study CD95-SBP-His oligomerization *in vitro*, I performed size exclusion chromatography (SEC) with Superdex 75 10/300 GL (Cytiva) using ÄKTA prime plus (Cytiva). The column was equilibrated with 2 column volume (CV), 20 % ethanol, 2 CV water, and 2 CV running buffer (8 M urea,10 mM DTT, 1 x phosphate buffer pH 7.5). All buffers were filtered and degassed for at least 1 h before loading on the column. 500 µl protein (stock concentration of CD95-SBP-His at 5 mg/ml) was reduced with 10 mM DTT for 1 h at 4 °C followed by column load. The sample was eluted in 30 ml running buffer with a flow rate of 0.3 ml/min and a fraction size of 1 ml. After analysis, the column was washed with 2 CV water and 2 CV 20 % ethanol.

CD95-SBP-His refolding by rapid dilution and dialysis. 15 mg purified protein CD95-SBP-His was drop-wise diluted in 60 ml dilution buffer (3 M urea 0.4 M L-arginine monohydrochloride, 20 mM reduced L-glutathione, 2 mM oxidized L-glutathione, 100 mM phosphate buffer pH 7.5), stirring by magnetic overnight at 4°C. The next day, the diluted sample was loaded into a 7 kDa cut-off dialysis membrane (Spectrum™ Labs Spectra/Por™) followed by dialysis against 1.6 L 1 x PBS at pH 7.5 supplemented with 1 mM EDTA overnight at 4°C. The sample was dialyzed a second time against 1.6 L 1 x PBS at pH 7.5 overnight at 4°C. Afterward, the protein was concentrated by ultracentrifugal filter using Amicon Ultra-15 3 K (Merck Millipore Ltd., Burlington, MA, USA) at 5,000 x g for 60 min.

CD95-SBP-His *in vitro* chemical cross-linking. To study CD95-SBP-His oligomerization *in vitro*, I performed SDS-PAGE analysis under non-reduced conditions or with chemical cross-linking. The loading scheme was as follows: first lane: 10 µl CD95-SBP-His (stock concentration 1 mg/ml) + 4 µl 5 x sample buffer without TCEP, loaded without heating. Second lane: 10 µl

protein + 3.3 µl 4 % formaldehyde (FA) was incubated at 4 °C for 30 min. Afterward, 4 µl of 5 x sample buffer without TCEP + 2.7 µl water was added. The sample was loaded without heating. Both samples were loaded on 10 % precast gel (BioRad) for SDS-PAGE running at 130 V with around 1.5 h at room temperature.

CD95-SBP His-tag cleavage. To cleave His-tag on CD95-SBP-His, dialysis buffer (25 mM Tris•HCl, 150 mM NaCl, pH 8.0, 14 mM ß-ME), and reaction buffer (50 mM Tris•HCl, 0.5 mM EDTA, 1 mM dithiothreitol (DTT)) were prepared. 1 ml of protein was taken and loaded into a dialysis bag (2,000 MWKO Slide-A-Lyzer Dialysis Cassette, Thermo Fischer Scientific) against reaction buffer at 4 °C around 8 h with stirring. Afterward, the protein was taken out and mixed with 17 µl TEV protease (Sigma Aldrich) and injected back into the dialysis bag against dialysis buffer at 4 °C for 16 h with stirring. Protein was afterward taken out and loaded on Ni-NTA magnetic beads (Thermo Fischer Scientific) following the manufacturer‘s protocol. Flow-through containing CD95-SBP without His-tag was collected, and the TEV protease (His-tagged) and uncleaved His-tag on CD95-SBP bound on beads were discarded. To remove DTT, the collected protein was dialyzed against 1 x PBS buffer at least twice for 5 h at 4 °C each time. SDS-PAGE was used to check protein size change after His-tag cleavage. 10 µl of protein + 10 µl 2 x sample buffer containing ß-ME, was heated at 99 °C for 10 min, loaded on 10 % precast gel (Biorad) for SDS-PAGE running at 130 V for 1.5 h. CD95-SBP without His-tag was calculated with Expasy with M.W. of 24.0 kDa and pI of 6.55.

CD95-SBP N-terminus labelling with ATTO-643 NHS ester. CD95-SBP without His-tag at 1 mg/ml in 100 µl was buffer exchanged with 1 x PBS at pH 6.4 using Amicon Ultra 0.5 3 K. ATTO-643 NHS ester (ATTO-TECH GmbH) was freshly dissolved in 80 µl dimethyl sulfoxide (DMSO), results in a stock concentration 13.1 mM. 100 µl CD95-SBP protein received 4.8 µl dye (with a molar ratio of dye to protein 15:1) followed by incubation overnight at 4 °C. Next day, excess dyes were removed by PD SpinTrapTM G-25 (Cytiva) with PBS buffer at pH 7.5. The degree of labeling (*DOL*) was determined using nanodrop measuring absorbance at 280 nm (A_{280}) and 643 nm (A_{max}) (see Table 2). The calculation used the following equation:

$$DOL = \frac{A_{max} \times \varepsilon_{protein}}{\varepsilon_{max} \times [A_{280} - (A_{max} - CF_{280})]} \tag{16}$$

With the correction factor CF_{280}, the molar extinction coefficient of the fluorescent dye ($\mathcal{E}_{max}$, provided by the manufacturer), and the molar extinction coefficient of the protein ($\mathcal{E}_{protein}$) (calculated from Expasy).

Table 2 Calculation of DOL of CD95-SBP with NHS-ester.

	A_{280}	A_{max}	CF_{280}	$\mathcal{E}_{max}$	$\mathcal{E}_{protein}$	*DOL*
CD95-SBP_ATTO-643	0.023	0.178	0.004	1.5 x 10^5 M^{-1}•cm^{-1}	20605	1.5

Identification of CD95-Avi-biotin-His expression and *in vivo* biotinylation. Two cell lines were sequentially transformed with CD95-Avi and BirA for testing: cell line 1 is *E. coli* BL21 pLysS and cell line 2 is *E. coli* BL21 Rosetta™ pLysS. The bacterial expression in both cell lines

was induced with IPTG and biotin, growing overnight at 18 °C as described above. The next day, cell line 1 *E. coli* BL21 pLysS was harvested at OD = 3.12, and cell line 2 *E. coli* BL21 Rosetta™ pLysS was harvested at OD = 1.54. 5.8 x 10^8 cells were harvested for each cell line by centrifugation at 13,000 g for 5 min. The collected cell pellet was dissolved in 10 µl 1 x SDS sample buffer supplemented with 2.5 M urea and 10 mM DTT. Samples were heated at 99 °C for 10 min and analyzed on a precast 4-20 % gel (BioRad) at 130 V for 1 h followed by western blot analysis at 2.5 A 25 V for 20 min. The blot was probed for biotinylation with AF488-streptavidin (AAT Bioquest, Pleasanton, CA, USA) at 30 µg/ml in 2 ml TBST, and with anti-CD95 rabbit (Invitrogen, 1: 1000) at 1 µg/ml for probing CD95. Both were performed at 4 °C overnight.

CD95-Avi-biotin-His purification and refolding. After overnight induction, cells were collected by centrifugation at 6000 rpm at 4 °C for 30 min the next day. The cell pellet was lysed in 100 mM phosphate buffer at pH 7.5 containing 8 M urea and 10 mM imidazole on ice using 30 s sonication + 30 s rest on ice repeated 5 times (UP200ST). The insoluble part was removed by centrifugation at 12100 rpm for 30 min at 4 °C (Eppendorf). The supernatant was filtered through a 0.2 µm cut-off filter (Filtropur S 0.2, Sarstedt) and purified by His trap HP column 5 ml (Cytiva) using next-generation chromatography (NGC) purification system (Biorad). Protein was eluted with 500 mM imidazole, 8 M urea, and 100 mM phosphate buffer at pH 7.5. The CD95-Avi-biotin refolding was performed similarly as described in the case of CD95-SBP-His. Specifically, 18.95 mg (15 ml) of purified CD95 was reduced with 6.67 mM DTT followed by diluting into 15 ml dilution buffer (100 mM phosphate buffer, 0.55 M L-arginine, 1 M urea, 27 mM reduced L-glutathione, 2.7 mM oxidized L-glutathione, pH 7.5). The mixed solution was incubated with rotation at 450 rpm, 4 °C for 40 h. Afterward, the reaction mix was loaded into a 12-14 kDa cutoff tubing (Spectrum Labs™, Fischer Scientific) dialyzed against 1 L dialysis buffer 1 (1 x PBS, pH 7.5, 1 mM EDTA, 5 mM reduced L-glutathione, 1 mM oxidized L-glutathione) for 3 h at 4°C with 450 rpm, this step was repeated once for 2 h. A second dialysis was performed using 2 L dialysis buffer 2 (PBS, pH 7.5) twice at 4 °C o/n at 450 rpm, this step was repeated for another 4.5 h. Finally, the protein was taken out and concentrated using a protein concentrator with four sets of 3 K MWCO (Pierce, 20 ml, Thermo Scientific) for centrifugation at 6000 g for 4.5 h at 4 °C. The final yield was 2.25 mg/ml x 7 ml = 19 mg (yield: 83 %).

His-tag cleavage of CD95-Avi-biotin-His and ATTO dye labelling. 4 ml of 2.25 mg/ml CD95-Avi-biotin-His + 1 ml PBS buffer = 1.8 mg/ml protein was added with 5 mM DTT and 45 µl of TEV protease (Thermo Scientific). The reaction was dialyzed against 500 ml reaction buffer (1 x PBS pH 7.5, 5 mM DTT, 0.5 mM EDTA) at 4 °C o/n. The next day, reaction buffer was exchanged with 500 ml dialysis buffer 1 (1 x PBS pH 7.5, 5 mM reduced L-glutathione, 1 mM oxidized L-glutathione) at 4°C for 6 h. Afterward, buffer 1 was exchanged with 500 ml dialysis buffer 2 (1 x PBS pH 7.5) at 4°C o/n. After all dialysis steps, the protein was at 0.9863 mg/ml in ~ 7 ml. 700 µl Ni-NTA beads resuspension was freshly taken and washed with the first 2.8 ml and a second 7 ml 1 x PBS at pH 6.6 and collected by a magnetic stand. The beads were loaded with a 7 ml protein sample (1 x PBS pH 7.5) at R.T. for 30 min incubation with end-over-end rotating. The supernatant was collected, and the concentration was determined by nanodrop: 0.91 mg/ml in ~ 6 ml. The protein sample was concentrated in a 20 ml ultracentrifugal filter at 4°C for 1.5 h until there was 2 ml left. The concentrate was mixed and washed with another 4 ml 1 x PBS at pH 6.6

and centrifuged again until 2 ml left. The final concentration of CD95-Avi-biotin was 2.4 mg/ml determined by a nanophotometer (NP80, Implen GmbH). The His-cleaved CD95-Avi-biotin was labelled with ATTO 643-NHS and ATTO 594-NHS ester protein to dye molar ratio 1:15. In each labelling reaction 100 µl CD95-biotin was diluted at 1 mg/ml in 100 µl.

Table 3 Reaction mix of labelling reaction using NHS ester chemistry.

	Dye stock	Dye amount	Protein amount	PBS at pH 6.6	Protein stock
Reaction 1	ATTO-643 NHS ester 13.1 mM	6 µl	41.67 µl	52.33 µl	2.4 mg/ml CD95-biotin
Reaction 2	ATTO-594 NHS ester 18 mM	4 µl	41.67 µl	54.44 µl	2.4 mg/ml CD95-biotin

The labeled protein was purified from free dyes by NAP-5 column (Cytiva) separately. The DOL was determined by nanodrop (NP80, Implen GmbH).

Table 4 Calculation of DOL of CD95-biotin with NHS-ester.

	A_{280}	A_{max}	CF_{280}	ε_{max}	$\varepsilon_{protein}$	*DOL*
CD95-biotin_ATTO-594	2.150	3.855	0.5	1.2 x 10^5 M^{-1}•cm^{-1}	8480	1.22
CD95-biotin_ATTO-643	0.238	2.634	0.04	1.5 x 10^5 M^{-1}•cm^{-1}	8480	1.12

His-tag affinity purification of His-IZ-CD95L. The cell debris was removed from 1.35 L collected cell culture medium by centrifugation at 1300 g for 5 min and passing through a 0.2 µm membrane filter (Sarstedt). Filtered medium was concentrated using 3 K cutoff centrifugal filters (Amicon® Ultra-15) into 80 ml as a manageable volume and to increase the binding yield. Agarose beads coupled with anti-His-tag antibody were used for His-IZ-CD95L purification due to the high affinity of antigen/antibody binding. To this end, 2 ml of anti-His-tag affinity resin (GenScript Biotech) was added into the concentrated culture medium and incubated at 4 °C o/n on a rotor. Nextday, two empty polypropylene columns with 1 ml volume (QIAGEN GmbH) were equilibrated with (5 ml of each) 20 % ethanol, MilliQ water, and TBS buffer (Tris-buffered saline, 50 mM Tris·HCl, 150 mM NaCl, pH 7.4). The culture medium containing resin was loaded on both columns with equal amounts (i.e. 40 ml flow through for each). The resin collected was washed with 30 ml TBS. The His-IZ-CD95L was eluted with 12 ml alkaline elution buffer (0.1 M Tris·HCl, 0.5 M NaCl, pH 12.0) according to the manufacturer's protocol. 12 ml elution was concentrated again using Amicon® Ultra-15 3 K filters. The final concentration of purified protein was 0.409 mg/ml, as determined by BCA assay (Pierce® BCA Protein Assay Kit). Purity of protein was checked by 10% SDS-PAGE (Mini-PROTEAN® TGX™, Bio-Rad), where 1 µg purified protein was loaded into 25 µl Laemmli sample buffer/50 mM TCEP·HCl with heating (95 °C for 5 min). Electrophoresis was performed at 180 V for 1 h. SimplyBlue™ Safe Stain was used for gel staining according to the manufacturer's protocol.

His-tag cleavage of IZ-CD95L. 200 µg of purified His-IZ-CD95L was reduced with 5 mM dithiothreitol (DTT) and treated with 13 µg (1:15 w/w) TEV protease (Sigma-Aldrich) at 4 °C overnight. The second day, 50 µl Ni-NTA magnetic beads (HisPur™, Thermo Fisher Scientific) were taken and added in a 1.5 ml Eppendorf tube. The beads were washed with a first 200 µl and a second 500 µl of PBS buffer and collected by a magnetic stand. The supernatant was discarded, and 200 µg of the reduced protein was mixed with beads by briefly pipetting for 10 s. The binding of Ni-NTA beads with His-IZ-CD95L was incubated for 30 min at r.t. with rotation. Afterward, the flowthrough was collected, which contains IZ-CD95L without His-tag. His-tag cleavage was checked by western blot, with 60 ng of His-IZ-CD95L and IZ-CD95L loaded first on a 10% SDS-PAGE followed by a western blot probed with anti-His-tag antibody 1:1000 (BioLegend).

Site-specific biotinylation of IZ-CD95L. After His-tag cleavage step, DTT was removed by buffer exchange with PBS buffer using Amicon® Ultra-0.5 3 K centrifugal filters (Merck Millipore Ltd.). Before biotinylation, 100 µg of His-tag free protein in PBS was freshly reduced with 2 mM TCEP·HCl at 4 °C for 30 min. 2 µl of 10 mg/ml (10 x molar excess) of biotin-C5-maleimide (Sigma-Aldrich) was incubated with IZ-CD95L at 4 °C o/n. The second day, NAP™-5 column (Cytiva) was used to remove the extra biotin, where 120 µl of protein/biotin mixture was loaded on the equilibrated (10 ml PBS buffer) NAP-5 column. Next, 0.38 ml PBS was used to equilibrate the column. The protein was eluted with 0.53 ml PBS. The final yield of the biotinylated protein was 0.189 mg/ml in 550 µl. Successful biotinylation was verified by western blot analysis, with 300 ng of IZ-CD95L and biotin-IZ-CD95L loaded on 10 % SDS-PAGE followed by western blot. The blot was probed by 30 µg/ml AF488-streptavidin (AAT Bioquest, Pleasanton, CA, USA) overnight at 4 °C.

4.4.4 Surface Plasmon Resonance Measurements

Surface plasmon resonance measurement was performed with Dr. Andreas Neusch. The surface plasmon resonance experiments were carried out to analyze the binding affinity of CD95L variants with CD95 using a Reichert® 2SPR (Ametek Reichert Technologies, New York, USA) 2-channel surface plasmon resonance system. Purified IZ-CD95L and Flag-CD95L (Enzo Life Science, Inc.) were tested as analytes. The sensor chips with NTA derivatized linear polycarboxylate hydrogel SCR NiHC30M (Xantec, Düsseldorf, Germany) was used to immobilize His-tagged CD95 and streptavidin derivatized linear polycarboxylate hydrogel SCR SAH30M was used to immobilize CD95-Avi-biotin (lab-purified). The level of immobilization was 250 resonance units (RU). Binding of CD95L variants were assayed at different concentrations at a flow rate of 30 µl/min for 6 min. The second chip was regenerated with either EDTA washing followed by Ni^{2+} recharging or with 4 M $MgCl_2$.

5 Advanced Optical Microscopy and Spectroscopy Techniques

5.1 Widefield Microscopy

5.1.1 Olympus IX83 Microscope Setup

The IX83 inverted microscope (Olympus Europa SE & CO. KG, Hamburg, Germany) was used for all time-lapse measurements of live cells. The microscope is equipped with a fully motorized stage (TANGO, Märzhäuser Wetzlar GmbH & Co. KG, Wetzlar, Germany). An internal halogen lamp (IX3) is used as a light source for transmitted imaging techniques (such as brightfield (BF) or phase contrast (PH) microscopy). The LED light engine (Lumencor SOLA SE II, Lumencor Inc., Beaverton, OR, USA) produces white light with a continuous spectrum ranging from 380 nm to 680 nm, used as a light source for fluorescence microscopy. Four different filters were used for fluorescence imaging: a DAPI HC filter set (with excitation filter 377/50 nm and emission filter 447/60 nm), an EGFP ET filter set (with excitation filter 470/40 nm and emission filter 525/50 nm), a DsRed ET filter set (excitation filter 545/30 nm, emission filter 620/60 nm), and a Cy5 ET filter set (excitation filter 463/30 nm, emission filter 690/50 nm). All are from AHF analysentechnik AG, Tübingen, Germany. A variety of objectives were used in this work, including a 20x air objective (NA 0.85, UPLSAP 20x) a 60x oil objective (NA 0.65-1.25, UPLFLN 60x OIPH), and a 100x oil objective (NA 1.49, UAPON 100x OTIRF). All are from Olympus Europa SE & CO. KG. Images were recorded on a sCMOS camera (Photometrics prime BSI, Teledyne photometrics, Tucson, AZ, USA) and visualized on cellSens dimension 2.3 software (Olympus). Live cell imaging was achieved with temperature control at 37 °C on an incubator (PM 2000 RBT), a heating insert (P lab-Tek Tm 2000), and a temperature controller (2000-1, PeCon GmbH, Ulm, Germany).

5.1.2 Time-lapse Imaging for Apoptosis Dynamics

Apoptosis dynamics assays were performed to demonstrate the killing efficiency of IZ-CD95L and to compare with soluble CD95L variants (Enzo). Hela WT cells were seeded in the wells of an 8-well glass slide with thickness No.1.5 (Sarstedt). The 8-well chamber was mounted on the inverted IX83 microscope (Olympus) using a 20x air objective (NA 0.85, UPLSAP 20x) on a temperature-controlled motorized stage at 37 °C. 5 different positions in each chamber were imaged under phase contrast or bright field mode. Each position was recorded at intervals of every 5-15 minutes over 15 h with an autofocus system (Z-drift compensation system, IX-ZDC) on the CellSense Dimensions Software (Olympus). The time-lapse image stacks were analyzed using ImageJ (version 1.49v, U. S. National Institutes of Health, Bethesda, MD, USA). Specifically, the death time of each apoptotic cell was identified manually by distinguishable morphology changes (including membrane blebbing, cell fragmentation, and so on). Frame numbers of the identified apoptosis event were marked and exported in a .csv file. Afterward, Matlab (R2018a, The MathWorks, Inc.) was used to load CSV file and analyse data fitted with Hill eqution:

$$P(t) = P_{\max} - \frac{P_{\max} - P_{\min}}{1 + \left({}^{t}/_{t_{\text{half}}}\right)^{n}} \tag{17}$$

with P_{max} and P_{min} being the maximal and minimal fractions of apoptotic cells and t_{half} being the time when half of all cells died. n is the Hill coefficient representing the speed of the apoptosis dynamics. From different independent measurements, standard deviations were calculated.

5.2 Confocal Microscopy and Polarization-Resolved TCSPC

5.2.1 Abberior Expert Line Microscope Setup

STED measurements were performed on a custom-designed Abberior Expert Line system (Abberior Instruments GmbH, Göttingen, Germany). Excitation lasers at 561 nm and 635 nm are pulsed with a width < 100 ps. The depletion laser at 775 nm with a pulse width of 1.2 ns was synchronized at 40 MHz (25 ns) for depletion of both fluorophores. The STED 775 nm laser is generated by a spatial light modulator (SLM) with a 2D donut shape. A quarter-wave plate and a half-wave plate are placed before each excitation laser. STED lasers are circularly polarized, and excitation lasers are linearly polarized. The excitation and depletion lasers are superimposed by three notch filters N1 (for the 561 nm excitation laser, NF03-594E (Semrock)), N2 (for the 640 nm excitation laser, NF03-658E (Semrock)), and N3 (for the 775 nm STED laser (Abberior)). The fluorescence signal was collected by a 100x oil objective (NA 1.4, UPLSAPO 100x O) and passed through a pinhole with a size of 1.3 Airy units. Afterward, the fluorescence signal is first split by orientations into parallel and perpendicular channels using a polarizing beam splitter (PBS). A dye-specific band-pass filter is placed before each APD, with Cy3 filter cubes for APD1 and APD3 (Abberior ET608/44) and Cy5 filter cubes for APD2 and APD4 (Abberior ET685/70M). Cy3 filter cube contains a dichroic beam splitter that transmits light with wavelength > 640 nm. Fluorescence photons at two colors and two polarizations are registered by four APD (Excelitas, SPCM-AQRH-13-TR) detectors. The photon detection is synchronized with a time-correlated single photon counting unit (TCPSC, Hydra Harp 400, PicoQuant GmbH, Berlin, Germany).

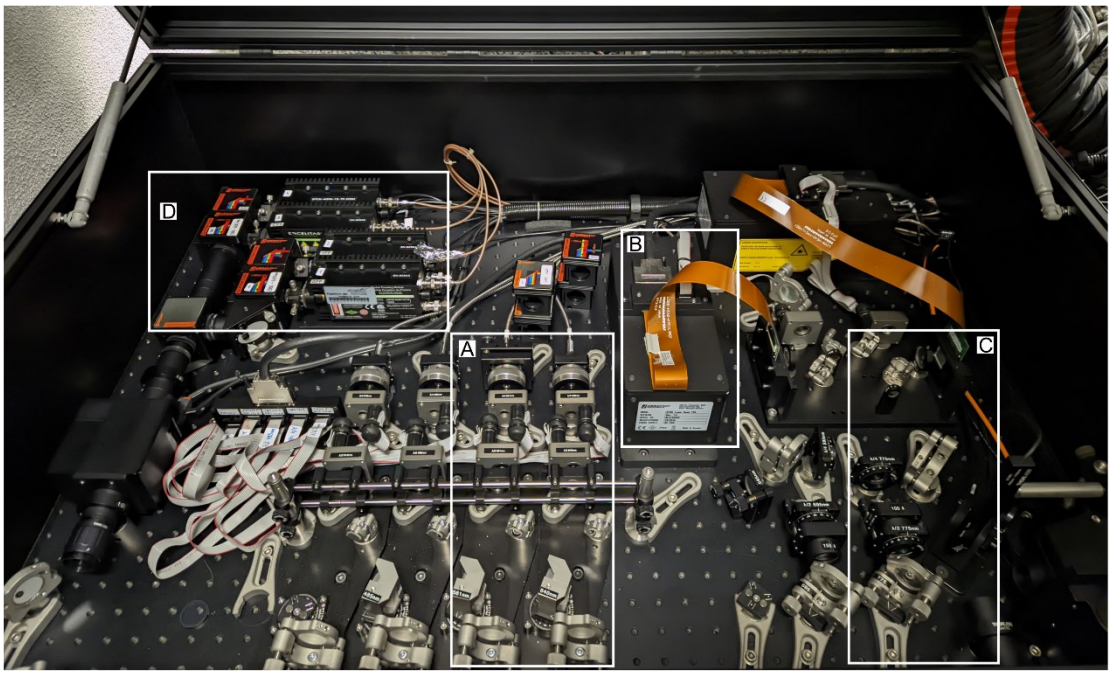

Figure 5. 1 Overview of the Abberior STED microscope alignment. A. Excitation lasers (561 nm pulsed and 640 nm pulsed) alignment. B. STED laser (775 nm pulsed) head. C. STED laser alignment. D. Four filter-based APD detectors.

5.3 Stimulated Emission Depletion (STED)

5.3.1 Abberior STED microscope alignment

The best imaging quality can be achieved when the light path in the microscope is aligned correctly. This includes detector alignment, excitation laser alignment, and STED laser alignment, which will be explained in the following parts.

Abberior STED microscope startup/shutdown. The microscope was switched on by the following steps (see Figure 5. 2): 1) Switch on the PC. 2) Switch on the following item in order of (B-C-A) the Olympus halogen illumination CBH box (2B) (bottom left). Wait for the beep and then switch on the stage controller (2C) (bottom right), and then the LED control (Cool LED PE-2, top) (2A). 3) Switch on the touchpad. 4) Switch on the TCPSC unit (on the ceiling). 5) Switch on the monitor and log in. 6) Start the Imspector software. 7) Initialize all. The microscope was switched off by operation the other way around.

Laser power measurement. The laser power was measured using a power meter with photodiode sensor s175c for 775 nm STED laser and s170c for 561 nm/ 640 nm excitation lasers (Thorlabs, Newton, NJ, USA). Before the measurements, all lasers should run warm for at least 1 h. The measurement was performed in the dark following steps: 1) Set the correct wavelength of the tested lasers. 2) Set the laser power in Imspector software as 0 % and reset the power meter to zero. 3) Adjust the laser power at increasing settings (e.g. for 775 nm STED laser, set 0 %, 10 %, 20 % 30 %, …, 100 %) and measure the corresponding apparent power value (mW/μW).

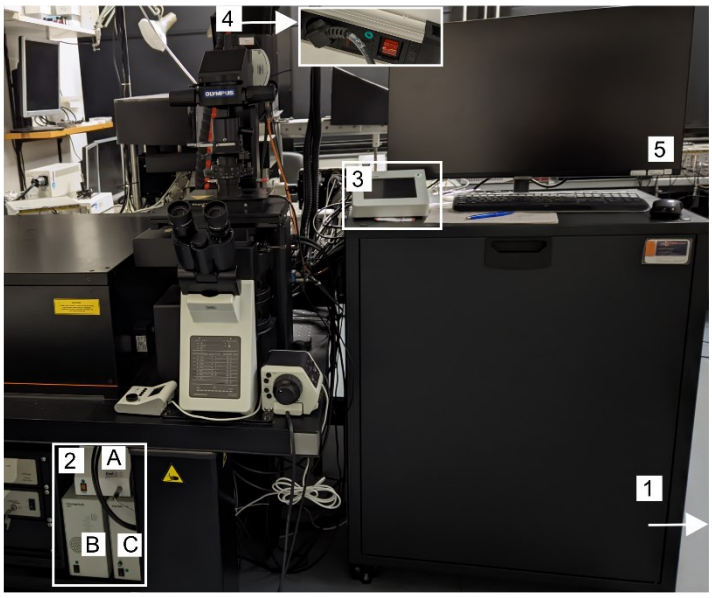

Figure 5. 2 Startup or shutdown of the Abberior STED microscope. Switch on the microscope by 1) PC → 2) Controllers (anticlockwise B→C→A) → 3) Touchpad → 4) TCSPC 5) Monitor 6) Imspector software. 7) Initialize all. Switch off the software by reverse operation.

Detector alignment. Before switching on the microscope, the correct filter cubes were placed in front of the four detectors. Specifically, Cy3 filter cubes were used for APD1 and APD3 (Abberior ET608/44) and Cy5 filter cubes for APD2 and APD4 (Abberior ET685/70M). Afterward, the beam needs to be realigned using two screws for each detector to achieve the best detection efficiency (see Figure 5. 3, shown in asterisks). The adjustment was visualized *via* Symphotime software (PicoQuant, Berlin, Germany) showing the time trace of the fluorescence signal. 50 µl of diluted fluorescent dyes Alexa fluor 594 (for APD 1 and 3) and ATTO 643 (for APD 2 and 4) were applied on a cover glass (No.1.5, Paul Marienfeld GmbH & Co. KG, Germany). By adjusting the two screws on the parallel and perpendicular detector for each color, the signal time trace on Symphotime should show the highest signal and low difference between parallel and perpendicular. Specifically, the alignment was done by the following steps: 1) Tick/activate the APD boxes 1, 2, 3, and 4 in Imspector software. Set lasers e.g. 561 nm 10 % (the specific number needs to be adjusted). 2) Rest Hydraharp and open Symphotime software. Select → Timetrace → channels 1 and 3 → Start. 3) Tick off the STED laser and wait until it returns to zero intensity. Open the laser box and adjust two screws on APD 1 and APD 3 (See Figure 5. 3**,** orange asterisks). 4) When both detectors reach the highest signal, close the Symphotime and initialize Hydrharp to record. 5) Save both .msr and ptu files.

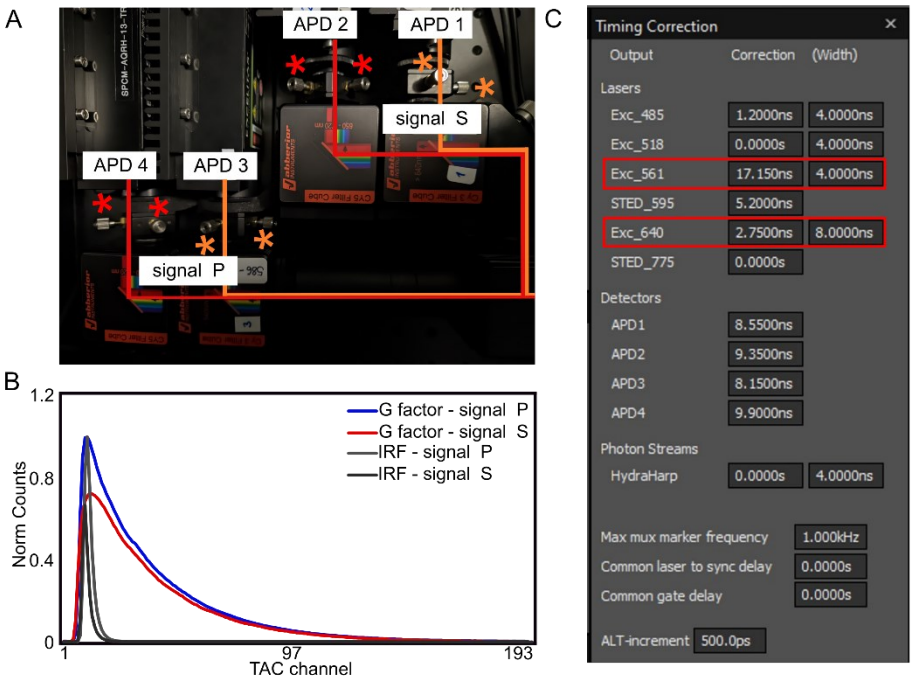

Figure 5. 3 Alignment of detectors. A. Four APD detectors are shown in the figure, with polarization filtered and color-filtered signal detections. B. An example image of polarized detection from P and S channels along with IRF curves. Counts were normalized.

Excitation and STED laser alignment. The STED beam should be symmetric and centered with two excitation lasers for the best depletion effect. Excitation and STED lasers were aligned using TetraSpeck^{TM} beads (0.1 μm, Invitrogen). The overlay of two excitation lasers can be achieved by the two screws on the excitation light path, indicated by asterisks with orange color for excitation at 561 nm and red color for excitation at 640 nm (See Figure 5. 4A). A good alignment should show an overlapped image under 561 nm and 640 nm as shown in B C indicated by the orange color. The positioning adjustment of the STED laser with the excitation laser is done by phase modulation of the STED beam along the X-axis (Grating X) and Y-axis (Grating Y) in the spatial light modulator (SLM_STED775) box of Imspector software (see Figure 5. 4D E F). The confocal and STED resolution can be calculated by fitting Figure 5. 4 F with Gaussian and calculating the full width at half maximum (FWHM) as 263 nm for confocal and 111 nm for STED. Therefore, the corresponding resolutions /sigma (σ) are 112 nm for confocal and 47 nm for STED mode. This is used further in quantitative STED data analysis as ROI size in AnI colocalization with ROIs of 11 x 11 pixels (10 nm pixel size, 100 nm x 100 nm).

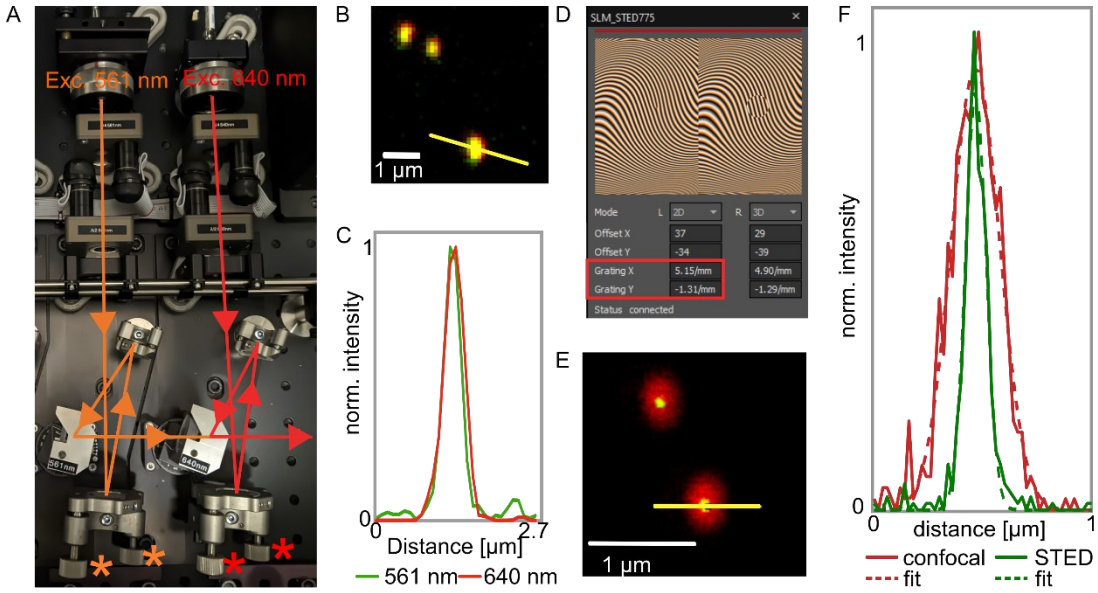

Figure 5. 4 Alignment of the excitation lasers and the STED laser. A. Laser alignment of excitation at 561 nm (orange arrows) and 640 nm (red arrows). The asterisk signs indicate the screws used for aligning lasers at 561 nm and 640 nm respectively. B. Example of an overlay image of TetraSpeck beads under confocal mode excited by 561 nm (green) and 640 nm (red) lasers. Scale bar: 1 µm. One yellow line was drawn to select the intensity profiles of the bead. C. Intensity profiles of the selected bead with 561 nm (green) and 640 nm (red). D. SLM_STED775 panel in Imspector software with Grating X and Y indicated by a red box. E. The STED image (red) overlaid with the confocal image (green) of TetraSpeck beads. Scale bar: 1 µm. One yellow line was drawn to select the intensity profiles of the bead. F. Intensity profiles of the selected bead under confocal at 640 nm (red) and STED 775 nm (green) with Gaussian fits in dashed lines.

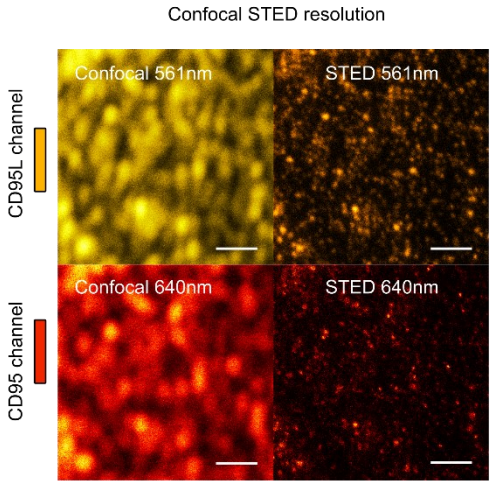

Figure 5. 5 Comparison of resolution in STED and confocal imaging. Scale bars are 1 µm. CD95L channels are orange colored (AbberiorSTAR Orange stained) and CD95 channels are red colored (AbberiorSTAR Red stained). Left: confocal images, right: STED images.

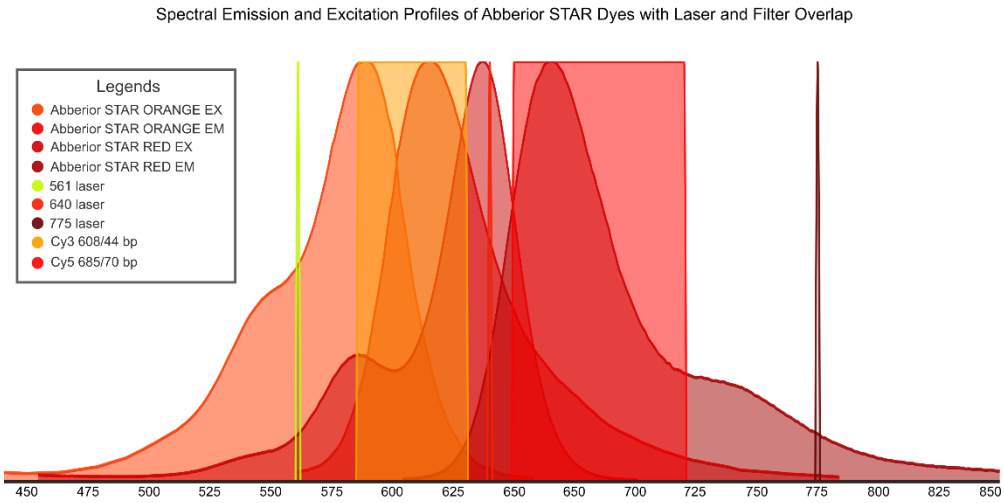

Figure 5. 6 Excitation and emission spectra of Abberior STAR dyes with laser and filter overlap. The figure was generated from the fluorescent protein data base (FPbase::) (https://www.fpbase.org/). From the fluorophore spectra and filter specifications, it can be inferred that, 1) a crosstalk of orange dye detection in red channel is possible in the prompt window. 2) orange dye induced red dye FRET signal is possible in the prompt window.

Crosstalk correction for Abberior Star dyes. Upon excitation with 561 nm laser, the Abberior STAR Orange dye emits a fluorescence with emission spectrum ranging from 561 nm to 784 nm with a peak centred at 615 nm. When the fluorescence signal arrives at Cy3 filter, the dichroic mirror transmits the fluorescence signal which is larger than 640 nm (640 nm to 784 nm) and reflect the wavelength smaller than 640 nm (561 nm to 640 nm). The transmitted fluorescence signal arrives at the Cy5 filter cube, which collects signal from 650 to 720 nm. Thus APD 2 and APD 4 can detect the signal from orange channel as a false positive, causing a crosstalk effect in the prompt measurement window. The percentage of orange signal detection in red channel can be calculated by integrating the spectrum of Aberrior STAR orange (650 nm to 720 nm) and the spectrum of 586 nm to 630 nm which is the true positive signal. The discrete integration was used for calculation as described in equation:

$$\int_a^b f(x)dx \approx \sum_{i=1}^{n-1} \frac{f(x_i) + f(x_{i+1})}{2} \cdot (x_{i+1} - x_i) \tag{18}$$

The calculated area is in total 60.42 A.U., 586 nm to 630 nm is 33.29 A.U., 650 nm to 720 nm is 12.21 A.U.. Therefore, the correction factor of red signal should be 12.2137 / 33.295 = 36.7 %. The true signal of red dye in red detection in the prompt window should be corrected as:

$$True_{\text{red signal}} = Total_{\text{red signal}} - 36.7\ \% \text{ x } Total_{\text{orange signal}}$$

Upon excitation with 640 nm laser, the Abberior STAR red dye emits a fluorescence with emission spectrum ranging from 604 nm to 874 nm with a peak centred at 666 nm. The

fluorescence emission at 604 nm to 630 nm will not pass the Cy3 filter cube and detected by APD 1 and APD 3, which contribute to the false positive signal of orange channel from red dyes in the delay window. The true positive signal will be contributed by emission at 650 nm to 720 nm. Therefore, the percentage of detection (604 nm to 630 nm), detection (650 nm to 720 nm) and total fluorescence can be calculated by same integration described above. The calculated area is in total area: 67.10 A.U., area between 604 nm to 630 nm is 0.59 A.U., 650 nm to 720 nm is 44.95 A.U.. Therefore, the correction factor of orange signal should be 0.58574 / 44.9513 = 1.3 %. However, in the delayed window only red signal is analysed, this error is therefore neglected.

FRET correction. After excitation with 561 nm laser, the orange dye will be excited and if the red dye is nearby within 10 nm, then the FRET occurs. FRET efficiency under STED condition after gating was considered zero, therefore ungated signal was used for distance calculation. This is discussed and calculated in the manuscript (92).

5.3.1 Measurement Settings of fixed Cell STED imaging

STED imaging was performed on a customized Abberior Instrument Expert Line Setup (Abberior Instruments) with a TCSPC counting unit (PicoQuant GmbH). All immunostained samples were imaged with one or two linear polarized excitation lasers at 561nm (~ 2.9 µW) and 640nm (~ 19 µW) along with a single circular polarized STED depletion laser at 775 nm (~ 31.50 mW) using a 100x oil objective (Olympus). Before the measurements, excitation and depletion lasers were aligned using TetraSpeck beads (Invitrogen, 0.1 µm). Confocal mode was first used to find the best focal plane of cells. Afterward, 10 regions of interest (ROIs) with the size of 5 µm x 5 µm (10 nm pixel size, 3.00 µs dwell time, 5 frames) were recorded using Imspector softwrae. The emitted photons were separated by a polarizing beam splitter and bandpass filters and then detected by four APDs.

5.3.2 Measurement Settings DNA Origami FRET nanoscopy

Sample preparation. DNA origami/ streptavidin/ CD95-biotin complex preparation. The rectangular DNA origami with concentration at ~ 100 nM was incubated with 50 x molar excess of streptavidin per binding site at 37 °C for 30 min. Unbound streptavidin was washed away by 3-4 repeats using Amicon Ultra-0.5 100 K centrifugal filters (Sigma-Aldrich) at 8000 g for 4 min. The washing buffer was TE (tris-EDTA buffer) supplemented with 12.5 mM $MgCl_2$. Afterward, DNA origami/streptavidin complex was incubated 10x molar excess of each binding site with CD95-biotin-ATTO594 mixed CD95-biotin-ATTO543 (1:1 molar ratio mixed in advance) and washed using the same centrifugation steps as above.

Flow chamber preparation. The rectangle coverglass 24 x 60 mm (No. 1.5 H, Marienfeld, VWR) was cleaned with 5 % Hellmanex III (Hellma Analytics) in an ultrasonic water batch at 40 °C for 20 min. Afterward, Hellmanex was removed by rinsing with milliQ water thoroughly. The cover glass was dried under nitrogen flow and placed on a lens tissue until used. The dried cover glass was placed on the sticky slide (sticky-slide VI 0.4, ibidi) bottom with the air-facing side always up. Surface passivation was achieved using poly L-lysine passivation to cover the glass surface with a positive charge for better DNA origami capture. To this end, 180 µl of 0.01 % poly L-lysin was incubated in each chamber for 5 min and removed. 2 ml milliQ water for each

chamber was flushed in each chamber to remove unattached residue poly L-lysine. The origami/protein complex sample was diluted freshly into ~ 1 pM concentration in TAE (tris, acetic acid, EDTA) buffer supplemented with 1 mM Trolox freshly.

Image recording. The automated single-molecule imaging of DNA origami was achieved by custom-written algorithm in Python programming language (92) on the Imspector software. First, an overview image with 20 µm x 20 µm on an acceptor channel with 640 nm excitation laser (8 % around 13.6 µW, dwell time: 5 µs, pixel size: 50 nm) was recorded. Spots in each overview image were identified by setting a proper threshold setting (R_{min} 120, Area 2000, Threshold 50-88). R_{min} stands for the minimal distance between spots, which should be larger than 120 nm. Area 2000 means the measurement will stop after 2000 overviews, as a maximum measurement. Threshold 50-88 stands for intensity threshold set for minimal intensity and can be considered as distinguishable spots. For each identified spot imaging was recorded at both channels. The recording setting follows the following settings: dwell time5 µs, pixel size 10 nm, ROI size 1 µm x 1 µm, number of frames 61, laser 561 nm 90 % linear, laser 640 nm 10 % linear, laser 775 nm circular. Each ROI with 1 µm x 1 µm area was recorded 61 times and saved in the format of a PicoQuant .ptu file. Line interleaved donor and acceptor excitation was applied to reduce potential crosstalk.

5.3.3 STED Cell Image Analysis

The resolution of images was increased firstly by time-gating of the 25-150 TAC bins (3.2-19.2 ns) using the customer-written software AnI. Photons from both parallel and perpendicular polarized images were summed up for further analysis. Huygens Professional (HuPro Version 21.10.1p2 64b or later) was used for deconvolution and quantitative data analysis. The deconvolution was performed using the CMLE (Classic Maximum Likelihood Estimation) algorithm with a signal-to-noise ratio (SNR) of 4, a maximum of 25 iterations as the convergence stop criterium, acuity of 97, and fixed background at 0.7. After deconvolution, the mass centres X Y (CmassX CmassY) and coordinates of each spot was calculated by the Huygens Object Analyzer, with a watershed threshold of 7, a seeding level of 0 and the garbage volume of 1 voxels. Afterward, the mass centre of each spot was overlaid on photon-gated raw images with AnI software, where Gaussian fitting was performed on raw images with fixed background at 0.1, ROI size with 11 x 11 pixels, initial sigma guess of 2.5 pixels for both channel, minimum spot size of 10 pixels, and segmentation object threshold of 10. Objects touching borders were ticked out. Parameters with extracted sigma, brightness were then plotted on customer-written Margarita software, where number of photons per pixel ($<N_{ph}>$ per pixel) and sigma of each spot was plotted in the format of 2D histogram with marginal frequencies of each parameter. A detailed workflow will be explained in the following paragraphs.

Time gating workflow using Ani-32F_GPU_12.07.2021. Batchwise time gating workflow is as follows: for each STED image, a .ptu file and .msr file were saved. In the .msr file the parallel and perpendicular channels were separated, these can be added up using Huygens software. We operate the .ptu files using Ani, by operating with .ptu file, the parallel and perpendicular files were added up. All .ptu files were saved in the same folder and the resolution of all images was

increased by time gating with 25-150 TAC bins (3.2-19.2 ns) and exported in .tif files batch-wise. The detailed workflow is shown in Figure S 1.

1) Import ptu file: options → Select Setup → TCSPC data/rasters-canning
2) Load ptu file: 'Folder' symbol → choose ptu. file →'Get parameters from file' → select STED microscope, PQ PTU → Set Line Steps
3) Main channel: Select ptu file → Accept
4) Main channel: TAC gate on → TAC gate channel: 25 to 150 → enlarge region of interest
5) Main channel: Import all ptu files: File → Export → All color images in batch → check TAC gate channel: 25 to 150 → Accept → Select All → Accept
6) Example images of before and after gating. This will generate 3 folders for each .ptu file: green photons (D signal after D excitation), red photons (A signal after D excitation), and yellow photons (A signal after A excitation). We will use Green (donor channel) photons and yellow (acceptor channel). Afterward, the mass centre X Y values were obtained by using deconvolution with Huygens software.

Huygens Deconvolution workflow. Deconvolution, also referred as noise correction or deblurring, is a computational technique used to enhance image resolution. Deconvolution reverses the blurring effects by using mathematical methods. Specifically, if f is the true signal and g is the point spread function (PSF), then h is the recorded signal by integration of two functions f and g: $f * g = h$. In a real measurement, noise effect should be included. Thus, the equation is modified as $(f * g) + \varepsilon = h$, In the deconvolution process, the f is calculated by inverse Fourier transform: $f = h/g$, that the image contrast can be increased. In this study, the spot size and brightness of stained CD95 and CD95L is to be analysed by Gaussian fittings, where the mass centre is important to get better initial guess for the fitting on a noisy image. In Huygens Professional software (HuPro Version 21.10.1p2 64b or higher version), the classic maximum likelihood estimation (CMLE) algorithm is used for deconvolution with a signal-to noise ratio (SNR) of 3. The convergence stop criterium was set to 0.01 or a maximum of 40 iterations. The applied background mode was manual, with a fixed of 0.7. After deconvolution, the mass centres X Y (CmassX CmassY) and coordinates of each spot was calculated by the Huygens Object Analyzer. The global object threshold was 1.2 with a seeding level of 1.3, the garbage volume was 2 voxels. The detailed workflow is shown in Figure S 2:

1) Load .tif files of photon gated image from Ani →
 i) Drag and drop files into Huygens software main user interface
 ii) Right click Add image → Open → select file
2) Set microscopic parameters → right click image → microscopic parameters → Load template for different channels
3) Set microscopic parameters for 561 nm and 640 nm channels → set general parameters and channel parameters
4) i) Join donor and acceptor channels → Tools → Join images →
 ii) Deconvolution: Deconvolution Wizard → Use deconvolution template → Load or make a template.

5) Object analysis: right-click image → Analyze image → Object Analyzer → Workflow Designer → Load or make a template → Verify all → Execute Window → This will export/save a .csv file of the result all spots analysis (size, position...).
6) Colocalization analysis: right click image → Analyse image → Colocalization Wizard → Threshold settings → Select coefficients → Export colocalization map / Save coefficients table.

Ani colocalization analysis. Afterward, the mass centres of each spot were overlaid on photon-gated images using Ani software and then plotted on customer-written Margarita software, where the number of photons per pixel (<N_{ph}> per pixiel) and sigma x of each spot was plotted in the format of 2D scatter plot and histogram. Analyzed results were exported and plotted in Origin. The detailed workflow is shown in Figure S 3 and description of Ani colocalization software is shown in Figure S 5:

1) Open Anni → Colocalization Analysis →
2) Load files → Import photon gated .tif files → Click on 'Exported Images_0-3' folder.
3) Set analysis for different channels, orange dye: Green Photons, Red dye: Yellow Photons;
4) Set 'ROI size +- pixels 5' → Threshold 10.
5) Generate Huygens ROI's → load CSV file (Summarize all spots data in one CSV file from Huygens Object Analysis with
CMassX, CMassY; Filename with the same nomenclature as Exported Images_0-3 folder) → Select as Export Folder → OK.
6) Overlay of ROI's: Operate → Selected ROIs Overlay → select 'Both_Huygens ROIs_+-5' → select one file → ok.
7) Save fitting result: File → Export → Imagewise Colocalization fit results → select *.ptu.
8) Margarita → Import Imagewise Colocalization fit results: File → Import Colocalization/Fit results → select 'sigma x_cl' and '<N_ph> per pixel_cl' → 2D bins: 15 → outliers.
9) Move red/blue cursor in the image (cut out 0 photons per pixel and 0 sigma values) → select region.
10.) Saving for Origin plots: File → Save → Probabilities as ASCII: Origin 8.6.

5.3.4 FRET nanoscopy of DNA Origami

Detailed data analysis workflow using FRET nanoscopy code is shown in Figure S 4. The whole analysis code contains spot localization, spot-integrated fluorescence lifetime calculation, spot-integrated FRET calculation, and sub-ensemble analysis. Some important equations used in the code are explained here. The following derivations are based on (92).

Spot localization. The point spread function (PSF) of each detected spot is fitted with multiple 2D Gaussian functions. In each ROI, up to three Gaussian functions were fitted with the following function:

$$G_{\mathrm{n}}(x,y)_{x_0 y_0,\sigma_{\mathrm{PSF}},A,bg} = \sum_{\mathrm{i}=1}^{3} A_{\mathrm{i}} \cdot exp\left[\frac{\left(x-x_{0,\mathrm{i}}\right)^2+\left(y-y_{0,\mathrm{i}}\right)^2}{2\sigma_{\mathrm{PSF,i}}^2}\right] + A_{\mathrm{bg}} \qquad (19)$$

In the equation, A_i is the amplitude of the i_{th} distribution, $x_{0,i,}$ and $y_{0,i}$ are the center coordinates of a pixel, $\sigma_{PSF,i}$ is the standard deviation of the i_{th} spot, and A_{bg} is a global background value.

Spot-integrated fluorescence lifetimes. From each ROI image, the tail of spot-integrated fluorescence decay was fitted using a single-exponential equation:

$$f(t) = f_0 e^{-t/\tau} + bg \tag{20}$$

With f_0 being the initial amplitude of the distribution and *bg* is the background value.

Intensity-based spectroscopic parameters. Apparent FRET was described as proximity ratio E_{prox} was calculated from intensity-based FRET under STED conditions without gating:

$$E' = \frac{F_{A|D}}{\gamma' F_{D|D} + F_{A|D}} \tag{21}$$

$F_{A|D}$ and $F_{D|D}$ are the signals detected in the red (acceptor) and green (donor) channels after donor excitation in the prompt window. γ' is the correction factor for bias in detection yield towards donor and acceptor channels. Although time gating increases STED resolution as described in the previous chapter. This reduces the FRET efficiencies detected under STED conditions. Therefore, the ungated detection signal contains depleted and undepleted molecules with different quantum yields. The accurate FRET efficiency *E* is corrected by including the different quantum yields of depleted and undepleted molecules:

$$E = E' \cdot \left(1 + \frac{x_D^d \cdot \Phi_{F,D}^d}{x_D^0 \cdot \Phi_{F,D}^0}\right) \tag{22}$$

With x_D^d and $\Phi_{F,D}^d$ being the fraction of depleted molecules and their corresponding quantum yields, x_D^0 and $\Phi_{F,D}^0$ being the fraction of undepleted molecules and their corresponding quantum yields. The quantum yields and fractions of depleted and undepleted molecules were obtained by fitting lifetime decay using bi-exponential functions as described in (92).

Sub-ensemble fluorescence decay analysis. The total fluorescence decay was detected from a sum up of parallel and perpendicular signals. The fluorescence decay of the donor-only sample in the absence of acceptors was fitted with a bi-exponential model for both undepleted and depleted molecules:

$$f_{D|D}^{(D0)}(t) = x_{STED}^{(D0)} \cdot e^{-t/\tau_{D0,STED}} + \left(1 - x_{STED}^{(D0)}\right) \cdot e^{-t/\tau_{D0}} \tag{23}$$

Here, *t* is the TCSPC time after the excitation pulse and $x_{STED}^{(D0)}$ is the portion of undepleted donor fluorophores. τ_{D0} describes donor-only lifetimes and $\tau_{D0,STED}$ describes donor lifetimes under

STED conditions. The donor fluorescence decay in the presence of the acceptor is described by the following equation:

$$f_{\mathrm{D|D}}^{(\mathrm{DA})}(t) = x_{\mathrm{STED}}^{(\mathrm{DA})} \cdot \mathrm{e}^{-t/\tau_{\mathrm{DA,STED}}} + \left(1 - x_{\mathrm{STED}}^{(\mathrm{DA})}\right) \cdot \left((1 - x_{\mathrm{D0}}) \cdot \int_0^{\infty} x_{\mathrm{FRET}}\left(R_{\mathrm{DA}}\right) \cdot \mathrm{e}^{-\left(\tau_{\mathrm{D0}}^{-1} + k_{\mathrm{FRET}}(R_{\mathrm{DA}})\right)\mathrm{t}} \mathrm{d}R_{\mathrm{DA}} + x_{\mathrm{D0}} \cdot \mathrm{e}^{-t/\tau_{\mathrm{D0}}} \right) \quad (24)$$

Here, $x_{\mathrm{STED}}^{(\mathrm{DA})}$ is the fraction of depleted donor fluorophore in the presence of the acceptor. $\tau_{\mathrm{DA,STED}}$ is the lifetime of depleted donor in the presence of acceptor. x_{D0} is the fraction of undepleted donors without acceptors. $x_{\mathrm{FRET}}(R_{\mathrm{DA}})$ is the fraction of FRET events between donor and acceptor with an inter-dye distance R_{DA}. The FRET rate constant of R_{DA} is described as:

$$k_{\mathrm{FRET}}(R_{\mathrm{DA}}) = \frac{1}{\tau_{\mathrm{D(0)}}} \left(\frac{R_0}{R_{\mathrm{DA}}}\right)^6 \quad (25)$$

With R_0 being the Föster distance, R_{DA} being the distance between the donor and acceptor molecules. $x_{\mathrm{FRET}}(R_{\mathrm{DA}})$ is described as a Gaussian distribution centered at the average interdye distance $\langle R_{DA} \rangle$ and the width σ_{DA} caused by the flexible linkers effect.

$$x_{\mathrm{FRET}}(R_{\mathrm{DA}}) = \frac{1}{\sqrt{2\pi}\sigma_{\mathrm{DA}}} \cdot \exp\left(-\frac{(R_{\mathrm{DA}} - \langle R_{\mathrm{DA}} \rangle)^2}{2\sigma_{\mathrm{DA}}^2}\right) \quad (26)$$

5.4 Transmission Electron Microscopy (TEM)

5.4.1 Measurement Details

Transmission electron microscope alignment. The electron beam was generated by the electron gun, passing through an accelerating tube. The sample was inserted on a goniometer stage and pressure was released less than 2.5 x 10^{-5} Pa. The electron beam was first minimized and centered then focused by adjusting the Z position to eliminate beam rings. Then the condenser lens was centered, and the wobbling ('X/Y' wobble and 'HT' wobble) alignment was accomplished to center the beam Z position. An objective lens was inserted optionally. The camera was switched on and 'FFT' is always checked for circular shape, if not, correct the astigmatism.

Transmission electron microscopy imaging. DNA origami coupling: the DNA origami sheet was prepared as previously described (101). DNA origami sheets containing two biotins were first incubated with 50x molar excess of streptavidin per biotin at 37 °C for 30 min. Unbound streptavidin was washed away by 3-4 times of centrifugation using Amicon Ultra-0.5 100 K centrifugal filters (Sigma-Aldrich) at 8000 g for 4 min. The washing buffer TE (tris-EDTA buffer) was supplemented with 12.5 mM $MgCl_2$. The coupled construct was collected with filters turned upside down at 5000 g for 2 min. Afterward, 50x molar excess of biotin-IZ-CD95L to DNA origami per binding site was added and incubated at 37 °C for 30 min. Extra biotin-IZ-CD95L was removed same as streptavidin above. DNA origami (i) plain or (ii) DNA origami complex coupled with streptavidin/biotin-IZ-CD95L were diluted to a concentration around 5-10 nM. 6 µl of the diluted construct was added onto a formvar coated nickel grid (200 mesh, S162N-100, Plano GmbH, Wetzlar, Germany) and left for sediment for 1 min. Between each step, the solution on the grid was soaked away using filter paper. The samples were stained with 2 % uranyl acetate (UA) first briefly and thereafter for 30 s before the grid was air dried for 20 min. Imaging was performed on a Jeol JEM-2100Plus (Akishima, Tokyo, Japan), operating in bright field mode at an acceleration voltage of 80 kV.

IV Results and Discussion

6 Design and Characterization of CD95 and CD95L variants

6.1 CD95L Variants for Cell Signal Initiation

In this study, two CD95L variants were used, the soluble CD95L ordered from Enzo company, named here as Flag-CD95L. Another one is customer designed soluble CD95L fused with isoleucine zipper as trimerization domain, named as IZ-CD95L. The structure of two constructs is shown in the following figure.

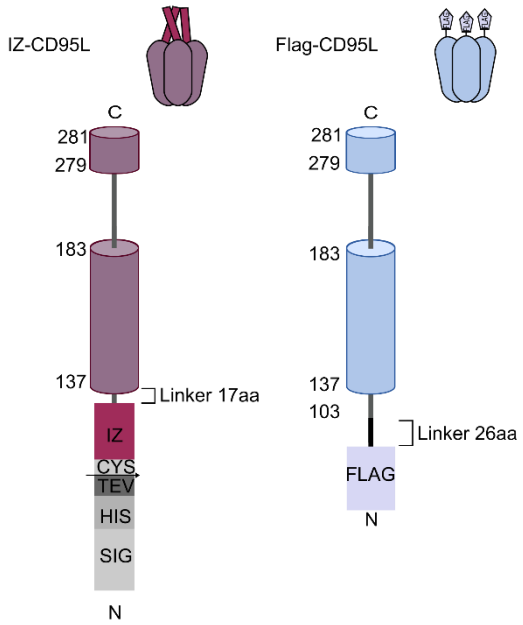

Figure 6. 1 Sketch of designed CD95L with isoleucine zipper (IZ-CD95L) or Flag-CD95L (Enzo life science). The full length CD95L harbors CD95 binding domain with amino acid 279-281, tumor necrosis factor (TNF) homology domain (aa137-183), transmembrane domain (TM) and aa 45-71 proline-rich domain (PRD). The designed IZ-CD95L construct consists of main domains include: the CD95 binding domain (CD95 Bind), the TNF homology domain (THD), a 17-aa linker, the isoleucine zipper (IZ) motif, a cysteine (Cys), TEV protease cleavage site (TEV), 6x His-tag (HIS), a signalling peptide (SIG). The Flag-CD95L construct consists of domains including CD95 Bind, THD, a 26-aa linker, a FLAG tag for crosslinking with anti-Flag mAb.

6.1.1 Flag-CD95L (Enhancer) and its Enhancer

As shown in the Figure 6. 1: Design of Flag-CD95L construct. The recombinant protein consists of amino acid 103-281 from the mCD95L, with 26 aa linker and a FLAG tag at N-terminus which can be cross-linked/stabilized by an anti-FLAG tag antibody. According to the manufacturer's information, this protein was produced in HEK293 cells. The extracellular domain of human CD95L with aa 103-281, containing the stalk region, was fused with 26 aa linker and a N-terminus FLAG-tag. Glycosylation was verified by SDS-PAGE with 95 % purity and an apparent

molecular weight of 35 kDa. The enhancer is the mouse anti-FLAG tag monoclonal antibody which crosslinks different FLAG tags fused on CD95L. Soluble CD95L has been known for weak induction of apoptosis than membrane bound form due to the lack of high order clustering and less stability of trimer (42). Therefore, additional cross-linkers need to be used either to enhance the stability of CD95L or to render it with additional clustering. In this case, the FLAG-tag was fused for crosslinking with an anti-FLAG tag mAb. This enhances the apoptosis rate to around three-fold and will be discussed in chapter 7.

6.1.2 IZ-CD95L and its functionalized variants

The recombinant IZ-CD95L was designed with an isoleucine zipper (IZ) motif at the N-terminus for stabilizing the trimeric CD95L, which has been demonstrated with high apoptosis induction efficiency (50). As shown in Figure 6. 1, the engineered protein consists of the extra cellular domain (ECD) of membrane-bound CD95L with aa 137-281, followed by a signal peptide (Sig), a His-tag (His), a TEV protease sequence (TEV), an additional Cysteine (Cys), and an isoleucine zipper domain (IZ) fused via a linker. The additional cysteine was used as a versatile coupling site for biotinylation or DNA hybridization, which can be used for further bionanotechnological applications or biomedical assays. This construct was produced *via* the HEK293T secretory expression system using a 10-layer cell factory and was purified by affinity purification. This achieved a fast, cheap, and production of IZ-CD95L with sufficient yield. The oligomerization states of the purified protein were verified by western blot and size exclusion chromatography, which identified the trimeric IZ-CD95L structure. The biological activity of IZ-CD95L was verified by apoptosis dynamics and ELISA assay. This part of results was written in the preprint manuscript (109). Besides, this ligand was also used for coupling with DNA origami for tumoriod treatment (110).

The purification result is shown in the following Figure 6. 2. In total, 455 µg His-IZ-CD95L was purified from 1.3 L medium using anti-His tag mAb coupled agarose beads. Purity of protein was checked by SDS-PAGE shown in lane 1 with ~ 86 % purity, by intensity calculation of the integrated CD95 band over the total band signals. A signal band at ~ 35 kDa identifies the expected monomer, yet the secreted His-IZ-CD95L without modification after signalling peptide cleavage was calculated as 24.1 kDa. N-linked glycosylation is considered 3-4 kDa per site, therefore the 11 kDa discrepency in molecular weight comes from three glycans, which is in accordance with identified three N-glycosylation sites (Asn184, Asn250, and Asn260) of CD95L ECD. The signal band at ~ 68 kDa shows His-IZ-CD95L as SDS-stable dimer even under reduced conditions. This has been seen before in previous study (46). Since the molecular weight difference between His-IZ-CD95L and IZ-CD95L is only ~ 1.8 kDa. No visible bands shift can be observed using SDS-PAGE. Therefore, western blot was used to verify His-tag cleavage. Lane 2-3 shows the efficient His-tag cleavage with absence of signal in lane 3 and presence of signal in lane 2, yielding an estimated cleavage ratio of ~ 98 %. Afterward, biotinylation was varified by western blot probed with AF488-streptavidin. The positive signal in lane 5 proved successful biotinylation of biotin-IZ-CD95L, with increased viscosity of protein manifested as a smear.

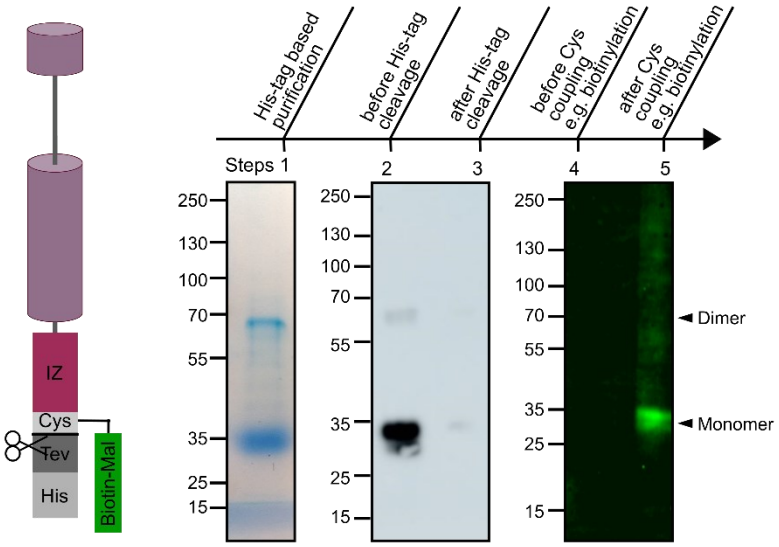

Figure 6. 2 Purification and modification of IZ-CD95L. Lane 1: His-tag agarose beads purification checked by 10 % reduced SDS-PAGE with 1 µg of purified protein. Lane 2-3: His tag cleavage checked by western blot analysis using 100 ng His-IZ-CD95L and IZ-CD95L. Anti-His tag mAb (clone: J099B12, 1:1000, Biolegend) was used for staining. Lane 4-5: biotinylation checked by western blot with 300 ng of ligand w or w/o biotinylation, probed with AF488-streptavidin (AAT Bioquest). All blots were transferred from reduced SDS-PAGE gels. The figure is modified from a preprint manuscript (109).

6.2 CD95 Variant for Single Molecule Studies

6.2.1 Expression, Purification and Labeling of engineered CD95 variants

In this work, two CD95 constructs were designed, expressed and purified. The design of CD95 plasmids was described in chapter 4.1. I started with purification and assay of CD95-SBP-His construct, as it does not need additional biotinylation. The western blot analysis revealed that CD95-SBP-His was expressed in BL21 cell line primarily as inclusion bodies, as shown in Figure 6. 3 A. A signal band was showing up only in insoluble pellet rather than soluble lysate. Therefore, protein purification was performed under denatured conditions using 8 M urea shown in Figure 6. 3 B. The purification process was monitored by SDS-PAGE shown in Figure 6. 3 C with different stages including cell lysis, insoluble pellet, flow through, and multiple elution fractions. As shown in Figure 6. 3 C, CD95-SBP-His predominately expressed as insoluble pellet with a strong signal band. Negligible amount of CD95-SBP-His signal was detected in flow through suggesting an effective column binding. Elution fraction 1-6 showed consistent signal bands around 25 kDa with minimal background, in accordance with the expected molecular weight of CD95-SBP-His. Overall, this shows a successful purification of high quality CD95-SBP-His.

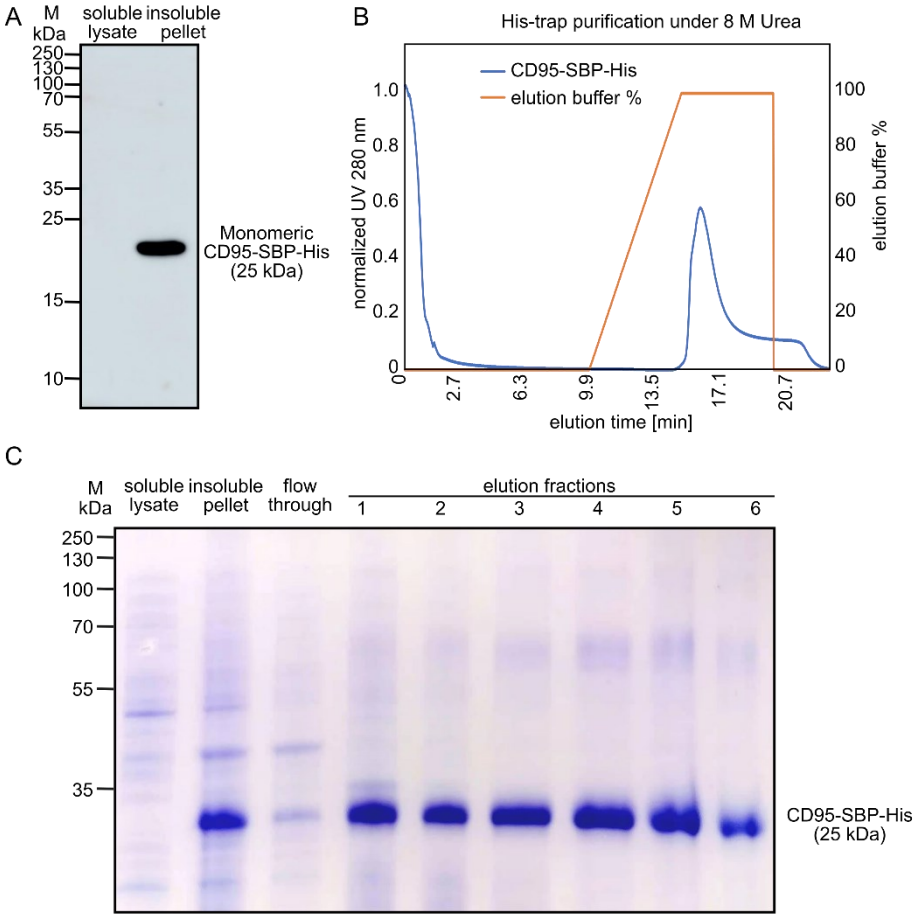

Figure 6. 3 Purification of CD95-SBP-His. A. Identification of CD95-SBP-His expression as inclusion bodies detected by western blot analysis. Left lane: 50 µg soluble lysate, right lane: 200 ng insoluble pellet. The blot was probed primarily by rabbit anti-CD95 (Invitrogen, MA5-32499, JJ0942) flowed by HRP conjugated goat-anti-rabbit secondary antibody CD95. B. Chromatograph of His-trap column purification of CD95-SBP-His. Blue curve: normalized UV 280 nm signal. Orange line: percentage of imidazole supplemented in elution buffer in gradient manner. C. Protein purity checked by SDS-PAGE. Lanes from left to right: 50 µg soluble lysate, 50 µg insoluble pellet, 50 µg flow through, and 5 µg elution fractions.

Next, protein purity was further improved by size exclusion chromatography (SEC), as shown in Figure 6. 4 A. The gel filtration was performed under denatured conditions, identical as the purification step. The elution peak of CD95-SBP-His was shown as multimers with characteristic elution volume from 7.70 ml to 11.55 ml. Due to the lack of standard protein mix as ruler, the precise size of denatured CD95-SBP-His wasn't calculated from the SEC curve. Impurities with elution volume from 19.25 -23.10 ml were successfully removed. His-tag cleavage was verified by SDS-PAGE (Figure 6. 4 B) and WB (Figure 6. 4 C). CD95-SBP-His has theoretical pI/MW of 6.75 /24.9 kDa, and CD95-SBP without His-tag has theoretical pI/MW of 6.55 /23.9 kDa. The difference in molecular weight can be seen as a slight shift in SDS-PAGE band shown in Figure

6. 4 B. His-tag cleavage was also verified by WB, as shown with the absence of signal band in lane 2 in Figure C. Dimer and trimer of CD95-SBP-His can be resolved under non-reduced conditions, which disappeared after adding the reductant, as shown in Figure 6. 4 C lane 1 and lane 3. Multimers of CD95-SBP-His can be also noticed in non-reduced SDS-PAGE (Figure 6. 4 D lane 1), and chemical crosslinking does not lead to difference of oligomerization (Figure 6. 4 D lane 2). Those SDS-stable high-order oligomers have been observed before (111).

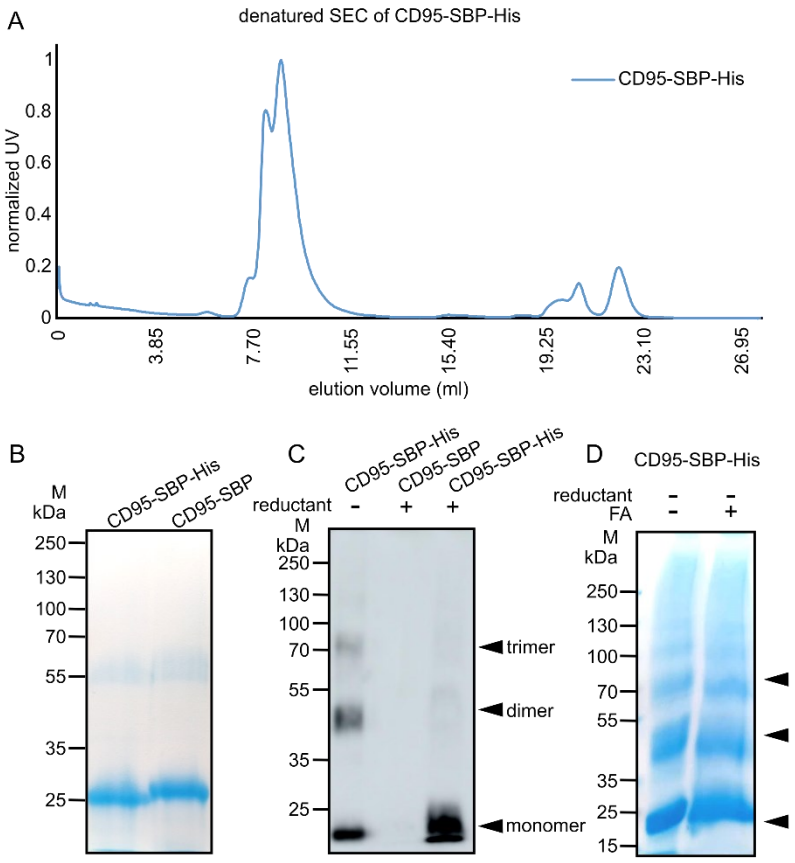

Figure 6. 4 Modification and characterization of CD95-SBP-His. A. Denatured size exclusion chromatography (SEC) analysis of CD95-SBP-His. The CD95-SBP-His was eluted at 7.7 ml – 11.55 ml identified by SDS-PAGE or WB as shown in B and C. B. His-tag cleavage of CD95-SBP-His checked by SDS-PAGE. Lane left: ~ 10 µg CD95-SBP-His before His-tag cleavage. Lane right: ~ 10 µg CD95-SBP after His-tag cleavage. C. His-tag cleavage of CD95-SBP checked by WB. Lanes from left to right: ~ 100 ng of CD95-SBP-His without heating and reduction, CD95-SBP after His-tag cleavage, and CD95-SBP-His with heating and reduction. The blot was probed by anti-His-tag antibody (Biolegend, 1:1000). D. SDS-PAGE analysis of 10 µg CD95-SBP-His under non-reducing condition in lane left and crosslinked by 2 % FA in lane right.

Due to the low binding affinity of SBP-tag with streptavidin in the preparation of CD95 coupling with DNA origami, this construct was not used for further experiments. Therefore, CD95-biotin was purified by using CD95-Avi-biotin-His construct. First, the expression (Figure 6. 5 A) and *in vivo* biotinylation (Figure 6. 5 B) of CD95 was checked by WB analysis. Two cell lines were tested: *E.coli* BL21 PlysS and *E.coli* BL21 Rosetta PlysS. The result showed signal band appearing in Rosetta cell line but not from PlysS cell line. Next, protein purification was

performed using His-trap purification using NGC (Biorad) purification system as shown in Figure 6. 5 C. Blue curve represents the normalized signal of UV 280 nm and green curve shows the percentage of imidazole in elution buffer with linear gradient. The chromatograph shows a successful purification of CD95-Avi-biotin-His construct. The purification process was monitored by SDS-PAGE shown in Figure 6. 5 D with lanes from left to right containing cell lysate, flow through, column wash and elution fractions. The black arrows (Figure 6. 5 A B D) indicate the correct protein size at around 22 kDa as predicted previously.

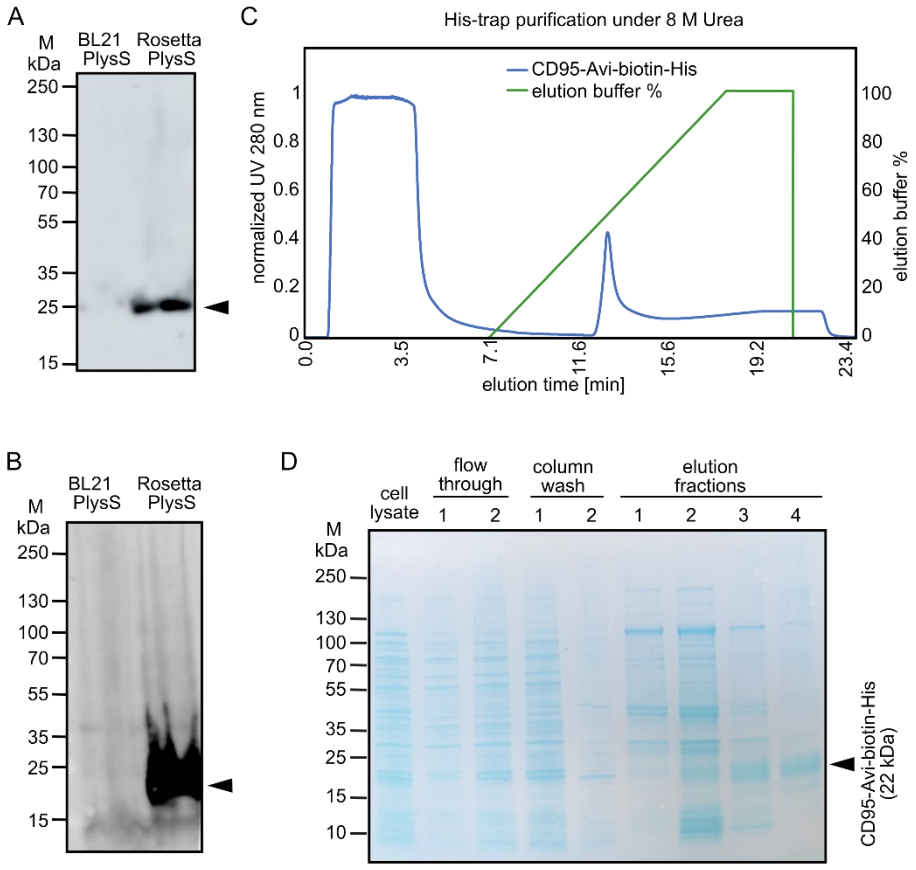

Figure 6. 5 Identification and purification of CD95-Avi-biotin-His. A. Identification of CD95-Avi-biotin-His expression by western blot analysis. Two cell lines were tested after co-transformation of BirA and CD95-Avi-His plasmids. Lane left: BL21 PlsS, lane right: BL21 Rosetta PlysS. The blot was probed primarily by rabbit anti-CD95 (Invitrogen, MA5-32499, JJ0942) flowed by HRP conjugated goat-anti-rabbit secondary antibody. B. Identification of in vivo biotinylation was performed by WB probed by 30 µg/ml Strep-488 o/n at 4°C. C. His-trap column purification of CD95-Avi-biotin-His using NGC system. D. Protein purity checked by SDS-PAGE. Lanes from left to right: cell lysate, flow through, column wash, elution fractions (1 µl of protein mix and 5 µl of purified protein in each fraction was loaded). Concentration of each lane was: cell lysate: 91.2 mg/ml; flow through 1-2: 60.5 mg/ml and 87.0 mg/ml; column wash: 85.6 mg/ml and 7.5 mg/ml; elutions: 1.0 mg/ml, 2.8 mg/ml, 1.0 mg/ml, 0.5 mg/ml. Samples were reduced with 2 µl 5x sample buffer/BME/heating at 99 °C 5 min. 10 µl of final volume at each condition was loaded with 5 µl prestained marker running ar 200 V for ~ 35 min.

7 Apoptosis Dynamics of CD95-expressing Cells as a function of CD95L.

To test the biological activity of IZ-CD95L and compare the induction efficiency of apoptosis with soluble CD95L, the apoptosis dynamics experiment was performed. To do this, the CD95L variants (biotin-IZ-CD95L, Flag-CD95L (ENZO) or Flag-CD95L (ENZO) crosslinked with 100x anti-Flag mAb (the enhancer)) at varying concentration was incubated on Hela WT cells overnight, monitored under IX83 widefield microscope. I used biotin-IZ-CD95L primarily since this is the final product of ligand production. Nevertheless, IZ-CD95L and His-IZ-CD95L was also tested for comparison of cytotoxicity of ligand at each preparation step. Figure 7. 1 shows snapshots of Hela WT cells received with X-CD95L at 200 ng/ml at different time points.

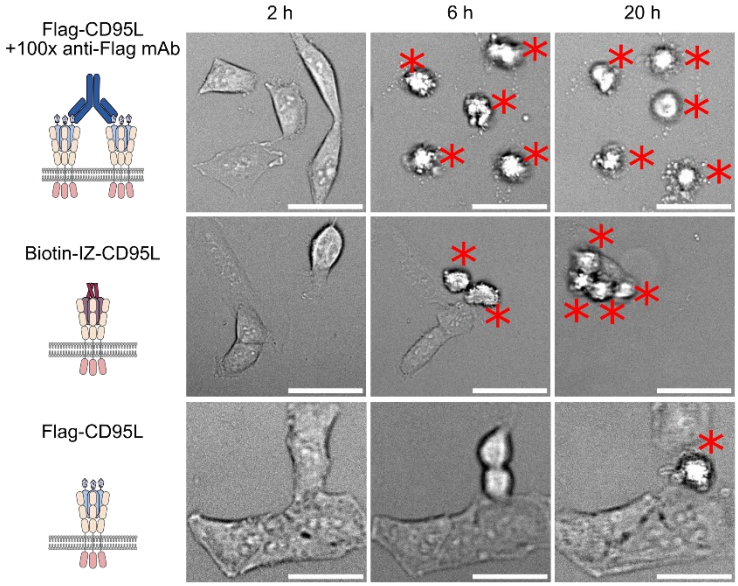

Figure 7. 1 Snapshot of cells at different time points after addition of CD95L variants at 200 ng/ml. Lane 1: Flag-CD95L (Enzo) crosslinked with 100x excess concentration of anti-Flag mAb (the enhancer). Lane 2: biotin-IZ-CD95L. Lane 3: Flag-CD95L (Enzo) only. The apoptotic cells were marked with red asterisks by the judgement of characteristic cell shrinkage, blebbing or formation of apoptotic bodies. From left to right is at time point of 2 h, 6 h or 20 h. All scale bars are 50 µm.

Figure 7. 1 shows the morphology changes of cells during overnight incubation with X-CD95L. Increasing rate of cell apoptosis can be observed from bottom to up, with an increasing degree of ligand clustering. In detail, for Flag-CD95L at the 2 h time point, 4 living cells can be distinguished. At the 6 h time point, two dividing daughter cells at top right can be observed. At the 20 h time point, one divided cell appeared membrane blebbing and was marked in red asterisk. For biotin-IZ-CD95L at 2 h, 3 living cells and one dividing mother cell can be observed. At the 6 h time point, 2 divided daughter cells showed formation of apoptotic bodies marked by asterisks. At the 20 h observation point, 4 out of 5 cells underwent apoptosis. For Flag-CD95L + 100x anti-Flag mAb at 2 h, 5 individual cells were captured and all of them apoptosed after 6 h incubation. To summarize, at the concentration of 200 ng/ml, the killing efficiency can be rated that, Flag-CD95L + enhancer was more efficient than biotin-IZ-CD95L than Flag-CD95L.

From the overnight measurements, each apoptotic cell was marked with frame numbers exported in an excel file, which were then converted to death time and fitted with the Hill equation. The maximum apoptosis percentage (*max*), apoptosis rate (*n*) and the time when half number of maximum cells apoptosed (T_{half}) can be derived. The apoptosis rate *n* represents the speed/slope of the apoptosis curve, manifesting an ensemble rate of cell death in a population.

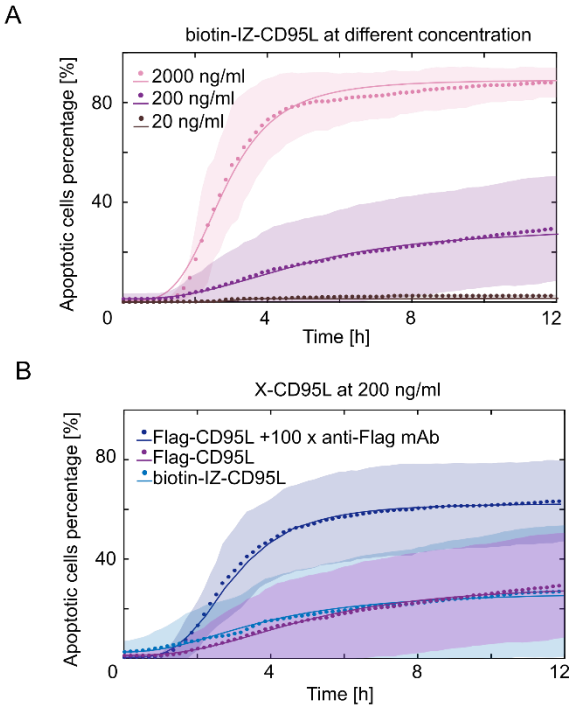

Figure 7. 2 Apoptosis dynamics curve fitted with Hill equation. A. Hela WT cells were incubated with biotin-IZ-CD95 at different concentration from 20 ng/ml (*n* = 3.2, *max* = 2.6 %, T_{half} = 3.7) through 200 ng/ml (*n* = 2.6, *max* = 29.9 %, T_{half} = 5) to 2000 ng/ml (*n* = 3.8, *max* = 89.2 %, T_{half} = 2.8). B. Hela WT cells were incubated with biotin-IZ-CD95L (*n* = 2.6, *max* = 29.9 %, T_{half} = 5), Flag-CD95L (*n* = 2.2, *max* = 27.1 %, T_{half} = 3.8) and Flag-CD95L + anti-Flag mAb (*n* = 3.4, *max* = 62.8 %, T_{half} = 2.8) at 200 ng/ml respectively. Dotted lines are data points, solid lines are fittings, and shaded areas are standard deviations from independent experiments.

I first tested concentration dependency of apoptosis initiation using biotin-IZ-CD95L at varying concentrations at 20 ng/ml, 200 ng/ml, or 2000 ng/ml. The result is shown in Figure 7. 2 A. At 20 ng/ml, no significant apoptotic cells detected with a fitting result of maximum apoptosis percentage (*max*) = 2.6 %. The minimal amount of died cells might be caused by natural death. At the concentration of 200 ng/ml, a noticeable increasement in apoptosis events can be observed, with a fitting result of the maximum apoptosis percentage (*max*) = 29.9 % with half lifetime (T_{half}) = 5 h. At 2000 ng/ml, abundant apoptosis events were detected with the highest apoptosis percentage of 89.2 % and shorter half-life time (T_{half} = 2.8 h), which is threefold of *max* and half of T_{half} at 200 ng/ml. Since sufficient amount of apoptosis events can be resolved at 200 ng/ml biotin-IZ-CD95L, this concentration was used to compare cytotoxicity of X-CD95L variants as shown in Figure 7. 2 B. However, maximum apoptosis percentage between soluble Flag-CD95L

(Enzo) (blue curve) and biotin-IZ-CD95L (purple curve) didn't show significant differences at 200 ng/ml, with *max* = 27.1 % and 29.9 % respectively. The apoptosis maximum of Flag-CD95L (Enzo) + Enhancer is twofold higher than the other two conditions with fitted *max* = 62.8 %. suggesting an efficient enhancement in cytotoxicity induction with higher oligomerization by crosslinking.

To sum up, the apoptosis dynamics analysis provides a multi-parameter measurement with concentration sensitivity to probe apoptosis induced by CD95L variants. From this experiment, the following conclusions can be drawn. First, it helps with understanding of timing of cellular response. When it is too early, no apoptosis initiates. When it is too late, cells fragmented due to the formation of apoptotic bodies. Neither of them is suitable for STED staining nor imaging. The onset of apoptosis at 200 ng/ml can be observed from curve, appearing at around 2 h or later, this provides me the time point for further experiment design in STED nanoscopy. Therefore, all cells in immunostaining experiments were treated with 2 h of conditioned CD95L. Second, it raises the question from the macro perspective: what is the molecular mechanism behind the difference in apoptosis induction. As a first speculation, improved apoptosis induction efficiency can be caused by increasing structure hierarchy/stability, where Flag-CD95L (Enzo) + Enhancer is more complex than biotin-IZ-CD95L than Flag-CD95L (Enzo).

Afterward, more concentration series of CD95L variants at 20 ng/ml, 200 ng/ml, 1000 ng/ml and 2000 ng/ml were assayed, and the maximum apoptosis percentage *max* and half lifetime T_{half} were derived and plotted in heat map as shown in Figure 7. 3 A and Figure 7. 3 B for understanding correlation of ligand concentration and degree of complexity. In Figure 7. 3 A, the brighter color code indicates higher apoptosis ratio, increased with increasing concentration of X-CD95L and degree of clustering. At 20 ng/ml, all of the variants showed no significant apoptosis. A noticeable cytotoxicity was observed at 200 ng/ml for all variants. There is no significant difference Among biotin-IZ-CD95L, His-IZ-CD95L and Flag-CD95L, yet crosslinked Flag-CD95L showed two-fold better performance. The difference of CD95L variants can be better resolved with distinguishable percentages from 40 % - 60 % at 1000 ng/ml. Measurement at 2000 ng/ml of Flag-CD95L (Enzo) + Enhancer was not available (N.A.) due to the cost. Measurements at 2000 ng/ml obscure the difference among other variants due to saturation effects. Compared with straightforward trend observed from apoptosis percentage heatmap in Figure 7. 3 B, the half lifetime heatmap is intricate. Principally, low dose leads to a slow kinetics and high does leads to fast kinetics, which derive long and short T_{half} respectively. However, at the low concentration, it's possible plateau of curve reaches quickly, yielding a fitted short T_{half}. Overall, the positive correlation of both concentration with apoptosis efficiency and oligomerization with apoptosis efficiency can be observed. Due to the symmetrical distribution of two heatmaps, the two factors play quasi equally important roles. Likely, high order oligomerization of X-CD95L leads to high binding affinity, due to compact structures and higher local concentrations. Besides, crosslinked CD95L improves orientation towards CD95.

Next, the apoptosis rate at 1000 ng/ml of each CD95L variant was calculated by taking the reciprocal of death time for each cell and plotted boxplot in Figure 7. 3 C with equation:

$$k_i = {}^{1}/_{\tau_i}\,[\mathrm{h}^{-1}] \tag{27}$$

In Figure 7. 3 C, the median of Flag-CD95L+Enhancer is 0.28, with upper quartile Q3 = 0.35, lower quartile Q1 = 0.20, upper whisker at 0.53 and lower whisker at 0.06. The median of biotin-IZ-CD95L is 0.23, with lower quartile Q1 = 0.06 and upper quartile Q3 = 0.35, upper whisker at 0.53 and lower whisker at 0.06. In the case of Flag-CD95L (Enzo), with median of 0.06, upper quartile Q3 = 0.14, lower quartile Q1 = 0.06, upper whisker at 0.25 and lower whisker at 0.06. To sum up, the median value represents apoptosis rate with tendency of Flag-CD95L (Enzo) + Enhancer faster than IZ-CD95L than Flag-CD95L (Enzo). The variability shown by box size indicates IZ-CD95L is larger than Flag-CD95L (Enzo) + Enhancer than Flag-CD95L (Enzo).

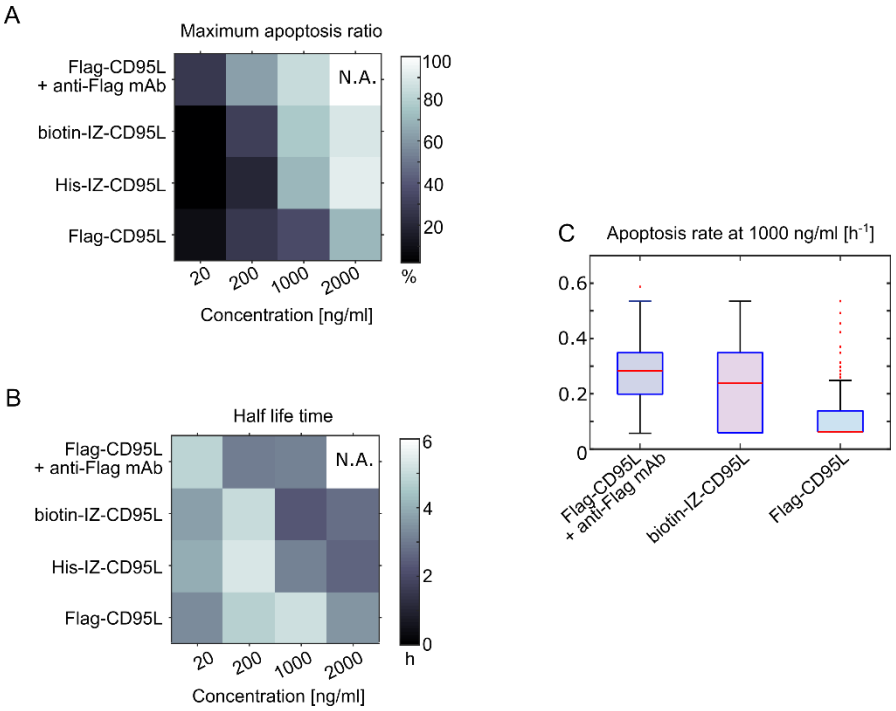

Figure 7. 3 Colormap of apoptosis dynamics analysis and apoptosis rate. A. The colormap of maximum apoptosis percentage. B. The colormap of half-life time. N.A.: not available measurement due to cost of reagent. C. Apoptosis rates [h^{-1}] of CD95L variants at 1000 ng/ml. Outliers of apoptosis rate is not all included (Y axis: 0 - 0.7).

8 Organization of CD95 and CD95L variants on the Plasma Membrane

8.1 STED Microscopy of CD95 and CD95L

8.1.1 STED reveals Resolution Limited Receptor

To study the dependency of stability and oligomerization of CD95L variants on mCD95 geometries, I first performed STED imaging of Hela WT cells incubated with Flag-CD95L and biotin-IZ-CD95L at identical concentration of 200 ng/ml. Each well was first stained with primary antibody overnight using 10 µg/ml rabbit anti-CD95 (Invitrogen, MA5-32499, JJ0942) diluted in 200 µl blocking buffer (1 % BSA in DPBS without glycine). Next day, the primary antibody in each well was removed and each well was washed with DBPS-T and incubated with secondary AbSTAROrange goat-anti-rabbit (5 µg/ml (1:200)).

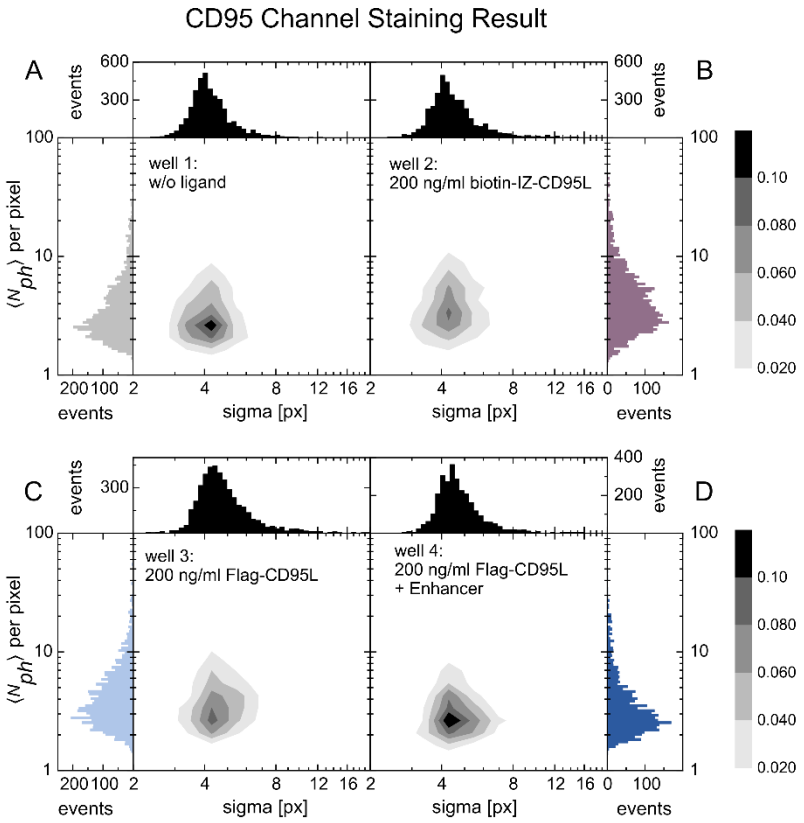

Figure 8. 1 One color-stained STED imaging analysis. A. Without ligand. B. 200 ng/ml biotin-IZ-CD95L. C. 200 ng/ml Flag-CD95L. D. 200 ng/ml Flag-CD95L + Enhancer. In A-D all plots are plotted with log Y-axis of number of photons per pixel ($<N_{ph}>$ per pixel) and log X-axis of sigma of each spot (unit: pixel). Scale bars are probability densities of data shown in grayscale 2D contour plots. The frequency histograms on the top and side of each graph show distributions of $<N_{ph}>$ per pixel and sigma. Colormap was set from 0.02 to 0.10 with 4 levels shown in probability scale bars in the left.

In this experiment, after ligand incubation, only CD95 was stained to see the change of CD95 spots size using STED imaging and data analysis described in the previous chapter. Afterward, individual spot with local background was fitted Gaussian using the customer written software Ani. The sigma [px] is the standard deviation of each Gaussian distribution, representing the width of each spot. $<N_{ph}>$ per pixel is the integrated photon numbers divided by the pixel numbers within each spot, representing the brightness of each spot. In Figure 8. 1 A, cell staining results without ligand incubation was used as a control. Since the data here shows a basal distribution of size and brightness of CD95 on Hela WT cell membrane. It can be observed from spots distribution that the median of $<N_{ph}>$ per pixel was ~ 2.5 and of sigma was ~ 4 pixels. Both frequency histograms showed broad distributions, representing large varieties. At 200 ng/ml biotin-IZ-CD95L, spots distribution did not change. At 200 ng/ml Flag-CD95L, brightness distribution did not show significant change while sigma slightly shifted to 4.5, compared with no ligand control. At 200 ng/ml Flag-CD95L + Enhancer, with no change in the sigma distribution, the distribution of $<N_{ph}>$ per pixel was narrower compared with other three conditions, indicating less staining effect due to the blocking effect of adding Enhancer (anti-Flag mAb). The very bright spots with > 10 $<N_{ph}>$ per pixel were contributed by concentration fluctuations on Hela cell membrane.

Next, to study the concentration dependency and type of CD95L variants on oligomerization, I performed two-colour STED imaging of Hela WT cells incubated with Flag-CD95L / biotin-IZ-CD95L at various concentrations: 200 ng/ml, 1000 ng/ml, 2000 ng/ml. After ligand incubation and cell fixation step, each well was first stained with primary antibody overnight with 5 µg/ml mouse anti-CD95 (Biotium, BNUB0305-100, clone number: B-R18, mouse monoclonal antibody) and 10 µg/ml rabbit anti-CD95L (Abcam, ab134401, rabbit polyclonal antibody). According to the manufacture's description, B-R18 binds on the membrane part of CD95 on Hela WT cells. This ensures the imaging of membrane rather than cellular part. Next day, each well was incubated with secondary antibody AbSTARRED goat-anti-mouse and AbSTAROrange goat-anti-rabbit both at 5 µg/ml (1:200) (both from Abberior). The result of CD95L staining is shown in Figure 8. 2 and of CD95 staining result is shown in Figure 8. 3.

Figure 8. 2 showed the CD95L/AbSTAROrange channel staining results. At 200 ng/ml Flag-CD95L, distributions of sigma with median ~ 2.5 and ~ 4 px and $<N_{ph}>$ per pixel with median of ~ 4 can be observed. The brightness distribution suggests two populations of CD95L existing on Hela WT membrane. At 200 ng/ml biotin-IZ-CD95L, sigma distribution showed a median of 4 px, but $<N_{ph}>$ per pixel showed median of ~ 2. The distribution of Flag-CD95L at 1000 ng/ml resembles the distribution of 200 ng/ml biotin-IZ-CD95L. At 1000 ng/ml biotin-IZ-CD95L, the sigma distribution does not change but brightness is broader compared with 1000 ng/ml Flag-CD95L. At 2000 ng/ml, the median of $<N_{ph}>$ per pixel ~ 3 of biotin-IZ-CD95L was higher than that of Flag-CD95L ~ 2. Very bright spots with > 10 $<N_{ph}>$ per pixel are from concentration fluctuations, which are more pronounced at 2000 ng/ml. In summary, the resolved sub-ensemble population implies a native CD95L on Hela WT that can be distinguished from added ligands, which was verified in further experiments. The results showed all diffraction limited spots from stained CD95L on Hela WT cells.

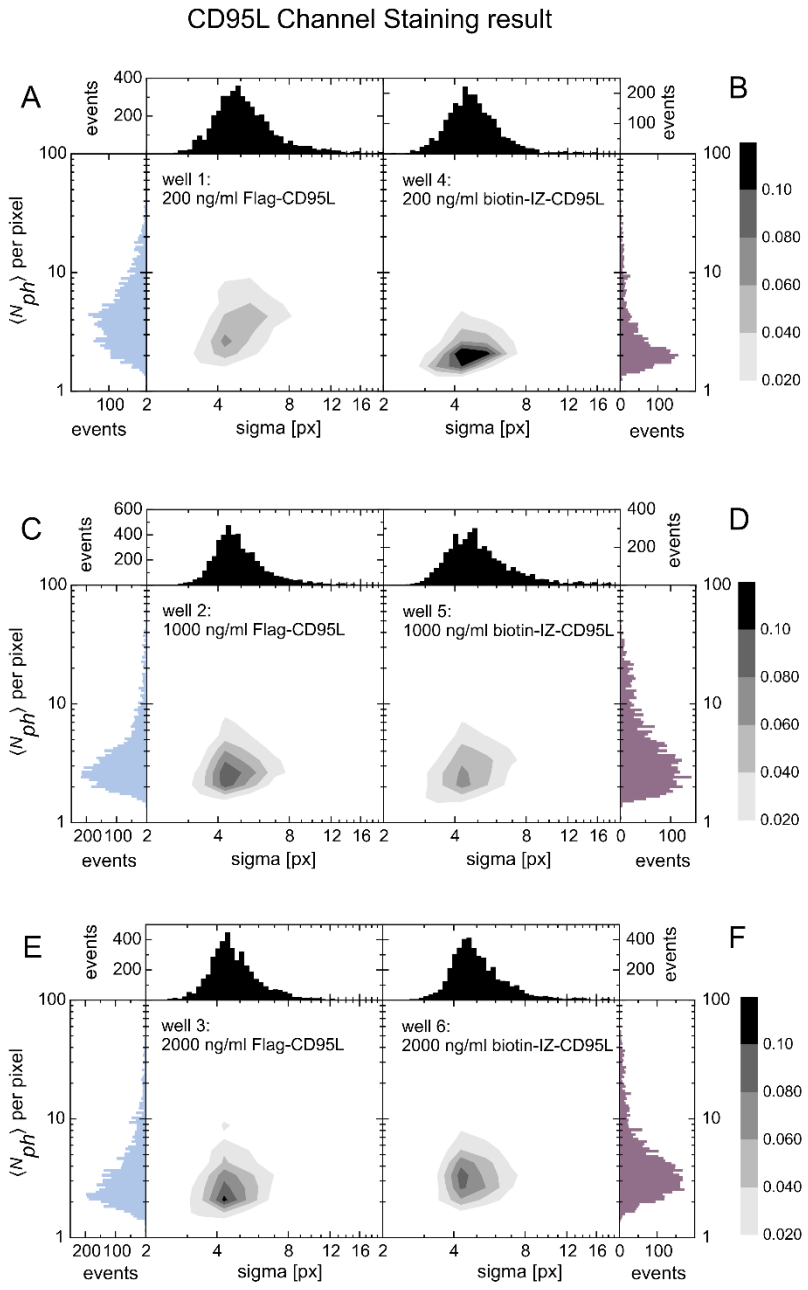

Figure 8. 2 Two color-stained STED imaging analysis: CD95L/AbSTAROrange staining result. A. 200 ng/ml Flag-CD95L. B. 200 ng/ml biotin-IZ-CD95L. C. 1000 ng/ml Flag-CD95L. D. 1000 ng/ml biotin-IZ-CD95L. E. 2000 ng/ml Flag-CD95L. F. 2000 ng/ml biotin-IZ-CD95L. All plots were plotted with Y-axis of number of photons per pixel (<N_{ph}> per pixel) and X-axis of sigma of each spot (unit: pixel). Scale bars represent the probability density with grayscale contour lines. Frequency histograms are on the edges.

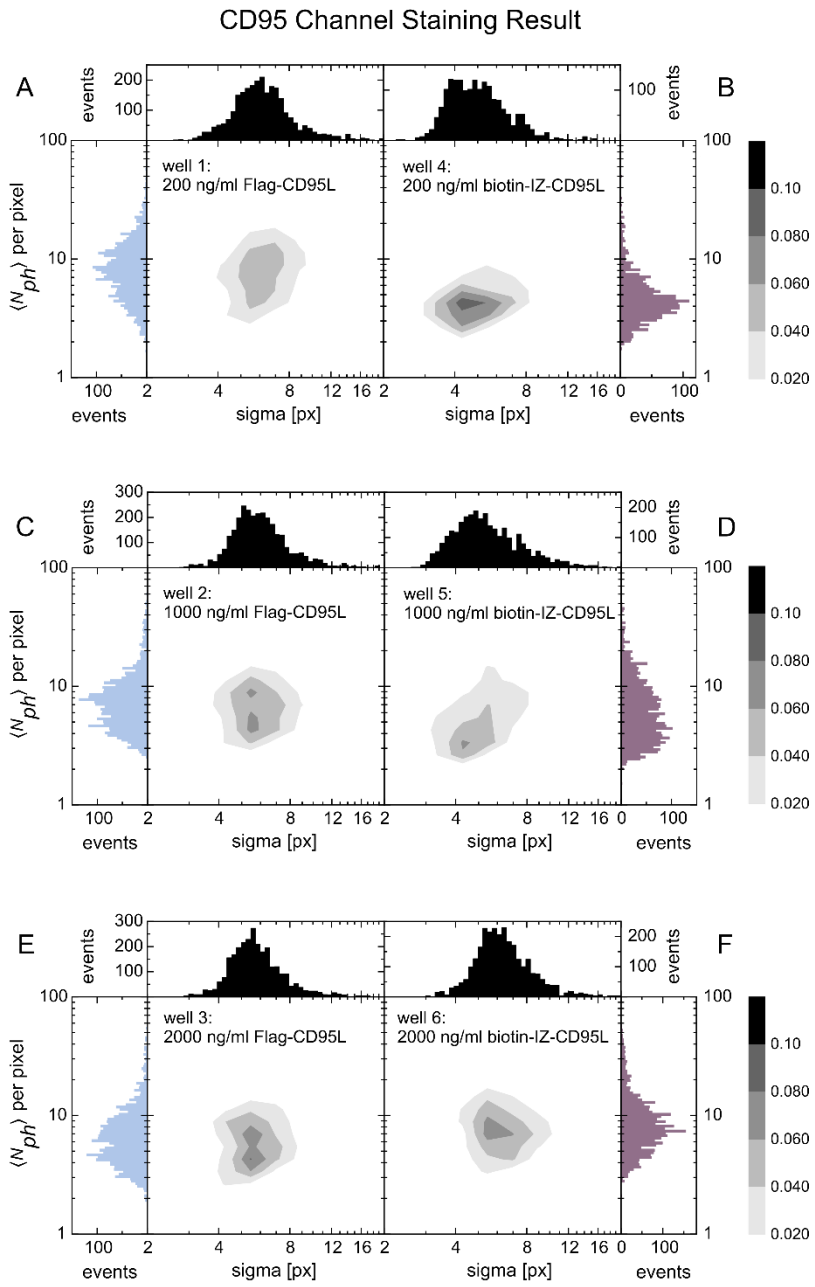

Figure 8. 3 Two color-stained STED imaging analysis: CD95/AbSTARRed staining result. A. 200 ng/ml Flag-CD95L. B. 200 ng/ml biotin-IZ-CD95L. C. 1000 ng/ml Flag-CD95L. D. 1000 ng/ml biotin-IZ-CD95L. E. 2000 ng/ml Flag-CD95L. F. 2000 ng/ml biotin-IZ-CD95L. The figure layout is the same as previous ones.

Figure 8. 3 shows the CD95/AbSTARRed channel staining results. From A-C-E, it can be in general inferred that the $<N_{ph}>$ per pixel and sigma values saturated at 200 ng/ml Flag-CD95L. As there is no significant difference in distributions of sigma (ranging from 4-8) and $<N_{ph}>$ per pixel (ranging from 2-20). Compared between C/E and A, the distributions of brightness are narrower at 1000 ng/ml or 2000 ng/ml than 200 ng/ml of Flag-CD95L. The less variability indicates more sufficient CD95 staining after ligand incubation. The concentration dependency of staining with biotin-IZ-CD95L can be observed by comparison of B-D-F. By comparison of

Figure 8. 3 B-D, the medians of $<N_{ph}>$ per pixel for distributions at 200 ng/ml was ~ 4 and the median of sigma ~ 4 pixels. At 1000 ng/ml the medians of $<N_{ph}>$ per pixel was ~ 5 and the median of sigma ~ 5 pixels. In Figure 8.3 F, a prominent raise of the median of $<N_{ph}>$ per pixel ~ 8 and sigma ~ 6 can be observed, which accounts for nearly twofold increasement in brightness. Besides, large spots with sigma at ~ 6 were detected at 2000 ng/ml. Based on the magnitude of changes in distribution from Figure 8. 3 B – F, indicating small oligomerization changes from monomer to dimers/trimers of CD95 rather than hexagons, which should manifest as > 3-fold changes in brightness or size. In summary, the overall brightness detected from CD95 channel in Figure 8. 3 are better than CD95L channel in Figure 8. 2. This can be attributed to better specificity of CD95 antibody in staining than CD95L, or higher performance in laser power at 561 nm than at 640 nm and low signal-to-noise ratios of APD 1&3 than APD 2&4. Another factor can be FRET induced higher fluorescence in the yellow/CD95 channel than green/CD95L channel.

8.1.2 Native CD95L expression on Hela WT cell line revealed in STED imaging.

In this part, I performed STED imaging as control experiments and used them for corrections. 9 different wells were listed with experiment conditions in Table 5. Here I describe 6 experiments with well numbering not continuous due to notebook record. Well 3 and well 4 are sequential staining to test the influence of staining sequence on STED results, with well 3 on 1st day stained with α-CD95 at 4°C o/n and on 2nd day with α-CD95L at 4°C o/n, and well 4 was on 1st day stained with α-CD95L at 4°C o/n and on 2nd day α-CD95 at 4°C o/n. Well 5 was incubated with CD95L and stained with α-CD95L only. Well 6 was stained with α-CD95 only as antibody control. Well 7 was w/o CD95L incubation and stained with α-CD95L only. Well 8 and well 9 were stained with two secondary antibodies at 4°C o/n to test their specificities. In all wells, biotin-IZ-CD95L was used as apoptosis inducer.

Table 5 Cell preparation and staining antibodies for control experiments.

Wells	biotin-IZ-CD95L	Primary antibody	Secondary antibody
3	200 ng/ml	α-CD95 (Biotium, B-R18)	AbSTARRed, RT 1h followed by α-CD95L (Abcam), 4°C o/n
4	200 ng/ml	α-CD95L (Abcam, 134401)	AbSTAROrange, RT 1h followed by α-CD95 (Biotium), 4°C o/n
5	200 ng/ml	α-CD95L (Abcam, 134401)	AbSTAROrange, RT 1h
7	-	α-CD95L (Abcam, 134401)	AbSTAROrange, RT 1h
8	-	AbSTARRED, 4°C o/n	
9	-	AbSTAROrange, 4°C o/n	

Figure 8. 4 A-B shows difference between sequential staining with first α-CD95 (Figure 8. 4 A) or first α-CD95L antibody (Figure 8. 4 B). Sigma increased from ~ 4 in A to ~ 5.5 in B and $<N_{ph}>$ per pixel increased from ~5 in A to ~ 5 and ~ 15 in B. Same trends in brightness and size distributions can be also seen in the CD95 channel staining result (not shown here). This indicates that CD95L antibody (Abcam) with better staining efficiency than CD95 antibody (B-R18), and

the two antibodies may interfere each other. What is interesting is as shown in Figure 8. 4 C-D that 200 ng/ml CD95L was incubated with Hela WT in C but no additional ligand was added in D. Both cases only were stained with α-CD95L antibody. As a control in Figure 8. 4 D**,** it should not show any fluorescence signal since there is no additional ligand incubation. However, notable STED signal was detected with sigma ranging from 3-7 and brightness ranging from 2-20, indicating the native CD95L expression on Hela WT cells. By comparison, only one species in $<N_{ph}>$ per pixel for Figure 8. 4 D, whereas two populations in B can be distinguished, with two medians of $<N_{ph}>$ per pixel at ~ 5 and ~ 15. Compared to D, C showed higher brightness with median ~ 8 ranging from 3-30, and larger sigma with median ~ 4.5 ranging from 4-8, caused by additionally incubated biotin-IZ-CD95L. Well 8 and 9 showed no fluorescence signal as a proof of specificity in secondary antibody staining. Overall, STED spots analysis in Figure 8. 4 is more pronounced with narrower distributions than Figure 8. 3 and Figure 8. 2 due to the better alignment in Abberior STED microscope.

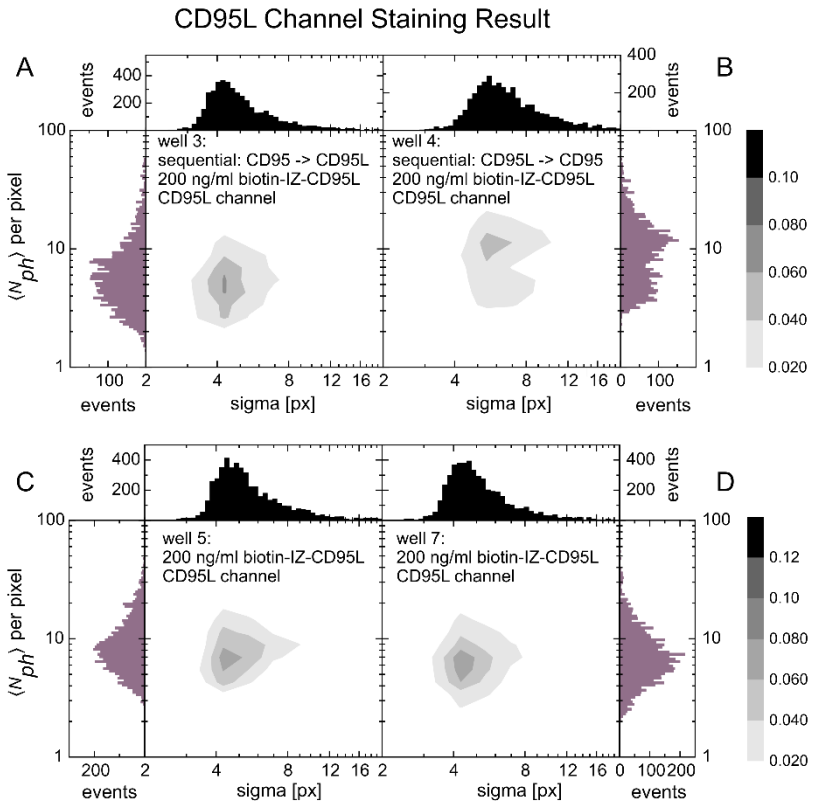

Figure 8. 4 Control experiment using two color-stained STED imaging analysis: CD95L/AbSTAROrange staining result. A. 200 ng/ml biotin-IZ-CD95L incubation sequential staining with first CD95 antibody. B. 200 ng/ml biotin-IZ-CD95L sequential staining with first CD95L antibody. C. 200 ng/ml biotin-IZ- CD95L with only IZ-CD95L antibody staining. D. Only with IZ-CD95L antibody staining. Figure layout is same as the previous ones.

8.1.3 Blocking of native CD95L for STED analyses

Due to the native expression of CD95L on Hela WT cells revealed in chapter 8.1.2. In this chapter, I tried to perform passivation of native CD95L using various α-CD95L antibodies recognizing different epitopes (listed in Table 6). After passivation with mouse1 µg/ml α-CD95L (clone NOK-1 or 2G9-G8) at 37 °C for 1.5 h, the cells were incubated with 200 ng/ml biotin-IZ-CD95L or Flag-CD95L at 37 °C for 2 h. In well 1 and 2, native CD95L was passivated by mouse monoclonal antibody NOK-1 (SantaCruz, sc-19681). According to the information provided by manufacturers, this antibody is generated by immunizing with recombinant human FASL. In well 3 and 4, native CD95L was passivated by mouse monoclonal antibody 2G9-G8 (Abnova, M02). This monoclonal antibody was raised against a full length recombinant FASLG (aa 1-281) fused with GST tag. However, their specific epitopes are not clear. After antibody neutralization, each well was incubated with additional biotin-IZ-CD95L (well 1 & 3) or Flag-CD95L (well 2 & 4). Cells were stained with primary mouse α-CD95 (B-R18) and rabbit α-CD95L (Abcam) followed by AbSTARRed and AbSTAROrange staining for well 1 & 2. Cells were stained only with primary α-CD95L antibody followed by AbSTAROrange for well 3 & 4. In well 5, without passivation and addition of CD95L, cells were stained with anti-CD95 and anti-CD95L antibody and secondary antibodies to image the native CD95 and native CD95L on Hela WT cell membrane. The results are shown in Figure 8. 5. Because AbSTARRed is an anti-mouse antibody, it binds with α-CD95 B-R18, NOK-1 and 2G9-G8 antibodies. The staining results therefore in Figure 8.5 B & D represent not only the native CD95 (detected by α-CD95 B-R18) but also native CD95L signals (detected by NOK-1 or 2G9-G8).

Table 6 Cell preparation and passivation antibodies for control experiments.

Wells	mouse α-CD95L	Apoptosis inducer	Primary antibody	Secondary antibody
1	SantaCruz NOK-1	biotin-IZ-CD95L	α-CD95 (B-R18) α-CD95L (Abcam)	AbSTARRed AbSTAROrange
2	SantaCruz NOK-1	Flag-CD95	α-CD95 (B-R18) α-CD95L (Abcam)	AbSTARRED AbSTAROrange
3	Abnova 2G9-G8	biotin-IZ-CD95L	α-CD95L (Abcam)	AbSTAROrange
4	Abnova 2G9-G8	Flag-CD95	α-CD95L (Abcam)	AbSTAROrange
5	-	-	α-CD95 (B-R18) α-CD95L (Abcam)	AbSTARRED AbSTAROrange

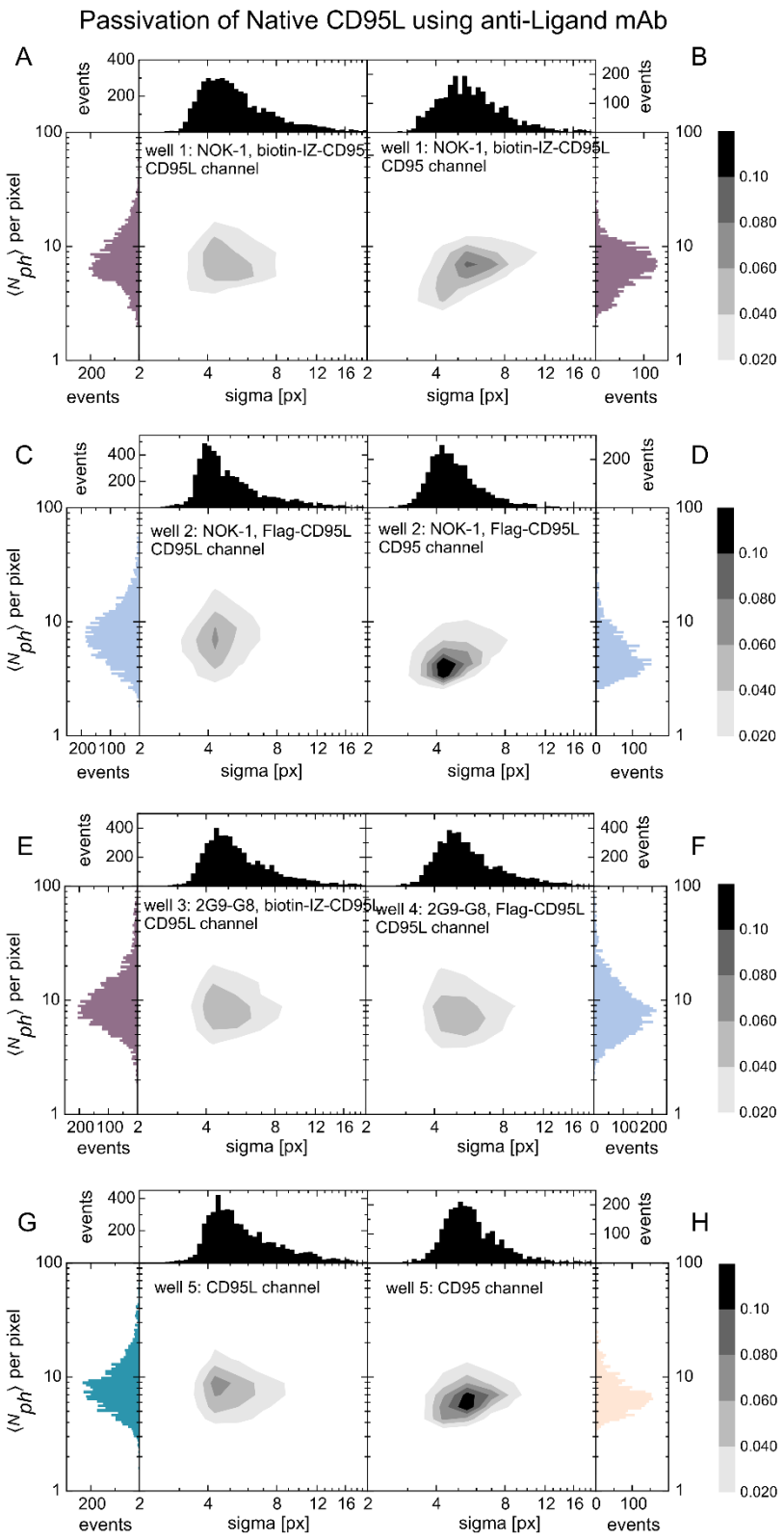

Figure 8. 5 Passivation of native CD95L using α-CD95L antibodies. CD95L/AbSTAROrange staining results are shown in A-C-E-G, and CD95/AbSTARed staining results are shown in B-D-F-H. A & B. NOK-1 + biotin-IZ-CD95L. C & D. NOK-1 + Flag-CD95L. E. 2G9-G8 + biotin-IZ-CD95L. F. 2G9-G8 + Flag-CD95L. Native CD95L in G. and native CD95 in H.

In Figure 8. 5 A-B, where native CD95L was passivated with mouse NOK-1, ideally it should show the STED signal of added biotin-IZ-CD95L, which are bound with CD95 on Hela WT cell membrane. The distributions show a median of sigma ~ 4 px and a median of $<N_{ph}>$ per pixel ~ 7. The everage of brightness in Figure 8. 5 A (ranging from 3-20) is larger than Figure 8. 5 B (ranging from 2-10). In the CD95 channel (Figure 8.5 B), the distributions are representing both native CD95 and native CD95L. Therefore, the sigma distribution shows an isoline at 0.02 from 4-11 px larger than Figure 8. 5 A. Because of overlapping Gaussians with reduced photon numbers and enlarged area, the median of brightness in B ~ 7 is smaller than A ~ 8. Figure 8. 5 C-D shows similar patterns as A-B. Here native CD95L was passivated with mouse NOK-1, showing the STED signal of nonnative Flag-CD95L. By comparison between Figure 8. 5 A and Figure 8. 5 C, the spot distribution of biotin-IZ-CD95L and Flag-CD95L does not show significant difference. This means the CD95 clusters triggered by Flag-CD95L or biotin-IZ-CD95L at 200 ng/ml does not differ from the nanoscale perspective. Figure 8. 5 D shows STED signal from native CD95 plus native CD95L, with broader sigma distribution and narrower brightness distribution than C.

In Figure 8. 5 E-F, cells were passivated with mouse mAb 2G9-G8 to test influence of potential different epitopes. This STED results show distributions of added biotin-IZ-CD95L in E and Flag-CD95L in F. By comparison, Figure 8. 5 F shows a slightly extended sigma distribution than E, whereas the brightness does not differ. By comparison of Figure 8. 5 A-C-E-F, there is no remarkable difference in antibody types for passivation. Overall, after passivation with NOK-1 or 2G9-G8, the STED result shows only one population of higher brightness compared with two distinguishable populations in Figure 8. 4 B, suggesting sufficient antibody binding. In Figure 8. 5 G and H, results show distribution of native CD95L in G and native CD95 in H. Theoretically, sum of G and A or G and C should present the result of Figure 8. 4 C.

8.1.4 Passivation of native CD95L using purified CD95 protein for STED staining

In this experiment, native CD95L on Hela WT membrane was neutralized by purified CD95 ECD (Sino biological) at 1 µg/ml at 37 °C for 1.5 h, followed by 200 ng/ml Flag-CD95L or biotin-IZ-CD95L addition for apoptosis induction. To stain the native CD95 on Hela WT membrane, mouse α-CD95 (SantaCruz sc-8009, clone B-10, used at 5 µg/ml) was used. This antibody is specific for binding with amino acids 316-335 at the C-terminus of human CD95 protein according to manufacturer's information. In this way, additional CD95 ECD (sino biological) won't be stained to prevent interference of STED imaging result analysis. The results are shown in Figure 8. 6.

Table 7 Cell preparation and passivation proteins for control experiments.

Wells	Neutralization with CD95	Ligand incubation	Primary antibody	Secondary antibody
2	CD95 ECD (Sino biological)	Flag-CD95L 200 ng/ml	Abcam ab134401 SantaCruz sc-8009	AbSTAROrange AbSTARRed
3	CD95 ECD (Sino biological)	IZ-CD95L 200 ng/ml	Abcam ab134401 SantaCruz sc-8009	AbSTAROrange AbSTARRed

Figure 8. 6 A shows the signals of added Flag-CD95L bound on Hela WT cell membrane after blocking the native CD95L using purified CD95-ECD. The isoline at 0.02 on sigma axis ranges from 3-7. The isoline at 0.02 of $<N_{ph}>$ per pixel ranges from 2 to 10 with the peak center at ~ 3. Figure 8. 6 B shows the CD95 signals after passivation, with median of $<N_{ph}>$ per pixel ~ 4 and median of sigma ~ 4.5. By comparison, the distribution is more pronounced and narrower in Figure 8. 6 B than Figure 8. 5 D, especially on sigma axis. This is reasonable, since no native CD95L was included and spots detected here were less bright and smaller. In Figure 8. 6 C, biotin-IZ-CD95L staining shows no significant different distribution than Flag-CD95L in A. In Figure 8. 6 D, spots distribution of CD95 after biotin-IZ-CD95L incubation does not show notable difference with Flag-CD95L, which is in accordance with previous results. If passivation worked sufficiently, in CD95/AbSTARed channels two scenarios were included: CD95 could be occupied by X-CD95L or free on cell membrane. Whereas in CD95L/AbSTAROrange channels, the only one scenario included was added X-CD95L bound with CD95. Therefore, distributions in B-D should be brighter and larger than A-C here. However, due to differences in staining efficiencies and detectors, results in this chapter are intricate to interpret. Last, it's noteworthy that distributions in Figure 8. 6 A-C show with less brightness compared with Figure 8. 5 A-C-E-F, despite they were all stained with rabbit α-CD95L (Abcam) followed by AbSTAROrange. This suggests a better performance of passivation using CD95 ECD than mAb NOK-1 or 2G9-G8.

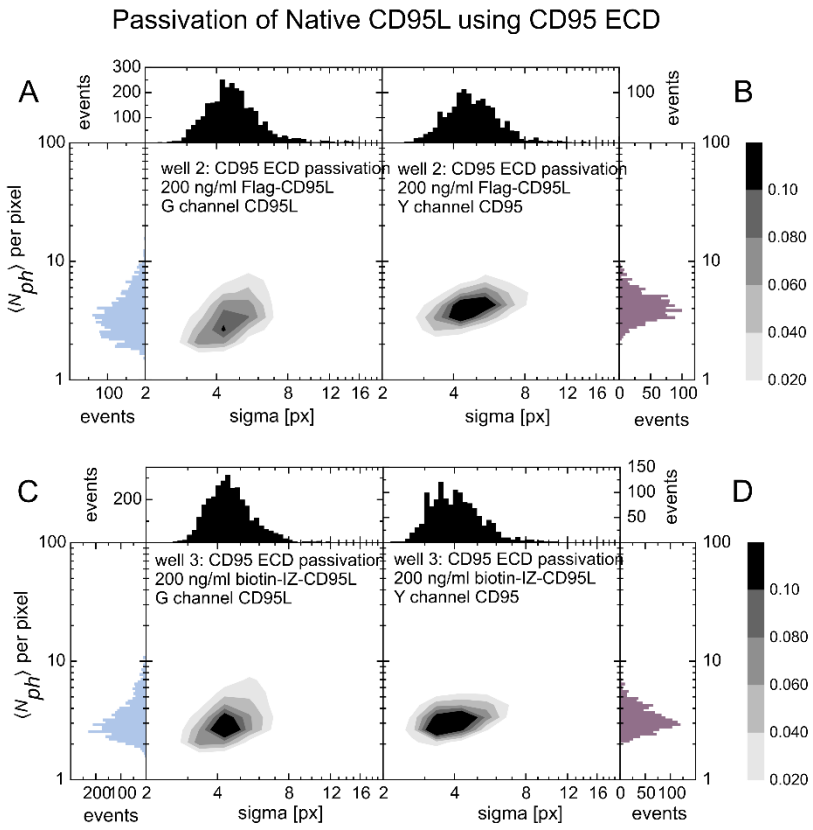

Figure 8. 6 Passivation of native CD95L using purified CD95. CD95L/AbSTAROrange staining results are shown in A-C, and CD95/AbSTARed staining results are shown in B-D. A & B. Incubation with Flag-CD95L. C & D. Incubation with biotin-IZ-CD95L.

8.2 Molecular Analysis of CD95L Variants

8.2.1 Blue Native-PAGE and Western Blot Analysis

To investigate the stability of His-IZ-CD95L and Flag-CD95L, BN-PAGE and western blot analysis were used. As shown in the following figure A-B. Protein stability was tested first by reducing or non-reducing SDS-PAGE followed by western blot. The influence of ligand binding with receptors was verified by band shift in BN-PAGE analysis.

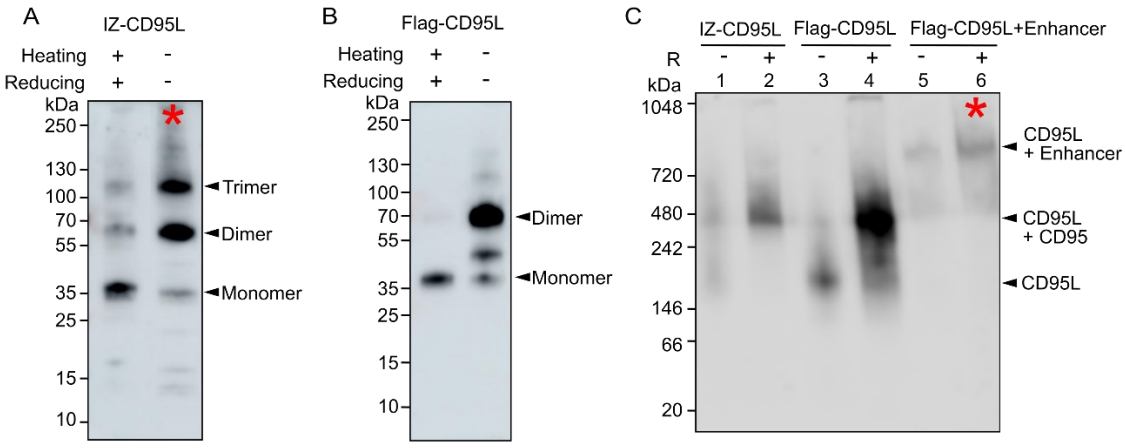

Figure 8. 7 Blue native-PAGE and western blot analysis. A. Western blot analysis of protein stability of 100 ng His-IZ-CD95L with (lane 1) or without (lane 2) heating and reducing condition. The membrane was probed with mouse anti-His-tag antibody (Biolegend, clone: J099B12, 1:1000) followed by horseradish peroxidase (HRP) linked secondary goat anti-mouse antibodies (Cell Signaling Technology (CST), 7076S, 1:1000). B. Western blot analysis of protein stability of 100 ng Flag-CD95L with (lane 3) or without (lane 4) heating and reducing condition. The membrane was probed with mouse anti-Flag-tag antibody (Enhancer, Enzo, 1:1000) followed by secondary goat anti-mouse antibodies linked with HRP (CST, 7076S, 1:1000). C. Blue native page analysis of 100 ng His-IZ-CD95L/100 ng Flag-CD95L/ 100 ng Flag-CD95L + 10x Enhancer with (lane 2, lane 4, and lane 6) or without (lane 1, lane 3, and lane 5) 10x CD95 ECD (Sino biological, 10217-H08H) incubation. The blot was probed with anti-CD95L rabbit polyclonal antibody (Abcam, ab134401, 1:1000) at 4°C o/n followed by 1 h goat HRP-anti-rabbit antibody incubation (CST, 7074S, 1:1000). 5 µl pre-stained protein standard (Thermo Fischer) or 10 µl unstained protein standard (Invitrogen) was used in A-B or C as rulers respectively.

As shown in Figure 8. 7 A lane 1 under reduced conditions, the monomer band at 35 kDa was detected as expected. Whereas under non-reducing conditions, the dimer band at around 68 kDa and trimer band at around 110 kDa can be resolved. The band intensity of trimer and dimer is higher than the monomer, which indicates that protein exists predominantly as trimer/dimer under non-reducing SDS-PAGE conditions. The higher molecular weight protein shown as a smear can be seen in lane 2 with an asterisk indicating a high order clustering of IZ-CD95L or partially denatured forms. Figure 8. 7 B lane 3 shows the detected monomer band at 35 kDa same as decribed in the manufcaturer's information. Under non-reduced conditions, dimer band of Flag-CD95L was detected with the highest signal. At around 35 kDa – 55 kDa, there are two bands compared with single band (~ 35 kDa) in lane 3. This can be contributed by different degrees of

glycosylations or alternative protein isoforms. In Figure C. The blue native PAGE was used to analyze the native protein complexes. In lane 1 and 2: IZ-CD95L shows a clear band shift after binding of CD95 (lane 2, ~ 480 kDa) compared to without CD95 (lane1, ~ 200 kDa), manifesting the change in complex size. In lane 3 and 4: Flag-CD95L shows a similar shift pattern but with less efficiency since more signal of CD95L left ~ 200 kDa in lane 4. In lane 5 and lane 6: Flag-CD95L-Enhancer shows high-order complexes at ~ 500 or 850 kDa, suggesting the stoichiometry of one mAb (150 kDa) crosslinking two Flag-CD95L or two mAb crosslinking three Flag-CD95L. The asterisk marked with even higher position after binding with CD95 at ~ 1000 kDa proving the addition of CD95 in complex size. To draw a conclusion, the comparison between Figure 8. 7 A and B shows the different stability profiles under heating and reducing conditions. His-IZ-CD95L forms more stable trimers whereas Flag-CD95L shows dimerized complexes under non-reducing SDS conditions. Both His-IZ-CD95L and Flag-CD95L can bind with CD95 to form complexes as shown in the band shifts (Figure 8. 7 C lane 2 and lane 4). Lane 4 shows higher signal intensity of Flag-CD95L which is due to putatively the low pI compared with His-IZ-CD95L (9.1), leading to better performance in gel migration. Enhancer indeed crosslinked Flag-CD95L with formation of high-order complex shown in lane 5 and binding pattern can be observed further by smear in lane 6.

8.2.2 Surface Plasmon Resonance of CD95 – CD95L interaction

The surface plasmon resonance (SPR) measurement employs a sensor chip for immobilization of CD95 and probes the binding kinetics of X-CD95L. An incident light is guided to the sensor chip with a fixed angle and the reflected light is collected on the detector, during which the electrons in the thin metal film are excited and travel parallel to the film, referred as surface plasmon resonance (SPR). This SPR phenomenon is very sensitive on small changes in refractive index, which can be changed by binding of CD95L on immobilized CD95, resulting in alteration of reflected light. The changes of angle can then be converted to a SPR sensor graph, where binding kinetics can be quantified. The SPR sensor graph follows Langmuir binding model (112) in two parts, as described by equation 28-29. Equation 28 describes the association phase of the SPR sensorgram, during which the analyte (X-CD95L) binds to the immobilized CD95 on the sensor chip, with increasing response unit (RU) until saturation. Equation 29 describes the dissociation phase, during which CD95L dissociates and RU starts to decline.

$$R_t = \frac{R_{max}[A]}{K_D + [A]}\left(1 - \frac{1}{e^{(k_a[A]+k_d)t}}\right) \tag{28}$$

$$R_t = R_0 e^{-k_d t}(b) \tag{29}$$

Here, [A] is analyte concentration, $k_\mathrm{a} = [M^{-1}S^{-1}]$ is the association rate constant, $k_\mathrm{d} = [S^{-1}]$ is the dissociation rate constant, and $K_\mathrm{D} = \frac{k_\mathrm{a}}{k_\mathrm{d}}$ [M] is the equilibrium dissociation constant. R_t is the response unit at time t, representing the amount of binding in real time. R_max is the maximum response unit (RU) when all available binding sites are occupied during association phase, representing the curve saturation. R_0 is the response unit at the beginning of the dissociation phase, indicating the amount of complex at the start of dissociation (113). To have

better fitting result, it is important to have a good initial guess, which is referenced from a previous study (114). The drift corrected data were then fitted globally with two parts of equation among four experiments shown in Figure 8. 8.

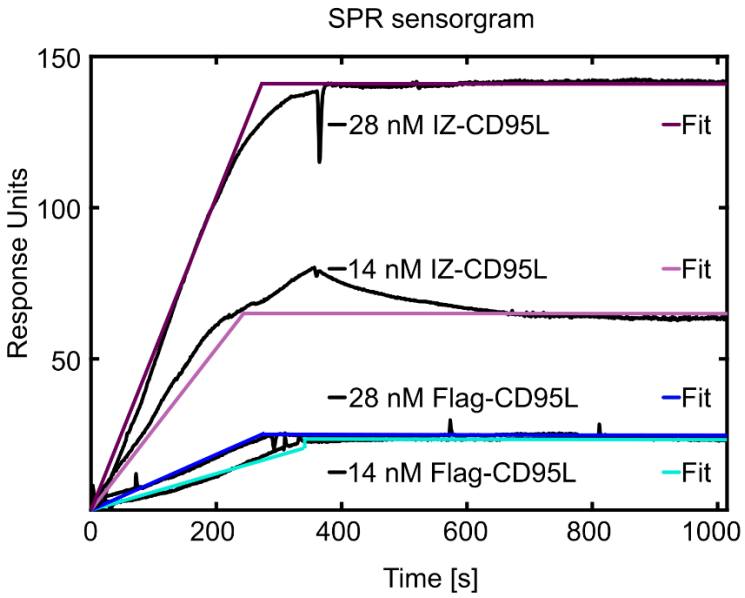

Figure 8. 8 Binding affinity probed by (SPR) measurements. Data points are shown in black lines, and the fitting result is shown in colored lines. The mauve line presents 27.6 nM IZ-CD95L, periwinkle for 13.8 nM IZ-CD95L, navy blue for 27.6 nM Flag-CD95L, and cyan for 13.8 nM Flag-CD95L, with fitting result of K_D (IZ-CD95L) = 1.2 nM and K_D (Flag-CD95L) = 14.5 nM.

Figure 8. 8 shows the SPR sensor graphs with fitted results showing CD95L variants binding affinities. Lower K_D values indicate higher affinity. In the case of Flag-CD95L, global fit results are $k_a = 1000\ [M^{-1}S^{-1}]$ $k_d = 0.000015\ [S^{-1}]$ $K_D = 14.5\ nM$. In the case of IZ-CD95L, global fit results are $k_a = 1000\ [M^{-1}S^{-1}]$ $k_d = 0.000001\ [S^{-1}]$ $K_D = 1.2\ nM$. The fitting result demonstrates a tenfold lower K_D of IZ-CD95L compared to Flag-CD95L. This suggests that the stability of IZ-CD95L/CD95 complex is stronger than Flag-CD95L/CD95. By comparison, the association rate constants k_a are the same for both variants, which suggests a similar speed of onset recognition. The dissociation rate k_d of IZ-CD95L is significantly slower than that of Flag-CD95L, contributing to an overall higher affinity to CD95. This can be explained by a sufficiently enhanced trimerization of soluble CD95L by fusing with IZ. To sum up, the SPR results show a higher binding affinity of IZ-CD95L with CD95, which is in accordance with PAGE results shown in chapter 8.2.1. They both imply that structural stability of soluble CD95L plays role in apoptosis initiation, which have been revealed in apoptosis dynamics analysis from chapter 7.

9 DNA Origami Platforms for Single Molecule Studies

9.1 DNA Origami Platforms for Single Molecule Studies

9.1.1 Design of the DNA Origami Platforms

The design and fabrication of DNA origami was performed by Johann Moritz Weck. Here I explain the concept of the design. In this study, two types of platforms were used based on a rectangular backbone as described from a previous study (101). Briefly, the DNA origami template was a single layer with a rectangle shape. On the one side, the template was labelled with fluorescent dyes and on the other side with biotins for immobilizing on the streptavidin coated glass surface. The rectangular DNA origami was designed with a length of ~ 85 nm and a width of ~ 61 nm as shown in Figure 9. 1 with fluorophores or biotin incorporated in the scaffold using modified staple strands. The first template is shown in Figure 9. 1 A with two FRET pairs as a control template. The first FRET pair donor 1 and acceptor 1 (D1A1) were used as an anchoring/pseudo marker for sports sorting in the later usage, and they were placed ~ 38 nm away from each other to ensure no FRET occurring between them. The second FRET pair, D2A2, were used as a measuring pair to evaluate the measurement settings and data analysis code which will be described in chapter 9.2. D2 A2 were placed with either ~ 10 nm (low FRET efficiency) or ~ 5 nm (high FRET efficiency) for lifetime- or intensity-based FRET evaluation. The two pairs D1A1 and D2A2 are placed farther with ~ 70 nm away from one another to ensure 1) no crosstalk occurring, 2) robust Gaussian fittings in the first data analysis step. Due to the diffraction-limited resolution of confocal imaging, the four dyes cannot be resolved in confocal mode. They appear together as one bright spot in overviews during data recording (one spot was identified as one origami molecule). Further, each molecule in each ROI was imaged under the STED mode. The time-gated STED image containing the correct and equally labelled dyes in each channel do not allow for a distinction of the fluorophores by eyes and will be judged by up to three Gaussian fittings in the data analysis step. The second template is shown in Figure 9. 1 B, which was labelled one FRET pair D1A1 as pseudo markers and two biotins as CD95 anchoring sites. D2A2 in the first template were replaced by two biotins in the second template placed 10 nm away, considering that 5 nm might obstruct two CD95 interactions. Because of the arbitrary labeling of biotin/streptavidin/CD95-biotin, multiple arrangements of DNA origami can be possible based on the number of CD95 binding. Assuming all CD95-biotin was selectively labeled with one fluorophore (ATTO 594 or ATTO 643) at the N-terminus correctly, origami can be bound with 0 CD95 (D1A1_ _), 1 CD95 (D1A1D2_, D1A1_A2), or 2 CD95 (D1A1D2D2, D1A1A2A2, D1A1D2A2). Up to two CD95-biotin can be bound on streptavidin due to the steric hindrance effect, if the streptavidin is bound correctly. This will be discussed in chapter 9.4.

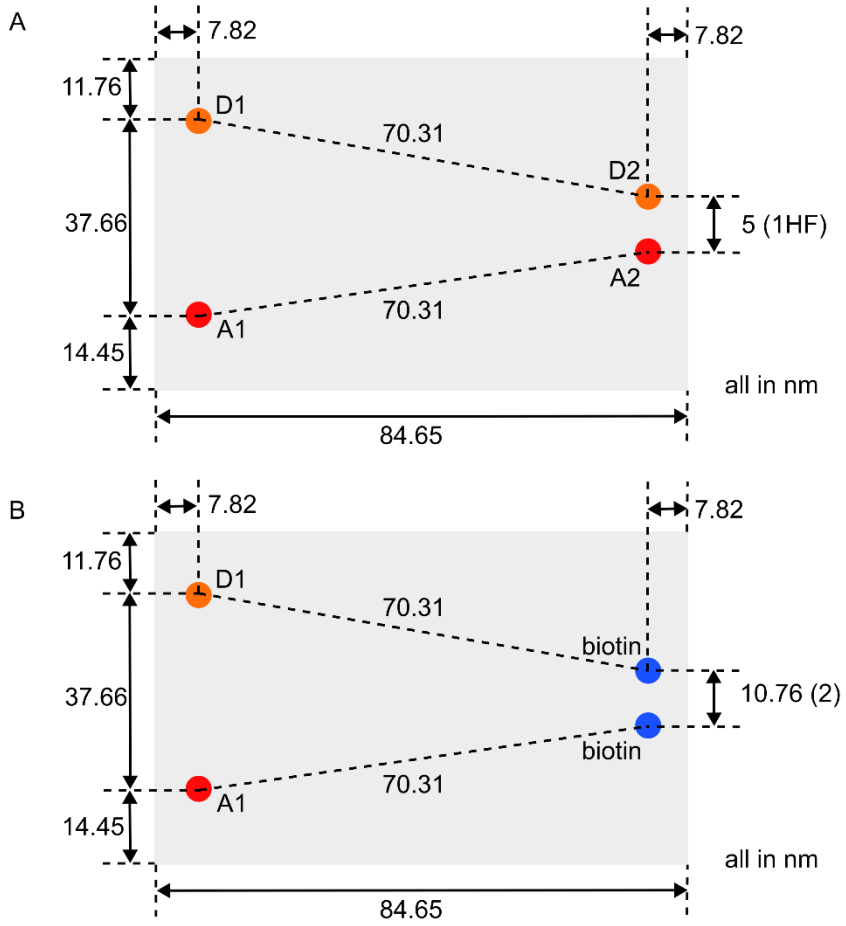

Figure 9. 1 The design of DNA origami. A. Template 1 with four fluorophores labeled DNA origami as a high FRET (1HF) control. The first FRET pair donor 1 acceptor 1 (D1A1) were used as pseudo markers. The second FRET pair donor 2 and acceptor 2 D2 A2 were used as probing pair. Fluorophores used for D1D2 were ATTO 594 or Alexa fluor 568, for A1A2 was ATTO 647N. B. Template 2 with only one FRET pair and with two biotins for CD95 anchoring. Biotins were placed 10.76 nm away from each other to provide enough space for potential CD95 interaction. All distances are shown in nanometer.

9.2 FRET Nanoscopy Image Analysis Software

Jan-Hendrik Budde & Nicolass van der Voort wrote, and Oleg Opanasyuk & Noah Salama updated the data analysis code. The full code is available here: https://github.com/Fluorescence-Tools/Seidel. Here I show a workflow to run the code using an example dataset from Michelle Paulina Rademacher (measurement date: 2021-12-13, in total 346 ROIs/molecules). It is noteworthy that the origami template used here is different from Figure 9. 1. It was designed with one side decorated with 4 fluorophores two Alexa 594 as donors and two Atto 643 as acceptors, and the other side with 8 biotins for immobilization on streptavidin surface and flattening origami sheets. The latter design of coupling 8 biotins to the streptavidin improved surface preparation and data quality. Data analysis in this chapter used jupyter notebook with a version of `2024_03_16_TempFixByOleg.jpynb`

Localization analysis. The ROI (1 µm x 1 µm with 10 nm pixel size = 100 pixels x 100 pixels) images were taken under STED mode and saved as .ptu formatted files. Those files are three-dimensional arrays including the information of collected photon stream with: i) their space coordinates by synchronization of a piezo scanner; ii) micro (ns regime) or macro (ms regime) timing recorded from TSCPC unit; iii) instrumental markers such as laser lines or detectors with different polarization or colors (115). STED resolution of each ROI was first increased by time gating of first 29 ns. Afterward, each .ptu file was split into green (green photons after green excitation) red (red photons after green excitation) and yellow (red photons after red excitation) channels based on the laser line and detectors used. Reading and processing of raw .ptu files were achieved by dynamic link library (dll) files (`PQ_PTU.dll` and `_ProcessPhotonStream.dll`) in the wrapped folder. Next, in each channel a smaller ROI (30 pixels x 30 pixels) was cropped out, where one two or three Gaussians were fitted and the best it was chosen (see Figure 9. 2). Each successful fit contains the information of coordinates, amplitude and background was added in a directory named `locLst`.

In detail, before the Gaussian fitting process, the local maxima were found from a cropped and smoothed ROI. A local peak detection algorithm was applied by employing a 'raindrop' model, as described in `findPeaksLib.py`. In this model, each pixel in the image was considered a raindrop, assigned with coordinates and intensity of each pixel. Based on continuous comparison of intensities with 3 neighbour pixels, the coordinates were sorted. The top three brightest peaks with sufficient distances were selected for Gaussian fitting later. This step was important to get a good initial guess, follow which the raw data (time gated STED image) was fitted with 1, 2 or 3 2D Gaussians and the best fit was chosen based on comparison of the goodness of fits (Table 8 and Table 9). The fitting process was described `GaussFitsNV.dll` and called by importing ctypes in python, and judgement and plotting were described in `GaussAnalysisPipeline.py`, which returned 18 parameters including coordinates and other information: [x_0, y_0, A_0, σ, ε, *setbg* (= 0.2), x_1, y_1, A_1,x_2, y_2, A_2, info, unkown, *fitbg* (= 0), ε, *model* (0 for 1 Gaussian, 1 for 2 Gaussians, 2 for 3 Gaussians), *2I**] (Table 10). Note that parameters include only one sigma and one fitted background, speculatively the fitting used global fit and assumed all spots are same in width.

Table 8 Parameters used for fitting evaluations.

Name	Function
`twoIstar` (`2I*`)	It calculates the quality of fit based on maximum likelihood estimation (78).
`DTwoIstar` = 0.03	It's the difference of `2I*` between two fits.
`garbageBrightness` = 20	It's the threshold for considering peak as noise.
`junkIstar` = 0.30	It's the threshold of `2I*` to be considered as junk.

Table 9 Parameters used in fitting judgement.

Name	Function
`isSignificantlyLower`	It's used to check that the `2I*` value of the new fit is at least `DTwoIstar` (0.03) lower than other fits.
`isNoGarbagePeaks`	If the brightness (estimated by A_i * 2π * σ^2) of each distribution are larger than 20, it will be excluded from evaluation as noise.
`isNoJunkIstar`	`2I*` values should be above `junkIstar` to be considered as a valid fit.

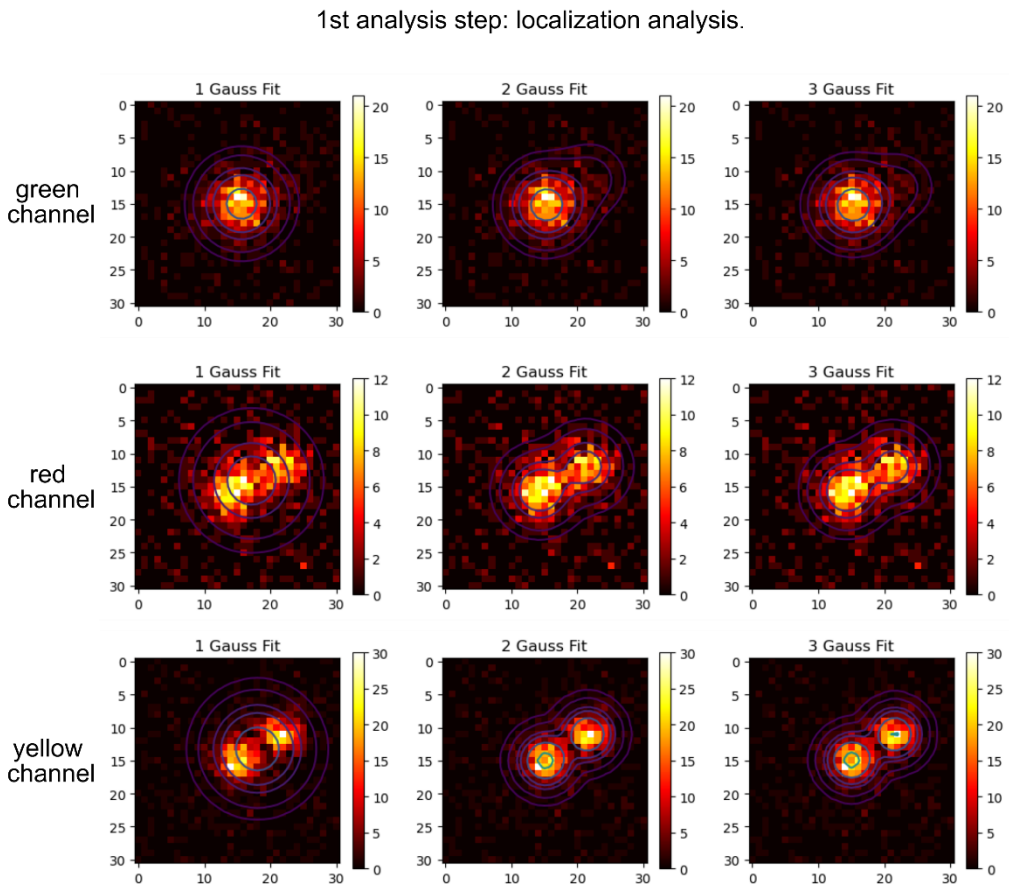

Figure 9. 2 Localization analysis of one example .ptu file. (PQSpcm_2021-12-13_17-54-52.ptu). The 1 µm x 1 µm image (10 nm pixel size) was cropped into 30 pixels x 30 pixels size

and split into green, red, and yellow channels. Each channel was fitted with one two or three 2D Gaussians, from where the best fit is selected.

As shown in Figure 9. 2, the 1, 2, and 3 Gaussian fittings were applied in each channel. The result of fittings with coordinates, amplitudes, widths, ellipticities, and background was printed in the terminal (Table 10). It chose the best fit based on the evaluation of fit qualities with `2I*`. For example, in optimized 1 Gaussian fit returns the coordinates of first peak with x_0 = 14.985 pixels, y_0 = 15.642 pixels, amplitude A_0 = 12.984 pixels, peak width σ= 3.034 pixels, ε = 1 A.U. (circular spot), and background bg = 0.272 A.U.. It returned the fit `2I*` = 0.694 A.U. for 1 Gaussian fit, `2I*` = 0.662 A.U. for 2 Gaussians fit, and `2I*` = 0.659 A.U. for 3 Gaussians fit. All were larger than the threshold (`junkIstar` = 0.30 A.U.), therefore `isNoJunkIstar` was 'True' for three cases. The estimated brightness per peak were calculated by using amplitude and sigma of first peak with A_i x 2π x σ^2 larger than 20 A.U. (`garbageBrightness`) for all three fitting conditions. Therefore, `isNoGarbagePeaks` was 'True' for three cases. The quality difference between 2 Gaussians fit and 1 Gaussian fit was `DTwoIstar` = 0.694 - 0.662 = 0.032 A.U. > 0.3 A.U., therefore 2 Gaussians fit was significantly better than 1 Gaussian fit. The quality difference between 3 Gaussians fit and 2 Gaussian fit was `DTwoIstar` = 0.662 - 0.659 = 0.003 A.U. < 0.3 A.U., therefore 3 Gaussians fit was not significantly better than 2 Gaussian fitting and 2 Gaussians were selected.

Table 10 Fitting results and selection criteria of the green channel.

optimised 1 Gauss fit is:
[14.985, 15.642, 12.984, 3.034, 1, 0.272, 9, 20, 5, 9, 25, 2, 1, 0, 0, 1, 0, 0.694]
optimised 2 Gauss fit is:
[15.168, 15.309, 13.799, 2.854, 1, 0.243, 11.296, 21.916, 1.409, 9, 25, 2, 1, 0, 0, 1, 1, 0.662]
optimised 3 Gauss fit is:
[15.174, 15.277, 14.152, 2.807, 1, 0.237, 12.563, 22.233, 1.221, 7.274, 20.209, 0.477, 1, 0, 0, 1, 2, 0.659]
isSignificantlyLower: [True True False]
isNoJunkIstar: [True True True]
isNoGarbagePeaks: [True True True]
2I*: [0.694 0.662 0.659]
fullfills all conditions [True True False]

Spots sorting. From the previous Gaussian fit step, all fitting results were listed and saved in `locLst`. Each DNA molecule obtained a `loc`, which contained information including color channels (green G, red R, yellow Y), positions (posx, posy) and so on. Since each molecule in one ROI ideally contains 4 dyes (D1D2A1A2), 4 possible pair distances can be obtained (D1A1, D1A2, D2A1, D2A2) between two channels G and Y. Pair distances were calculated by Euclidean distance formula and stored in a list:

$$d = \sqrt{(x_2 - x_1)^2 + (y_2 - y_1)^2} \tag{30}$$

Afterward, the closest distance of pairs (D1A1, D1A2, D2A1, D2A2) was sorted out (D2A2) by index and removed from the list. In each ROI/origami molecule, the sorted closest pair was considered as a potential FRET pair. Calculation of cross distances of spots and sorting were described in `developmental_functions.py`. The proximity ratio E_{prox}, and lifetime τ from green (*tau*G), red (*tau*R) and yellow (*tau*Y) channels were then calculated for the FRET candidate. At this step, the proximity ratio E_{prox} is the uncorrected, intensity-based apparent FRET efficiency.

The lifetime calculation. The lifetime calculation was described in `fitTau` function. In TCSPC measurement, photon streams were saved as .ptu files, which are 3-dimensional arrays containing space and time information. Namely, .ptu files save the laser scanning position (spatial X/Y coordinates) and photons distribution (time dimension Z) at each pixel, where the photon counts were saved in a binned histogram (TAC decay) and can be fitted to obtain the fluorescence lifetime. Attributed to the PIE mode, images can be split into green, red, and yellow channels based on distinguishable excitation laser pulses and detectors.

Specifically, in the TCSPC system, the timing difference is converted to voltage by the time to amplitude converter (TAC) and fed to an analog to digital converter (ADC) for building the histogram (116), which is an array of binned photon counts versus time. Here the photons histogram is named *TAC* decay. `TACCal` (= 0.128 ns) is the time per *TAC* bin to convert the bin index to real time `tactimes`. `ntacs` (= 256) is the number of bins in the histogram. For example, the 1st to 256th TAC bins (`TACCal` x `ntacs` = 256 x 0.128 ns = 33 ns) represent a histogram from 0 to 33 ns. `Verbose` is a Boolean tag, if it's set 'True' then it generates fitting plots in the terminal. The background values (e.g. Background = [0.5, 0.5, 0.5] A.U.) from G, R, and Y channels were read from the customer-written software Ani. The background photon arrival time (`bgArrivalTime`) was estimated by taking half of the bin time (e.g. 33 ns ÷ 2 = 16.5 ns). In the first analysis step, time gating (bin 26 to 150 cutoff) was applied to sharpen the STED image for Gaussian fitting. It sliced the photon counts from bin 26 -150 (~16 ns) of the complete *TAC* decay, which improved the precision of localization. Therefore, the lifetime from each channel with background correction was calculated by:

$$bgcorTAC = \frac{\sum(TAC * tactimes) - bgphotons * bgArrivalTime}{\sum TAC - bgphotons} \tag{31}$$

This *bgcorTAC* calculates the averaged arrival time of all photons with background correction. Therefore, it's used as an estimated lifetime τ, filled in a mono-exponential equation and plotted as a result in the terminal (*expDecay* versus *tactimes*) (see Figure 9. 3 A-C). Note that lifetime curve was enriched by summing up all pixels (axis = (0,1)) in cropped ROI as described in `calcFRETind` function.

$$expDecay = \frac{\sum(TAC) * TACCal}{\tau} \cdot \exp\left(-\frac{t}{\tau}\right) \tag{32}$$

Intensity-based FRET calculation. This calculation was described in the `calcFRETind` function. After the first step fitting, each ROI was cropped by using localized xy positions and

sigma (*posx*, *posy*, and *winSigma*) (see Figure 9. 3 D). The cropped ROI was presented as lifetime bitmaps with a sqaure size of [2* *winSigma* + 1] pixels. When *winSigma* was set 3, the ROI size was 7 x 7 pixels. The photon counts at each pixel was first added up in the time dimension (axis = 2) from bin 0 – 150 (without STED gating). Subsequently, the photon counts from each pixel were summed up from all dimensions (xyt) at green (*Gphotons*), red (*Rphotons*), yellow (*Gphotons*) channels respectively, referred as spot integrated photon counts. Note that number of red photons was summed by using localization from yellow channel, since this is the acceptor position. To sum up, the intensity-based FRET was calculated as:

$$proxRatio = \frac{R\text{photons}}{G\text{photons} + R\text{photons}} \tag{33}$$

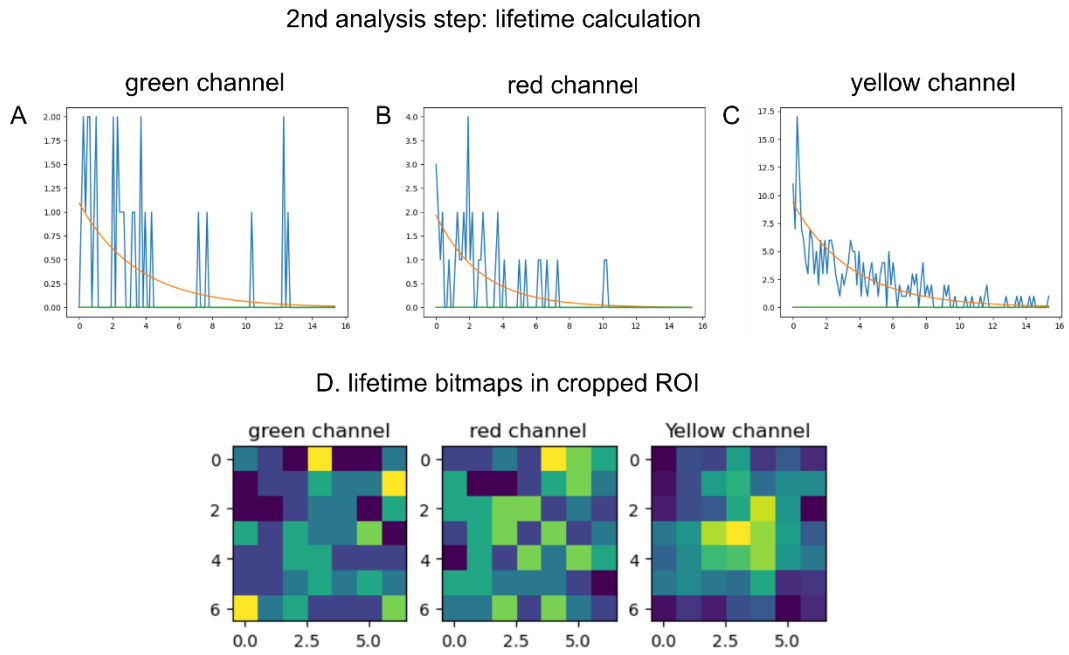

Figure 9. 3 Lifetime calculations and intensity-based FRET calculation. (PQSpcm_2021-12-13_17-54-08.ptu). A-C. lifetime calculation at green, red, and yellow channels. The blue lines are the raw TAC data. The orange lines are the mono-exponential equations filled with calculated lifetime. The green lines are background levels. X axis represents real time (*tactimes*). D. Lifetime bitmaps of cropped ROI with gated photon counts (26–150 bin) at each color channel. The ROI sizes are 7 x 7 pixels. FRET was calculated from integrated photon counts from green and red channels by equation 33.

Spot stoichiometry map. This map was drawn using the `plotOccurrence` function, where 2D scatter plots of detected green spots and yellow spots were presented (see Figure 9. 4 A-B). Number of green or yellow spots were obtained by finding the maximum of localizations in sorted `spotLst`. As shown in Figure 9. 4 A with red asterisks, despite up to 3 Gaussians being fitted at each channel, 4 or 5 fluorophores were unexpectedly detected. Figure 9. 4 B shows the cropped stoichiometry map where the most interested molecules are listed. This gives an overview of how

good the origami molecules were labelled and was used for next step A-A distances or FRET calculations by selecting desired labelling.

98 molecules with 1 donor and 2 acceptors labelled were detected with highest occurrence. 75 completely labelled molecules were detected and boxed in black. 0 x 0 spots represent the failed fitting process. 3 fitting results were attributed from 2 origami molecules placed nearby in the same ROI. Acceptor-only and donor-only molecules were boxed in red and green respectively, suggesting incomplete labelling during sample preparation. Figure 9. 4 C shows the E_{prox} versus $\tau_{D(A)}$ map, where the static molecules without deviations should follow a linear relationship as shown in Figure 2.6. In this map, two populations can be distinguished: the HF (high FRET in red circle) and NF (no FRET in blue circle) populations. Ideally, after 2 x 2 cuts filtering, the data points should only contain high FRET populations (red circle, Figure 9. 4 D). However, there were species still shown in NF circle (blue circle, Figure D), which can be caused by unprecise fitting or calculations from previous steps.

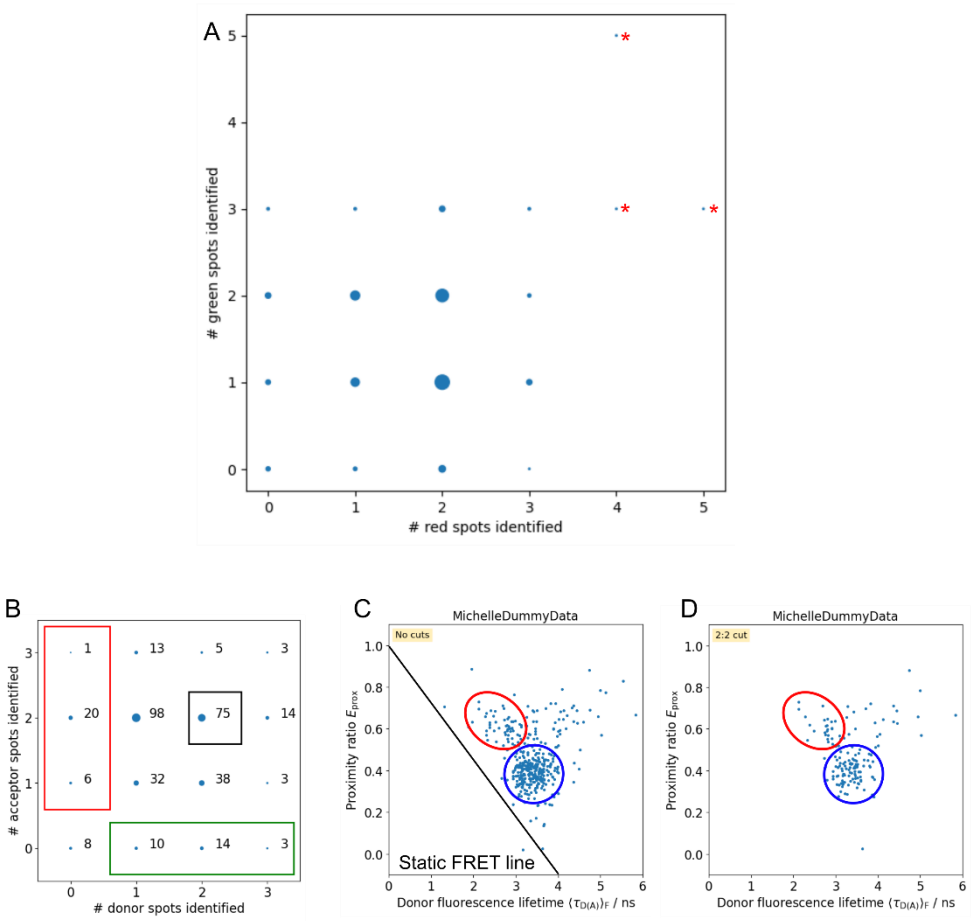

Figure 9. 4 Stoichiometry map and E_{prox} versus $\tau_{D(A)}$ map. A. The overview of detected red and green spots from 1st step localization analysis. B. Zoomed stoichiometry map without outliers. The black box shows the completely labelled molecules with 2 donors and 2 acceptors, and the red or green box shows the molecules only labelled with acceptor or donor fluorophores. C. Proximity ratio E_{prox} versus Donor lifetime $\tau_{D(A)}$ (*tauG*) map containing all molecules, with static

FRET line shown in black. D. Proximity ratio E_{prox} versus Donor lifetime $\tau_{D(A)}$ map with 2:2 cut off, which contains molecules labelled with 2 red and 2 green fluorophores (75 molecules boxed in black shown in B).

The mean lifetime at green (*tauG*), red (*tauR*) and yellow (*tauY*) for the data set is 3.4 ns, 3.5 ns, 3.4 ns respectively for Figure 9. 4 C. The mean lifetime is calculated from averaged lifetime of each spot. The mean lifetime at green (*tauG*), red (*tauR*) and yellow (*tauY*) for the data set (2:2 cutoff) is 3.4 ns, 3.5 ns, 3.4 ns respectively Figure 9. 4 D.

Acceptor acceptor (A-A) distance and XY scatter diagram. The A-A distance (A1A2) in each DNA origami platform was calculated using the yellow channel localizations. First, it selected the molecules with labelling of acceptor = 2 donor = 0, 1, or 2 from the stoichiometry map by applying filter [[0, 1, 2], [2]]. Second, it calculated the relative position (in pixel) between two spots by subtraction of apparent coordinates between 1st and the 2nd spot on X and Y axis. The real distance was converted by multiplying the pixel size (10 nm), referred as r_x and r_y. In this way, A2 was used as centre of circle and A1 evenly distributed on circumference, due to random orientation of DNA molecules. The average of all r_x and r_y was calculated and used as the centre of map (yellow star in Figure 9. 5 A, X = 2.99 and Y = – 0.96). The Euclidean norm distances of A-A pairs were calculated by:

$$r_{AA} = \sqrt{(r_x)^2 + \left(r_y\right)^2} \tag{34}$$

Afterward, norm distance *r* was binned into a histogram and fitted with non-centred Chi (*ncχ*) distributions (Figure 9. 5 B**)**. This calculation was described in `ncChidistr` function in `histogram_fitting.py` using the following equation:

$$f(r) = \frac{A \cdot r}{\sigma^2} \cdot \exp\left(-0.5 \cdot \left(\frac{r-\mu}{\sigma}\right)^2\right) \cdot J_0\left(\frac{\mu \cdot r}{\sigma^2}\right) + offset \tag{35}$$

With A as amplitude, r as A-A distance, σ as standard deviation, μ as mean. J_0 is the Bessel function of the first kind of order 0, introducing the radial character to the distribution. *offset* is the background. The `get_logLikelihood1DPoisson` function evaluates the fit quality using log-likelihood with equation:

$$L = \sum(-model + ydata \cdot \ln(model) - \ln(ydata!)) \tag{36}$$

With *model* being the fit, *ydata* being A-A distance *r* and *L* being the likelihood. The likelihood of different *mu*0 (R^{loc}_{mp}) and *sig*0 was calculated and plotted as 2D contour plot in gray colormap with marginal histograms (Figure 9. 5 C**)**.

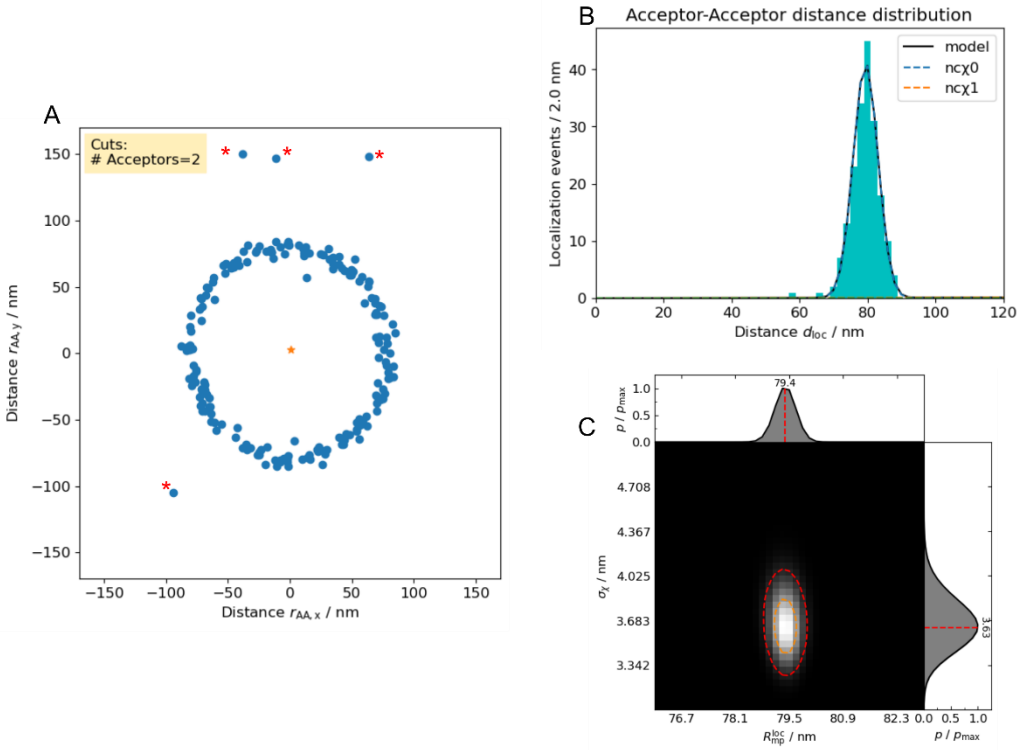

Figure 9. 5 A-A distance analysis. A. XY scatters plot of A-A pairs with the center of dataset at (2.99, -0.96). Outliers are shown in red asterisks. The maximum distance is 170 nm. B. The norm distance of A-A pairs was shown in a histogram with a bin size of 2 nm, fitted using nChi with two components ncχ0 (blue) and ncχ1 (orange), shown in dashed lines. C. Likelihood scanning of mu0 (R^{loc}_{mp}) and sigma0 (σ_χ), shown in gray colormap, with brighter spots presenting higher likelihood. The contour levels of 0.135 pmax (2σ) and 0.6 pmax (σ) were shown in red and orange respectively.

A-A distances with respect of XY coordinates were represented as scatter spots (blue dots), evenly distributed in a circle with radius of ~ 79 nm. The outliers (marked in red asterisks) can be caused by two single labeled origami detected in one ROI, so that A-A distance can be calculated longer than 85 nm (the length of rectangular DNA origami). The A-A distances distribution in Figure 9. 5 B presents a narrow distribution centered at ~79 nm, which was well matched with the structure prediction and TEM imaging with dimension in (88 ± 3) x (59 ± 4) nm^2 (92). The results of histogram fitted with two components were reported in Table 11, with *mu*0 *A*0 *sig*0 obtained from *ncχ*0 and *mu*1 *A*1 *sig*1 obtained from *ncχ*1. It helps to scrutinize the dependency of parameter changes with different combinations on the fitting quality. The scanning range was 76 – 83 nm for *mu*0 and 3-5 nm for *sig*0, each with 40 steps interval. As shown in Figure 9. 5 C, the scanned R^{loc}_{mp} and σ_χ present two distributions centered at 79.4 nm and 3.63 nm. The orange and red ellipses represent the confidence levels of distributions, with 0.6 pmax (σ) in orange and 0.135 pmax (2σ) in red of the R^{loc}_{mp} and σ_χ distributions.

Table 11 ncχ fitting results of A-A histogram.

Fit statistics		Variables	
fitting method	Nelder-Mead	*bg* A.U.	0 (fixed)
function eval	1394	*mu*0 nm	79.40 (init = 79)
data points	1	*A*0 A.U.	372.98 (init = 1200)
variables	6	*sig*0 nm	3.63 (init = 15)
chi-square	1910.67	*mu*1 nm	167.00 (init = 105)
reduced chi-square	1910.67	*A*1 A.U.	32.96 (init = 1200)
Akaike info crit	19.55	*sig*1 nm	88.05 (init = 15)
Bayesian info crit	7.55	*AIC* for custom fit is 99.42	

As reported in Table 11, the Nelder-Mead algorithm was used as fitting method with initial guess of amplitude A_i sigma σ_i and mean mu_i and fixed background *bg*. Minimization reached after 1394 evaluations. 1 histogram dataset was fitted and 6 variables included *A*0/*A*1, *sig*0/*sig*1, *mu*0/*mu*1. The goodness of fit was evaluated by chi-square, reduced chi-square, Akaike information criterion (AIC), and Bayesian information criterion (BIC) (117). The best model was chosen with lowest *AIC* using equation:

$$AIC = 2k - 2\ln(L) \tag{37}$$

with *k* being the number of fitting parameters and *L* being the likelihood of the model on histogram. The corrected AIC (*AICc*) was modified by including a correction for small sample size *n* with equation:

$$AICc = AIC + \frac{2k^2 + 2k}{n - k - 1} \tag{38}$$

Alternatively, BIC was used to increase sensitivity on fitting parameters and to avoid overfitting:

$$BIC = k \cdot \ln(n) - 2\ln(L) \tag{39}$$

No FRET (NF) analysis. NF species were selected by applying several filters. First spot stoichiometry filter was applied with [[1, 2], [1, 2]], where partially and completely labelled origami with one/two donors and one/two acceptors were selected. Second, molecules were selected by apparent FRET and donor lifetime with E_{prox} filter [0.2, 0.55] and $\tau_{D(A)}$ filter [2.7, 4.2] ns. Here, the apparent FRET was denoted as proximity ratio which was calculated based on summation of photon counts in ROI as described earlier. Note that Alexa Fluor 594 and Alex Flour 568 were used in donor labelling of DNA origami measured here, with theoretical lifetime of 3.9 ns and 3.6 ns respectively.

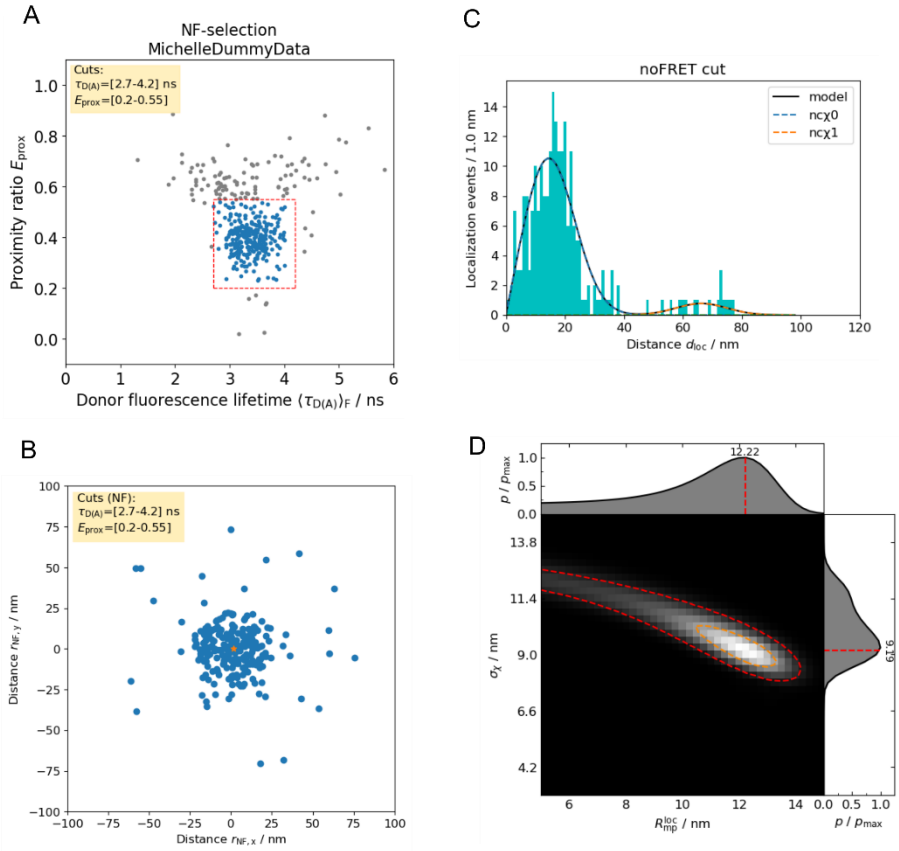

Figure 9. 6 NF analysis. A. 2D scatter plot with threshold settings for NF molecules. B. XY scatter plot of NF pairs with center of dataset (0.36 nm, -1.68 nm). The maximum distance is 100 nm. The center of dataset was presented as yellow star with (x = 0.36 nm, y = -1.68 nm). C. Histogram of NF norm distances with ncχ fitting of two components: *ncχ*0 and ncχ1 shown in blue and orange dashed lines respectively. Bin size is 1 nm. D. Likelihood scan map of *mu*0 (R^{loc}_{mp}) and *sigma*0 (σ_χ). The likelihood was shown in gray colormap.

In Figure 9. 6 A, the proximity versus tau plot with $E_{prox} < 0.2$ were likely caused by fluorescence blue shift due to dyes breakage (118), despite the usage of Trolox as anti-bleaching reagents (119). The filter settings with lower than 0.55 was considered with no FRET events. The scatter spots with larger $\tau_{D(A)} > 4$ ns were caused by aggregations. Afterward, the scatter plot was made by reading *distx* and *disty* from sliced list `slocLst` which has been filtered by above mentioned conditions as NF pairs. These were obtained from previously mentioned localization analysis by subtraction X and Y coordinates from the green (donor) and yellow (acceptor) channels (see Figure 9. 6 B). Same as Figure 9.5 A, the scatter spots presented relative XY positions between the donor and acceptor as $r_{NF, x}$ and $r_{NF, y}$. Averaged coordinates were marked as a yellow star with mean $r_{NF, x}$ = 0.36 nm and mean $r_{NF, y}$ = -1.68 nm. Ideally, the NF pair was calculated to obtain D1A1 distance from a fully labelled DNA molecule D1A1D2A2, which was predicted as ~ 14-15 nm (this is obtained from particle averaging see manuscript (92)). Therefore, the scatters should be distributed symmetrically on circumference with a consistent radius as a result of random orientation. However, the outliers showing norm distances ~ 75 nm can be observed,

which came from miscalculation of origamis labelled with 1 donor and 1 acceptor (D1__A2 or _A1D2_). Apparent FRET calculation was based on photon intensity at each spot position, if the molecules were labelled with only one donor and one acceptor, then D1-A2 (~ 75 nm) distance was calculated and assigned as 'NF' molecules. Similarly, molecules showing norm distances < 10 nm came from __D2A2 molecules. Incomplete fluorophores can be attributed to insufficient labelling of origamis or photobleaching events. The outliers showing distance between 15 nm and 75 nm can be caused by image drifting during data acquisition or defective Gaussian fitting. In summary, drift errors need to be improved on sample fixation on Abberior STED microscope and localization analysis need to be corrected from compiler computation step. Besides, origami molecules can be bent or curved during surface preparation, leading to incorrect localization result.

Next step, norm distances of each pair were calculated and plotted as binned histogram in Figure 9. 6 C and fitted with ncχ (results exported in Table 12). The dominant distribution (*ncx*0) centered at 12.22 nm and the side distribution (*ncx*1) centered at 65.75 nm. The corresponding parameter scan plot for shown in Figure 9. 6 D, with 5 nm to 15 nm for *mu*0 (R^{loc}_{mp}) and 3 nm to 15 nm for the *sig*0 (σ_χ) both in 40 steps. The best likelihood for *mu*0 is at 12.22 nm and for *sig*0 at 9.16 nm. The orange and red ellipses represent the contours of distributions at 60 % pmax and 13.5 % pmax.

Table 12 ncχ fitting results of NF histogram.

Fit statistics		Variables	
fitting method	Nelder-Mead	*bg* A.U.	0 (fixed)
function eval	1797	*mu*0 nm	12.22(init = 60)
data points	1	*A*0 A.U.	211.00 (init = 266.12)
variables	6	*sig*0 nm	9.18 (init = 4.25)
chi-square	14033.89	*mu*1 nm	65.75 (init = 80)
reduced chi-square	14033.89	*A*1 A.U.	16.96 (init = 26.61)
Akaike info crit	21.55	*sig*1 nm	8.76 (init = 2.12)
Bayesian info crit	9.55	*AIC* for custom fit is 248.93	

High FRET (HF) analysis. Potential HF pairs were first selected by applying stoichiometry filter [[1, 2], [1, 2]], that 1 or 2 donors labeled and 1 or 2 acceptors labeled molecules were selected, which was same as before. Differently, molecules were selected with proximity ratio E_{prox} [0.53, 0.9] and donor lifetime $\tau_{D(A)}$ [0.5, 3.5] ns (dashed red box shown in Figure 9.7 A). Here, $\tau_{D(A)}$ < 3.5 ns and E_{prox} > 0.53 was considered as acceptor quenched FRET. The XY coordinates were extracted from `slocLst` for selected molecules. The relative coordinates between green and yellow channels on XY axis of selected spots were plotted in Figure 9. 7 B as $r_{HF,\,x}$ and $r_{HF,\,y}$. Blue colored dots were distributed symmetrically around the center with consistent distances, expected as a result of random orientation. The mean of $r_{HF,\,x}$ and $r_{HF,\,y}$ was plotted as a yellow marker in the center (-1.11 nm, -3.66 nm). Afterward, norm distances were plotted in binned histogram (Figure 9. 7 C) with bin size 3 nm, fitted with ncχ0 and ncχ1 shown in Table 13, which was not robust due to lack of statistics. Nevertheless, parameter scanning was performed for *mu*1 with 3 nm to 13 nm and *sig*1 with 1 nm to 9 nm range, both in 40 steps. In Figure 9. 7 C, the main

distribution (ncx1) was centered at 8.58 nm. In Figure 9. 7 D, the likelihood contour shows the best fit of *mu*1 being 8.58 nm and *sig*1 being 4.34 nm.

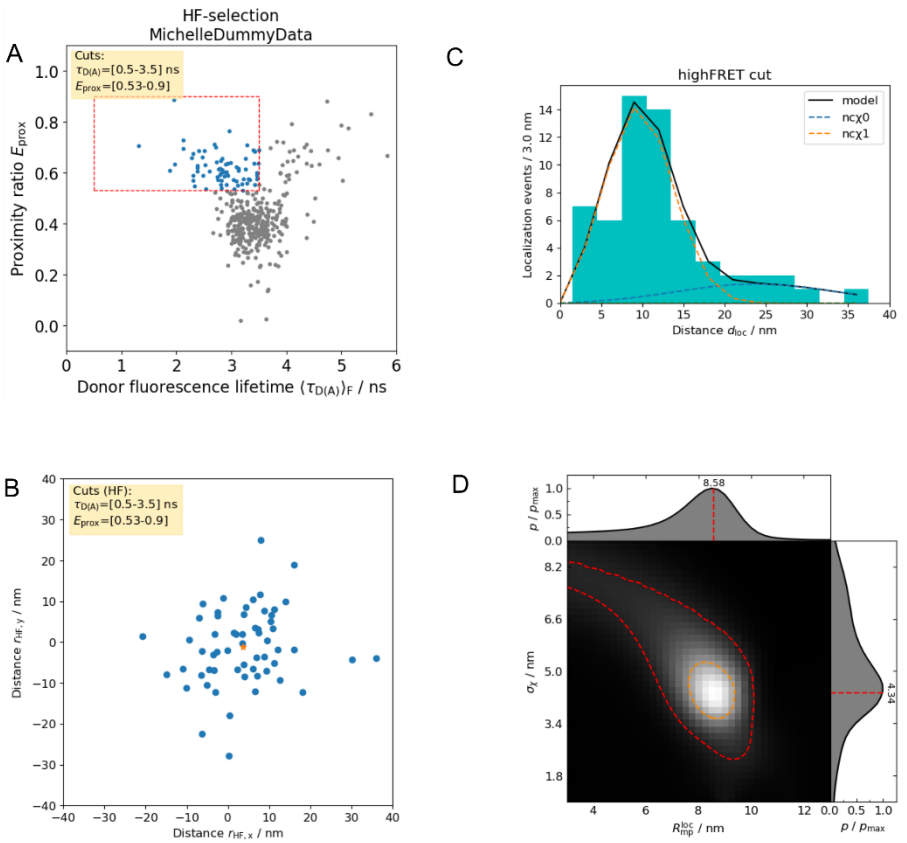

Figure 9. 7 HF analysis. A. Proximity ratio versus donor fluorescence lifetime plot with threshold settings for HF molecules (dashed red box). B. XY scatter plot of selected HF pairs with center of dataset (x = -1.11 nm, y = -3.66 nm). The maximum distance is 40 nm. C. Histogram of HF norm distances fitted with ncχ of two components: ncχ0 and ncχ1 shown in blue and orange dashed line. D. Likelihood scan plot of *mu*1 (R^{loc}_{mp}) and *sigma*1 (σ_χ). The likelihood was shown in gray colormap. HF pair structural prediction is 4.8 nm.

Table 13 ncχ fitting results of HF histogram

Fit statistics		Variables	
fitting method	Nelder-Mead	*bg* A.U.	0 (fixed)
function eval	1347	*mu*0 nm	21.81 (init = 15)
data points	1	*A*0 A.U.	32.98 (init = 26.61)
variables	6	*sig*0 nm	9.90 (init = 2.12)
chi-square	414.61	*mu*1 nm	8.58 (init = 5)
reduced chi-square	414.61	*A*1 A.U.	145.52 (init = 4.26)
Akaike info crit	18.03	*sig*1 nm	4.34 (init = 0.85)
Bayesian info crit	6.03	*AIC* for custom fit is 52.72	

In Figure 9. 7 B, ideally HF population should present a circle with 4.8 nm radius according to structural prediction. However, spots with longer HF distances ~ 20 - 30 nm were observed. This

can be caused by singularly labelled origamis with 1 donor and 1 acceptor from insufficient labelling. Note that both NF and HF were judged by proximity ratio and donor lifetime, which were calculated primarily based on coordinates of each spot. If coordinates were obtained correctly from Gaussian, each spot theoretically contains 4 dyes and will be sorted into D_iA_i pairs from short to long. Only if the 4 dyes were correctly localized NF and HF can be distinguished and sorted in pairs. The calculation bias can be observed with more NF than HF populations, despite origami being evenly labelled with four dyes in 2 pairs. These can be caused by overlook in design of origami spacing. Since the structural prediction for NF and HF were ~ 15 nm and 5 nm respectively, considering of introduced noise, Gaussian fitting can be not robust to distinguish the two populations. Therefore, NF pair should be designed with longer distances such as ~ 40 nm shown in Figure 9.1 A. Besides, the measurement needs to be elongated for larger statistics, since only 346 ROIs were recorded and analyzed.

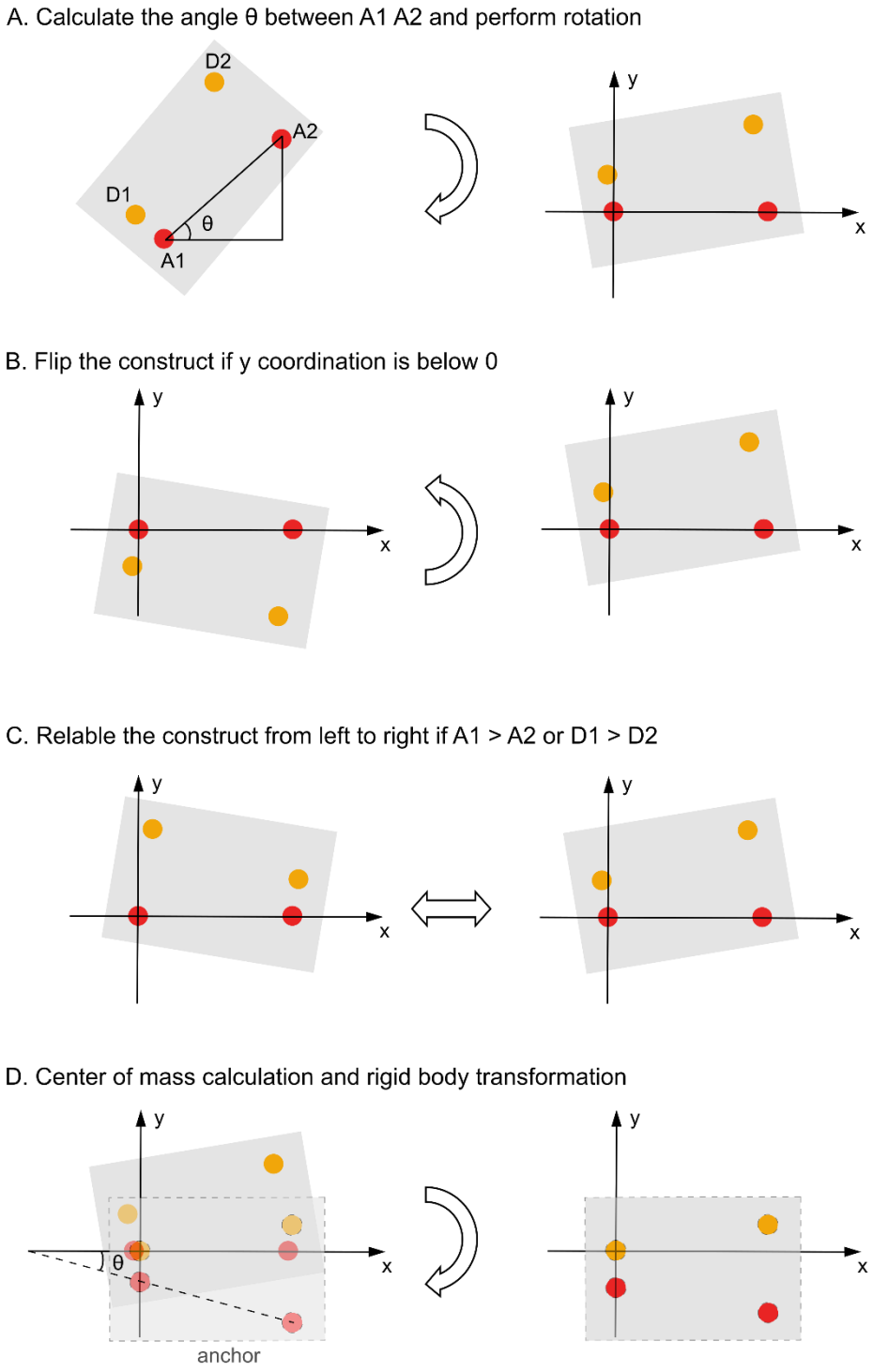

Figure 9. 8 Workflow of particle averaging. A. Calculation of the angle θ between A1 and A2 followed by rotation using A1 as anchor. B. Mirror the construct upside down when the coordinates of D1D2 are below 0. C. Mirror the construct left to right when A1 > A2 or D1 > D2. D. Fine alignment of using model construct as anchor by shift and rotation.

Coarse alignment. The particle averaging function was described in `AlignStructure.py`. It first coarsely aligned fully labelled origamis based on their structure symmetry. First, only constructs fully labelled with 2 donors and 2 acceptors were selected for analysis by applying the stoichiometry filtering [[2], [2]]. The `DADApointset` was assembled by collecting information of D1 D2 A1 A2 from localization result in `locLst`. The donor and acceptor channels were aligned by a shift with displacement between the two channels. Each molecule was first coarsely aligned by `Orient` function. A1 was chosen as an origin (0 nm, 0 nm), and the angle between A1 A2 was calculated by `arctan2` and the structure was rotated by `dot` to lay A2 on x-axis. Next, the structure was mirrored upside down if coordinates of D1 + D2 were below 0. Besides, if A1 > A2 or D1 > D2, the structure was mirrored left to right (see Figure 9. 8 A-B-C). The coarsely aligned result is shown in Figure 9. 9 A.

Fine alignment. For fine alignment, a model with predicted distances was used as an anchor. Specifically, D1 from the model was now used as an origin (0 nm, 0 nm). From the above coarsely aligned structures, mean of coordinates from all points A1 A2 D1 D2 were calculated row by row (axis = 0). The angle between the means of pooled A1 and A2 was calculated and used for rotation. All structures were aligned to the model by a shift on x axis with mean displacement from the model Figure 9. 8 D. The fine aligned result is shown in Figure 9. 9 B. Alternatively, a new anchor can be selected by using each measured pointset as a new model and aligning all other structures, from where the average RMSD (root mean square deviation) can be calculated. As described in `batchRmsd` function, the mass center of the new structure was calculated by `centroid` and alignment was performed by kabsch algorithm (120). The best anchor was selected using the new model with the lowest average RMSD. A threshold of RMSD score (here 50 nm) can be set to filter junk structures (Figure 9. 9 C). The minimal number of structures (`minconstructs` = 30) asked for at least 30 structures of good alignment with RMSD < 50 nm. The best anchor number is printed out in the terminal and should be used as particle averaging in the line showing (`anchorstruct` = 59).

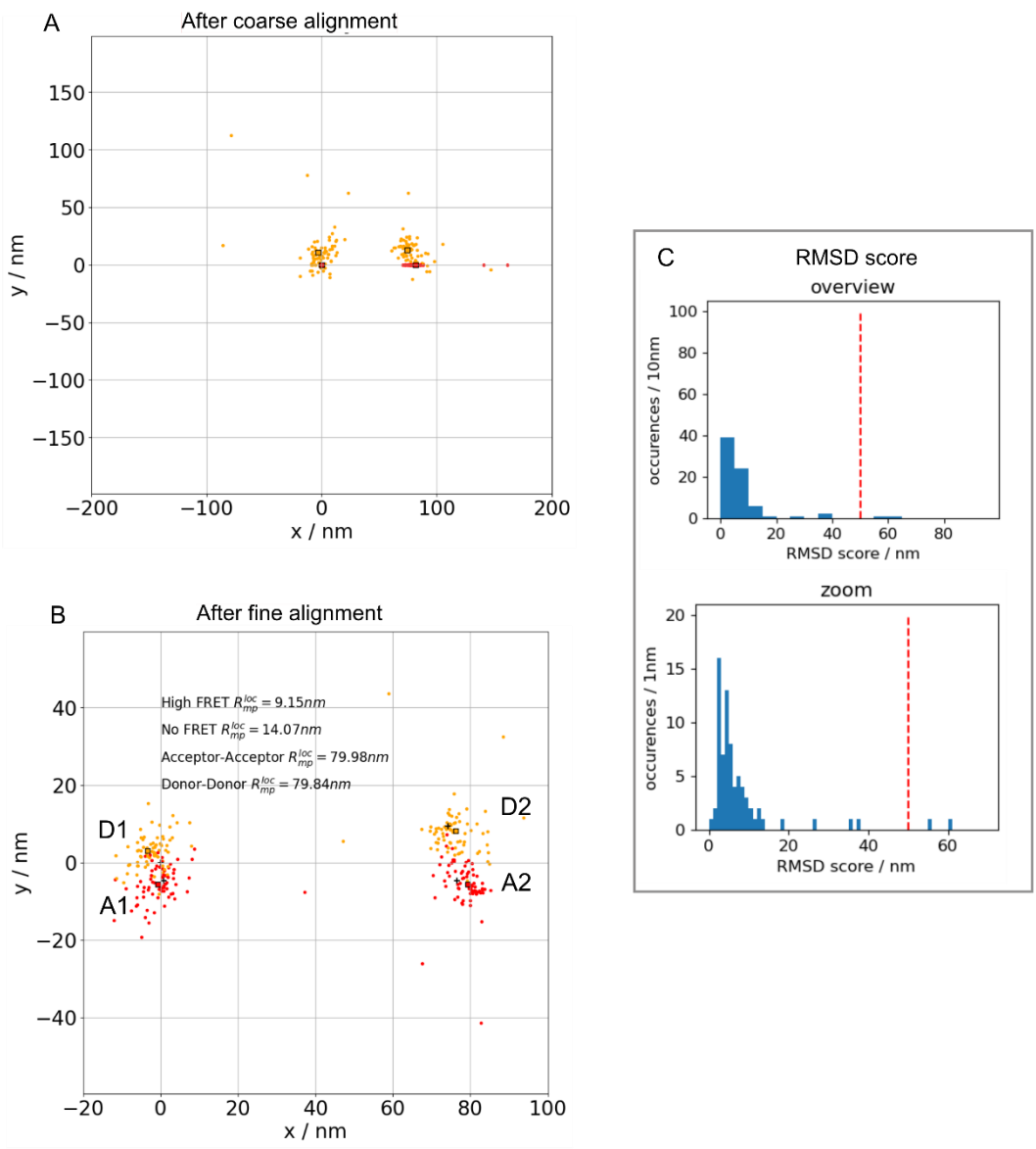

Figure 9. 9 Particle averaging results. A. Coarse alignment of structures. B. Fine alignment of structures with averaged high FRET R^{loc}_{mp} = 9.15 nm, NF R^{loc}_{mp} = 14.07 nm, A-A distance R^{loc}_{mp} = 79.98 nm, D-D distance R^{loc}_{mp} = 79.84 nm. C. Histogram of RMSD scores with 50 nm cutoff (shown as a dashed red line).

9.3 Analysis of bare DNA Origami Platforms with 4 organic fluorophores

The 4 dyes labeled DNA origami with 5 nm spacing of D2A2 (template 1HF) was tested as the positive control (D1D2: Alexa Fluor 568, A1A2: ATTO 647N). The measurement settings were following the standard settings as usual. 341 molecules were analyzed for data analysis and the results are shown in Figure 9. 10.

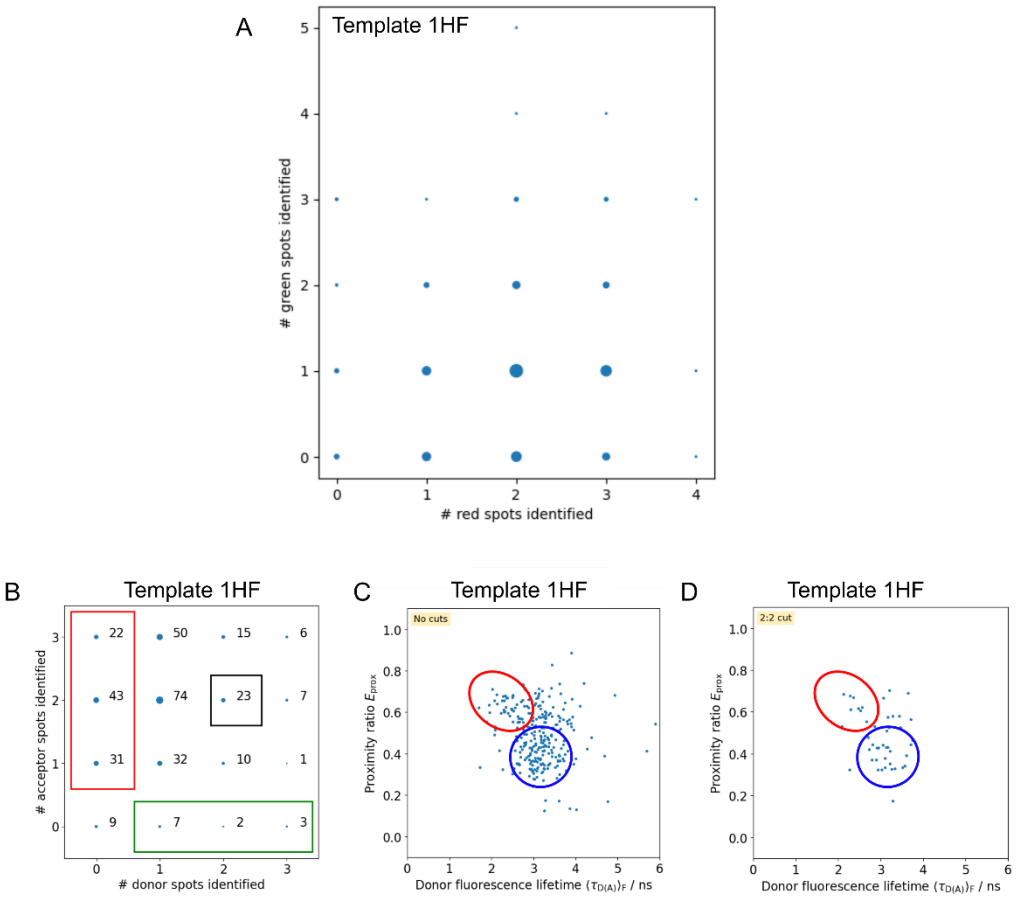

Figure 9. 10 Stoichiometry map and E_{prox} versus $\tau_{D(A)}$ map. A. The overview of identified red and green spots. B. Zoomed stoichiometry map without outliers. The black box shows the completely labelled molecules with 2 donors and 2 acceptors, the red box shows the acceptor only molecules and the green box contains the donor only molecules. C. Proximity ratio E_{prox} versus Donor lifetime $\tau_{D(A)}$ map containing all molecules. D. Proximity ratio E_{prox} versus Donor lifetime $\tau_{D(A)}$ map with 2:2 cut off, containing molecules labelled with 2 red and 2 green fluorophores (23 molecules boxed in black shown in B). The mean lifetime at green (*tauG*), red (*tauR*) and yellow (*tauY*) for the 2:2 cutoff data set is 3.0 ns, 4.2 n, 3.8 ns respectively.

Figure 9. 10 A shows an overview of fitting result with identified donor and acceptor fluorophores shown on Y and X axis respectively. While most localization results are as expected with maximum 3 Gaussians, few outliers shown with 4 or 5 spots can be still observed. Figure 9. 10 B shows the cropped stoichiometry map of ROIs with an ideal 3 x 3 spots matrix, with donor (green)

and acceptor (red) spots showing on X and Y axis respectively. The donor only and acceptor only molecules are boxed in green and red respectively. 23 completely labelled molecules with 2 donors x 2 acceptors are shown in the black box. The most populated species belongs to 1 donor 2 acceptors labelled origami with 74 counts. Overall, localization from the donor channel [7, 3, 2] was not as robust as the acceptor channel [31, 43, 22]. This can be speculated from several aspects: 1) The absolute power of 561 nm laser (~ 8 µW at 100 % software settings) is much lower than that of 641 nm laser (~ 60 µW at 100 % software settings); 2) The signal to noise ratio of detector in green channel is lower than that in red channel; 3) The excitation efficiency of Alexa Fluor 568 by laser line at 561 nm is more compromised than that of ATTO 647N by laser line at 641 nm. 4) The potential FRET quenches donor fluorescence, making Gaussian fitting at green channel less efficient than yellow channel. Figure 9. 10 C and D shows the E_{prox} versus $\tau_{D(A)}$ lifetime map, where two populations HF (red circle) and NF (blue circle) can be identified and used for further data analysis.

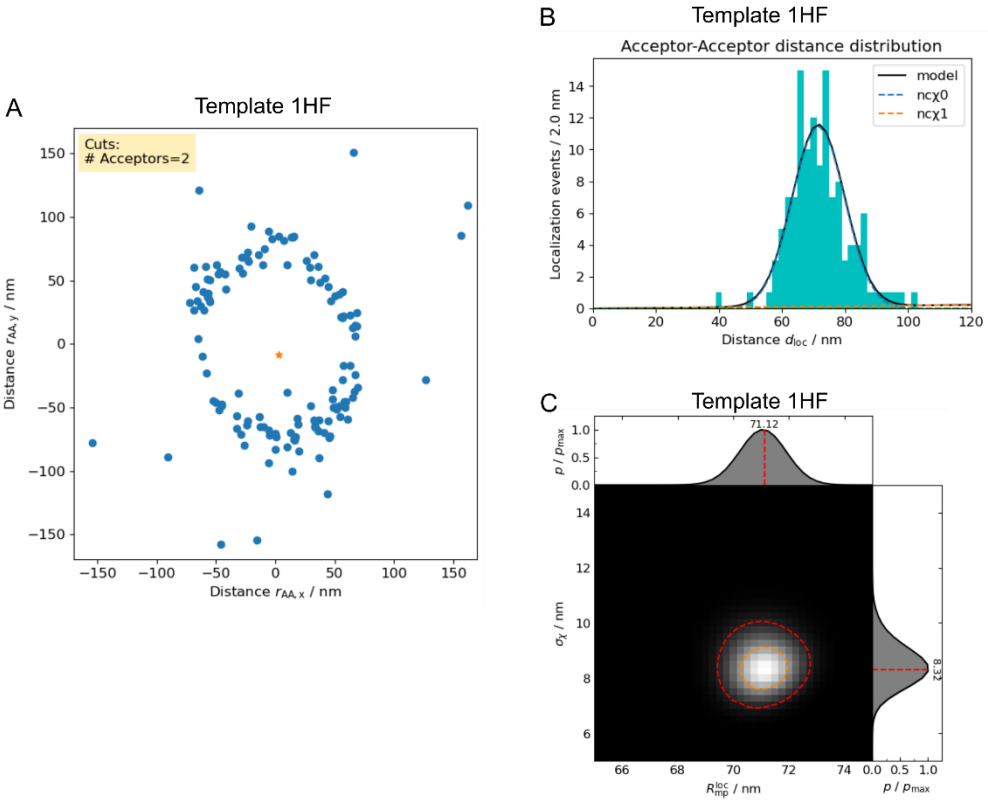

Figure 9. 11 A-A distance analysis. A. XY scatter plot of A-A distances with relative coordinates $r_{AA,x}$ and $r_{AA,y}$. The center of dataset is at (-8.18 nm, -3.05 nm), marked with a yellow star. The maximum distance is 170 nm. B. The norm distance of X Y coordinates from A-A pairs shown in a histogram with a bin size of 2 nm, fitted by nChi with two components ncχ0 and ncχ1shown in blue and orange dashed lines. C. Likelihood scan plot of mu0 ($R^{loc}{}_{mp}$) and sigma0 (σ_χ). The upper to lower boundaries are 65-75 nm for mu0 and 5-15 nm for sigma0 and 40 steps for both. Likelihood is shown in gray colormap. Dished red and orange lines present 0.135 and 0.6 pmax levels respectively.

Figure 9. 11 A shows the relative XY coordinates between two acceptors. The center of the data set is marked at (-8.18, 3.05) nm by taking average of coordinates. The circularly distributed

scatter spots indicate randomly distributed molecules, where dots with norm distance larger than 100 nm belong to two adjacent DNA origami molecules detected in one ROI. Dots with norm distance less than 50 nm belong to incorrect DNA origami folding or incorrect Gaussian fitting during data analysis at step 1. The norm distances from all molecules in Figure 9. 11 A were plotted as binned histogram in Figure 9. 11 B and fitted with two components ncχ. The fitting statistics are shown in Table 14, with 1149 iterations performed using Nelder-Mead method until the minimum. The histogram in Figure 9. 11 B showed a characteristic distribution with mu0 of 71.12 nm and sigma0 of 8.32 nm, which is well matched with the predicted A-A distance of 70.31 nm. Next, a likelihood scan of two parameters was plotted in Figure 9. 11 D, which represents the dependence of fitting quality on changes of sigma0 or mu0. The best fit was shown as the brightest dot at (71.12 nm, 8,32 nm) with confidence level shown in dashed orange/red lines.

Table 14 ncχ fitting results of A-A histogram.

Fit statistics		Variables	
fitting method	Nelder-Mead	*bg* A.U.	0 (fixed)
function eval	1149	*mu*0 nm	71.12 (init = 70)
data points	1	*A*0 A.U.	237.98 (init = 1200)
variables	6	*sig*0 nm	8.32 (init = 15)
chi-square	5139.97	*mu*1 nm	167.00 (init = 105)
reduced chi-square	5139.97	*A*1 A.U.	68.54 (init = 1300)
Akaike info crit	20.54	*sig*1 nm	98.58 (init = 20)
Bayesian info crit	8.54	*AIC* for custom fit is 155.39	

Figure 9. 12 shows the NF and HF analysis. NF pairs were chosen by filters including stoichiometry [[1, 2], [1, 2]], E_{prox} [0.2, 0.55], and τ_G [2.7, 4.2] ns. Molecules were plotted in Figure 9. 12 A, with relative XY distances of each NF pair as $r_{NF,x}$ and $r_{NF,y}$. The calculated data center was at (2.93, -7.57) nm. The circularly distributed points around 40 nm indicate randomly distributed molecules with 40 nm spacing as predicted in Figure 9. 1 (37.66 nm). Molecules with norm distances less than 25 nm or larger than 50 nm were calculation errors introduced by detection or fitting. Norm distances of XY coordinates were plotted as histogram with 2 nm bin size in Figure 9. 12 B, with a fitting result of μ0 = 41.83 nm and σ0 = 8.37 nm (shown in Table 15). Despite of high variance in the dataset, a single peak was fitted with a matching result as prediction, featuring a robust calculation on NF distances.

Figure 9. 12 C shows the scatter plot of XY distances for HF pairs. HF pairs were chosen by filters including stoichiometry [[1, 2], [1, 2]], E_{prox} [0.53, 0.9], and τ_G [0.5, 3.5] ns. The center of the data set is marked at coordinates (-3.27, -3.68) nm. Compared with Figure 9. 12 A, the trend of tighter cluster can be estimated in HF pairs Figure 9. 12 Figure 9. 12C. In Figure 9. 12 D, the distance distribution for HF pairs appears to be shifted towards shorter distances compared to the NF distribution, with fitting results shown in Table 15, indicating potential buried FRET events. However, due to low statistics, a precise measurement of mean value cannot be obtained since only 3 molecules were calculated correctly with 5 nm HF spacing. As discussed in the previous chapter, FRET calculation was based on summation of photon counts from fitted localizations between green and red channels. Based on the facts with well calculated A-A distances and

accommodated NF distances, localizations of A1 A2 D2 were vigorously performed. However, D1 was quenched by FRET, resulting in poor localization and unprecise HF calculation. Besides, the overall donor channel detection needs to be improved from multiple perspectives including sample selection (dyes), microscope alignment (lasers, detectors) and software improvement (fittings etc.).

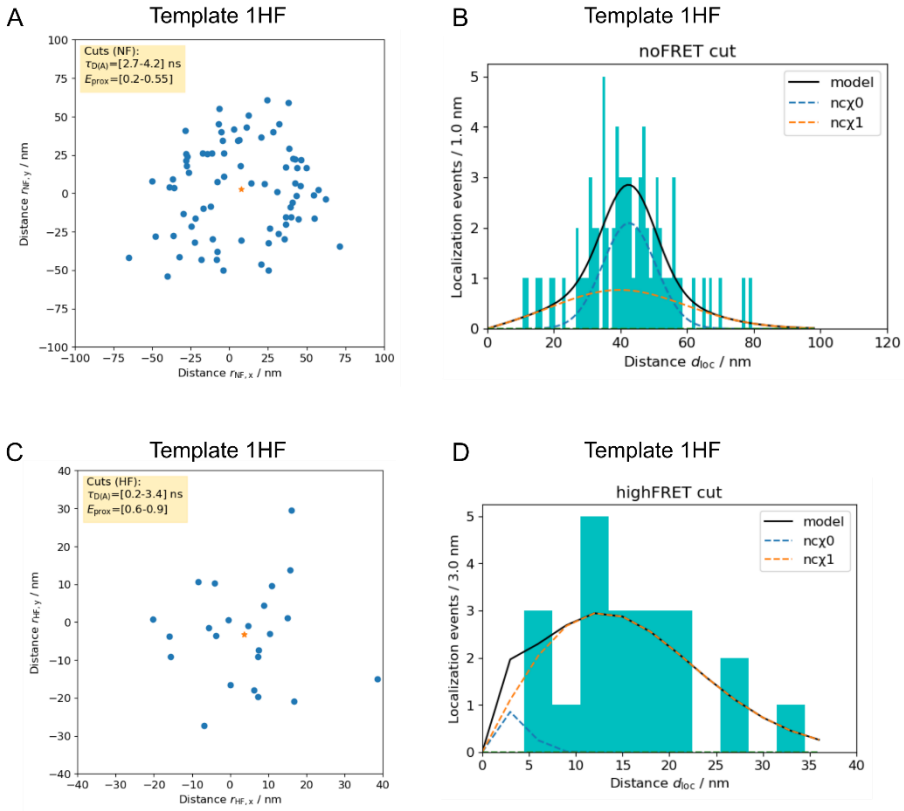

Figure 9. 12 NF and HF analysis. A. XY scatters plot of NF pairs. The center of dataset is (2.93 nm, -7.57 nm) (orange star). The maximum distance is 40 nm. B. Histogram of NF norm distances fitted with ncχ of two components: ncχ0 (blue dashed line) and ncχ1 (orange dashed line). C. XY scatter plot of HF pairs. The center of dataset is (-3.27 nm, -3.68 nm). D. Histogram of HF norm distances with ncχ fitting.

Table 15 ncχ fitting results of NF histogram.

Fit statistics		Variables	
fitting method	Nelder-Mead	*bg* A.U.	0 (fixed)
function eval	1512	*mu*0 nm	41.8051767 (init = 30)
data points	1	*A*0 A.U.	41.7705328 (init = 53.22)
variables	6	*sig*0 nm	8.03229061 (init = 4.25)
chi-square	7000.54	*mu*1 nm	35.1079552 (init = 50)
reduced chi-square	7000.54	*A*1 A.U.	36.2876575 (init = 106.45)
Akaike info crit	20.85	*sig*1 nm	20.5292326 (init = 4.25)
Bayesian info crit	8.85	*AIC* for custom fit is 179.34	

Table 16 ncχ fitting results of HF histogram.

Fit statistics		Variables	
fitting method	Nelder-Mead	*bg* A.U.	0 (fixed)
function eval	1853	*mu*0 nm	7.3453e-04 (init = 4)
data points	1	*A*0 A.U.	3.80786337 (init = 42.58)
variables	6	*sig*0 nm	2.65511557 (init = 1.70)
chi-square	327.73	*mu*1 nm	1.32774825 (init = 6)
reduced chi-square	327.73	*A*1 A.U.	62.4127273 (init = 70.25)
Akaike info crit	17.79	*sig*1 nm	12.7744335 (init = 2.55)
Bayesian info crit	5.79	*AIC* for custom fit is 48.21	

9.4 Analysis of protein functionalized DNA Origami Platforms with fluorophores labeled CD95

CD95-biotin labeled with ATTO-594 and ATTO-643 were unselectively conjugated on streptavidin/DNA origami (D1A1: Atto-594 and ATTO-647N). Depending on the degree of labeling, the platform can be labeled with multiple fluorophores per molecule (each streptavidin bound on one side with the biotin anchor on DNA origami, on the other side with 2 binding sites effectively available for CD95-biotin-fluorophore). Note that two biotins were placed 10 nm away from each other (template 2). In total 3959 ROIs were recorded and analyzed.

Figure 9. 13 A shows the stoichiometry map of the Gaussian fitting result. With the number of donor spots shown on X axis and acceptor spots on Y axis. The most populated molecules were labelled with 1 donor 1 acceptor with 1023 molecules identified. The second most pronounced molecules were labelled with 1 donor 2 acceptors with 605 counts. Completely labelled species with 2 donors x 2 acceptors were detected with 222 counts. The green box shows donor only molecules and red box shows acceptor only molecules with 525 molecules labelled with single acceptor without donor. 153 molecules at 0 x 0 spots indicates failed Gaussians fitting on ROI images due to too much noise or lost focus. Overall speaking, despite large statistics available, the percentage of 2 x 2 spots were not satisfactory, suggesting a low efficiency of biotin/streptavidin/biotin sandwich complexation or N-terminus labelling of dyes. Another reason is that the CD95-ATTO-X/streptavidin/Origami complex was conjugated sufficiently, however, due to the large size of CD95 (~ 8 nm in length and ~ 2 nm in width) (13), N-terminus labelled dyes were placed far away from each other. Therefore, the spacing between two biotins needs to be calculated carefully so the potential CD95 dimer formation is not limited by flexibility. Besides, due to the high amount of failed Gaussian fittings, except for expected improvement on the analysis code, sample imaging workflow needs to be stabilized with less focus lost.

Figure 9. 13 B shows corresponding E_{prox} versus $\tau_{D(A)}$ map with mostly only NF population detected circled in blue curve. Only a few events were identified as HF events circled in red. 2:2 cuts shown in Figure 9. 13 C further confirms no FRET occurs in the detected spots. Since enough statistics were recorded, one cannot criticize just calculation errors from data analysis step. The

absence of HF events suggests potentially no FRET between labelled CD95, namely CD95 exists as parallel configurations instead of anti-parallel configurations. With 10 nm spacing of two parallel monomers, no FRET should occur. Another consideration is that should anti-parallel configuration exist, the biotin linker must provide flexibility for protein-protein interactions. Cares must be taken on linker selection so that it won't introduce extra localization deviations. To validate this, one should use a well characterized dimer protein such as CTLA4 as a positive control, such that no HF events do not come from system flaws.

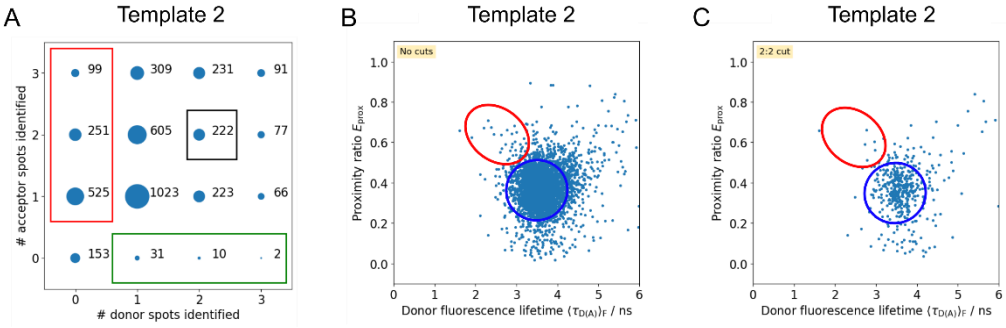

Figure 9. 13 Stoichiometry map and E_{prox} versus $\tau_{D(A)}$ map. A. Zoomed stoichiometry map without outliers. Black box shows the 2 x 2 spots, red box contains the acceptor only spots, green box contains the donor only spots. B. Proximity ratio E_{prox} versus Donor lifetime $\tau_{D(A)}$ map containing all molecules from A. The mean lifetime at green (*tauG*), red (*tauR*) and yellow (*tauY*) for the dataset is 3.7 ns, 4.3 ns, 4.0 ns respectively. C. Proximity ratio E_{prox} versus Donor lifetime $\tau_{D(A)}$ map with 2 donors and 2 acceptors cut off. The mean lifetime at green (*tauG*), red (*tauR*) and yellow (*tauY*) for the sub-dataset is 3.7 ns, 4.5 ns, 4.0 ns respectively.

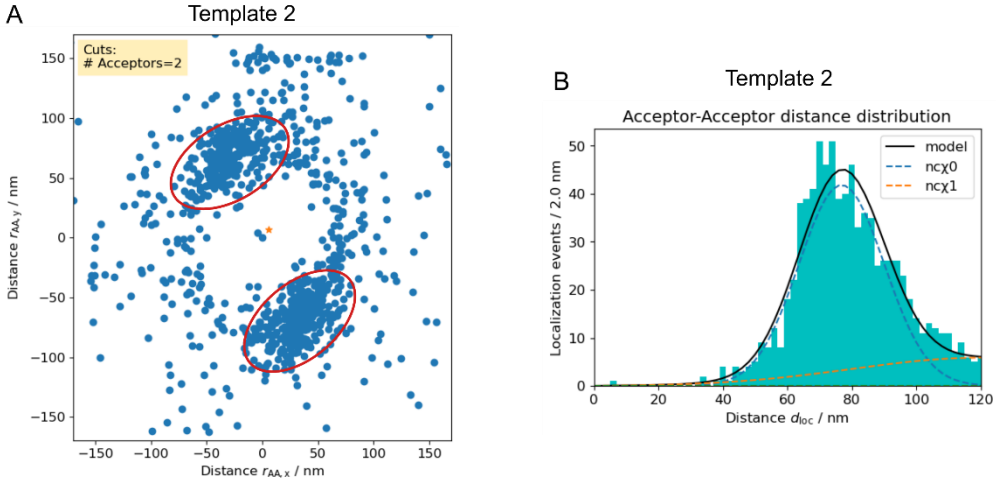

Figure 9. 14 shows the measured A-A distances, with relative XY distances plotted as scatter spots in

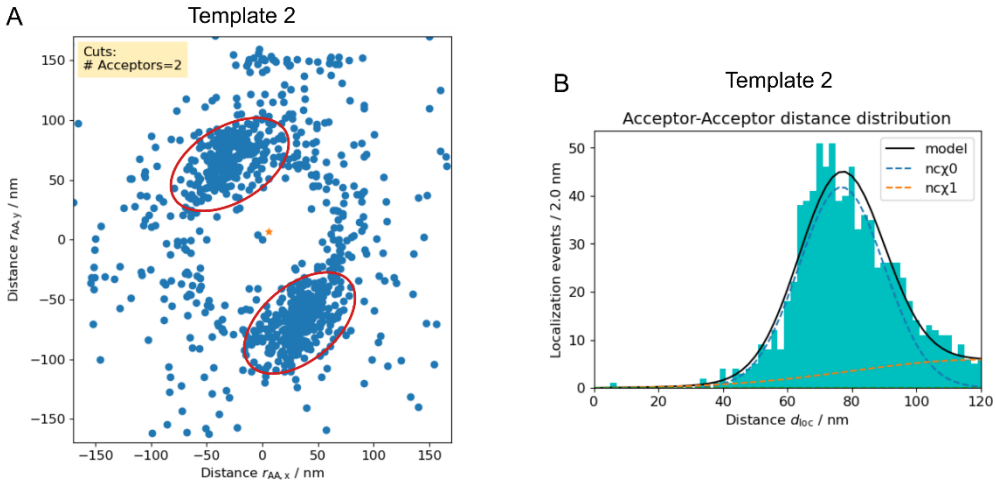

Figure 9. 14 A. While the whole dataset shows a trend of circular distribution, some populations were concentrated obliquely on an axis deviated from y axis with ~ 30 degrees to the left (shown in red circles). The norm distances were fitted with two components using two ncχ shown in

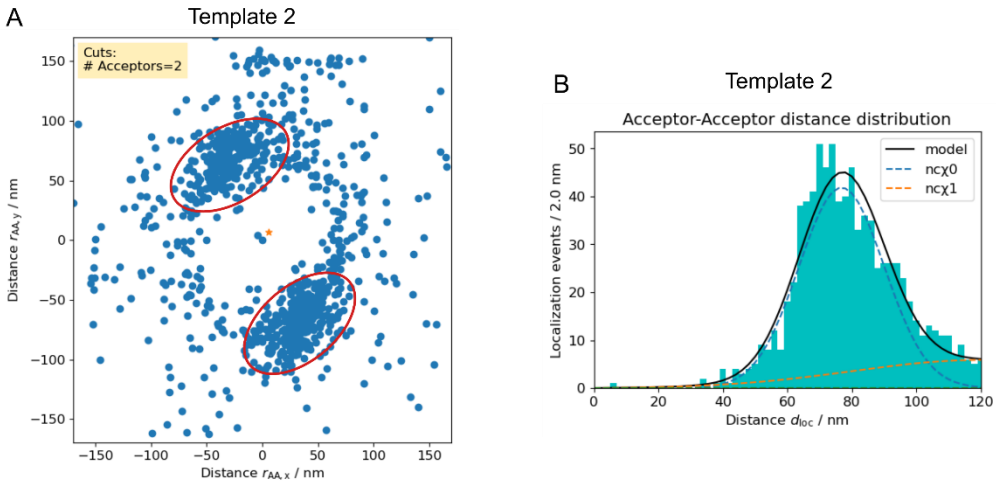

Figure 9. 14 B, with fitting result showing in Table 17. The measured mu0 was at 75.7 nm with sigma0 of 13.3 nm, which is in accordance with predicted value of 70.31 nm. This verified correct labelling of acceptor dyes as well as their localizations. Since the skewness of circular distribution wasn't observed from the dummy dataset, which was measured years before. This bias could come from microscope alignment rather than data analysis, where the detectors are placed in a specific angle that is favored for photons with specific orientation. However, one needs to scrutinize it carefully.

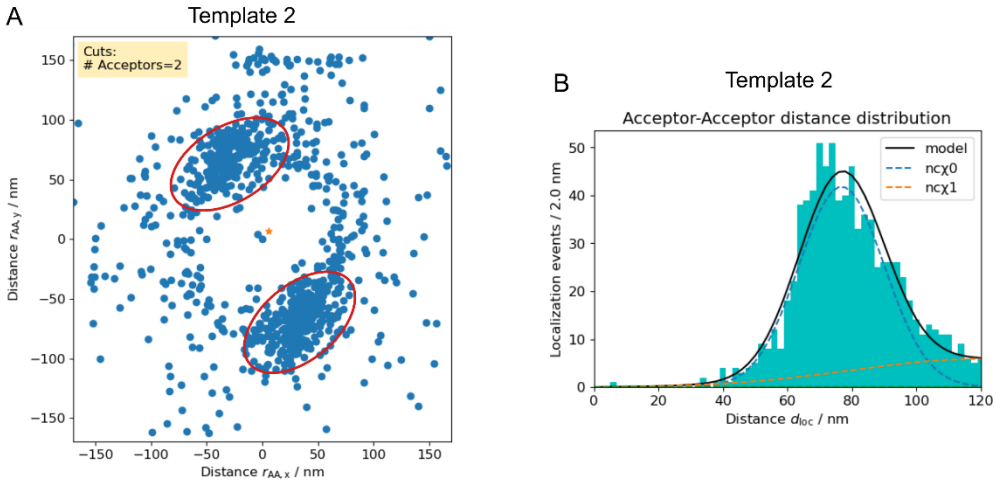

Figure 9. 14 A-A distance analysis. A. XY scatter plot of A-A distances with the center of dataset at (-6.50 nm, -5.72 nm), marked with a yellow star. The maximum distance is 170 nm. B. The norm distance of A-A pairs shown in a histogram with a bin size of 2 nm. nChi fits with two components ncχ0 (blue) and ncχ1 (orange) were shown with dashed lines.

Table 17 ncχ fitting results of A-A histogram.

Fit statistics		Variables	
fitting method	Nelder-Mead	*bg* A.U.	0 (fixed)
function eval	562	*mu*0 nm	75.70 (init = 79)
data points	1	*A*0 A.U.	1388.05 (init = 1200)
variables	6	*sig*0 nm	13.34 (init = 15)
chi-square	33147.37	*mu*1 nm	113.54 (init = 105)
reduced chi-square	33147.37	*A*1 A.U.	587.23 (init = 1000)
Akaike info crit	22.41	*sig*1 nm	41.29 (init = 15)
Bayesian info crit	10.41	*AIC* for custom fit is 376.13	

Due to the absence of HF events, only NF pairs were analyzed in this part. Figure 9. 15 shows the measured NF distances. With relative XY distances plotted as scatters in Figure 9. 15 A, where the data set shows a nice hallow circular shape with norm distance as predicted. The norm distances were fitted with two components using two ncχ shown in Figure 9. 15 B, where the main distribution is shown in ncχ1 with another component contributed to shorter distances. The fitting result is shown in Table 18, with measured mu1 at 39.4 nm and sigma1 at 6.8 nm. This is in line with the predicted value of 37.66 nm in Figure 9. 1. The shorter distances measured 20 nm might be caused by curled origami sheet, where the D1 A1 distances were shortened. The NF analysis verified correct labelling and localization of D1 A1. Together with A-A distances analysis, the results shown here demonstrate the completeness of DNA origami with D1 A1 A2 correctly labelled. The lack of FRET events possibly was due to parallel CD95 configurations in vitro, suggesting a monomeric CD95 at picomolar concentration, which is in line with STED imaging of membrane CD95 on Hela WT with only diffraction limited spots detected (Chapter 8.1). However, as mentioned earlier, a positive control of dimers showing HF must be performed to validate the system.

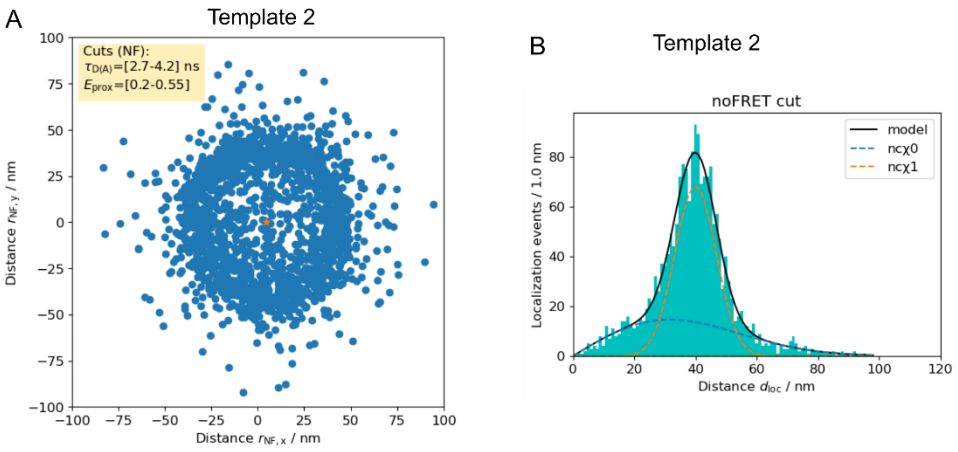

Figure 9. 15 NF analysis. A. XY scatter plot of NF pairs. The center of dataset is (-3.27 nm, -3.68 nm) (orange star). The maximum distance is 100 nm. B. Histogram of NF norm distances with ncχ fitting of two components: ncχ0 (blue dashed line) and ncχ1 (orange dashed line).

Table 18 ncχ fitting results of NF histogram.

Fit statistics		Variables	
fitting method	Nelder-Mead	*bg* A.U.	0 (fixed)
function eval	954	*mu*0 nm	22.56 (init = 35)
data points	1	*A*0 A.U.	729.18 (init = 266.12)
variables	6	*sig*0 nm	25.77 (init = 4.25)
chi-square	53291.87	*mu*1 nm	39.46 (init = 72)
reduced chi-square	53291.87	*A*1 A.U.	1152.27 (init = 26.61)
Akaike info crit	22.88	*sig*1 nm	6.80 (init = 2.12)
Bayesian info crit	10.88	*AIC* for custom fit is 473.70	

V Conclusion & Perspective

10 CD95L Dependent Activation of the CD95 Signaling Pathway

Conclusion of this work. CD95/CD95L signaling pathway plays an important role in apoptosis signaling interpretation. However, the stoichiometry of membrane CD95 as well as their spacing information have not been solved yet. To this end, I designed engineered CD95L using IZ trimerization domain and aimed at interpreting apoptosis initiation from macro to micro perspectives using different CD95L variants. First, I successfully established a lab-based protocol of efficient purification of IZ-CD95L using a 10-layer cell factory. I used an adherent cell line HEK293T cells for secretory protein expression with transient transfection. Due to the extensive usage of transfection reagent, PEI was used. By using anti-His tag mAb coupled agarose beads, his-tagged protein can be purified with a final yield of 350 µg per 1 L culture medium. This makes the downflow modification and application in biomedical or biotechnological assays possible. The purified His-IZ-CD95L was further modified with his tag cleavage and biotinylation. The biological activity of purified IZ-CD95L was tested by apoptosis dynamics assay, where conditioned ligands at varying concentrations were applied on Hela WT cells overnight and supervised by IX83 microscope with phase contrast mode. In this study, I used IZ trimerization domain for enhancing biological activity of CD95L. This domain has been used before for soluble CD95L (50,108) and TRAIL before (121). To compare the cytotoxicity of IZ-CD95L and soluble CD95L, I used commercially available Flag-CD95L (Enzo) as a control to make systematic comparison.

To this end, I probed the cytotoxicity of CD95L variants: His-IZ-CD95L, biotin-IZ-CD95L, Flag-CD95L and Flag-CD95L crosslinked with anti-Flag mAb, at different concentrations using apoptosis dynamics measurements. The ligand variants were analyzed to test the concentration dependence of IZ-CD95L on Hela WT cell line, where at 20 ng/ml IZ-CD95L there is no significant cytotoxicity but at 200 ng/ml cells can be killed with a maximum apoptosis ratio of 30 %. By comparison with Flag-CD95 (Enzo), we noticed that at 200 ng/ml, the cytotoxicity of Flag-CD95 (Enzo) does not differ significantly from X-IZ-CD95L but at 1000 ng/ml the difference can be resolved. Afterward, I used biochemical methods to probe the binding affinity of X-CD95L with CD95 by blue native PAGE or surface plasmon resonance measurements. The result shows that IZ-CD95L binds more efficiently with CD95 and the binding affinity between IZ-CD95L/CD95 is 10 times higher than Flag-CD95 (Enzo)/CD95.

Next, considering X-CD95L at 200 ng/ml is sufficiently high enough for triggering apoptosis signaling, I incubated conditioned ligands at this concentration with Hela WT cells for STED imaging and data analysis. I improved staining efficiency by using urea as antigen retrieval reagent and overnight incubation with primary antibody at 4°C. The staining fixed cell sample were measured by Abberior STED microscope and analyzed by customer-written software Ani. From STED staining result, I draw the conclusion that only diffraction limited spots were detected. Which is in accordance with the result of previous work in our group (31). The previously proposed large hexagon network can be excluded from our model (15). By using only

Hela WT staining without ligands incubation as control, it can be inferred that CD95 exists as predominant monomer/dimers. After ligands incubation, it can be inferred that CD95 form dimers/trimers but not higher oligomers.

Limitation of this work. In this study, I mainly used STED imaging for oligomer study of purified IZ-CD95L with CD95 on Hela WT. Care needs to be taken that, IZ-CD95L should be tested by various CD95-sensitive cells such as Jurkat cell line. Besides, I tested IZ-CD95L staining for Hela WT cells under the conditions of 200 ng/ml for 2 h based on the speculation that it's sufficient time for signaling initiation. Different concentrations and incubation time should be tested to have a more comprehensive understanding. For STED staining, I assume Hela WT without ligands incubation staining result as a speculative monomer control based on the previous study of the group (31). To be more strictly speaking, real biological samples such as monomer CD86 staining should be performed as true monomer control. Second, data analysis of STED results largely depends on microscope alignment and threshold settings in softwares. Therefore, for comparable analysis of different experiments, care must be taken to repeat the microscope and threshold settings as much as possible. Besides, in SPR measurement, the surface passivation method differs from IZ-CD95L and Flag-CD95L (Enzo), CD95-His-biotin was first immobilized on Ni-NTA surface chip and then Flag-CD95L (Enzo) was incubated. However, due to the unknown cleavage ratio of IZ-CD95L from His-IZ-CD95L, I did not use Ni-NTA chip to prevent unwanted binding from chip itself. Therefore CD95-His-biotin was secondly immobilized in streptavidin surface. System errors could occur from two different immobilizations. This experiment needs to be repeated for a more robust comparison between two chips.

Perspectives. In this work, I successfully tested the IZ fusion for stabilizing CD95L and corresponding apoptosis initiation effects. Other stabilizing methods such as TNF tag fusion and DNA origami fusion can be further applied for both in vitro biological assays, signaling pathway studies or structural studies. However, some studies have reported that CD95/CD95L pathway showed lethal effect in vivo tests (122,123). This makes it difficult to apply CD95 as cancer therapy. Other death-inducing ligand members in TNFSF family such as TNF or LTα also have been reported with toxicity in vivo. However, a high potential candidate TRAIL has been recently well studied. IZ fusion or TNC fusion has been applied to enhance TRAIL stability and cytotoxicity both in vitro and in vivo (48,124). What is more interesting is the coadministration of TRAIL and DR5 agonist showed promising results (125). This is possibly caused by antibody stabilized TRAIL/DR5 oligomerization in the recently reviewed paper (15). This raised the interest of studying TRAIL signaling pathway DR4/DR5 as well as validation of the proposed signaling model.

11 DNA Origami Platforms to Study Single Molecule Dynamics

Conclusion of this work. As an interesting member in TNFSF/TNFRSF family, CD95/CD95L signaling pathway has been recently studied. CD95 was previously considered to form anti-parallel dimer as an inactivate state. Upon binding with CD95L, CD95 form parallel trimers (15). However, the spacing between two monomers of the dimer or trimer has not been solved yet. Besides, this model has not been proved by experimental data yet. To achieve this goal, CD95 was engineered with biotin and FRET dyes. I used DNA origami as nano platform to anchor CD95 protein and measured the distance by FRET signal on Abberior STED microscope. In this work, I designed, purified and modified CD95 receptor protein with extra cellular domain to be immobilized on DNA origami. I successfully expressed the CD95-biotin-His by co-transformation of BirA plasmid and CD95 plasmid in *E.coli* cell line. In vivo biotinylation was achieved by BirA enzymatic catalysis. CD95 ECD was purified by Ni-NTA column using NGC purification system under denatured conditions with 8 M urea. The denatured protein was renatured by combination of rapid dilution and stepwise dialysis. His tag was cleaved afterward and CD95 was labelled with ATTO594/ATTO643 dyes separately. Two variants of CD95: CD95-biotin and CD95-sbp were produced. Due to the low binding affinity of CD95-sbp with streptavidin, CD95-biotin was used for further experiments.

I performed STED/FRET nanoscopy imaging of CD95/streptavidin/DNA origami. Two types of origami were provided. The first template was labelled with two fluorophores (a pseudo-FRET pair with ～ 30 nm spacing) and two biotins for CD95/streptavidin coupling (blank template, negative control). As a positive control, the second template was labelled with two FRET pairs (one pseudo-FRET pair with ～ 30 nm spacing and FRET pair with ～ 5 nm spacing) were tested for probing CD95 distances. I successfully measured the two templates using an adapted sample preparation protocol. In my case, I used poly-L-lysin for non-specific surface passivation in a flow chamber. By employing FRET nanoscopy code for data analysis, no FRET and high FRET were both calculated as expected. My goal is to use the two templates for improving current sample preparation, data acquisition and data analysis. This will help with interpreting unknown FRET signal from labelled CD95 immobilized on DNA origami.

To this end, samples of CD95-ATTO594(643)/streptavidin/DNA origami with two FRET pairs (one pseudo-FRET pair and unknown FRET pair) were tested for probing CD95 distances (Chapter 9.4). So far, no FRET signal was detected from established FRET/STED imaging protocol (Figure 9.13). There are some possible reasons: 1. From the imaging perspective: As the state-of-the-art nanoscopy imaging technique, STED/FRET imaging can be challenging. The customerized Abberior STED microscope was used, with two excitation lasers at 561/640 nm. The laser line at 561 nm has 10 times lower power than the laser at 640 nm even at 100 % settings, making it difficult to measure single fluorophore on origami molecules. 2. From the sample preparation perspective: CD95 was expressed from *E.coli* as inclusion bodies, meaning that this protein has intrinsic instability. Besides, this protein was labelled with N-terminus labeling with pH controlled under 7. The efficiency of the labeling reaction was not high enough for origami imaging. 3. From the data analysis perspective: The Gaussian fittings in FRET nanoscopy code were not robust enough, especially when origami was labelled with CD95 containing multiple

fluorophores. If the fitting works not well, positions of CD95 spots cannot be found, and the following FRET calculations can be estimated wrongly lower than the true signal of CD95.

Perspectives. In the future, I will work on the test of FRET nanoscopy analysis code and improve the robustness of it. For example, data simulations of single images can be made and to be tested by snippets of the data analysis code. First, the Gaussian fitting must be improved to find the correct local maximum, that's to say, to find the correct position of CD95 molecules. Second, care should be taken for Abberior STED microscopy maintenance for correct alignment and data acquisition. For improving data quality, DNA origami needs to be prepared with better labeling chemistry so that CD95 can be anchored with single labeling for high specificity. Single molecule studies have been in recent years explored as benchmark tool (126) for protein-protein interaction, protein dynamics or protein structural studies. Therefore, to explore the CD95 dimers interaction with nanoscale resolution, except for FRET nanoscopy, smFRET measurement should also be performed to provide supplementary information for protein interaction measurement.

Supplementary Information

Table S1. Antibodies information and catalog numbers and manufactures

	Manufacturer	Catalog number	Clone	Host	Stock Concentration
anti-CD95	Biotium	BNUB0305-100	B-R18	Mouse anti-human	0.2 mg/ml
anti-CD95	Invitrogen	MA5-32489	JJ0942	Rabbit anti-human	1 mg/ml
anti-CD95	SantaCruz	Sc8009	B-10	Mouse anti-human	0.2 mg/ml
Anti-CD95	miltenyibiotec	130-108-066	DX2	Mouse anti-human	1 mg/ml
anti-CD95L	Abnova	H00000356-M02	2G9-G8	mouse anti-human	1 mg/ml
anti-CD95L	Abcam	Ab134401	polyclonal	rabbit anti-human	1 mg/ml
anti-CD95L	SantaCruz	sc-19681	NOK-1	Mouse anti-human	200 µg/ml
Abberior Star Orange	Abberior	STRANGE-1002-500UG	Polyclonal	Goat anti-rabbit	1 mg/ml
Abberior Star Red	Abberior	STRED-1001-500UG	polyclonal	Goat anti-mouse	1 mg/ml
Anti-rabbit IgG, HRP-linked	Cell Signaling Technology	7074S	Polyclonal	Goat Anti-rabbit	60 µg/ml
Anti-mouse IgG, HRP-linked	Cell Signaling Technology	7076S	polyclonal	Goat Anti-rabbit	184 µg/ml

Photons gating workflow using AnI-32F_12.07.2021_GPU

1. Import ptu file: options --Select Setup -- TCSPC data/rasterscanning
2. Load ptu file: Folder symbol -> choose ptu.file -> "Get parameters from file"
-> select STED microscope, PQ PTU -> Set Line Steps

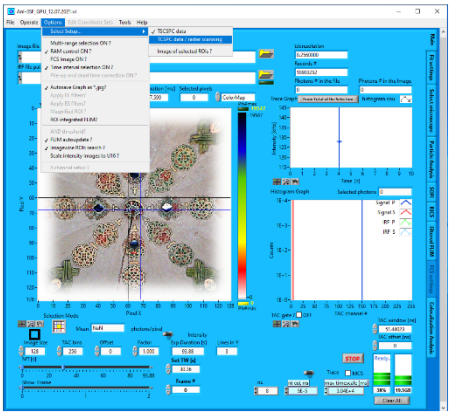

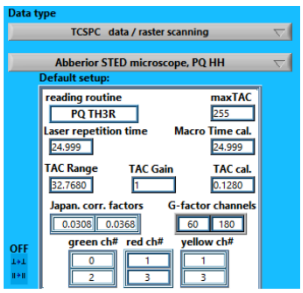

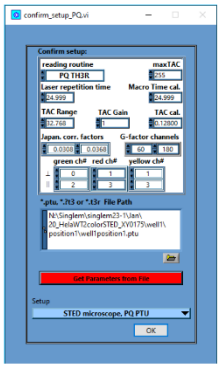

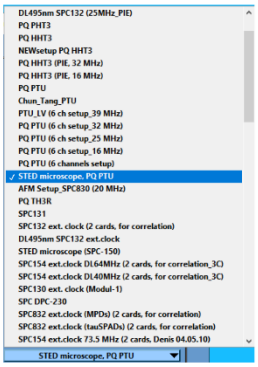

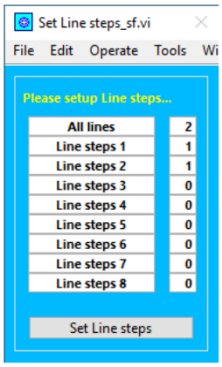

3. Main channel: Select ptu file -> Accept
4. Main channel: TAC gate on -> TAC gate channel: 25 to 150 -> increase region of interest

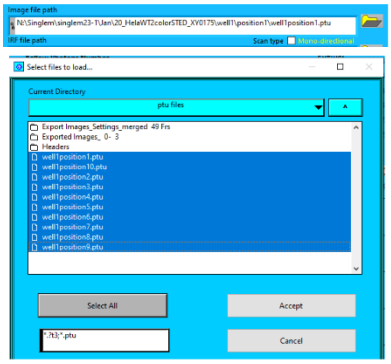

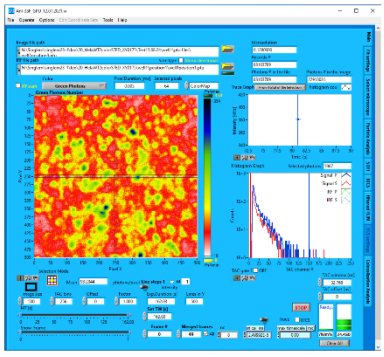

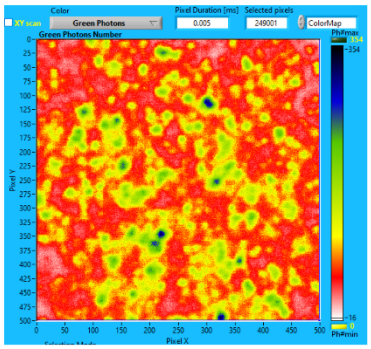

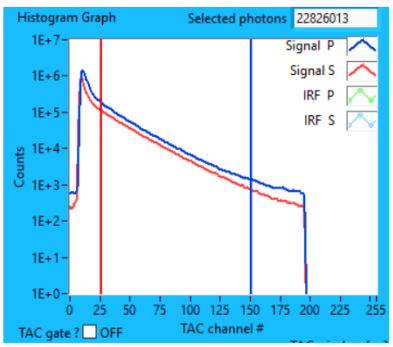

5. Main channel : Import all ptu files: File -> Export -> All color images in batch -> check TAC gate channel: 25 to 150 -> Accept -> Select All -> Accept

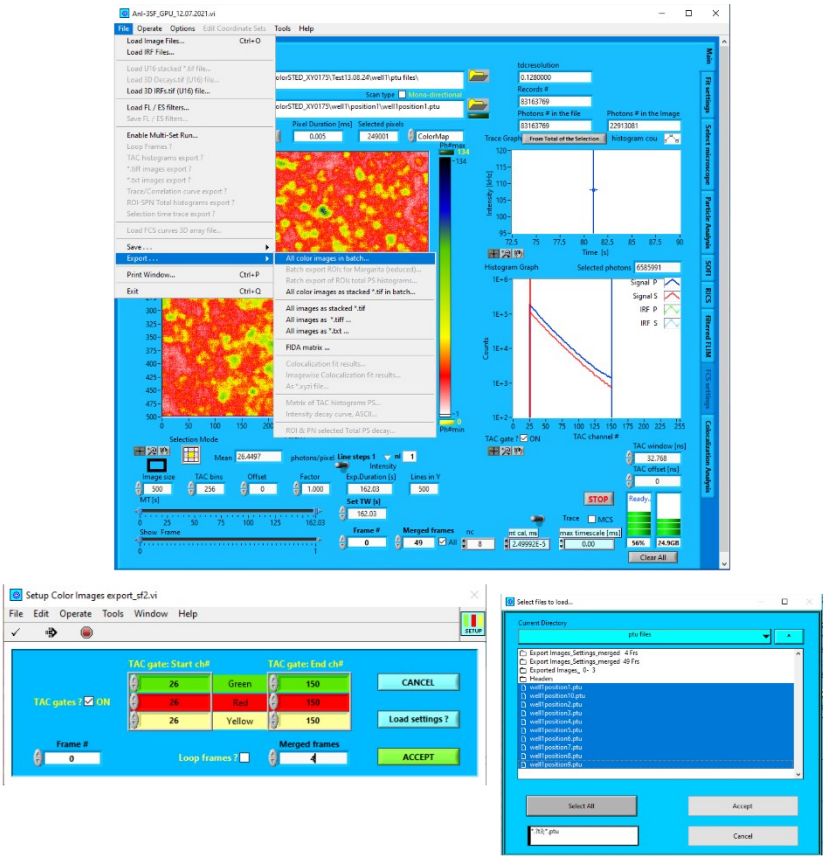

6. Example images of before and after gating

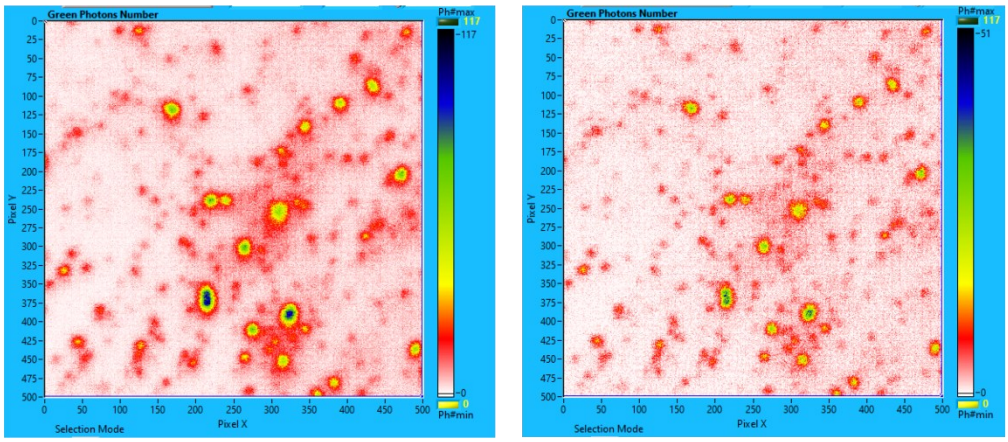

Figure S 1. Workflow of batch-wise photon gating using custom-written software Ani.

Spot size analysis using Hyugens Professional

1. Load .tif files of photon gated image from Ani -- i) Drag and drop files into Huygens software main user interface
ii) Right click Add image -- Open -- select file

2. Set microscopic parameters -- right click image -- microscopic parameters -- Load template for different channels

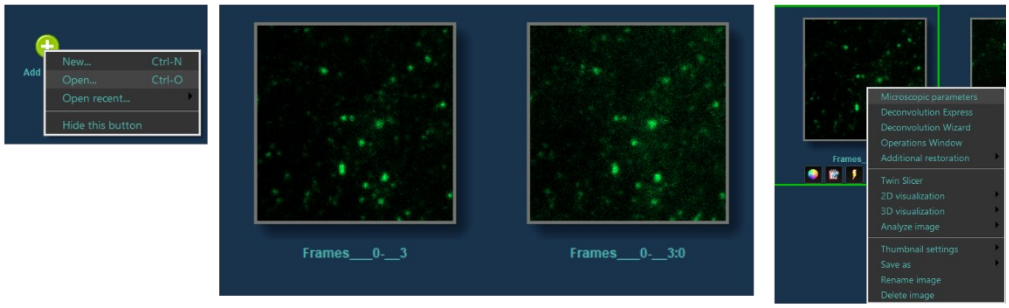

3. Set microscopic parameters for 561 nm and 640 nm channels -- set general parameters and channel parameters

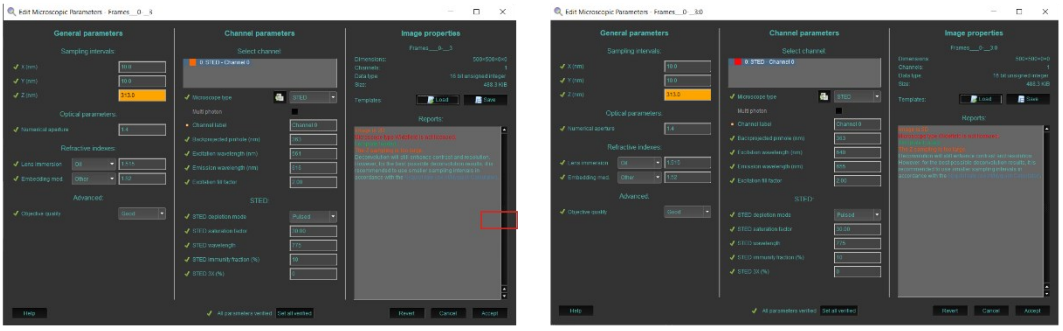

4. i) Join donor and acceptor channels -- Tools -- Join images --
ii) Deconvolution: Deconvolution Wizard -- Use deconvolution template -- Load or make a template

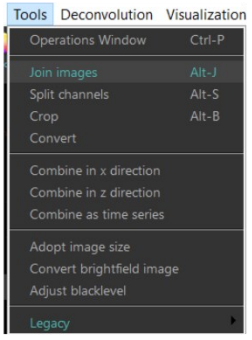

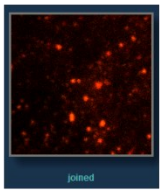

Merged channel

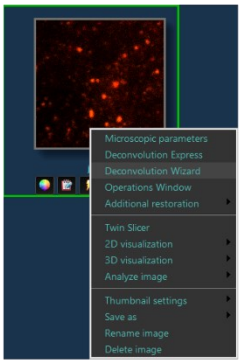

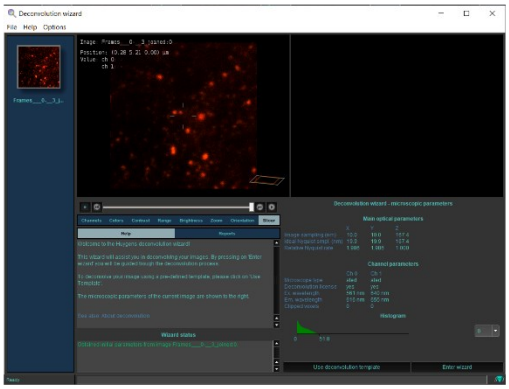

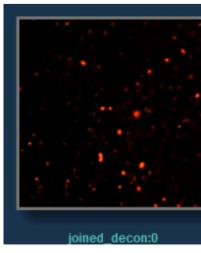

Deconvolved image

5. Object analysis: right click image -- Analyze image -- Object Analyzer -- Workflow Designer -- Load or make an template -- Verofy all -- Execute Window -- this will export/save an CSV file of result all spots analysis (size, position...)

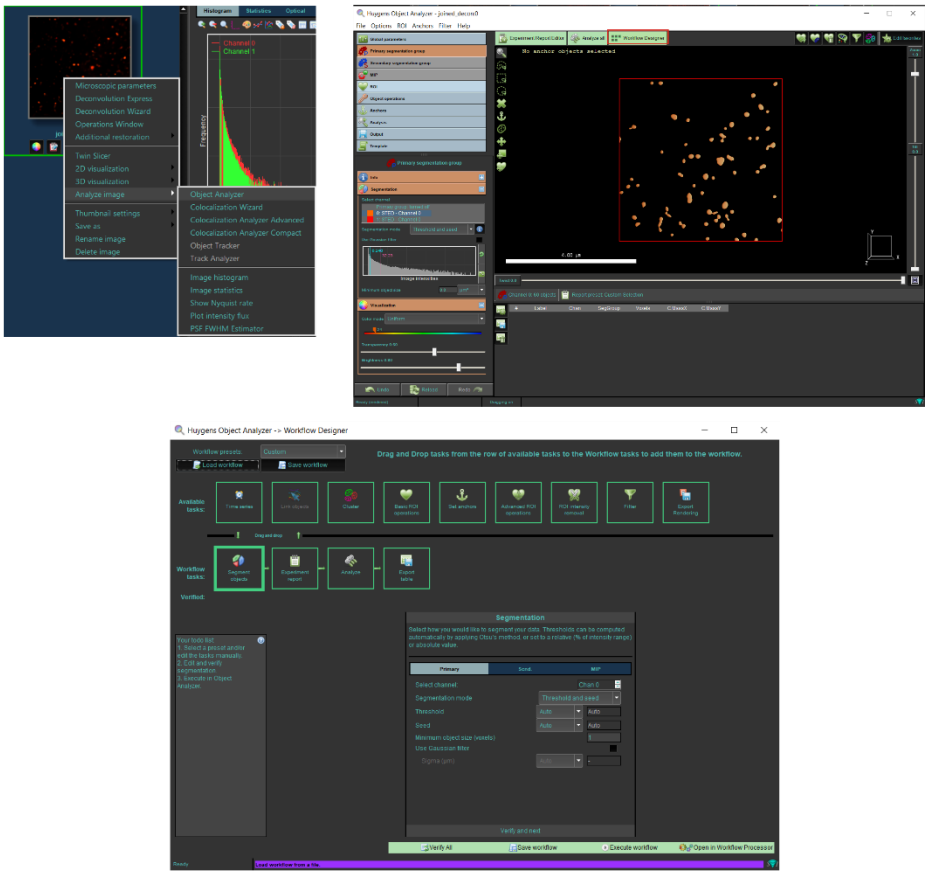

6. Colocalization analysis: right click image -- Analyze image -- Colocalization Wizard -- Threshold settings -- Select coefficients -- Export colocalization map / Save coefficients table

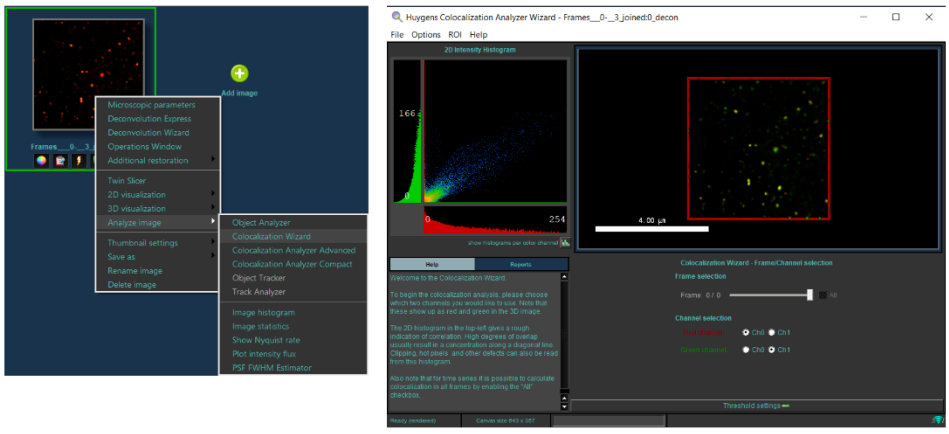

Figure S 2. Huygens deconvolution workflow.

Anni Colocalization Analysis Protocol

1. Open Anni -- Colocalization Analysis -- 2. Load files -- import photon gated tif files -- Click on Exported Images_0-3 folder
3. Set analysis for different channels, Orange dye: Green Photons, Red dye: Yellow Photons;
4. Set ROI size +- pixels 5 -- Threshold 10.

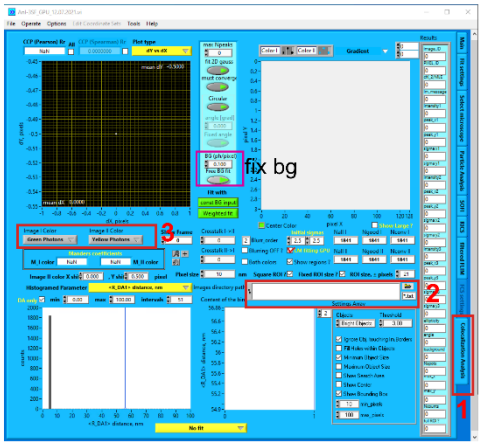

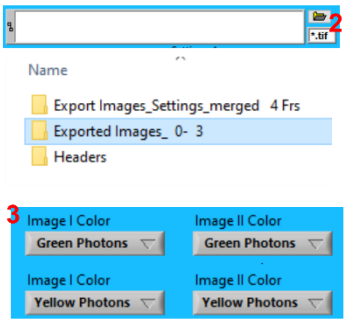

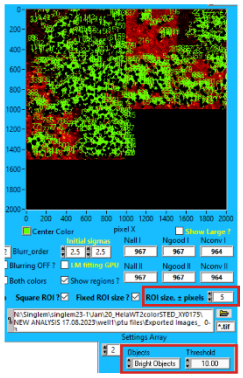

5. Generate Huygens ROI's -> load csv file (Summarize all spots data in one CSV file from Huygens Object Analysis with CMassX, CMassY; Filename with the same nomenclature as Exported Images_0-3 folder) -> Select as Export Folder -> OK

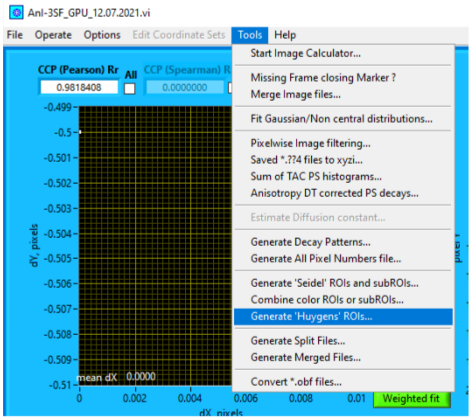

Label	Chan	SegGroup	Voxels	CMassX	CMassY	CMassZ	Filename
1	0	1	27	3.16E+02	3.23E+00	0.00E+00	well1position1
2	0	1	115	3.60E+02	2.97E+00	0.00E+00	well1position1
3	0	1	90	4.20E+02	3.39E+00	0.00E+00	well1position1
4	0	1	96	2.70E+02	6.57E+00	0.00E+00	well1position1
5	0	1	12	7.28E+01	1.11E+01	0.00E+00	well1position1
6	0	1	8	7.96E+01	1.13E+01	0.00E+00	well1position1
7	0	1	13	2.24E+01	1.44E+01	0.00E+00	well1position1
8	0	1	25	3.06E+02	1.51E+01	0.00E+00	well1position1
9	0	1	62	1.61E+02	1.84E+01	0.00E+00	well1position1
10	0	1	168	3.83E+02	1.85E+01	0.00E+00	well1position1

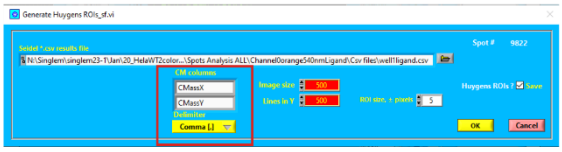

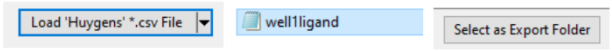

6. Overlay of ROI's: Operate -> Selected ROIs Overlay -> select "Both_Huygens ROIs_+-5 -> select one file -> ok
7. Save fitting result: File -> Export -> Imagewise Colocalization fit results -> select *.ptu

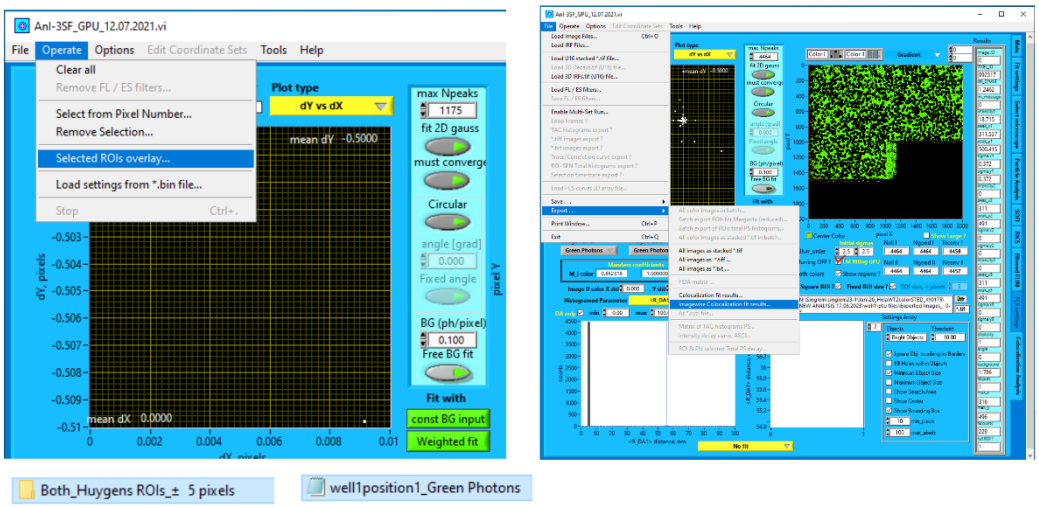

8.Margarita- Import Imagewise Colocalization fit results: File -> Import Colocalization/Fit results -> select "sigma x_cl" and "<N_ph> per pixel_cl" -> 2D bins: 15 -> outlyers
9. Move red/blue cursor like in the image (cut out 0 photons per pixel and 0 sigma values) -> select region

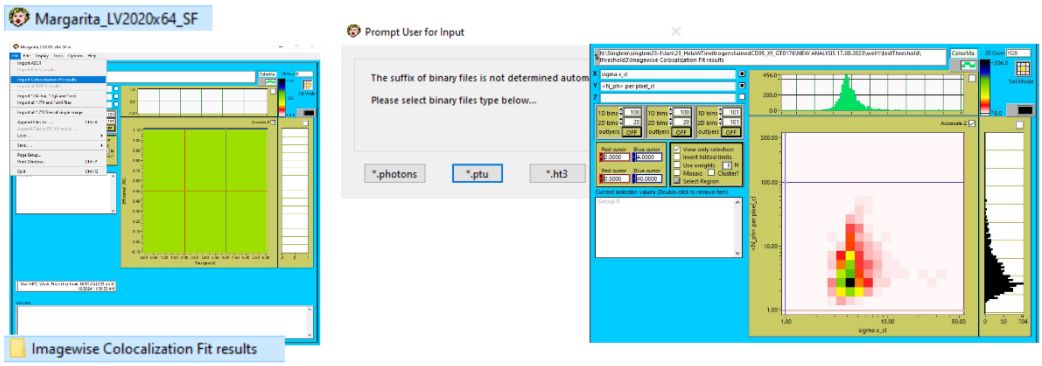

10. Saving for Origin plots: File -> Save -> Probabilities as ASCII: Origin 8.6

Figure S 3. Ani colocalization workflow.

1. Make a local folder in D:/ drive with the data folder and code package folder saved in the same main folder

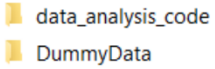

2. Run the code using Jupyter notebook by Anaconda Prompt command

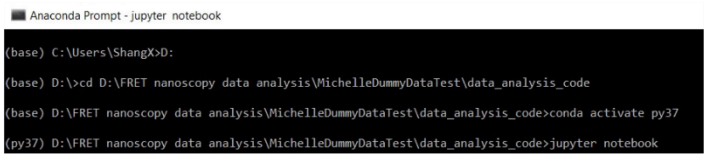

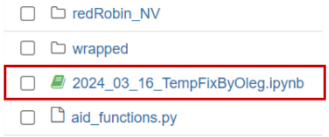

3. Change the data path and the sample name in the global settings, then run each cell step by step

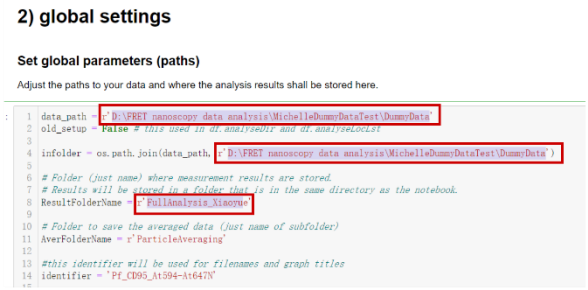

4. Localization analysis: Change the gating value read from Anni. Set verbose to 'True' for visualize fittings or 'False' to get faster fittings

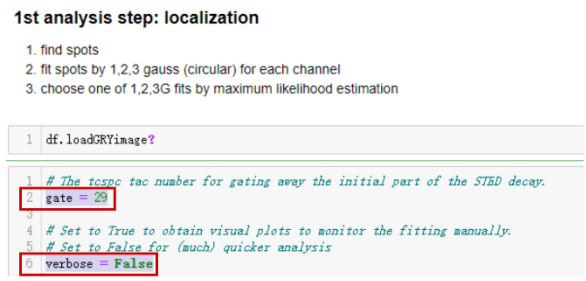

5. FRET analysis: change the background value read from Anni). Set verbose to 'True' for visualize fittings or 'False' to get faster fittings

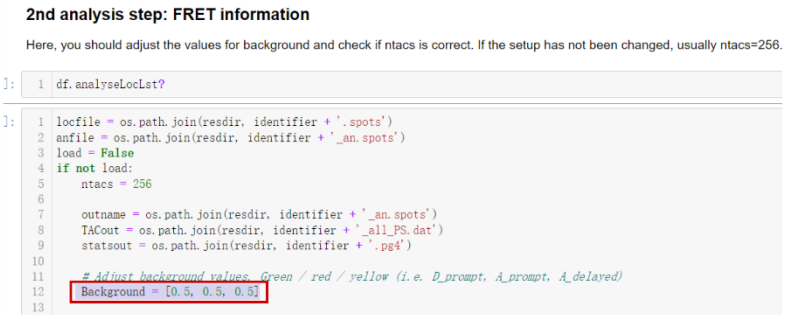

6. Non-centered Chi fit (ncChi) of A-A distance:
change the initial guess/boundaries for better fitting results

Non-centered chi Fit

To judge the ideal number of components, the Akaike Information Criterion (AIC) can be considered. Given a set of candidate models for the data, the **preferred model** is the one with the **minimum AIC** value:

$$AIC = 2 \cdot (\#\text{ of parameters} - ln(\hat{L}))$$

where $\hat{L}$ is the max. value of the likelyhood function for the model.

```
# [Noah]: Up to 3 gaussians possible. Oleg: not gaussians but ncChi
A  = [1200, 1000]     # Amplitudes
my = [79, 105]        # Means
sigma = [15, 15]      # Width
BG = 0                # Noise level
```

7. Support plane: copy and paste the results from ncChi fit into the code and change boundaries and parameters of scanning

```
———————— Results for copy-pasting ————————

p = hfit.genPeakEst(2, counts, bincenters)
p['bg'].set(vary = False, value = 0)
p['mu0'].set(vary = True, value = 79.4)
p['A0'].set(vary = True, value = 372.85)
p['sig0'].set(vary = True, value = 3.63)
p['mu1'].set(vary = True, value = 158.24)
p['A1'].set(vary = True, value = 70560.0)
p['sig1'].set(vary = True, value = 8701.12)
#p['mu2'].set(vary = False, value = 1)
#p['sig2'].set(vary = False, value = 1)
#p['A2'].set(vary = False, value = 1)
```

Support plane

OPEN QUESTION: Are the contour values of 0.6 pMax and 0.135 pMax arbitrarily chosen or is there a specific reason behind this?

As of now, the matrix plot looks distorted. This needs to be fixed. In module hfit, there is quite a lot going on, especially with regards to how axis ticks are being defined/generated etc.. I strongly consider to rewrite the function and use the module seaborn instead, rather than matplotlib. It seems relatively easy to use for such plots. Further, since in the current state, the axis ticks tend to go haywire every now and then, I do not think it seems too good of a decision to continue using them in the current form. Probably we should therefore consider a different way of setting axis ticks.

```
from importlib import reload
reload(hfit)
```

```
<module 'histogram_fitting' from 'D:\\FRET nanoscopy data analysis\\MichelleDummyDataTest\\data_analysis_code\\histogram_fitting.py'>
```

```
#once you've created your support plane surface, you may re-load it.
load = False

#set the parameters you'd like to scan.
Scan_mu = [75, 83, 40]     # Lower val, upper val, steps
Scan_sig = [3, 5, 40]      # Lower val, upper val, steps

# [Noah: LB, UB, Inc.] Adjustment of entered parameters to match required format for parameter scan.
muScan = np.arange(Scan_mu[0], Scan_mu[1]+0.5*(Scan_mu[1]-Scan_mu[0])/Scan_mu[2], (Scan_mu[1]-Scan_mu[0])/Scan_mu[2])
sigmaScan = np.arange(Scan_sig[0], Scan_sig[1]+0.5*(Scan_mu[1]-Scan_mu[0])/Scan_mu[2], (Scan_sig[1]-Scan_sig[0])/Scan_sig[2])

#print(muScan)
#print(sigmaScan)

param_ranges={"sig0":sigmaScan,"mu0":muScan}
#set these settings the same as your optimal fit
p = hfit.genPeakEst(2, counts, bincenters)
p['bg'].set(vary = False, value = 0)
p['mu0'].set(vary = True, value = 79.4)
p['A0'].set(vary = True, value = 372.85)
p['sig0'].set(vary = True, value = 3.63)
p['mu1'].set(vary = True, value = 158.24)
p['A1'].set(vary = True, value = 70560.0)
p['sig1'].set(vary = True, value = 8701.12)
#p['mu2'].set(vary = False, value = 1)
#p['sig2'].set(vary = False, value = 1)
#p['A2'].set(vary = False, value = 1)
```

you can change it to "sig1" and "mu1"

copy and paste here

7. FRET distance analysis: select no FRET (NF) and high FRET (HF) species using filter criteria

6) no FRET distance analysis ¶

settings and filter settings

Execute these functions in order to obtain your result. Select the NF-s
expected at low proxRatios. For further refinement, you can add a filt
pairs. As a rule of thumb, in case you decide to use the tauG-cut: Tak
most donor dyes, D-only lifetime is around (3.5-4.0) ns.

```
# we want to isolate the noFRET species using these se
# we want to include as many potential FRET pairs as p
slocLst = df.selectSpotOccurence(locLst_an, [1, 2], [1

# It would probably be safer to only include correctly
# so if it does not change the result, it is likely a

# Filter criteria
EproxFilter = [0.2, 0.55]    # Proximity ratio
TauG_Filter = [2.7, 4.2]     # Donor lifetime
```

7) high FRET distance analysis

settings and filter settings

execute these functions in order to obtain your result.

Same as above for NF, filter your data using the given criteria. We expect the HF populat
fluorescence lifetime.

```
# we want to isolate the high FRET species using these selection crite
# we want to include as many potential FRET pairs as possible, so we ir
slocLst = df.selectSpotOccurence(locLst_an, [1, 2], [1, 2])

# It would probably be safer to only include correctly labeled structur
# so if it does not change the result, it is likely a valid decision to

# Filter criteria
EproxFilter = [0.53, 0.89]    # Proximity ratio
TauG_Filter = [0.5, 2.5]      # Donor lifetime
```

8. Particle averaging: choose the best anchor from data anaylsis of next cell and repeat this step

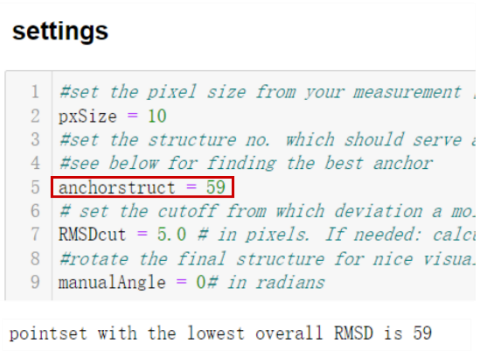

9. Make a new folder an empty text file for D0Aonly populations and theoretical precision export

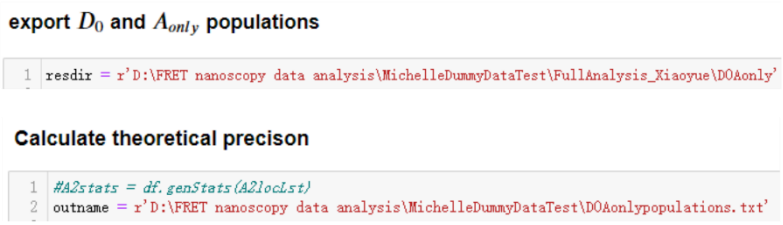

Figure S 4. FRET nanoscopy data analysis workflow.

Load images batchwise, Anl colocalization analyzes localization of each spot from different channels automatically

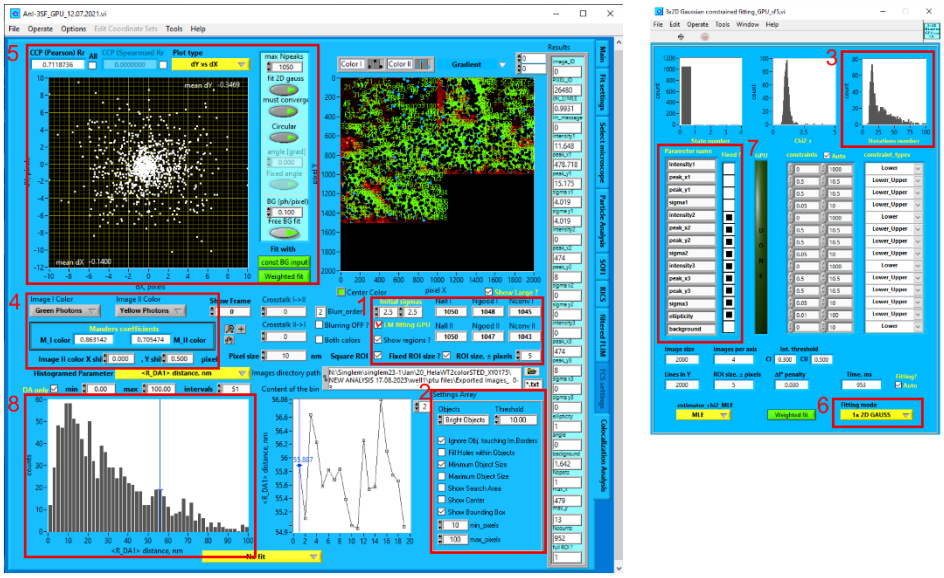

1. Initial sigmas --- initial guess from color I and II; ROI size --- fitting is affected by defined ROI size (5-7 is good)
   Nall I/II --- all ROIs from color I/II; Ngood I/II --- spots # not hitting on borders; Nconv I/II: # of fits converging;
2. Threshold --- Segmentation object threshold (relative threhold);
   Minimum Object Size --- The minimum size of Gaussian should be more than 10 pixels
3. Iteration numbers: a fit will converge after 100 iteractions and find minimum otherwise it will fail

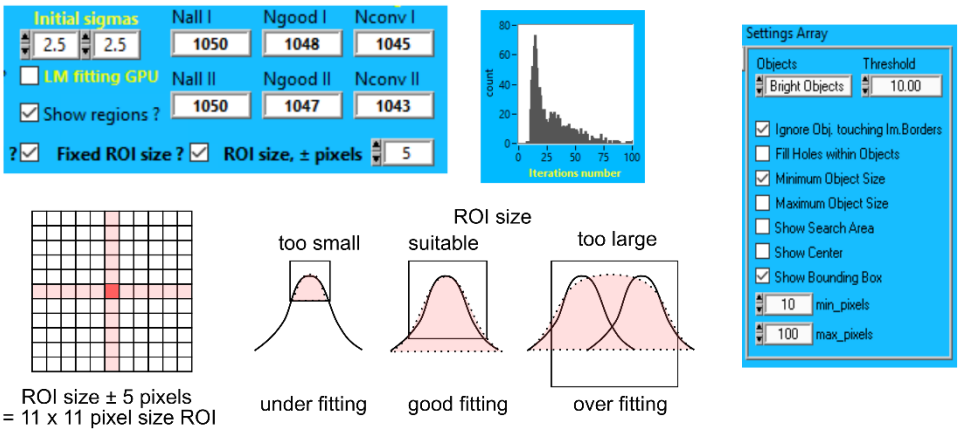

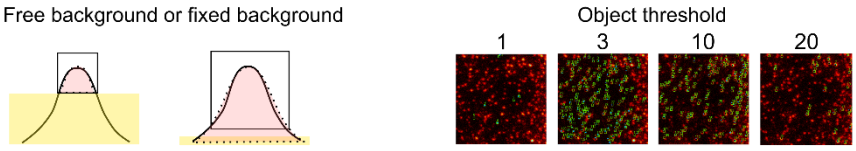

4. Calculation of colocalization between two channels with: Manders coefficients --- I in II and II in I;
   Scanner correction --- on Y axis, scanner introduced channel shift with 0.5 pixel between line step 1 and 2

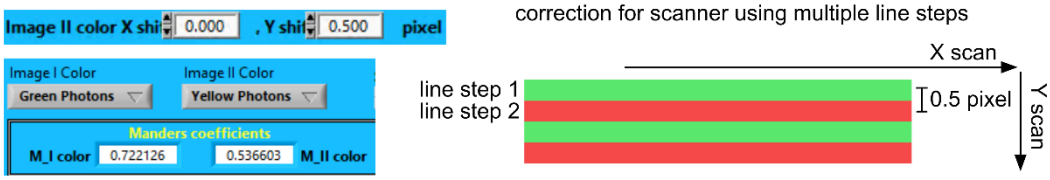

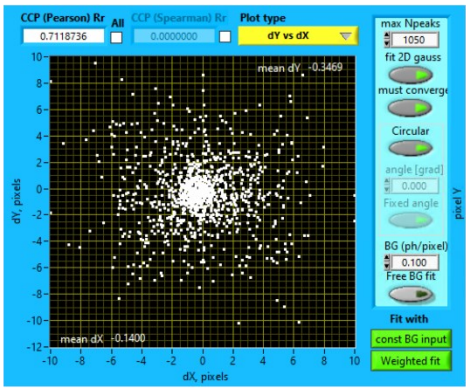

5. Relative X/Y distance of fitted spots between channel I/II:
   fit 2D Gaussian --- 1, 2, 3 or Auto N (1-3) Gaussians
   must Converge --- yes
   Circular ---- circular or elliptical spots fittinh
   BG (ph/pixel) --- fits can be fixed with defined background

Coloalization coefficient in two channels:
i) First, two channels I/II were merged;
ii) Second, intensities were merged to find ROI
iii) Keep the ROIs same for I/II channel to fit Gaussians separetely

6. Fitting mode: 1/2/3 x 2D GAUSS, Auto N spot (max 3) --- Each ROI can be fitted with 1, 2, 3 or 1-3 Gaussians
7. Parameter name Fixed or not --- depends on how much Gaussian will be used in the fit (sigmas, intensities...)
8. R_DA1 distance --- from 5. the norm distance of relative X Y distances are calculated and binned in histogram

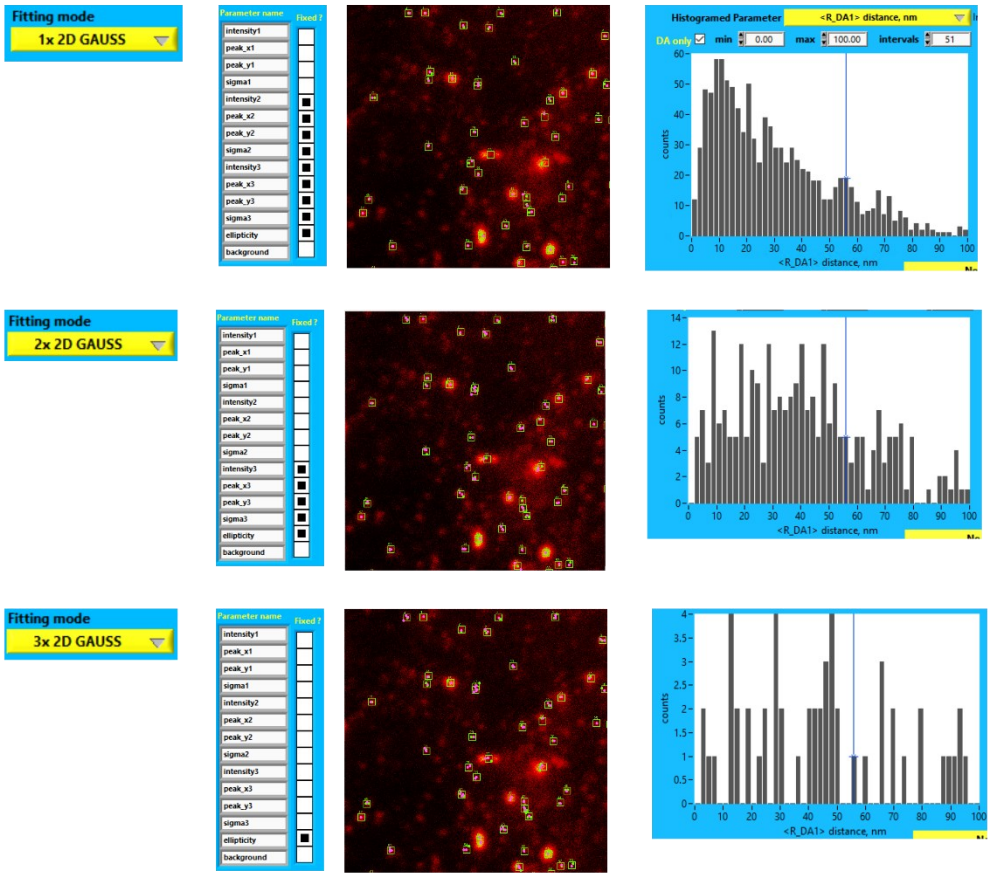

In each ROI spots fitting in two color: green and pink as well as numbers of fits can be visualized.
Histograms are getting deteriorated with 2/3 Guassian

Figure S 5. Description of Ani colocalization software.

Abbreviations

Abbreviation	Definition
PCD	Programmed cell death
BAX	Bcl-2-associated protein x
BAK	Bcl-2 homologs killer
APAF1	apoptotis peptidase activating factor 1
DISC	death-inducing signaling complex
CD95	Cluster of Differentiation 95
CD95L	CD95 ligand
TNF-α	tumor necrosis factor-α
TRAIL	TNF-related apoptosis-inducing ligand
GITRL	glucocorticoid-induced TNFR-related protein
LTαβ	lymphotoxin αβ
THD	TNF homology domain
CRD	cysteine-rich domains
TMD/TM	transmembrane domain
PRD	proline-rich domain
ICD	intracellular domain
ECD	extracellular domain
MMP	metalloprotease
TM	transmembrane
TRAF	tumor necrosis factor TNF receptor-associated factors
FADD	FAS-associated death domain
RIP	ribosome-inactivating protein
DD	death domain
DR	death receptor
DcR	decoy receptor
DED	death effector domain
MAPK	mitogen-activated protein kinases
NF-κB	nuclear factor kappa B
PI3K	phosphoinositide 3-kinase
RAF-1	RAF proto-oncogene serine/threonine-protein kinase
MEF	myocyte enhancer factor
ERK	extracellular signal-regulated kinase
Akt	protein kinase B
FRET	Förster resonance energy transfer
CTLA4	cytotoxic T-lymphocyte associated protein 4
STED	stimulated emission depletion
cPBSA	confocal photobleaching step analysis
CELFIS	cell lifetime FRET (Förster resonance energy transfer) image spectroscopy
DISC	death-inducing signaling complex
IZ	isoleucine zipper

TNFSF	tumor necrosis factor super family
TNFRSF	tumor necrosis factor receptor super family
SFK	src-family kinase
mCD95L	membrane bound CD95 ligand
sCD95L	soluble CD95 ligand
TNC	tenascin-C
PLAD	pre-ligand assembly domain
Cys	cysteine
Asn	asparagine
RMSD	root mean square deviation
GFP	green fluorescent protein
ND	neutral density
PH	pinhole
APD	avalanche photodiode
PSF	point spread function
TEM	transmission electron microscopy
PIE	pulsed interleaved excitation
SLM	spatial light modulator
PBS	polarized beam splitter
CCD	charge-coupled device
CMOS	complementary metal oxide semiconductor
TCSPC	time-correlated single photon counting
IRF	instrument response function
PTM	photomultiplier detector
FWHM	full-width half maximum
ELISA	enzyme-linked immunosorbent assay
SPR	surface plasmon resonance
SBP	streptavidin binding peptide
IPTG	isopropyl-ß-D-thiogalactopyranoside
ß-ME	ß-mercaptoethanol
E.coli	*Escherichia coli*
2 x YT	2 x yeast extract tryptone
pI	isoelectric point
LB	lysogeny broth
SDS-PAGE	Sodium dodecyl-sulfate polyacrylamide gel electrophoresis
HEK293	human embryonic kidney 293
DMEM	Dulbecco's modified eagle medium
DPBS	Dulbecco's phosphate-buffered solution
BSA	bovine serum albumin
FBS	fetal bovine serum
P/S	penicillin/streptomycin
PEI	polyethylenimine
TBS	tris-buffered saline
TCEP	tris(2-carboxyethyl)phosphine

PBS	phosphate-buffered saline
SDS-PAGE	sodium dodecyl-sulfate polyacrylamide gel electrophoresis
WB	western blot
HRP	horseradish peroxidase
ECL	enhanced chemiluminescence
CN PAGE	clear native polyacrylamide gel electrophoresis
SEC	size exclusion chromatography
DTT	dithiothreitol
FA	formaldehyde
TRAIL	TNF related apoptosis inducing ligand
UA	uranyl acetate
dll	dynamic link library
RMSD	root mean square deviation

List of Tables

List of Figures

References

1. Hotchkiss RS, Strasser A, Mcdunn JE, Swanson PE. Cell Death. N Engl J Med. 2009;361:1570–83.
2. Kerr JFR, Wyllie AH, Curriet AR. APOPTOSIS: A BASIC BIOLOGICAL PHENOMENON WITH WIDE-RANGING IMPLICATIONS IN TISSUE KINETICS. Br J Cancer. 1972;26:239.
3. Elmore S. Apoptosis: A Review of Programmed Cell Death. Vol. 35, Toxicologic Pathology. 2007. p. 495–516.
4. Green DR, Llambi F. Cell death signaling. Cold Spring Harb Perspect Biol. 2015 Dec 1;7(12).
5. Thomas D. Pollard, William C. Earnshaw, Jennifer Lippincott-Schwartz, Graham Johnson. Cell Biology. 3rd Edition. Thomas D. Pollard, Jennifer Lippincott-Schwartz, William C. Earnshaw, Graham T. Johnson, editors. Elsevier Health Sciences; 2016. 797–815 p.
6. Jacobson MD, Weil M. Programmed Cell Death Review in Animal Development. Vol. 88, Cell. 1997.
7. Bertheloot D, Latz E, Franklin BS. Necroptosis, pyroptosis and apoptosis: an intricate game of cell death. Cell Mol Immunol. 2021 May 1;18(5):1106–21.
8. Aggarwal BB. Signalling pathways of the TNF superfamily: A double-edged sword. Vol. 3, Nature Reviews Immunology. Nature Publishing Group; 2003. p. 745–56.
9. Dostert C, Grusdat M, Letellier E, Brenner D. The TNF Family of Ligands and Receptors: Communication Modules in the Immune System and Beyond. Physiol Rev [Internet]. 2019;99:115–60. Available from: www.prv.org
10. Chattopadhyay K, Ramagopal UA, Brenowitz M, Nathenson SG, Almo SC. Evolution of GITRL immune function: Murine GITRL exhibits unique structural and biochemical properties within the TNF superfamily. 2008; Available from: www.pnas.org/cgi/content/full/
11. Tschopp J, Schneider P, Bodmer JL. The molecular architecture of the TNF superfamily. Trends Biochem Sci [Internet]. 2002;27(1). Available from: http://tibs.trends.com
12. Locksley RM, Killeen N, Lenardo MJ. The TNF and TNF Receptor Review Superfamilies: Integrating Mammalian Biology. Cell [Internet]. 2001;104:487–501. Available from: http://www.gene.
13. Levoin N, Jean M, Legembre P. CD95 Structure, Aggregation and Cell Signaling. Front Cell Dev Biol. 2020 May 5;8:314.
14. Liu W, Zhan C, Cheng H, Kumar PR, Bonanno JB, Nathenson SG, et al. Mechanistic basis for functional promiscuity in the TNF and TNF Receptor superfamilies: Structure of the light:DcR3 assembly. Structure. 2014 Sep 2;22(9):1252–62.
15. Vanamee ÉS, Faustman DL. Structural principles of tumor necrosis factor superfamily signaling [Internet]. Vol. 11, Sci. Signal. 2018. Available from: http://stke.sciencemag.org/

16. Scott FL, Stec B, Pop C, Dobaczewska MK, Lee JJ, Monosov E, et al. The Fas-FADD death domain complex structure unravels signalling by receptor clustering. Nature. 2009 Feb 19;457(7232):1019–22.
17. Dickens LS, Boyd RS, Jukes-Jones R, Hughes MA, Robinson GL, Fairall L, et al. A Death Effector Domain Chain DISC Model Reveals a Crucial Role for Caspase-8 Chain Assembly in Mediating Apoptotic Cell Death. Mol Cell. 2012 Jul 27;47(2):291–305.
18. Risso V, Lafont E, Le Gallo M. Therapeutic approaches targeting CD95L/CD95 signaling in cancer and autoimmune diseases. Cell Death Dis. 2022 Mar 1;13(3).
19. Chen L, Park SM, Tumanov A V., Hau A, Sawada K, Feig C, et al. CD95 promotes tumour growth. Nature. 2010 May 27;465(7297):492–6.
20. Neumann L, Pforr C, Beaudouin J, Pappa A, Fricker N, Krammer PH, et al. Dynamics within the CD95 death-inducing signaling complex decide life and death of cells. Mol Syst Biol. 2010;6:352.
21. Dhillon AS, Hagan S, Rath O, Kolch W. MAP kinase signalling pathways in cancer. Oncogene. 2007 May 14;26(22):3279–90.
22. Krens SFG, Spaink HP, Snaar-Jagalska BE. Functions of the MAPK family in vertebrate-development. FEBS Lett. 2006 Sep 18;580(21):4984–90.
23. Kreuz S, Siegmund D, Rumpf JJ, Samel D, Leverkus M, Janssen O, et al. NFκB activation by Fas is mediated through FADD, caspase-8, and RIP and is inhibited by FLIP. Journal of Cell Biology. 2004 Aug 2;166(3):369–80.
24. Liu T, Zhang L, Joo D, Sun SC. NF-κB signaling in inflammation. Signal Transduct Target Ther. 2017;2.
25. Tauzin S, Chaigne-Delalande B, Selva E, Khadra N, Daburon S, Contin-Bordes C, et al. The naturally processed CD95L Elicits a c-yes/Calcium/PI3K-driven cell migration pathway. PLoS Biol. 2011;9(6).
26. Scott FL, Stec B, Pop C, Dobaczewska MK, Lee JJ, Monosov E, et al. The Fas-FADD death domain complex structure unravels signalling by receptor clustering. Nature. 2009 Feb 19;457(7232):1019–22.
27. Wang L, Yang JK, Kabaleeswaran V, Rice AJ, Cruz AC, Park AY, et al. The Fas-FADD death domain complex structure reveals the basis of DISC assembly and disease mutations. Nat Struct Mol Biol. 2010 Nov;17(11):1324–9.
28. Vanamee ÉS, Lippner G, Faustman DL. Signal Amplification in Highly Ordered Networks Is Driven by Geometry. Cells. 2022 Jan 2;11(2).
29. Torrey H, Butterworth J, Mera T, Okubo Y, Wang L, Baum D, et al. Targeting TNFR2 with antagonistic antibodies inhibits proliferation of ovarian cancer cells and tumor-associated T regs. Sci Signal [Internet]. 2017;10(462):eaaf8608. Available from: https://www.science.org
30. Tuthill MH, Montinaro A, Zinngrebe J, Prieske K, Draber P, Prieske S, et al. TRAIL-R2-specific antibodies and recombinant TRAIL can synergise to kill cancer cells. Oncogene. 2014 Jun 9;34(16):2138–44.
31. Bartels N, M van der Voort NT, Opanasyuk O, Felekyan S, Greife A, Shang X, et al. Advanced multiparametric image spectroscopy and super-resolution microscopy reveal a minimal model of CD95 signal initiation. Sci Adv [Internet]. 2024;10(35):eadn3238. Available from: https://www.science.org

32. Itoh N, Yonehara S, Ishii A, Yonehara M, Mizushima SL, Sameshima M, et al. The Polypeptide Encoded by the cDNA for Human Cell Surface Antigen Fas Can Mediate Apoptosis. Cell. 1991;66:233–43.
33. Chodorge M, Züger S, Stirnimann C, Briand C, Jermutus L, Grütter MG, et al. A series of Fas receptor agonist antibodies that demonstrate an inverse correlation between affinity and potency. Cell Death Differ. 2012 Jul;19(7):1187–95.
34. Kischkel FC, Hellbardt S, Behrmann I, Germer M, Pawlita M, Krammer PH, et al. Cytotoxicity-dependent APO-1 (Fas/CD95)-associated proteins form a death-inducing signaling complex (DISC) with the receptor. EMBO Journal. 1995;14(22):5579–88.
35. Scaffidi C, Fulda S, Srinivasan A, Friesen C, Li F, Tomaselli KJ, et al. Two CD95 (APO-1/Fas) signaling pathways. EMBO J. 1998;17(6):1675–87.
36. Krueger A, Fas SC, Baumann S, Krammer PH. The role of CD95 in the regulation of peripheral T-cell apoptosis. Immunol Rev. 2003 Jun;193:58–69.
37. Tanaka M, ltaj T, Adachi M, Nagata S. Downregulation of Fas ligand by shedding. Nat Med. 1998;4:31–6.
38. Blott EJ, Bossi G, Clark R, Zvelebil M, Griffiths GM. Fas ligand is targeted to secretory lysosomes via a proline-rich domain in its cytoplasmic tail. J Cell Sci. 2001;114(13):2405–16.
39. Fu Q, Fu TM, Cruz AC, Sengupta P, Thomas SK, Wang S, et al. Structural Basis and Functional Role of Intramembrane Trimerization of the Fas/CD95 Death Receptor. Mol Cell. 2016 Feb 18;61(4):602–13.
40. Risso V, Thomas M, Guével B, Lavigne R, Com E, Martin S, et al. Metalloprotease-mediated cleavage of CD95 ligand. FEBS J. 2023;290(12):3145–65.
41. O Reilly LA, Tai L, Lee L, Kruse EA, Grabow S, Fairlie WD, et al. Membrane-bound Fas ligand only is essential for Fas-induced apoptosis. Nature. 2009 Oct 1;461(7264):659–63.
42. Suda T, Hashimoto H, Tanaka M, Ochi T, Nagata S. Membrane Fas Ligand Kills Human Peripheral Blood T Lymphocytes, and Soluble Fas Ligand Blocks the Killing. Journal of Experimental Medicine, J Exp Med. 1997;186(12):2045–50.
43. Chen J, Lu Y, Xu Z, Cen P, Fang X. Efficient expression and primary purification of 6-his tagged human Fas ligand in Dictyostelium discoideum. Biotechnol Lett. 2007 Jun;29(6):859–63.
44. Suda T, Takahashi T, Golstein P, Nagata' S. Molecular Cloning and Expression of the Fas Ligand, a Novel Member of the Tumor Necrosis Factor Family. Cell. 1993;75(6):1169–76.
45. Suda T, Nagata S. Purification and Characterization of the Fas-ligand that Induces Apoptosis. Journal of Experimental Medicine. 1994;179(3):873–9.
46. Sun KH, Sun GH, Tsai CY, Wang HH, Chung-I C, Lin G, et al. Expression, purification, refolding, and characterization of recombinant human soluble-Fas ligand from Escherichia coli. Enzyme Microb Technol. 2005 Mar 2;36(4):527–34.
47. Tanaka M, Suda T, Takahashi T, Nagata S. Expression of the functional soluble form of human Fas ligand in activated lymphocytes. EMBO J. 1995;14(6):1129–35.
48. Berg D, Lehne M, Müller N, Siegmund D, Münkel S, Sebald W, et al. Enforced covalent trimerization increases the activity of the TNF ligand family members TRAIL and CD95L. Cell Death Differ. 2007 Dec;14(12):2021–34.

49. Harbury PB, Zhang T, Kim PS, Alber T. A Switch Between Two-, Three-, and Four-Stranded Coiled Coils in GCN4 Leucine Zipper Mutants. Science (1979). 1993;262(5138):1401–7.
50. Shiraishi T, Suzuyama K, Okamoto H, Mineta T, Tabuchi K, Nakayama K, et al. Increased cytotoxicity of soluble Fas ligand by fusing isoleucine zipper motif. Biochem Biophys Res Commun. 2004 Sep 10;322(1):197–202.
51. Liesche C, Berndt J, Fricke F, Aschenbrenner S, Heilemann M, Eils R, et al. CD95 receptor activation by ligand-induced trimerization is independent of its partial pre-ligand assembly Insights into CD95 receptor activation by quantitative fluorescence microscopy approaches. 2018 Apr 2; Available from: https://doi.org/10.1101/293530
52. Kleber S, Sancho-Martinez I, Wiestler B, Beisel A, Gieffers C, Hill O, et al. Yes and PI3K Bind CD95 to Signal Invasion of Glioblastoma. Cancer Cell. 2008 Mar 11;13(3):235–48.
53. Holler N, Tardivel A, Kovacsovics-Bankowski M, Hertig S, Gaide O, Martinon F, et al. Two Adjacent Trimeric Fas Ligands Are Required for Fas Signaling and Formation of a Death-Inducing Signaling Complex. Mol Cell Biol. 2003 Feb 15;23(4):1428–40.
54. Schneider P, Holler N, Bodmer JL, Hahne M, Frei K, Fontana A, et al. Conversion of Membrane-bound Fas(CD95) Ligand to Its Soluble Form Is Associated with Downregulation of Its Proapoptotic Activity and Loss of Liver Toxicity. J Exp Med [Internet]. 1998;187(8):1205–13. Available from: http://www.jem.org
55. Shiraishi T, Suzuyama K, Okamoto H, Mineta T, Tabuchi K, Nakayama K, et al. Increased cytotoxicity of soluble Fas ligand by fusing isoleucine zipper motif. Biochem Biophys Res Commun. 2004 Sep 10;322(1):197–202.
56. Vanamee ÉS, Faustman DL. Structural principles of tumor necrosis factor superfamily signaling [Internet]. Vol. 11, Sci. Signal. 2018. Available from: http://stke.sciencemag.org/
57. Berger RML, Weck JM, Kempe SM, Hill O, Liedl T, Rädler JO, et al. Nanoscale FasL Organization on DNA Origami to Decipher Apoptosis Signal Activation in Cells. Small. 2021 Jul 1;17(26).
58. Siegel RM, Frederiksen JK, Zacharias DA, Chan FKM, Johnson M, Lynch D, et al. Fas preassociation required for apoptosis signaling and dominant inhibition by pathogenic mutations. Science (1979). 2000 Jun 30;288(5475):2354–7.
59. Cao J, Meng F, Gao X, Dong H, Yao W. Expression and purification of a natural N-terminal pre-ligand assembly domain of tumor necrosis factor receptor 1 (TNFR1 PLAD) and preliminary activity determination. Protein Journal. 2011;30(4):281–9.
60. Pan L, Fu TM, Zhao W, Zhao L, Chen W, Qiu C, et al. Higher-Order Clustering of the Transmembrane Anchor of DR5 Drives Signaling. Cell. 2019 Mar 7;176(6):1477-1489.e14.
61. Chodorge M, Züger S, Stirnimann C, Briand C, Jermutus L, Grütter MG, et al. A series of Fas receptor agonist antibodies that demonstrate an inverse correlation between affinity and potency. Cell Death Differ. 2012 Jul;19(7):1187–95.
62. Huang B, Eberstadt M, Olejniczak ET, Meadows RP, Fesik SW. NMR structure and mutagenesis of the Fas (AP0-1/CD95) death domain. Nature. 1996;384:638–41.

63. Liu W, Ramagopal U, Cheng H, Bonanno JB, Toro R, Bhosle R, et al. Crystal Structure of the Complex of Human FasL and Its Decoy Receptor DcR3. Structure. 2016 Nov 1;24(11):2016–23.
64. Bajorath J. Analysis of Fas-ligand interactions using a molecular model of the receptor-ligand interface. J Comput Aided Mol Des. 1999;13(4):409–18.
65. Schneider P, Bodmer JL, Holler N, Mattmann C, Scuderi P, Terskikh A, et al. Characterization of Fas (Apo-1, CD95)-Fas ligand interaction. Journal of Biological Chemistry, JBC. 1997;272(30):18827–33.
66. Bajorath J. Identification of the ligand binding site in Fas (CD95) and analysis of Fas-ligand interactions. Proteins: Structure, Function and Genetics. 1999 Jun 1;35(4):475–82.
67. Murphy DB., Davidson MW. Fundamentals of light microscopy and electronic imaging. Second edition. Wiley-Blackwell; 2013.
68. Agrawal M, Prasad VVSH, Nijhawan G, Jalal SS, Rajalakshmi B, Dwivedi SP. A Comprehensive Review of Electron Microscopy in Materials Science: Technological Advances and Applications. E3S Web of Conferences. 2024 Mar 25;505.
69. Sahl SJ, Hell SW, Jakobs S. Fluorescence nanoscopy in cell biology. Nat Rev Mol Cell Biol. 2017;18(11):685–701.
70. Masters BR. Mathematical Description of Abbe's Theory of Image Formation in the Microscope Based on Diffraction. In: Springer Series in Optical Sciences. Springer; 2020. p. 153–61.
71. Müller T, Schumann C, Kraegeloh A. STED microscopy and its applications: New insights into cellular processes on the nanoscale. ChemPhysChem. 2012 Jun 4;13(8):1986–2000.
72. Blom H, Brismar H. STED microscopy: Increased resolution for medical research? Vol. 276, Journal of Internal Medicine. Blackwell Publishing Ltd; 2014. p. 560–78.
73. Price SP, Davidson MW. The Stimulated Emission Depletion (STED) Concept.
74. Renk KF. Graduate Texts in Physics Basics of Laser Physics [Internet]. Second Edition. Springer; 2017. 17–26 p. Available from: http://www.springer.com/series/8431
75. Jameson DM, Ross JA. Fluorescence polarization/anisotropy in diagnostics and imaging. Chem Rev. 2010 May 12;110(5):2685–708.
76. Lea WA, Simeonov A. Fluorescence polarization assays in small molecule screening. Expert Opin Drug Discov. 2011 Jan;6(1):17–32.
77. Hendrix J, Lamb DC. Pulsed interleaved excitation: Principles and applications. In: Methods in Enzymology. Academic Press Inc.; 2013. p. 205–43.
78. Kudryavtsev V, Sikor M, Kalinin S, Mokranjac D, Seidel CAM, Lamb DC. Combining MFD and PIE for accurate single-pair förster resonance energy transfer measurements. ChemPhysChem. 2012;13(4):1060–78.
79. Zambrana-Puyalto X. Waveplates: physical principles, uses and purchase tips. Photoniques. 2020 Sep;(104):53–7.
80. Träger F. Springer Handbook of Lasers and Optics. 2nd Edition. Springer; 2012.
81. Neupane B, Chen F, Sun W, Chiu DT, Wang G. Tuning donut profile for spatial resolution in stimulated emission depletion microscopy. Review of Scientific Instruments. 2013 Apr;84(4).
82. Lakowicz JR. Principles of Fluorescence Spectroscopy. Third Edition. Springer; 2019.

83. TCSPC – What is Time-Correlated Single Photon Counting? 2023.
84. Vicidomini G, Schönle A, Ta H, Han KY, Moneron G, Eggeling C, et al. STED Nanoscopy with Time-Gated Detection: Theoretical and Experimental Aspects. PLoS One. 2013 Jan 18;8(1).
85. Vicidomini G, Moneron G, Han KY, Westphal V, Ta H, Reuss M, et al. Sharper low-power STED nanoscopy by time gating. Nat Methods. 2011 Jul;8(7):571–5.
86. Anderson N, Beeson R, Erdogan T. Angle-Tuned Thin-Film Interference Filters for Spectral Imaging. Opt Photonics News [Internet]. 2011;22(1):12–3. Available from: www.osa-opn.org
87. Wu Z, Xu X, Xi P. Stimulated emission depletion microscopy for biological imaging in four dimensions: A review. Microsc Res Tech. 2021 Sep 1;84(9):1947–58.
88. Singh H, Lu R, Rodríguez PFG, Wu Y, Bopassa JC, Stefani E, et al. Visualization and quantification of cardiac mitochondrial protein clusters with STED microscopy. Mitochondrion. 2012 Mar;12(2):230–6.
89. Hein B, Willig KI, Hell SW. Stimulated emission depletion (STED) nanoscopy of a fluorescent protein-labeled organelle inside a living cell. PNAS [Internet]. 2008;105(38):14271–6. Available from: www.pnas.orgcgidoi10.1073pnas.0807705105
90. Steffens H, Wegner W, Willig KI. In vivo STED microscopy: A roadmap to nanoscale imaging in the living mouse. Methods. 2020 Mar 1;174:42–8.
91. Szabó Á, Szöllősi J, Nagy P. Principles of Resonance Energy Transfer. Curr Protoc. 2022 Dec 1;2(12).
92. Budde JH, Van Der Voort N, Felekyan S, Folz J, Kühnemuth R, Lauterjung P, et al. FRET nanoscopy enables seamless imaging of molecular assemblies with sub-nanometer resolution. arXiv:210800024 . 2021 Jul 30;
93. Vicidomini G, Bianchini P, Diaspro A. STED super-resolved microscopy. Nat Methods. 2018 Mar 1;15(3):173–82.
94. Agarwal RP. Pythagorean Theorem Before and After Pythagoras. Advanced Studies in Contemporary Mathematics. 2020;30(3):357–89.
95. Hellenkamp B, Schmid S, Doroshenko O, Opanasyuk O, Kühnemuth R, Rezaei Adariani S, et al. Precision and accuracy of single-molecule FRET measurements—a multi-laboratory benchmark study. Nat Methods. 2018 Sep 1;15(9):669–76.
96. Barth A, Opanasyuk O, Peulen TO, Felekyan S, Kalinin S, Sanabria H, et al. Unraveling multi-state molecular dynamics in single-molecule FRET experiments. I. Theory of FRET-lines. Journal of Chemical Physics. 2022 Apr 14;156(14).
97. Rothemund PWK. Folding DNA to create nanoscale shapes and patterns. Nature. 2006 Mar 16;440(7082):297–302.
98. Pumm AK, Engelen W, Kopperger E, Isensee J, Vogt M, Kozina V, et al. A DNA origami rotary ratchet motor. Nature. 2022 Jul 21;607(7919):492–8.
99. Douglas SM, Marblestone AH, Teerapittayanon S, Vazquez A, Church GM, Shih WM. Rapid prototyping of 3D DNA-origami shapes with caDNAno. Nucleic Acids Res. 2009;37(15):5001–6.
100. Yang YR, Liu Y, Yan H. DNA Nanostructures as Programmable Biomolecular Scaffolds. Bioconjug Chem. 2015 Aug 19;26(8):1381–95.

101. Berger RML, Weck JM, Kempe SM, Hill O, Liedl T, Rädler JO, et al. Nanoscale FasL Organization on DNA Origami to Decipher Apoptosis Signal Activation in Cells. Small. 2021 Jul 1;17(26):2101678.
102. Perrault SD, Shih WM. Virus-inspired membrane encapsulation of DNA nanostructures to achieve in vivo stability. ACS Nano. 2014 May 27;8(5):5132–40.
103. Zadegan RM, Jepsen MDE, Thomsen KE, Okholm AH, Schaffert DH, Andersen ES, et al. Construction of a 4 Zeptoliters switchable 3D DNA box origami. ACS Nano. 2012 Nov 27;6(11):10050–3.
104. Kramm K, Schröder T, Gouge J, Vera AM, Gupta K, Heiss FB, et al. DNA origami-based single-molecule force spectroscopy elucidates RNA Polymerase III pre-initiation complex stability. Nat Commun. 2020 Dec 1;11(1):2828.
105. Tsukanov R, Tomov TE, Masoud R, Drory H, Plavner N, Liber M, et al. Detailed study of DNA hairpin dynamics using single-molecule fluorescence assisted by DNA origami. Journal of Physical Chemistry B. 2013 Oct 10;117(40):11932–42.
106. Harbury PB, Kim PS, Alber T. Crystal structure of an isoleucine zipper trimer. Nature. 1994 Sep 1;371:80–3.
107. Zhang L, Leng Q, Mixson AJ. Alteration in the IL-2 signal peptide affects secretion of proteins in vitro and in vivo. Journal of Gene Medicine. 2005 Mar;7(3):354–65.
108. Liesche C, Venkatraman L, Aschenbrenner S, Grosse S, Grimm D, Eils R, et al. Death receptor-based enrichment of Cas9-expressing cells. BMC Biotechnol. 2016 Feb 16;16:17.
109. Shang X, Bartels N, Weck JM, Suppmann S, Basquin J, Heuer-Jungemann A, et al. High yield purification of an Isoleucine zipper modified CD95 Ligand with either biotin or DNA-oligomer binding domain for efficient Cell Apoptosis Induction. 2024 Oct 13; Available from: http://biorxiv.org/lookup/doi/10.1101/2024.10.12.618001
110. Weck JM, Nair R, Kesici MZ, Shang X, Monzel C, Heuer-Jungemann A. Effects of DNA Origami-Based Nanoagent Design on Apoptosis Induction in a Large 3D Spheroid Model. 2025 Feb 17; Available from: http://biorxiv.org/lookup/doi/10.1101/2025.02.12.637807
111. Feig C, Tchikov V, Schütze S, Peter ME. Palmitoylation of CD95 facilitates formation of SDS-stable receptor aggregates that initiate apoptosis signaling. EMBO Journal. 2007 Jan 10;26(1):221–31.
112. Oshannessy DJ, Brighamburke M, Soneson KK, Hensley P, Brooks I. Determination of Rate and Equilibrium Binding Constants for Macromolecular Interactions Using Surface Plasmon Resonance. Anal Biochem. 1993;212(2):457–68.
113. Daghestani HN, Day BW. Theory and applications of surface plasmon resonance, resonant mirror, resonant waveguide grating, and dual polarization interferometry biosensors. Sensors. 2010 Nov;10(11):9630–46.
114. Daburon S, Devaud C, Costet P, Morello A, Garrigue-Antar L, Maillasson M, et al. Functional Characterization of a Chimeric Soluble Fas Ligand Polymer with In Vivo Anti-Tumor Activity. PLoS One. 2013 Jan 9;8(1).
115. Wahl M, Orthaus-Müller S. Time Tagged Time-Resolved Fluorescence Data Collection in Life Sciences [Internet]. Berlin; 2014 [cited 2025 Apr 10]. Available from: https://www.picoquant.com/images/uploads/page/files/14528/technote_tttr.pdf
116. Wahl M. The Principle of Time-Correlated Single Photon Counting. Berlin; 2014.

117. Brewer MJ, Butler A, Cooksley SL. The relative performance of AIC, AICC and BIC in the presence of unobserved heterogeneity. Methods Ecol Evol. 2016 Jun 1;7(6):679–92.
118. Ren TB, Xu W, Zhang W, Zhang XX, Wang ZY, Xiang Z, et al. A General Method to Increase Stokes Shift by Introducing Alternating Vibronic Structures. J Am Chem Soc. 2018 Jun 20;140(24):7716–22.
119. Gong W, Das P, Samanta S, Xiong J, Pan W, Gu Z, et al. Redefining the photo-stability of common fluorophores with triplet state quenchers: Mechanistic insights and recent updates. Chemical Communications. 2019;55(60):8695–704.
120. Lawrence J, Bernal J, Witzgall C. A purely algebraic justification of the Kabsch-Umeyama algorithm. J Res Natl Inst Stand Technol. 2019;124.
121. Walczak H, Miller RE, Ariail K, Gliniak B, Griffith TS, Kubin M, et al. Tumoricidal activity of tumor necrosis factor related apoptosis inducing ligand in vivo. Nat Med. 1999;5:157–63.
122. Tanaka M, Suda T, Yatomi T, Nakamura N, Nagata S. Lethal effect of recombinant human Fas ligand in mice pretreated with Propionibacterium acnes. Journal of immunology . 1997;158(5):2303–9.
123. Ogasawara J, Watanabe-Fukunaga R, Adachi M, Matsuzawa A, Kasugai T, Kitamura Y, et al. Lethal effect of the anti Fas antibody in mice. 1993.
124. Rozanov D V., Savinov AY, Golubkov VS, Rozanova OL, Postnova TI, Sergienko EA, et al. Engineering a leucine zipper-TRAIL homotrimer with improved cytotoxicity in tumor cells. Mol Cancer Ther. 2009 Jun;8(6):1515–25.
125. Graves JD, Kordich JJ, Huang TH, Piasecki J, Bush TL, Sullivan T, et al. Apo2L/TRAIL and the death receptor 5 agonist antibody AMG 655 cooperate to promote receptor clustering and antitumor activity. Cancer Cell. 2014 Aug 11;26(2):177–89.
126. Roy R, Hohng S, Ha T. A practical guide to single-molecule FRET. Vol. 5, Nature Methods. 2008. p. 507–16.

Statutory Declaration

I hereby confirm that, I presented this dissertation independently and without undue outside assistance under the compliance with the 'Principles for the Safety of Good Scientific Practice at the Heinrich Heine Universität Düsseldorf'.

Date and Place:
Xiaoyue Shang: